HZDR-096

ANNUAL REPORT 2018

INSTITUTE OF RESOURCE ECOLOGY

HZDR

HELMHOLTZ ZENTRUM
DRESDEN ROSSENDORF

Wissenschaftlich-Technische Berichte
HZDR-096

Annual Report 2018

Institute of Resource Ecology

Editorial board:

Prof. Dr. Thorsten Stumpf
Dr. Harald Foerstendorf
Dr. Frank Bok
Dr. Anke Richter

Impressum

Contact

Cover picture

After extensive upgrade works in 2018, The Rossendorf Beamline (RoBl) at the European Synchrotron Facility (ESRF) in Grenoble, France, now provides four different experimental stations to conduct X-ray absorption and emission spectroscopy, as well as surface, single crystal and high resolution powder diffraction. For actinide research, the alpha-nuclide laboratory environment was developed in such a way as to enable an easy transfer of samples between the experimental stations. Thus, samples can be easily investigated by several methods within one period of an allocated experiment (typically six days). After the completion of the ESRF storage ring rebuilt in 2020, the beamline will benefit from the superb beam brilliance, small source size and small beam divergence of the by then world leading synchrotron.

Photos taken by Denis Morel (www.denis-morel.com), floorplan by Juergen Claussner (HZDR)

Preface

THE INSTITUTE OF RESOURCE ECOLOGY (IRE) IS ONE of the eight institutes of the Helmholtz-Zentrum Dresden – Rossendorf (HZDR). The research activities are mainly integrated into the program "Nuclear Waste Management, Safety and Radiation Re-search (NUSAFE)" of the Helmholtz Association (HGF) and focused on the topics "Safety of Nuclear Waste Disposal" and "Safety Research for Nuclear Reactors".

Additionally, various activities are on-going investigating chemical and environmental aspects of processing and recycling of strategic metals, namely rare earth elements. These activities are located in the HGF program "Energy Efficiency, Materials and Resources (EMR)". Both programs, and therefore all work which is done at IRE, belong to the research sector "Energy" of the HGF.

Our research objective is the protection of humans and the environment from hazards caused by pollutants resulting from technical processes that produce energy and raw materials. Treating technology and ecology as a unit is the major scientific challenge in assuring the safety of technical processes and gaining their public acceptance. We investigate the ecological risks exerted by radioactive and non-radioactive metals in the context of nuclear waste disposal, the production of energy in nuclear power plants and in processes along the value chain of metalliferous raw materials. A common goal is to generate better understanding about the dominating processes essential for metal mobilization and immobilization on the molecular level by using advanced spectroscopic methods. This, in turn, enables us to assess the macroscopic phenomena, including models, codes and data for predictive calculations, which determine the transport and distribution of contaminants in the environment.

The extraordinary broadness of research topics and activities is illustrated below by some selected highlights:

At the Rossendorf Beamline in Grenoble, three new experimental stations for high-energy-resolution X-ray absorption and emission spectroscopy, single-crystal and surface diffraction were established in an alpha-lab environment. These three stations are linked to the existing XAFS station to allow measurements of radionuclide samples with all four techniques during a typical experiment cycle of six days. First multi-method experiments were already conducted on PuO_2 nanoparticles in the framework of the newly established ERC grant "TOP".

Driven by nuclear applications, classical ODS steels have taken a leap towards nanostructured ferritic alloys (NFA) within a decade. In a collaborative study led by researchers from HZDR, it was found that strengthening due to oxide nanoparticles, forest dislocations and grain boundaries, each counteracting dislocation glide, are the dominant strengthening mechanisms. Furthermore, the features responsible for the strength of NFAs have been shown to operate as point defect sinks and helium traps. This insight paves the way for application-dependent tailoring of materials in terms of irradiation tolerance and helium management. The work received the best paper award of the Journal of Nuclear Materials ($\rightarrow$ p. 71).

For the reactor dynamics program DYN3D being a part of the Helmholtz core simulator, a new solver for the neutron diffusion equation was developed and implemented ($\rightarrow$ p. 74). Test results with the new numerical method demonstrate a very good agreement with the reference solution and a higher accuracy than the solvers available so far without an increase of computation time.

In 2018, the powerful combination of analytical and numerical approaches to improve existing reactive transport concepts was exemplified. By using positron emission tomography and both conservative and reactive radiotracers, they reveal fluid pathways in and quantify surface reactivity of complex porous media. Thereby, updated numerical reactive transport codes allow for a realistic prediction of contaminant mobility in the environment ($\rightarrow$ p. 26).

In order to determine the influence of microbes on the behavior of radionuclides in the near and far field of a final disposal site for nuclear waste, the microbial diversity was investigated in rock salt. In this habitat, the halophilic archaeon *Halobacterium noricense* was identified as dominant organism. Spectroscopic and microscopic investigations of its interaction with U(VI) have shown, *H. noricense* forms phosphate minerals and thus contributes to the immobilization of uranium in rock salt ($\rightarrow$ p. 36).

Our endeavors regarding the complexation chemistry of the early actinides, have led to the synthesis of the first Pu(IV), Np(III), and U(V) complexes at HZDR. All complexes could be characterized spectroscopically in solution (NMR, UV-vis, IR, ESI-MS) and in the solid state (XAS, SC- and P-XRD) and could be further described by quantum chemical methods ($\rightarrow$ pp. 45).

Spectroscopic investigations of Eu(III) and Cm(III) aqueous complexation with phosphates were for the first time extended to higher temperatures ($25-80\,°C$). The species $Eu(H_2PO_4)^{2+}$ and $Cm(H_2PO_4)^{2+}$ could be proven and respective thermodynamic parameters $\Delta_r H°$ and $\Delta_r S°$ be derived. They allowed identifying an endothermic, entropy-driven complexation. This in turn is basis for a more realistic modelling of sorption processes and secondary phase formations at increased temperatures ($\rightarrow$ p. 58).
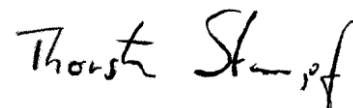
Beside these highlights, we obtained many other new scientific results in the past year, which are presented in this annual report. Furthermore, 95 original papers were published in peer-reviewed international scientific journals. In 2018, we increased the average impact factor to a value of 5.07. In the last year, more than 130 scientists, technicians, and students working on their Ph.D., diploma, master, or bachelor thesis, were employed at the Institute of Resource Ecology. Thereof, 32 Ph.D. students worked at the institute in 2018. Support of young scientists is an important tool to ensure the competence and further scientific excellence in future times. Therefore, we are pleased that Moritz Schmidt successfully defended his habilitation at TU Dresden, and was awarded the status Privatdozent in 2018. Furthermore, the HZDR Junior Research Group MicroSalt of Andrea Cherkouk was evaluated successfully in this year.

Another highlight in 2018 was the start of the professorship „Theoretical Chemistry" in April. Thomas Heine and his working group will be funded by both institutions HZDR and TU Dresden and will strengthen our link to the local university. I am sure that Thomas Heine and his coworkers will increase the visibility of our institute in the future.

Some new strategic partnerships were established in 2018. A vivid collaboration with teams from the HGF Research Field "Earth and Environment" will be funded by the Helmholtz Association of German Research Centers within the joint project iCross. Its final target is the setup of a Radioactive Waste Research Competence Center, building a unified and interoperable knowledge platform for all experimental data, knowledge and thermohydraulic-mechanical-chemical-biological (THMCB) simulation results across scales. Within the FORKA (Research for the decommissioning of nuclear installations) initiative of the German government, our institute develops interdisciplinary methods and tools for the minimization of radioactive waste through detailed material characterization and quantification before the start of the dismantling process. Hereby, our researchers rely on their broad experience in development and application of reactor safety analyses codes. The Helmholtz European Partnering funding program strengthens collaborative research in Europe. HZDR together with the Jožef Stefan Institute (JSI, Ljubljana, Slovenia) successfully applied for funding of a multidisciplinary project. During the next three years, a new junior research group at the Institute of Re-

source Ecology and at the Department of Environmental Sciences (JSI) is analyzing the interaction of technical nanomaterials with soil components by using novel radiolabeling methods.

In retrospect of a successful year 2018, I would like to thank the visitors, German and international ones, for their interest in our research and for their participation in the institute seminars. We would also like to thank our scientific collaborators and the visiting scientists for coming to Dresden – Rossendorf in 2018 to share their knowledge and experience with us. We will continue to strongly encourage the collaborations and visits by scientists in the future. Special thanks are due to the executive board of the HZDR, the Ministry of Science and Arts of the Free State Saxony (SMWK), the Federal Ministry of Education and Research (BMBF), the Federal Ministry of Economics and Energy (BMWi), the Deutsche Forschungsgemeinschaft (DFG), the European Commission, and other organizations for their support.

Prof. Dr. Thorsten Stumpf
Director of the
Institute of Resource Ecology

Contents

PART II: LONG-LIVED RADIONUCLIDES IN BIOLOGICAL SYSTEMS

PART III: THE CHEMISTRY OF LONG-LIVED RADIONUCLIDES

PART IV: NUCLEAR REACTOR SAFETY RESEARCH

PUBLICATIONS

SCIENTIFIC ACTIVITIES

PERSONNEL

ACKNOWLEDGEMENTS

INDEX OF AUTHORS

Long-Lived Radionuclides & Transport Phenomena in

GEOLOGICAL SYSTEMS

Cm(III) retention by calcium silicate hydrate (C-S-H) gel and secondary alteration phases in saline carbonate solutions

J. M. Wolter, N. Huittinen, K. Schmeide

Cm(III) retention by calcium silicate hydrate (C-S-H), portlandite (Ca(OH)₂) and their CaCO₃ polymorph alteration products calcite, vaterite, and aragonite was studied in saline carbonate-containing solutions. C-S-H gel with two different calcium to silicon (C/S) ratios of 1.0 and 2.0 were synthesized both in the absence and presence of Cm(III). Cm(III)-free C-S-H gel was analyzed with powder X-ray diffraction (XRD) for phase identification purposes, while the Cm(III)-doped samples were characterized applying site-selective time-resolved laser-induced luminescence spectroscopy (TRLFS). Subsequently, the time-dependent release of Cm(III) from the Cm(III)-doped C-S-H gel into surrounding brines containing 2.5 M NaCl/0.02 M NaHCO₃ or 0.02 M NaHCO₃ was monitored over a time period of 60 d. Results indicated that Cm(III) is not mobilized by carbonate but becomes either partially incorporated into secondary CaCO₃ phases or remains incorporated in the C-S-H structure. The presence of NaCl did not have an influence on the Cm(III) mobility in the investigated system.

The presence of concrete in a deep geological repository for the storage of spent nuclear fuel (SNF) and high-level nuclear waste is of high importance either as construction material for stabilization purposes or as barrier to seal shafts against water. Those concrete barriers contain hardened cement paste (HCP) which is a mixture of mineral phases such as C-S-H, portlandite, AF_t or AF_m.[1] Beside mechanical stability and the sealing of shafts, HCP and especially the C-S-H gel have been shown to retain radionuclides such as trivalent actinides which could potentially be released from SNF.[2, 3] The luminescent cation Cm(III) was chosen as a model for the actinides Pu(III) and Am(III) which contribute to the long-term radiotoxicity of SNF. Previous studies of U(VI) doped C-S-H gel exposed to saline carbonate solutions showed a significant release of incorporated U(VI) from C-S-H gel and a C-S-H structure decomposition.[4] Therefore, in the present work, Cm(III)-doped C-S-H gel was synthesized and exposed to saline carbonate-containing solutions to study the Cm(III) release from the C-S-H phase.

EXPERIMENTAL. All experiments were performed under inert gas conditions (N_2 atmosphere, CO_2 and $O_2 < 2$ ppm). C-S-H phases with two calcium-to-silicon (C/S) ratios (1.0 and 2.0) were prepared in alkaline background electrolyte (0.294 M NaOH, pH: 13.3) in the presence of 2.8×10^{-6} M Cm(III), starting from fumed silica and carbonate-free CaO, at a solid-to-liquid (S/L) ratio of 24 g/L. TRLFS measurements were performed at < 10 K using wavelengths between 600 and 625 nm for a selective excitation of the Cm(III) species. For leaching experiments, the C-S-H phases were equilibrated in 2.5 M NaCl/0.02 M NaHCO₃ or 0.02 M NaHCO₃ (S/L = 10 g/L) over a time period of 14 and 60 d.

RESULTS. Results of the binding mode study indicated the presence of at least two Cm(III) species: (*i*) Cm(III) with two to three water molecules in the first coordination sphere substituted against Ca^{2+} in the C-S-H interlayer and (*ii*) Cm(III) incorporated in the polyhedral CaO plane of the C-S-H structure with a total loss of the hydration sphere.
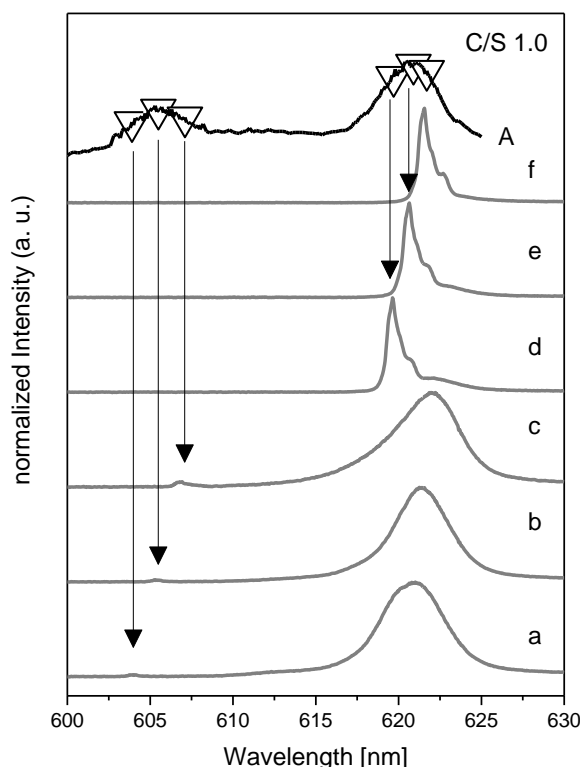
Fig. 1: Luminescence emission of Cm(III) incorporated into C-S-H (C/S 1.0). Excitation spectrum (A, top black line). Recorded emission spectra (a–f) after excitation at different wavelengths: 604.1 nm (a), 605.5 nm (b), 606.9 nm (c), 619.6 nm (d), 620.9 nm (e), 621.5 nm (f).

Additionally, a luminescence line narrowing effect was observed (Fig. 1) which is indicative of variations of the local surrounding of Cm(III) in C-S-H gel.

Leaching experiments showed a very low Cm(III) mobilization from C-S-H gel samples into the supernatant solution regardless of ionic strength, the presence of carbonate, leaching time, or C/S ratio. XRD and TRLFS investigations after leaching confirmed that Cm(III) was either partially incorporated into the secondary phase aragonite ($CaCO_3$) or remained in the C-S-H or portlandite phases. After the conversion of the metastable aragonite phase into calcite, Cm(III) remains in the newly formed calcite phase. Thus, an almost complete retention of Cm(III) by the concrete barriers of a deep geological repository and their alteration phases can be expected.

[1] Scrivener, K. *et al.* (2017) *A Practical Guide to Microstructural Analysis of Cementitious Materials*, CRC Press.
[2] Stumpf, T. *et al.* (2004) *J. Colloid Interf. Sci.* **276**, 118–124.
[3] Albinsson, Y. *et al.* (1996) *J. Contam. Hydrol.* **21**, 189–200.
[4] Wolter, J. M. *et al.* (2019) *Chemosphere* **218**, 241–251.

EXAFS structural investigations on the ternary system Am(III)-Malate-CSH

A. Rossberg, F. Taube,[1] M. Acker,[1] S. Taut,[1] T. Stumpf

[1]Technische Universität Dresden, Central Radionuclide Laboratory, Dresden, Germany

Concrete will be used as an engineering barrier in nuclear waste repositories due to the radionuclide(RN)-retarding properties of calcium-silicate-hydrate (CSH) minerals. Poly(hydroxyl)carboxylate additives used to enhance the physico-chemical and mechanical properties of the concrete, may form stable complexes with RN in case of water intrusion. Here we investigate the interactions of Am(III) with the aqueous phase and with CSH at different calcium(C):silicon(S) ratios in presence and absence of malic acid (MAL). MAL serves as a structural analog for the additives.

EXPERIMENTAL. Fluorescence Am L_{III} EXAFS spectra of Am-hosting (1,000 ppm) CSH solids with different C:S ratios (Fig. 1) were measured at cryogenic conditions (30 K) at ROBL. The Am:MAL ratios were 1:0, 1:20 and 1:1 for the samples 1–3, 4–6 and 7–8, respectively. pH varied between 10 and 12. In addition, aqueous samples were measured containing $[Am] = 1 \times 10^{-3}$ mol L^{-1} and $[MAL] = 2 \times 10^{-2}$ mol L^{-1} at different pH (Fig. 1), except for sample 11 which contained no MAL. At pH 10, precipitation occurred and both the precipitate and the aqueous phase were measured (samples 12 and 13). Iterative target factor analysis (ITFA) was used for decomposition of the 13 spectra into their spectral components.[1]

RESULTS. The whole set of spectra can be described by five components, *i.e.* structurally different Am complex species; VARIMAX gives the qualitative fractionation of the five components (Fig. 1). Components 1–3 occur solely in the CSH solids. In the aqueous phases two structurally different Am complexes are present (component 4 and 5). Component 5 represents the precipitate while component 4 occurs independently of the presence or absence of MAL. Thus, component 4 can be attributed to a polynuclear aqueous hydrolysis species without MAL interaction. Both, the aqueous hydrolysis species and the precipitated Am−MAL complex are structurally incompatible with the three Am complexes present in CSH, hence surface precipitation and outer sphere sorption of the hydrolysis species can be excluded for the CSH system. The isolated spectra of components 1–3 are shown in Fig. 2. The most prominent peak at 1.9 Å in the FT represents 6–7 oxygen atoms of the first Am coordination shell. For all three components a fingerprint region of higher shells appears in a radial distance
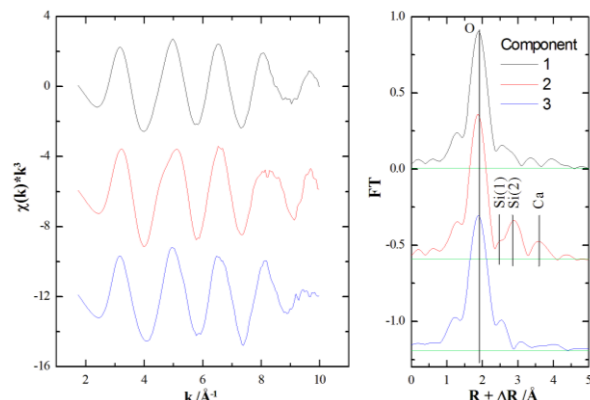
Fig. 2: Am L_{III} EXAFS spectra (left) and corresponding Fourier transform (FT) (right) of the three isolated CSH components with estimated error level (green).

> 2.38 Å which originates from scattering events stemming from O, Si and Ca atoms of the CSH phase.

In the case of component 2 the signals > 2.38 Å are more pronounced which probably points to a stronger interaction of Am with the CSH phase. For this component a tentative shell fit resulted in the following structural parameter: 6×O @ 2.41 Å, 1×Si @ 3.16 Å, 3×Si @ 3.66 Å, 2×Ca @ 4.19 Å. Similar distances were found in the system of Eu(III) with CSH for which sorption and coprecipitation of Eu placed at the Ca structural sites in a CSH-like environment was deduced.[2]

In the literature four possible interactions of RN with CSH are described: formation of outer sphere (OS) and inner sphere (IS) complexes, structural incorporation (SI), and surface precipitation.[3] Since surface precipitation and OS can be excluded the remaining components should correspond to IS and SI.

For SI, a rigid structure can be expected which leads to a reduction of the structural disorder and therefore to an enhancement of the backscattering signal beyond 2.38 Å, which is observed for component 2.

In summary, component 2 represents most probably SI, while we expect IS complexes for component 1 and 2.

To decipher the Am–CSH interactions in detail, future work will include *state-of-the-art* statistical methods like MCTFA and a new algorithm, which includes the substrate structure connected with FEFF calculations.[4, 5]

[1] Rossberg, A. *et al.* (2003) *Anal. Bioanal. Chem.* **376**, 631–638.
[2] Schlegel, M. L. *et al.* (2004) *Environ. Sci. Technol.* **38**, 4423–4431.
[3] Mandaliev, P. *et al.* (2010) *J. Colloid Interface Sci.* **342**, 1–7.
[4] Rossberg, A. *et al.* (2005) *Anal. Bioanal. Chem.* **383**, 56–66.
[5] Taube, F. *et al.* (2019) *Inorg. Chem.* **58**, 368–381.
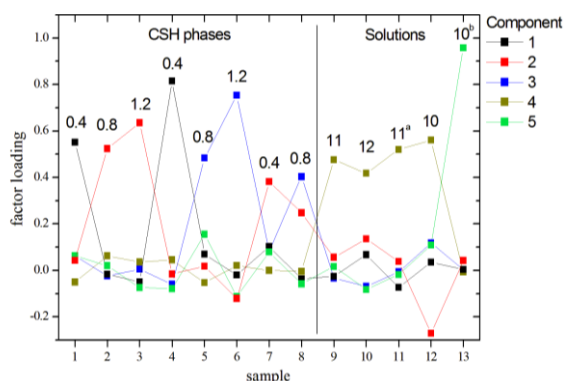
Fig. 1: VARIMAX factor loadings of the five components. For the CSH and aqueous samples the C:S and pH values are given, respectively (sample 11a – without MAL, sample 10b – precipitate).

Identification of U(VI) surface complexes on Ca-bentonite under hyperalkaline conditions with site-selective laser-induced luminescence spectroscopy

T. Philipp, N. Huittinen, K. Schmeide

Site-selective laser-induced luminescence spectroscopy was used to determine U(VI) retention mechanisms on Ca-bentonite surfaces at pH 11. The observation of luminescence line narrowing and the derived frequencies for the symmetric stretch vibration of the uranyl species indicate the presence of adsorbed U(VI) surface complexes and eliminate precipitation as predominant retention process under the given conditions. This finding proofs that also in chemical systems where anionic aquatic species prevail, effective retardation can be achieved by adsorption on negatively charged mineral surfaces.

Our previous batch sorption experiments have shown that U(VI) is quantitatively retained on Ca-bentonite between pH 10 and 12. Possible retention mechanisms are precipitation as Ca-uranate ($CaU^{VI}O_4$) or surface complexation, notwithstanding that both the predominant aqueous species ($UO_2(OH)_3^-$) and the clay surface are negatively charged. Site-selective luminescence spectroscopy was applied to distinguish between these processes. Conventionally, U(VI) luminescence is measured after indirect excitation of all species contained in the sample, leading to broadened spectra. This broadening can be overcome by applying a site-selective technique, where single species can be excited selectively by varying the excitation energy. While routinely used for trivalent actinides,[1] this technique has been applied to U(VI) only once.[2]

EXPERIMENTAL. Samples were prepared in the absence of CO_2 with 0.3 g/L Ca-bentonite in diluted Gipshut solution (2.5 M NaCl, 0.02 M CaCl$_2$, 0.02 M Na$_2$SO$_4$, 0.0051 M KCl) at pH 11. U(VI) concentrations were either 5×10^{-7} M (as in the previous sorption experiments) or 5×10^{-5} M (to provoke U(VI) precipitation). While mounted in a helium-refrigerated cryostat (~10 K), the U(VI)-loaded pellet was excited with a pulsed Nd:YAG (Continuum Surelite II, USA) pumped dye laser setup (Radiant Dyes Narrow Scan K). The emitted luminescence emission light was directed into a spectrograph (Shamrock 303i) and the emission was monitored with an intensified CCD camera (Andor iStar) in a time window of 10 ms. Spectra were recorded at excitation wavelengths between 460 and 520 nm with a step size of 0.2 nm.

RESULTS. In Fig. 1a, luminescence line narrowing can be clearly observed due to direct excitation of single species. The occurrence of luminescence line-narrowing alone already indicates the presence of adsorbed U(VI) surface complexes. In U(VI) precipitates the phenomenon of luminescence line narrowing is prevented by homo-resonance energy transfer between the U-atoms arranged in close distance to each other, leading to a mutual excitation and consequently to a broadening of the signal.[2] Such broadening is observed in the sample prepared with an initial U(VI) concentration of 5×10^{-5} M (Figure 1b), showing no luminescence line-narrowing, irrespective of the excitation energy. The position of the broad and unresolved maximum (at around 545 nm) and the luminescence lifetime (30–40 µs) correspond very well to those reported in literature for Ca-uranate.[2] No broadening was observable in the sorption
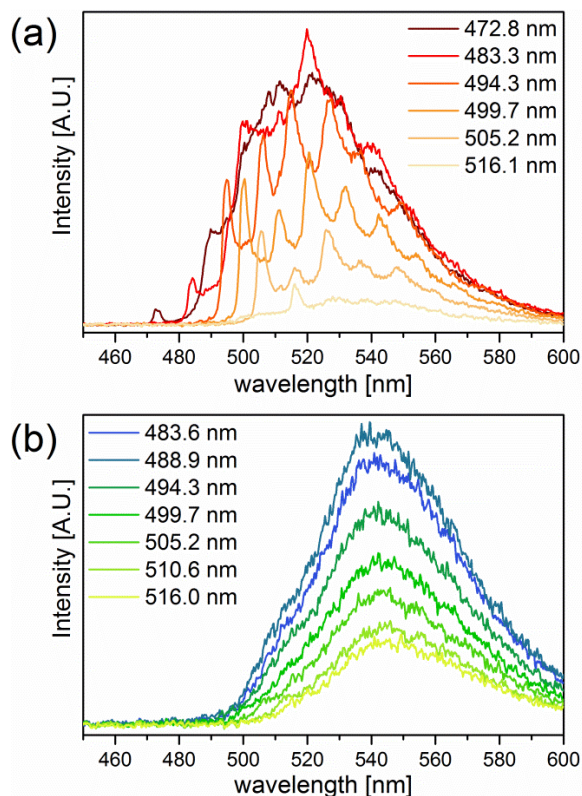
Fig. 1: Luminescence spectra of U(VI) sorbed on Ca-bentonite in diluted Gipshut solution at pH 11 at different excitation wavelengths. [U(VI)] = 5×10^{-7} M (a) and 5×10^{-5} M (b).

sample with 5×10^{-7} M U(VI), meaning that adsorption can be considered to be the only relevant retention mechanism at these experimental conditions. Specific information about the surface complexes can be obtained from the relative position of the maxima (*i.e.* the distance of the different electronic and vibronic transition lines). The spacing between the first two peaks of each species corresponds to the total symmetric stretching vibration (v_s) of the uranyl cation.[2] In the emission spectra, two species could be identified showing v_s frequencies of 758 cm^{-1} and 781 cm^{-1}. Both frequencies are significantly lower than those found for $UO_2(OH)_3^-$, which is dominating the aqueous speciation at pH 11.[3] The strong weakening of the axial U–O bond implies strong bonding in the U(VI) equatorial plane upon adsorption (*i.e.* inner-sphere surface complexation).

[1] Huittinen, N. *et al.* (2018) *Inorg. Chem.* **57**, 6252–6265.
[2] Tits, J. *et al.* (2015) *Dalton Trans.* **44**, 966–976.
[3] Nguyen-Trung, C. *et al.* (2000) *J. Solution Chem.* **29**, 101–129.

^{99}Tc reductive immobilization by iron sulfide (FeS$_2$)

D. M. Rodríguez, N. Mayordomo, V. Brendler, T. Stumpf, K. Müller

^{99}Tc is a fission product from ^{235}U and ^{239}Pu with a long half-life of 2.14×10^5 years. Under aerobic conditions, it is mainly found as pertechnetate (TcO$_4^-$), a highly mobile anion. Under reducing conditions, Tc(VII) will transform into Tc(IV), which has significantly lower solubility and, therefore, a lower mobility.[1] Fe(II) minerals have shown a remarkable ability to reduce and immobilize ^{99}Tc,[2−4] hence in this work a mixture marcasite-pyrite, redox sensitive Fe(II) sulfur minerals, was used to analyze the Tc(VII) removal from water.

EXPERIMENTAL. Iron sulfide (FeS$_2$) was synthetized using the methodology described by Huo *et al.*[5] The black powder obtained was characterized by powder XRD, BET and microscopy (SEM/TEM). The isoelectric point and the hydrodynamic diameter were also determined.

The batch experiments were carried out in N$_2$-glovebox (< 2 ppm O$_2$). Table 1 summarizes the experimental conditions of each experiment. The remaining Tc concentration in solution after each experiment was measured by LSC.

Tab. 1: Experimental conditions of the ^{99}Tc sorption experiments.

Experiment	Kinetics	Edge	Isotherm
FeS$_2$ (g/L)	1.33	1.28	1.57
[Tc(VII)]$_0$ (M)	5.07×10^{-6}	5.07×10^{-6}	nM−mM
pH	6.5	4.5−10	6.5
Time (days)	1−30	7	7

Scanning Electron Microscopy (SEM/EDX) images of the iron sulfide, as well as X-ray Photoelectron Spectroscopy (XPS) measures were carried before and after the technetium addition.

RESULTS. The FeS$_2$ yielded a black powder. After performing XRD the product was identified as a mixture of pyrite (cubic FeS$_2$) and marcasite (orthorhombic FeS$_2$) in a proportion 40:60. As the expected Tc removal mechanism begins with the reduction from Tc(VII) to Tc(IV) triggered by the oxidation from Fe^{2+} to Fe^{3+}, the purity of the FeS$_2$ phase was not considered relevant, therefore, we decided to keep using this mixture instead of pure pyrite. The isoelectric point of this iron sulfide is pH 7.40 with a particle size around 10 μm and a specific surface area of 5.3 ± 0.4 m^2/g. The batch experiments showed that 100 % removal of Tc was reached at pH between 6 and 9 after 7 days of contact (Fig. 1A and B), and the Pourbaix diagram confirms the reduction from Tc(VII) to Tc (IV); this trend was not significantly affected by the addition of 0.1 M NaCl to the system. The isotherm (not shown) has a slope of 0.5 suggesting a single reaction mechanism: sorption on one site, which would mean that the affinity of the mineral for the Tc is low,[6] or precipitation of Tc(IV).[7]

Figure 2 shows the SEM images of the iron sulfide before and after the technetium addition. The obvious change in the solid morphology suggests a reaction of FeS$_2$ with Tc. However, neither the use of EDX analysis nor XPS measurements, allowed to detect Tc due to its low concentration. Therefore, it is still necessary to clarify whether Tc(IV) is precipitated, sorbed or incorporated into the mineral structure.
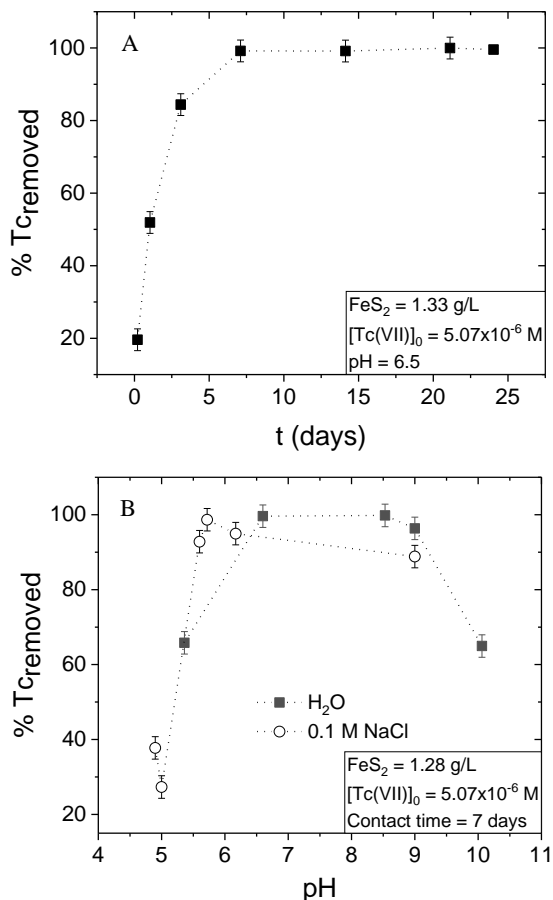
Fig. 1: Batch experiments of the ^{99}Tc removal by iron sulfide. Kinetics (A). Edge sorption experiments (B).
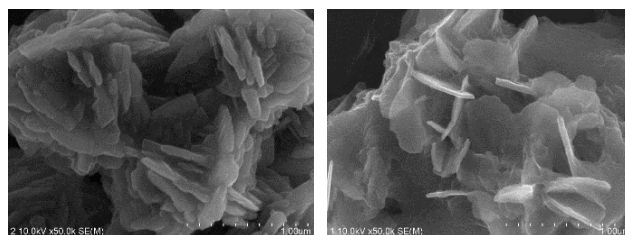
Fig. 2: SEM images of the iron sulfide before (left) and after (right) the ^{99}Tc addition. Scale: 1μm.

[1] Meena, A. H. *et al.* (2017) *Environ. Chem. Lett.* **15**, 241−263.
[2] Wharton, M. J. *et al.* (2000) *Appl. Geochem.* **15**, 347−354.
[3] Cui, D. *et al.* (1996) *Environ. Sci. Technol.* **30**, 2259−2262.
[4] Li, D. *et al.* (2012) *J. Hazard. Mater.* **243**, 1−18.
[5] Huo, L. *et al.* (2017) *Chemosphere* **174**, 456−465.
[6] Limousin, G. *et al.* (2007) *Appl. Geochem.* **22**, 249−275.
[7] Rard, J. *et al.* (1999) *Chemical thermodynamics of technetium.* Nuclear Energy Agency, France.

^{99}Tc retention by γ-alumina with and without pre-sorbed Fe^{2+}

N. Mayordomo, D. M. Rodríguez, D. Schild,[1] V. Brendler, K. Müller

[1]Institute for Nuclear Waste Disposal, Karlsruhe Institute of Technology, Karlsruhe, Germany.

The removal of ^{99}Tc(VII) by alumina without pre-sorbed Fe^{2+} (binary system) and with pre-sorbed Fe^{2+} (ternary system) has been studied by batch experiments and X-ray photoelectron spectroscopy (XPS). Tc uptake highly improves when Fe^{2+} is pre-sorbed on the alumina, which has been related to the reduction of Tc(VII) to Tc(IV) fastly promoted by the Fe^{2+} sorbed on the surface.

Tc is an element of environmental concern since ^{99}Tc is a fission product that can occur in the nuclear waste repository and is also used in radiopharmacy.[1] Tc(VII)O$_4^-$ is known to be a mobile anion that barely interacts with minerals, however, under reducing conditions Tc(IV)O$_2$ is formed and the mobility decreases.[1] Additionally, it is known that reduction of Tc(VII) occurs faster by Fe^{2+}-sorbed on a mineral surface than by Fe^{2+}-containing minerals.[2] In this work, we compare the efficiency of Tc retention by alumina with and without Fe^{2+} pre-sorbed as a function of pH and ionic strength.

EXPERIMENTAL. The alumina used in the experiments is has been previously characterized.[3] For the batch sorption experiments in the binary and ternary system we carried out a similar approach to the one reported by Peretyazhko,[4] performing all the experiments in a glove box free of CO$_2$ and O$_2$ (< 2 ppm). XPS measurements were carried out for analyzing the oxidation state of Tc in the ternary system using suspensions highly concentrated in pre-sorbed Fe^{2+} and Tc to achieve 3 atoms of Tc per nm^2 of alumina. Instrument details are reported elsewhere.[5]

RESULTS. Figure 1 shows the maximum Tc retention of the binary system which is 6.5 % and is achieved under acidic conditions. In contrast, when Fe^{2+} is pre-sorbed on the alumina surface, Tc removal highly increases with increasing pH, being complete for pH > 6.5 and independent on the ionic strength. In the case of the ternary system, the kinetics of Tc retention (Fig. 2) are also faster with increasing pH, being complete after 1 or 2 days of contact at pH 9.5 and pH 7, respectively. As well, we could observe a kinetic effect on the retention at pH 4.75, when the Tc uptake increased from 20 % uptake up to 40 % within 7 and 14 days of contact.

While Fe^{2+} and alumina were in contact, even in absence of Tc(VII), we observed the formation of a solid in suspension, which is identified as Fe(II)-Al(III)-Cl layered double hydroxide.[6] Moreover, thermodynamics predict the formation of accessory Fe^{2+} and/or Fe^{3+} minerals, like Fe(OH)$_2$, Fe$_3$O$_4$ and FeO(OH).[7] This resulting mixed mineral system hinders the use of XAS to identify the geometry of Tc in the system.

However, Tc(IV) was identified in the ternary system at pH 9.5 using XPS (Fig. 3).

According to the results, we conclude that ternary system promotes Tc retention due to the reduction of Tc(VII) to Tc(IV) carried out by the pre-sorbed Fe on the alumina surface.
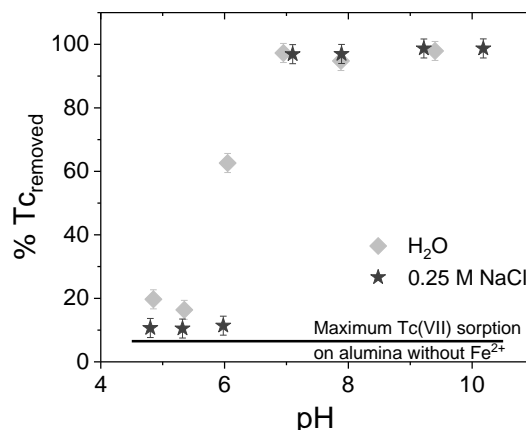
Fig. 1: ^{99}Tc removed from solution as a function of pH by alumina suspensions in water without (line) sorbed Fe^{2+} and with (dots) pre-sorbed Fe^{2+} at different ionic strengths.
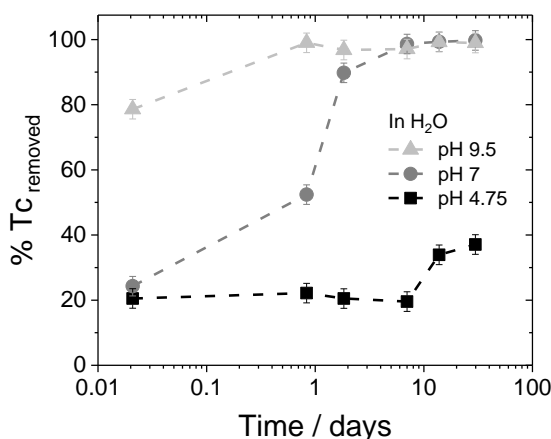
Fig. 2: Kinetics of ^{99}Tc removal by alumina with Fe^{2+} pre-sorbed at different pH values. Lines are drawn to guide the eye.
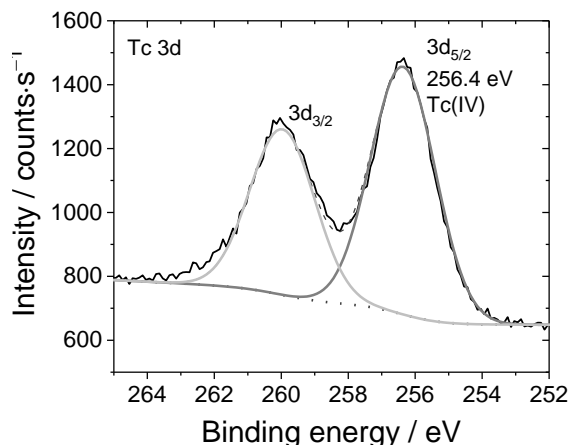
Fig. 3: Tc 3d XPS spectrum of Tc(IV) measured after interaction with alumina with pre-sorbed Fe^{2+} at pH 9.5.

[1] Meena, A. *et al.* (2017) *Environ. Chem. Letters.* **15**, 241–263.
[2] Zachara, J. M. *et al.* (2007) *Geochim. Cosmochim. Acta.* **71**, 2137–2157.
[3] Mayordomo, N. *et al.* (2018) *Environ. Sci. Technol.* **52**, 581–588.
[4] Peretyazhko, T. *et al.* (2008) *Environ. Sci. Technol.* **42**, 5499–5506.
[5] Huber, F. *et al.* (2017) *Appl. Geochem.* **80**, 90–101.
[6] Elzinga, E. (2012) *Environ. Sci. Technol.* **46**, 4894–4901.
[7] Lemire, R. J. *et al.* (2013) *Chemical thermodynamics of Fe. Part 1, NEA No. 6355*, OECD, Issy-les-Moulineaux.

Adsorption of Se(VI) onto nano-transition alumina

H. Foerstendorf, N. Jordan, J. Lützenkirchen,[1] D. Hering, S. Weiss, K. Heim, C. Franzen, V. Brendler

[1]Karlsruhe Institute of Technology, Institute for Nuclear Waste Disposal, Karlsruhe, Germany

The adsorption of the Se(VI)O$_4$$^{2-}$ anion onto nano transition alumina was investigated. A predominant bidentate outer-sphere surface species was identified spectroscopically. On the basis of these findings, the Se(VI) adsorption edges were successfully described by Surface Complexation Modeling (SCM).

Selenium (Se) as a fission product ($\tau_{1/2} \sim 3.27 \times 10^5$ a) contributes to the potential dose release of a future nuclear waste repository. Thus, the exploration of the surface speciation on nano transition alumina – serving as a representative of metastable alumina oxide phases and in turn as model oxides for clay minerals – is mandatory for the assessment of the processes controlling the mobility of selenium in a potential host rock.

EXPERIMENTAL. The set-up and the performance of the IR *in situ* experiments are described elsewhere.[1, 2] All experiments were carried out in D$_2$O due to strong absorption properties of bulk water in the range below 900 cm^{-1},[2] at an ionic strength of 0.1 M NaCl. Details of the characterization of the solid phase and of the performance of batch sorption studies and SCM are given elsewhere.[3]

RESULTS. From the IR spectra recorded in the pD range from 4.0 to 6.0, the formation of a single surface species can be derived. Upon sorption, the band representing the υ_3(Se–O) mode showed a frequency shift and a significant change of its shape indicating the abrogation of the triply degenerated υ_3 mode (Fig. 1). In fact, four components were derived by spectral decomposition, which is in line with a predominant C$_{2v}$ symmetry of the Se(VI) surface species. Due to high reversibility derived from IR desorption experiments, the shift of the isoelectric point upon Se(VI) adsorption, and the decrease of Se(VI) adsorption upon rising the ionic strength (0.01 to 0.1 M, data not shown), an outer spheric bidentate surface species was suggested.[2] Based on these findings, the adsorption model could be summarized in the following reaction:

Fig. 1: IR spectra of the aqueous Se(VI) species (black dotted line), of the surface species formed during sorption on nano transition Al$_2$O$_3$, and of species released from the surface during flushing of the solid (black lines). Grey dotted and solid lines represent the single components and the fitting result, respectively, obtained after decomposition of the spectrum of the sorbed species.

Fig. 2: Se(VI) adsorption envelopes onto transition alumina at two different initial Se(VI) concentrations and ionic strengths (see legend). Solid lines represent the corresponding fitting results obtained from SCM.

$$2(\equiv\text{AlOH}^{0.5-}) + 2\text{H}^+ + \text{SeO}_4^{2-} \rightleftharpoons \{(\equiv\text{AlOH}_2^{0.5+})_2\text{SeO}_4^{2-}\};$$
$$\log K^\circ = 19.5 \pm 1.0$$
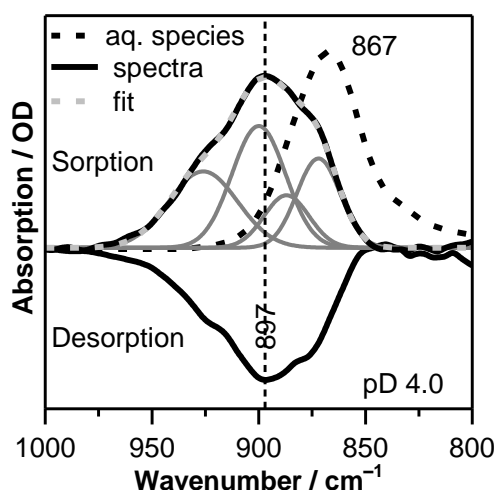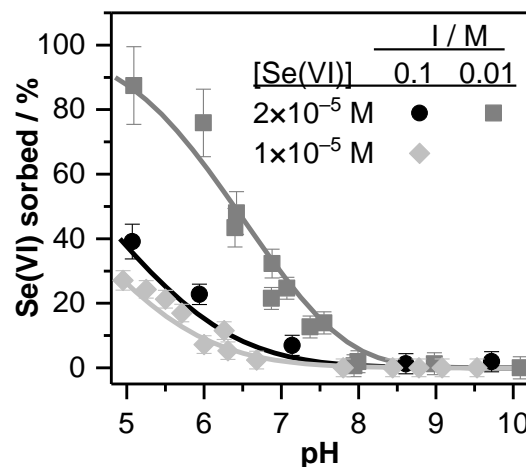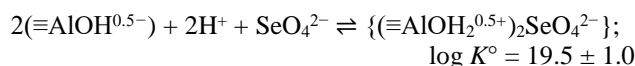
A satisfactory description of the adsorption data was obtained (Fig. 2), whatever the initial concentration of Se(VI) or the ionic strength of the suspensions. Moreover, blind application of our model to literature data was quite successful (Fig. 3).[4,5]
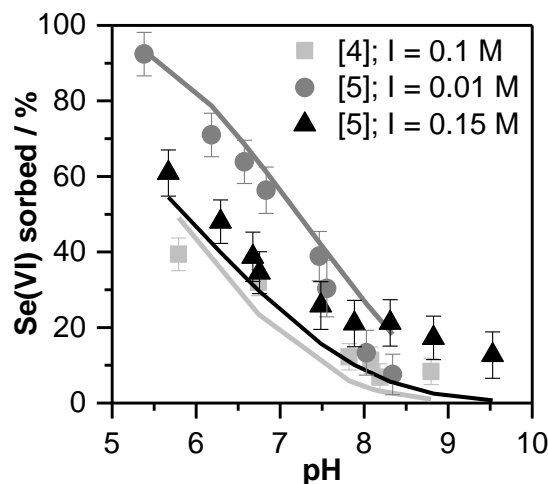
Fig. 3: Predictions of the model proposed in this study for published Se(VI) batch sorption data onto Al$_2$O$_3$ (in NaCl).

[1] Foerstendorf, H. *et al.* (2012) *J. Colloid Interface Sci.* **377**, 299−306.
[2] Jordan, N. *et al.* (2013) *Geochim. Cosmochim. Acta* **103**, 63−75.
[3] Jordan, N. *et al.* (2018) *Environ.−Sci. Nano* **5**, 1661−1669.
[4] Ghosh, M. M. *et al.* (1994) *Environ. Prog.* **13**, 79−88.
[5] Elzinga, E. J. *et al.* (2009) *J. Colloid Interface Sci.* **340**, 153−159.

Competitive adsorption of ZrO₂ nanoparticles and alkali cations on muscovite (001)

C. Qiu,[1] P. J. Eng,[2] C. Hennig, M. Schmidt

[1]Current address: Institute of Experimental and Applied Physics, Universität Kiel; Germany; [2]University of Chicago, Chicago, IL, USA

We studied the adsorption behavior of ZrO₂ nanoparticles on muscovite (001) surface in the presence of cations from the alkali group (Li⁺, Na⁺, K⁺, Rb⁺, and Cs⁺). The results of X-ray reflectivity (XR), i.e. specular crystal truncation rod (CTR) and resonant anomalous X-ray reflectivity (RAXR) in combination with AFM imaging, show that the sorption of ZrO₂ nanoparticles is significantly affected by the binding mode of alkali cations on the muscovite (001) surface.

Motivated by our findings regarding the effect of background electrolyte composition on the sorption of Th(IV) on the muscovite mica basal plane and based on our previous study of the aggregation of Zr(IV) nanoparticles at the same interface, we investigated the competitive sorption behavior of Zr(IV) in a series of alkali chloride (ACl, with A = Li⁺–Cs⁺) solutions.[1–3] For Th(IV) a highly unexpected behavior was observed, with the highest uptake from Li⁺ containing solutions, and lowest uptake from Na⁺ background electrolyte, K⁺ showed lower Th(IV) uptake than Li⁺, but higher than Na⁺.[1] The sorption of the A⁺ cations on muscovite (001) has been studied previously and it was found that Li⁺ and Na⁺ adsorb predominantly as outer sphere (OS) complexes, while Rb⁺ and Cs⁺ form almost exclusively inner sphere (IS) species.[4] K⁺ is an intermediate case, sorbing to about 60 % as an IS complex.[4]

EXPERIMENTAL. For each experiment a freshly cleaved mica single crystal (Asheville Schoon-maker) was submerged in a freshly prepared Zr solution ([Zr] = 0.1 mM, pH = 2.5, [ACl] = 100 mM) for ~24 h. Under these conditions, Zr is expected to be present in solution in the form of small nanoparticles.[2] For XR these crystals were transferred into a custom made liquid cell, covered with 100 μL Zr⁴⁺ solution, and a liquid film was trapped on the crystal surface using a thin Kapton membrane. XR experiments were performed at the Rossendorf beamline, ESRF and GSECARS, APS. AFM imaging was performed in situ using an Asylum Research Cypher AFM instrument equipped with a BRUKER MSNL-10 silicon tips on nitride cantilevers, between 26 and 50 kHz frequency, and force constant of 0.1 N/m. The two approaches are in good agreement throughout.

RESULTS. The interfacial electron density (ED) profiles derived from XR are shown in Fig. 1. The total ED profiles (black lines) share a common feature at ~2.5 Å (gray area), which could be identified as containing surface hydration as well as adsorbed A⁺ cations. This is followed by a broader peak at larger distance from the surface, which is directly associated with adsorbed Zr(IV) nanoparticles. A detailed analysis of nanoparticle size and amount of adsorbed Zr reveals two regimes for the surface reaction. In the presence of the predominantly OS adsorbing ions, Li⁺ and Na⁺, Zr uptake is high and unaffected by the type of cation, but with IS adsorbing cations (K⁺, Rb⁺, Cs⁺) a linear dependence of Zr surface coverage [given in Zr per area-of-the-unit-cell of muscovite (001)] on the hydration strength of A⁺ is found (Fig. 2, solid line).[5] The decreased uptake goes along with the adsorption of smaller Zr nanoparticles. This can be understood in the context of competitive sorption, where an IS
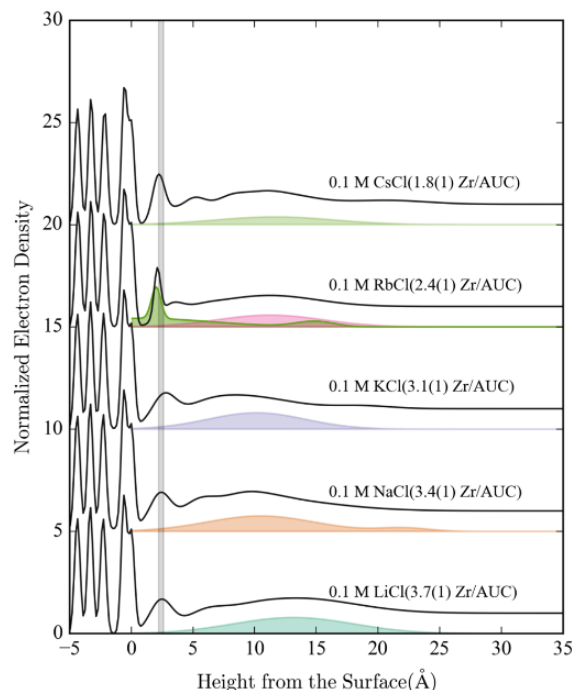
Fig. 1: Total ED (CTR, solid lines) and resonant ED (RAXR, filled peaks) above mica (001). For RbCl-Zr-mica both Rb (green) and Zr (pink) distributions are shown. Electron density is normalized to that of bulk water. Plots are shifted vertically for better visibility.

bound cations' sorption strength will increase with weaker hydration. Smaller nanoparticles are more competitive to such strongly bound cations, due to their larger charge density. This indicates ion (de)hydration is a significant energetic contribution to this interfacial exchange process.
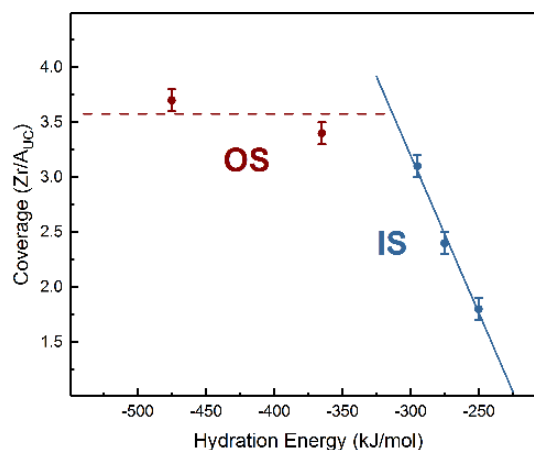
Fig. 2: Relationship between Zr surface coverage and hydration energy of the background electrolyte cations.[5]

It should be noted that the unusual behavior reported for Th(IV) cannot be fully explained by the systematic behavior of Zr(IV) observed here, emphasizing the requirement for actinide experiments to understand actinide behavior.

[1] Schmidt, M. *et al.* (2015) *Geochim. Cosmochim. Acta* **165**, 280–293.
[2] Qiu, C. *et al.* (2018) *J. Phys. Chem. C* **122**, 3865–3874.
[3] Qiu, C. *et al.* (2018) *Langmuir* **34**, 12270–12278.
[4] Lee, S. S. *et al.* (2012) *Langmuir* **28**, 8637–8650.
[5] Marcus, Y. (1991) *J. Chem. Soc., Faraday Trans.* **87**, 2995–2999.

2D crystals in three dimensions: electronic decoupling of single-layered platelets in colloidal nanoparticles

R. Kempt,[1] A. Kuc,[1,2] J. H. Han,[3,4] J. Cheon,[3,4] T. Heine[1,2,5]

[1]Universität Leipzig, Wilhelm-Ostwald-Institute for Physical and Theoretical Chemistry, Leipzig, Germany; [2]HZDR, Institute of Resource Ecology, Campus Leipzig, Germany; [3]Institute for Basic Science, Seoul, Republic of Korea; [4]Yonsei University, Seoul, Republic of Korea; [5]Technische Universität Dresden, Faculty of Chemistry and Food Chemistry, Dresden, Germany

2D crystals, single sheets of layered materials, often show distinct properties desired for optoelectronic applications, such as larger and direct band gaps, valley- and spin-orbit effects. Being atomically thin, the low amount of material is a bottleneck in photophysical and photochemical applications. Here, the formation of stacks of 2D crystals intercalated with small surfactant molecules is proposed. It is shown, using first principles calculations, that the very short surfactant methyl amine electronically decouples the layers. The indirect–direct band gap transition characteristic for Group 6 transition metal dichalcogenides is demonstrated experimentally by observing the emergence of a strong photoluminescence signal for ethoxide-intercalated WSe_2 and $MoSe_2$ multilayered nanoparticles with lateral size of about 10 nm and beyond. The proposed hybrid materials offer the highest possible density of the 2D crystals with electronic properties typical of monolayers. Variation of the surfactant's chemical potential allows fine-tuning of electronic properties and potentially elimination of trap states caused by defects.

Here, we show that electronic decoupling of the layers in 3D bulk transition-metal dichalcogenides is achieved in the surfactant-based intercalation approach, and that electronic layer separation is achieved upon lattice enlargement by about 4 Å (Fig. 1). This value is obtained for surfactants with the shortest side chain, such as methylamine, $MeNH_2$, and we show that the electronic structure of the 2D crystals can be fine-tuned by the surfactant's head group. In this paper, we combine DFT simulations with experiments, showing that the intercalation of such layered materials indeed results in 3D stacks of layers with specific electronic and optical properties of monolayered systems.[1]

METHODS. All calculations were performed using the DFT method as implemented in the ADF-BAND code. We have employed the Perdew-Burke-Ernzerhof (PBE) functional under the generalized gradient approximation,[2] van der Waals interaction corrections were included using the D3 approach proposed by Grimme.[3] The intercalated systems were simulated using the supercell approach. The photoluminescence experiments were performed on intercalated $MoSe_2$ and WSe_2 bulk materials to confirm that the obtained 3D stack of layers shows properties the same as for the corresponding monolayers.

RESULTS. Using DFT simulations, we show that the electronic properties of layered materials, especially Group 6, such as MoS_2 or WSe_2, in their bulk forms are decoupled, when the layers are separated by surfactant molecules. We confirm these findings experimentally, by photoluminescence experiments, which reveal peaks at the wavelengths similar to the corresponding monolayers (Fig. 1), which indicate the direct-gap semiconductors. Monolayers of Group 6 dichalcogenides have direct band gaps at the K point and very large spin-orbit splitting in the valence band. These properties are lost in centro-symmetric bilayers and bulk

Colloidal intercalation with surfactants

Electronic Decoupling
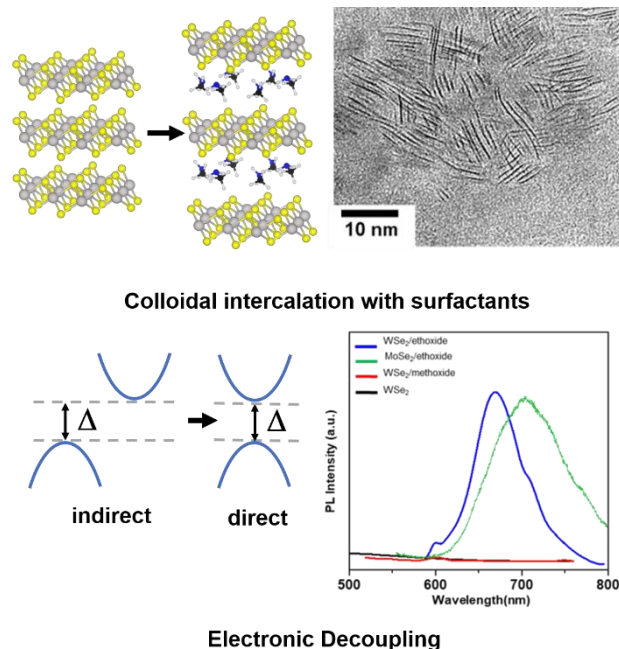
Fig. 1: Schematic representation of the 3D bulk intercalated with small surfactants (top left); experimental realization of the idea (top right); electronic structure of monolayer (direct band gap) recovered in 3D bulk intercalated materials (bottom).

materials. Therefore, possibility of having monolayer properties in the bulk systems is desired. The formation of 3D assembly of 2D monolayers by intercalation should be more promising than single layers for optoelectronic, photovoltaic, and photocatalytic applications, where increased cross-section of photoactive monolayers is desirable, and here it is offered by stacking of many of such layers by colloidal synthesis. We also note here that the inner layers of these hetero-structures are chemically stabilized, which offers an alternative to hBN encapsulation. In future, 3D integration of electronic devices made of single-layer transistors could become feasible using the surfactant intercalation approach.

[1] Kempt, R. *et al.* (2018) *Small* **14**, 1803910−1.
[2] Perdew, J. P. *et al.* (1996) *Phys. Rev. Lett.* **77**, 3865.
[3] Grimme, S. *et al.* (2011) *J. Comput. Chem.* **32**, 1456−1465.

Effect of DTPA on adsorption of Eu(III) onto quartz sand as a function of pH: batch sorption experiments and surface complexation modeling

L. Karimzadeh, H. Lippold

Sorption of radionuclides (RN) on mineral surfaces retards their migration in the environment of a repository. Presence of organic ligands (OL), however, affects sorption of RN and consequently influences their transport behavior. In this study, sorption of Eu(III) (as an analogue of trivalent actinides) onto quartz sand was investigated at variable pH in the absence and presence of diethylenetriaminepentaacetic acid (DTPA) as an OL, which is used as a decontamination agent. We conducted batch sorption experiments in binary and ternary systems and performed surface complexation modeling (SCM) to explain the effect of DTPA on sorption of Eu(III). Results showed that DTPA considerably increased the mobility of Eu(III).

EXPERIMENTAL. A stock solution of $[^{152}Eu]Eu(NO_3)_3$ was prepared with a concentration of 2×10^{-4} mol L^{-1} and an activity of 0.3 MBq. The solution was adjusted to pH 3 to avoid formation of colloids and sorption on walls. Batch sorption experiments were performed in 50 mL plastic tubes containing 0.2 g quartz sand (grain size 0.2–0.8 mm, Sigma-Aldrich) and 20 mL 10^{-6} M $[^{152}Eu]Eu(III)$ in 0.1 M NaClO$_4$ as a background electrolyte. The pH of the suspensions was varied between 3.5 and 9 to study its effect on sorption. Experiments were done in the absence and in the presence of DTPA (equimolar ratio). After shaking the suspension for about 40 h, the samples were centrifuged at 5000 rpm for 10 min. 8 mL of the supernatant solution where taken for analysis by γ-counting relative to reference solutions.

MODELING. For surface complexation modeling, the generalized double-layer model introduced by Dzombak and Morel was used to describe the effects of pH and DTPA on sorption of Eu(III) onto quartz.[1] We assumed a monodentate surface complexation of the metal on a single edge site. The equilibrium constant (log k) of surface complexation was fitted to the experimental data from batch sorption experiments using the parameter estimation code PEST[2] coupled with PHREEQC. A weighted residuals model was used for fitting.

RESULTS. Results of aqueous speciation modeling showed that at pH above 4 the total amount of Eu(III) is in the complex form with DTPA (Fig. 1). Sorption of Eu(III) onto quartz sand was considerably reduced in the presence of DTPA (by ~ 40 % at 1 : 1 molar ratio, Fig. 2). In addition, we observed that the effect of DTPA on Eu(III) sorption is strongly dependent on pH. As can be seen in Fig. 2, our SCM is capable of reproducing the sorption behavior of Eu(III) as a function of pH both in the absence and in the presence of DTPA.

To conclude, mobility of actinides can be considerably increased in case of contaminant release of complexants from the organic inventory of a repository.
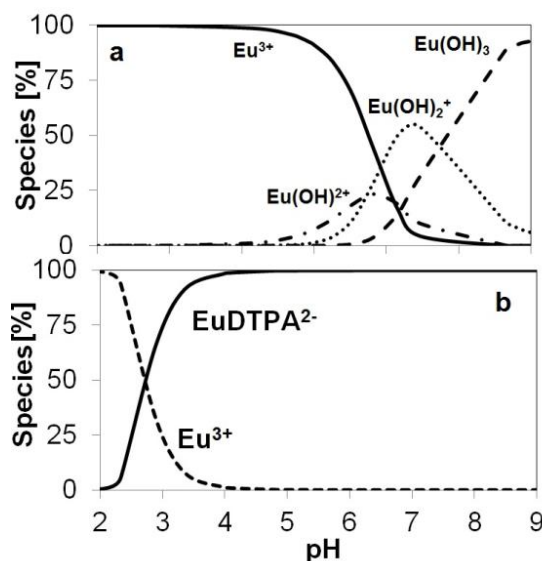
Fig. 1: Aqueous speciation of Eu(III) in the absence (a) and presence (b) of DTPA ([Eu]/[DTPA] = 1) calculated with PHREEQC v3,[3] using the LLNL database and additional data for Eu(III) and DTPA.[4, 5]
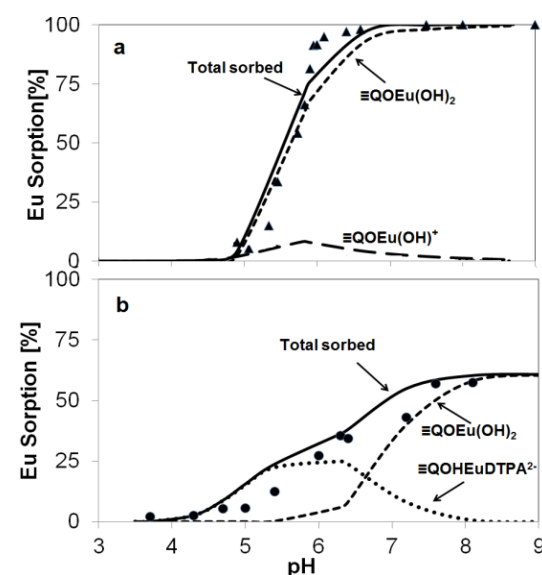
Fig. 2: Experimental data (symbols) and modeling results for sorption of Eu(III) onto quartz sand as a function of pH in the absence (a) and presence (b) of DTPA ([Eu]/[DTPA] = 1).

[1] Dzombak, D. A. *et al.* (1990) *Surface Complexation Modeling: Hydrous Ferric Oxide*, Wiley, New York, U.S.A.
[2] Doherty, J. (2016) *PEST user manual*, http://www.pesthomepage.org.
[3] Parkhurst, L. D. *et al.* (2013) *User's guide to PHREEQC*, U.S.G.S., Denver, p. 497.
[4] Bradbury, B. *et al.* (2002) *Geochim. Cosmochim. Acta* **66**, 2325–2334.
[5] Grimes, T. *et al.* (2014) *J. Solution Chem.* **43**, 298–313.

Eu³⁺ incorporation in LnPO₄ ceramics with xenotime structure

H. Lösch, A. Hirsch,[1] B. Xiao, L. Peters,[2] M. Schmidt, J. Holthausen,[3] S. Neumeier,[4] N. Huittinen

[1]Fraunhofer Technology Centre Semiconductor Materials, Freiberg, Germany; [2]Institut für Kristallographie, RWTH Aachen University, Germany; [3]ASK Chemicals GmbH, Hilden, Germany; [4]Forschungszentrum Jülich, Jülich, Germany

The incorporation of Eu³⁺ in LnPO₄ host materials predominantly crystallizing in the xenotime structure has been investigated on the molecular level. In single crystals of various xenotime end-members (Tb to Lu, and Y), the incorporation of Eu³⁺ results in a distortion of the crystallographic site symmetry. In Gd₁₋ₓLuₓPO₄ powder samples, Eu³⁺ is incorporated within a xenotime–type crystal structure for substitutions up to x = 0.5. Upon aging, however, a segregation of the initially incorporated Eu³⁺ from the crystal structure is observed, resulting in Eu³⁺ accumulation at grain boundaries. A similar partitioning from the crystal structure is absent in the single crystal samples.

In recent years, rare-earth orthophosphates LnPO₄ (Ln = La–Lu, Y) have attracted attention as potential hosts for the immobilization of long-lived high-level radioactive waste. It has been shown that the monazite hosts (LaPO₄-GdPO₄) form perfect solid solutions with the large trivalent actinide elements (Pu, Am, and Cm). Whether a similar incorporation can be expected to occur in the smaller lanthanide hosts crystallizing in the xenotime structure, however, is still not known. Thus, this study focuses on understanding the behavior of Eu³⁺, taken as analogue for the trivalent actinides, in xenotime single crystals and powder samples.

EXPERIMENTAL. Eu³⁺-doped LnPO₄ (Ln = Tb–Lu, Y) single crystals were synthesized by a flux-growth method.[1] Powder samples were obtained by precipitation of Eu³⁺:LnPO₄ rhabdophane (Gd₁₋ₓLuₓ, x = 0, 0.3, 0.5, 0.7) followed by sintering of the precursor powder at 1,450 °C for 5 hours.[2] XRD studies of the bulk material were complemented with laser-induced luminescence spectroscopy (TRLFS) to account for the incorporation of Eu³⁺ in the host materials. The bulk material is polycrystalline. Investigations were conducted directly after material synthesis and after an aging time of 9–12 months. For single crystals, additional polarization dependent, p-TRLFS, investigations capable of resolving the Eu³⁺ environment on the point group level were conducted.

RESULTS. Our p-TRLFS results of the xenotime single crystal end-members show that Eu³⁺ incorporation in the xenotime hosts from Tb to Yb causes a large distortion of the crystallographic site symmetry from D_{2d} to C_1. In LuPO₄ the lattice is no longer flexible enough to allow for a similar distortion, resulting in a small change of the site symmetry to S_4 upon Eu³⁺ incorporation. This is visualized in Fig. 1 (left) for the polarization geometries σ and π. The coordination environment is sufficiently distorted from the crystallographic D_{2d} point symmetry to exhibit a different splitting pattern. Eu³⁺ incorporation in the powder samples measured directly after synthesis show a very similar emission spectrum as recorded for the LuPO₄ single crystal, implying incorporation in a xenotime–type crystal structure. This is shown exemplarily for the Gd₀.₃Lu₀.₇PO₄ composition in Fig. 1 (right), red traces. After one year of aging, the emission spectra (black traces) show a broad dominant signal between the transitions regions of the ⁷F₁- and ⁷F₂-band, while the splitting pattern of the emission bands no longer
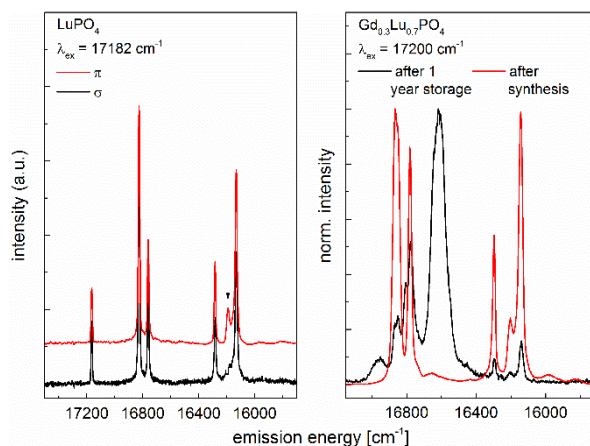
Fig. 1: Polarized emission spectra of Eu³⁺-doped LuPO₄ single crystal excited at 582.0 nm / 17182 cm⁻¹ (left). Emission spectra of Eu³⁺-doped Gd₀.₃Lu₀.₇PO₄ after synthesis and after one year storage excited at 581.4 nm / 17200 cm⁻¹ (right).

corresponds to Eu³⁺-incorporation in a xenotime environment only. These changes indicate a change in the local structure of the europium dopant during storage under ambient conditions, which does not take place in the single crystal samples after a similar aging period. Based on these observations we suggest an exclusion of Eu³⁺ from the crystal structure and subsequent migration of the cation to the grain boundaries during aging. The migration of Eu³⁺ in void spaces through the crystal structure could be responsible for the additional signals in the emission spectra, while the narrow void space forces an overlap between Eu³⁺ and oxygen atomic orbitals, resulting in an extreme splitting of the ⁷F₁-band. As single crystals possess only minor defects sites and no grain boundaries, a similar exclusion of Eu³⁺ from the host lattice is hampered.

In summary, the segregation of Eu³⁺ to grain boundaries after relative short aging in the xenotime materials, indicate that xenotime ceramics will not serve as a suitable waste form for trivalent actinides from high–level nuclear waste.

[1] Xiao, B. *et al.* (2018) *Chem. Eur. J.* **24**, 13368–13377.
[2] Lösch, H. *et al.* (2019) *Front. Chem.*, accepted.

Hydrothermal synthesis of actinide-zirconia solid solutions – Spectroscopic investigations

M. Eibl, S. Shaw,[1] K. Morris,[1] T. Stumpf, N. Huittinen

[1]Research Centre for Radwaste Disposal and Williamson Research Centre, University of Manchester, U.K.

The crystallization of zirconia under hydrothermal conditions has been studied with XRD as a function of hydrothermal treatment time. Results show that zirconia doped with either trivalent (Eu^{3+}) or tetravalent (Th^{4+}) dopants crystallizes slower in comparison to the non-doped material. Th^{4+} was seen to slow down the kinetics more than Eu^{3+}, presumably due to the introduction of oxygen vacancies into the lattice by the latter one, making the lattice more flexible. Furthermore, a stable tetragonal phase was observed in the non-doped zirconia samples, while only the monoclinic phase is typically stable at ambient conditions. This can be attributed to the small crystallite size of the material.

Zirconium(IV) oxide is a corrosion product of the zircalloy cladding material surrounding nuclear fuel rods.[1] Therefore, studies involving interactions such as structural incorporation of actinides into ZrO_2 at conditions relevant for a high-level waste repository are necessary to enable predictions about the long term safety of final repositories for nuclear waste.

EXPERIMENTAL. To study the ZrO_2 crystallization process, $ZrOCl_2$ was dissolved in dilute HCl with or without varying amounts of $EuCl_3$, or a Th(IV)-stock solution. The solutions were added dropwise to an alkaline solution of NaCl (0.5 M, pH 12) resulting in instantaneous formation of a white precipitate of non-doped or Eu^{3+}/Th^{4+}-doped hydrous zirconia. This suspension was stored at 80 °C in an oven for a duration of up to 264 h, followed by separation of the ZrO_2 product by centrifugation. The recovered wet paste was washed with water and dried at 80 °C. For XRD analysis the solid samples were mixed with a defined amount of Si-powder and analyzed with a Bruker D8 Advance diffractometer.

RESULTS. All samples show fairly fast crystallization rates. Already after 48 h at 80 °C Bragg peaks start to appear in the diffraction patterns. From thereon, the crystallization rate depends on the sample composition, where the non-doped zirconia shows a rather linear crystallization behavior until it reaches 100 % crystallinity after 264 h (Fig. 1). The Eu^{3+} doped samples first show a very fast rate comparable to the non-doped material, however, crystallization is seen to slow down after about 70 h. A complete crystallization of the doped material was not achieved even after 264 h, but it reaches an overall crystallinity of about 84 wt.-%. The Th^{4+} doped samples however, exhibit a rather slow crystallization rate, only reaching about 50 wt.-% crystallinity after 264 h. The incorporation of Eu^{3+} requires charge compensation within the lattice, which takes place *via* the formation of oxygen vacancies. This seems to facilitate the incorporation of this largely oversized cation in comparison to a tetravalent dopant like Th^{4+}, since the oxygen vacancies increase the flexibility of the lattice. Another interesting effect of the crystallization at hydrothermal conditions is that despite of the monoclinic phase being the thermodynamically stable crystal phase at ambient conditions, the tetragonal phase forms, even without the addition of a stabilizing dopant
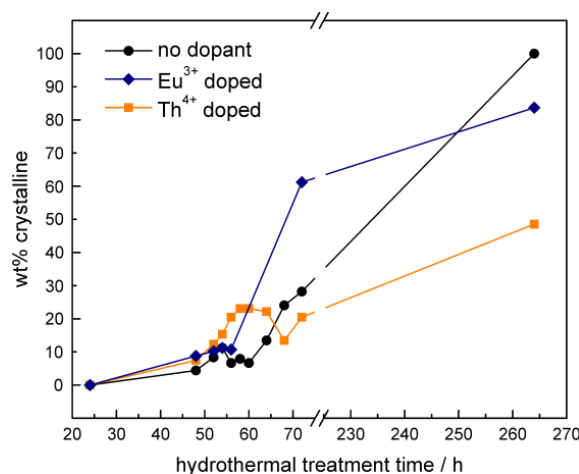
Fig. 1: Crystallization kinetics of zirconia at 80 °C in aqueous solution doped with Eu^{3+}, Th^{4+} and no dopant.

(Fig. 2). It is known that nanoparticular zirconia is stable in the tetragonal structure,[2] which is why it is assumed here, that the crystalline particles forming at these rather low temperatures are nanometer sized (< 20 nm) after short synthesis times, and only grow larger with increasing time. Once the critical crystallite size is reached after about 60 h the monoclinic phase is the dominating one. After that, both phase percentages increase due to the increasing overall crystallinity. Nevertheless, even after 264 h a considerable percentage of tetragonal zirconia stays stable which therefore must remain nano-sized. Future studies will show, whether the initially forming crystalline zirconia particles are purely tetragonal and if the stability of the tetragonal phase after even longer treatment times would be reduced due to proceeding Ostwald ripening.
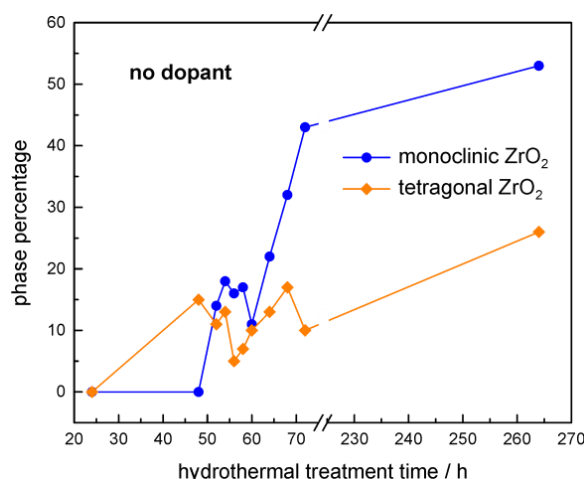
Fig. 2: Phase composition of non-doped zirconia during crystallization at 80 °C in aqueous solution.

[1] Cox, B. (2004) *J. Nucl. Mater.* **336**, 331−368.
[2] Pazhani, R. *et al.* (2011) *J. Alloy. Compd.* **509**, 6819−6823.

Nanoparticle fate in waste water treatment

S. Schymura, M. Neugebauer,[1] H. Hildebrand, K. Franke
[1]AUD Analytik- und Umweltdienstleistungs GmbH, Chemnitz, Germany

Waste water treatment plants (WWTPs) are a main sink for manufactured nanoparticles. In order to evaluate NP fate in waste water treatment, radiolabeled NPs were injected into a model WWTP, allowing for a sensitive determination of their distribution in the WWTP effluents.

Waste water treatment plants (WWTPs) serve as a major sink for manufactured nanoparticles (NPs) controlling their removal from waste water and possible reintroduction into the environment *via* the WWTP effluents, sludge and cleared water, respectively.[1] In order to evaluate the emerging risk associated with the application of nanotechnologies, a detailed quantification of NP fate in waste water treatment is mandatory. For this purpose, NPs, such as TiO_2, CeO_2, multi-walled carbon nanotubes (MWCNTs), and CdSe/ZnS quantum dots (QDs), were radiolabeled and injected into a model WWTP. Consecutive sampling allowed the determination of distribution coefficients between sludge and water in the WWTP and in the effluents.

EXPERIMENTAL. TiO_2 NPs were radiolabeled with ^{48}V by activation using the in-house cyclotron cyclone 18/19.[2] Likewise, MWCNT were radiolabeled with ^{7}Be *via* recoil labeling at the cyclotron.[3] CeO_2 NPs were radiolabeled isotopically with ^{139}Ce by in-diffusion[4] while CdSe/ZnS QDs were dual-labeled with ^{65}Zn and ^{75}Se *via* a radiosynthesis route. The NPs were dispersed in synthetic waste water and subsequently injected in a model WWTP (Fig. 1). The model WWTP was operated with activated sludge from a local WWTP and fed with synthetic waste water according to OECD standards. Samples of sludge and supernatant water were taken daily from each reactor, as well as filtered (450 µm syringe filters) samples to estimate the amount of free NPs in the water.

RESULTS. Sampling shows a fast association of all NP types with the activated sludge within minutes after injection. Due to internal recirculation and the return sludge settings, the NPs are distributed homogeneously throughout the model WWTP within hours. A distribution of about 10,000 : 1 between sludge-associated NPs and free NPs in water is reached. Thus, the elimination of the NPs from the WWTP is mainly controlled by the removal of surplus sludge taking place every day of operation. The NPs are eliminated from the WWTP with a half-life of about 6 days (Fig. 2) reflecting the preset sludge age. After about 22 days of operation 10 % of the initial NPs remain in the WWTP. Approximately 1 % of the NPs leave the WWTP *via* the cleared waste water, mainly associated with non-sedimented sludge particles, such that only about 1 ‰ of the NPs leave the WWTP as free particles *via* the cleared water while the rest remain in the sludge. An impact of the NPs on the clearing process, as monitored by chemical oxygen demand of the inflow *vs.* the outflow, was not observed. A detailed evaluation of the data with respect to NP transformation is still ongoing.

Fig. 1: Model waste water treatment plant KLD 4N/SR.: Supply of synthetic waste water (25 L) (1), cleared waste water (30 L) (2), denitrification reactor (3), nitrification reactor (4), clarifier (5), stirrers (6) & (7), aeration frit (8), oxygen flow regulation (9–11), return sludge regulation (12), inlet tube (A), internal recirculation (B), return sludge tube (C).

$$NP_{WWTP}/NP_0 = 1.135 \cdot e^{-\left(\frac{ln2}{6.24d}\right)t}$$
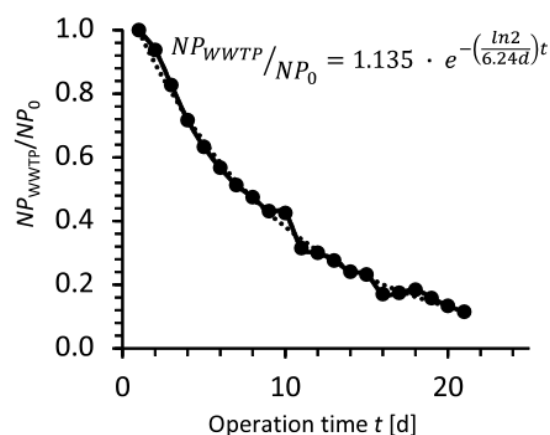
Fig. 2: Elimination of NPs from the model WWTP. The elimination process can be described by an exponential function with a half-life of 6.24 d representing the preset sludge age (the average residence time of the sludge in the WWTP).

[1] Lazareva, A. *et al.* (2014) *Sustainable Chem. Eng.* **2**, 1656–1665.
[2] Hildebrand, H. *et al.* (2015) *J. Nanopart. Res.* **17**, 278.
[3] Abbas, K. *et al.* (2013) *Appl. Rad. Isotop.* **73**, 44–48.
[4] Schymura, S. *et al.* (2017) *Angew. Chem. Int. Ed.* **56**, 7411–7414.

Inherited control of crystal surface reactivity

C. Fischer, I. Kurganskaya,[1] A. Lüttge[2]

[1]Institute of Geological Sciences, Universität Bern, Bern, Switzerland; [2]MARUM & Faculty of Geosciences, Universität Bremen, Bremen, Germany

Material and environmental sciences have a keen interest in the correct prediction of material release as a result of fluid-solid interaction. For crystalline materials, surface reactivity exerts fundamental control on dissolution reactions; however, it is continuously changing during reactions and governs the dynamics of porosity evolution. Thus, surface area and topography data are required as input parameters in reactive transport models. Consequently, the analysis of surface reaction kinetics and material release is a key to understanding the evolution of dissolution driven surface roughness and topography. Kinetic Monte Carlo (KMC) methods simulate such dynamic systems. Here we apply these techniques to study the evolution of reaction rates and surface topography in crystalline materials having contrasting defect densities.

SIMULATIONS. A KMC calculation simulates a series of single reactions at the atomic scale. Here, we apply a KMC model for a Kossel crystal. The bond energies Φ between all atoms are constant. The KMC model is based on the Bortz-Kalos-Lebowitz algorithm. The algorithm allows for a reactive event at each iteration step. The simulation provides the temporal evolution of a dissolving surface, based on a series of single reaction events on the crystal surface. Lasaga and Lüttge (2004) provide general information about KMC models for mineral dissolution.[1] In this study, the model simulates dissolution reactions under conditions far from equilibrium.

RESULTS. We analyzed rate spectra in order to investigate the relationship between reaction kinetics, surface topography, and potential inhibition of surface reactivity. Figure 1 illustrates the surface evolution (Fig. 1A–D) and the respective rate spectra (Fig. 1A′–D′). During dissolution of the upper crystal domain, the evolution of both surface topography and rate spectra reflects the situations of low defect density (Fig. 4A, A′) *vs.* high defect density (Fig. 4C, C′). Both rate spectra show an asymmetric shape. The less reactive crystal domain is characterized by a spectrum with a tail towards lower rate components. Accordingly, the more reactive crystal domain shows the opposite behavior. Then, the underlying domain gets partly and later completely exposed to dissolution during the ongoing removal of the upper domain. Figures 1B, D illustrate the crystal surface topography after complete removal of the uppermost domain. At this time, both surfaces are dominated by large etch pit structures. It is a surprising result that the high defect density of the newly exposed material in Fig. 1B does not impact significantly the reaction rate.[2]

The model system consists of domains with alternating reactivity, implemented by low *vs.* high defect densities. Our results indicate complex and dynamic feedbacks between domains of high *versus* low defect density, with the latter apparently limiting the overall dissolution rate of the former – a limitation that prevails even after their disappearance. We introduce the concept of "inherited" control, consistent with our observation that maximum dissolution rates in high defect density domains are lower than they would be in the absence of low defect density neighboring domains. The controlling factor is the spatial pattern of surface accessibil-
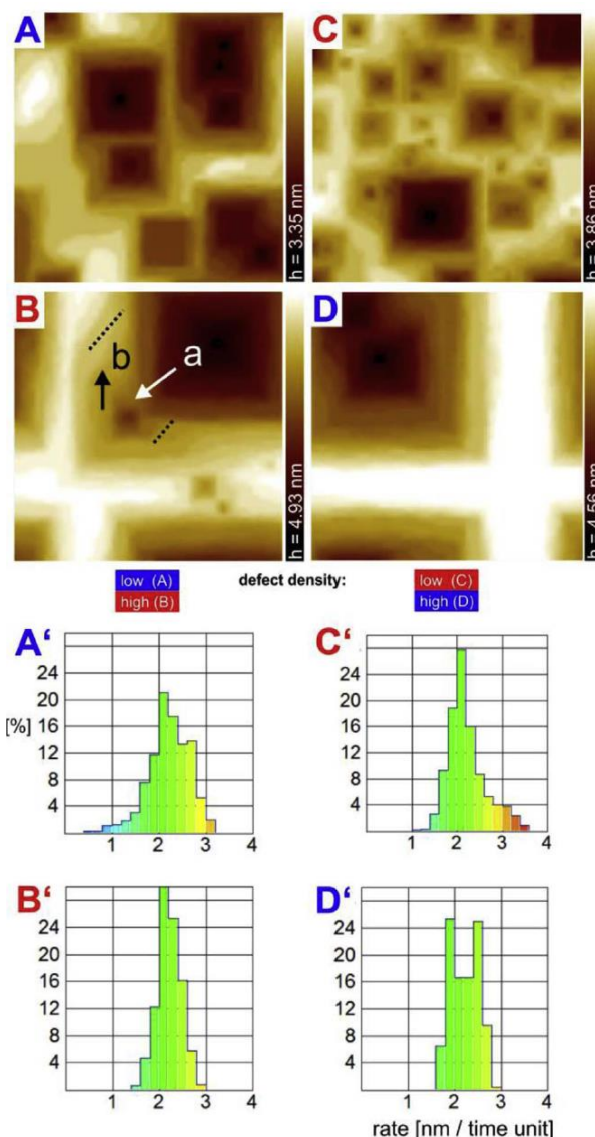
Fig. 1: Surface topography and rate spectra evolution of two different layered cake model structures. Left (A,B) with low (blue, upper part) and high (red, lower part) reactivity domains (dt = 5×10^9 s). Right (C,D) shows inverse order of domain reactivity (dt = 6×10^9 s). Corresponding rate spectra (A′, B′) and (C′, D′) are shown below, time unit (TU) = 6×10^9 s. System size = 300×300 nm².

ity of fluids. Thus, the distribution of large etch pits centers is inherited almost independently of spatial contrasts in crystal defect density during ongoing reactions.

As a critical consequence, the prediction of both the material flux from the reacting surface and the evolution of topography patterns in crystalline material is constrained by the reaction history. Important applications include the controlled inhibition of reactivity of crystalline materials as well as the quantitative evaluation and prediction of material failure in corrosive environments.

[1] Lasaga, A. C. *et al.* (2004) *Eur. J. Mineral.* **16**, 713–729.
[2] Fischer, C. *et al.* (2018) *Appl. Geochem.* **91**, 140–148.

Pulsating dissolution of crystalline matter

C. Fischer, A. Lüttge[1]

[1]MARUM & Faculty of Geosciences, Universität Bremen, Bremen, Germany

Fluid–solid reactions result in material flux from or to the solid surface. The prediction of the flux, its variations, and changes with time are of interest to a wide array of disciplines, ranging from the material and earth sciences to pharmaceutical sciences. Reaction rate maps that are derived from sequences of topography maps illustrate the spatial distribution of reaction rates across the crystal surface.

Highly spatially resolved rate maps reveal the existence of rhythmic pulses of the material flux from the crystal surface. This observation leads to a change in our understanding of the way crystalline matter dissolves. Rhythmic fluctuations of the reactive surface site density and potentially concomitant oscillations in the fluid saturation imply spatial and temporal variability in surface reaction rates. Knowledge of such variability could aid attempts to upscale microscopic rates and predict reactive transport through changing porous media.

The dissolution of crystalline matter plays a critical role in technical and natural processes. Reliable predictions of resulting material fluxes require a mechanistic understanding that includes both the dominant pattern and heterogeneous distribution of surface reactivity. However, a consistent dissolution model that includes such knowledge is still missing. Understanding the mechanisms requires spatially and temporally resolved observations of reacting surfaces. Numerous dissolution studies using laboratory experiments and surface-sensitive methods have supported the conclusion of a continuous surface step movement that results in the removal of crystal layers *via* surface steps.

EXPERIMENTAL. We generated a time-lapse sequence of maps that quantify the development of the ZnO topography over a time span of 12 h.[1] The resulting topography maps were used to generate a sequence of rate maps, that is, the first temporal derivative of the reacting crystal topography. Calculations of the second and third temporal derivatives then provide the maps of the rate acceleration and the so-called rate jerks.

RESULTS. The interpretation that crystal moieties (*e.g.*, atoms or molecules) are continuously removed during dissolution is now challenged by observations made possible through the analysis of reacting surfaces of high lattice symmetry and slow reaction kinetics. Zinc oxide (ZnO) is an example that allows for a "slowmotion" analysis of its dissolution kinetics. When we analyzed the measured rate distribution on (000−1) crystal surfaces of dissolving ZnO, we made a striking observation: the concentric distribution of rate pulses at and around etch pits (Fig. 1A).[1]

Conceptually, we base surface reactivity of crystalline matter on the dissolution stepwave model. This model describes the relationship between crystal lattice defects and the formation of reactive surface sites. These kink sites are self-replicating. Repeated removal of kink atoms accounts for the spatial motion of steps across the crystal surface. This continuous process results in the surface-normal retreat, and ultimately, in the destruction of any dissolving crystal. The stepwave model predicts an initial decrease in velocity close to a defect structure and an increase in velocity far from the

defect. The absolute values of the velocity and acceleration of a step are controlled by the saturation state or local deviation from equilibrium (*i.e.*, ΔG values) of the system.

Are those pulses, over several micrometers in lateral distance, ZnO-specific or a general trait of dissolving crystalline matter? To answer this question, we also analyzed calcite ($CaCO_3$) rate maps (Fig. 1B). Cleaved (104) surfaces of calcite have been well studied with respect to their dissolution kinetics. Investigations mostly conducted with AFM techniques have focused on the velocity of reacting surface steps. We have now produced rate maps of sufficient size by using interferometry techniques. They show rate distributions on the carbonate surface that are indeed reminiscent of the concentric flux pulses of ZnO.
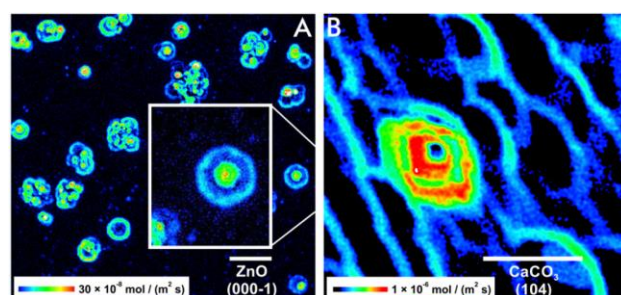
Fig. 1: Dissolution rate maps show quantitatively the spatial distribution of the time-normalized material flux. Note the intervals between two reaction fronts. Such surface areas are free of any material flux or show significantly lowered reactivity. The initially isolated rate pulses occur at etch pits that are formed around the outcrops of line defects. The locally regular material release is complicated after spatial superimposition of rate pulses. Rate maps of two dissolving crystal surfaces are shown. (A) ZnO (000−1) with concentric and equidistant rate pulses. (B) $CaCO_3$ (104) with repeated rate pulses (red) at a screw dislocation and single stepwave fronts (blue) originating from point defects. (Scale bar length: 10 µm.)

The rate maps show that higher rates are associated with the outcrops of screw dislocation defects. The sequence of maps illustrates the spatial development of the concentric rate pulses, manifested by the growth of their diameter. Previous theoretical considerations of the propagation of stepwaves did not predict such behavior.

The observed contrasts in reaction velocity are responsible for specific surface topography alterations. Ultimately, they predefine the evolution of pore structures within crystalline matter. Lateral and vertical heterogeneity of reacting surfaces are important constraints to reactive transport modeling and specific parameterization, thus providing boundary conditions for reactive transport models on the pore scales and larger.

[1] Fischer, C. *et al.* (2018) *Proc. Natl. Acad. Sci U.S.A.* **115**, 897–902.

Preferential flow in soil and reactive transport of Cu and the herbicide MCPA

J. Kulenkampff, M. Gründig, L. Karimzadeh, M. Kersten,[1] J. Lippmann-Pipke,[2] H. Lippold, M. Stoll,[1,3] C. Stuhlfauth[1]

[1]Institute of Geosciences, Johannes Gutenberg University, Mainz, Germany; [2]Bundesanstalt für Geowissenschaften und Rohstoffe (BGR), Hannover, Germany; [3]Karlsruhe Institute of Technology, Karlsruhe, Germany

Although MCPA has beneficial properties as a herbicide – it is non-toxic and it is claimed to be rather immobile in soil – it can have harmful environmental effects, for example mobilization of toxic elements by complexation or accelerated migration by preferential transport. Here, we studied mobilization effects with the help of ^{64}Cu-labelling. The radionuclide was applied as a tracer for sensitive detection and for spatiotemporal imaging of transport through artificial soil columns.

EXPERIMENTAL. Artificial soil columns were prepared, containing 94 % sand, 5 % illite, and 1 % goethite. After preconditioning with carrier solution (10 mM KF + 1 mM NaNO$_3$), a pulse of [^{64}Cu]Cu(MCPA)$_2$ was injected, and subsequently, after decay of the radionuclide, a pulse of [^{18}F]KF. The propagation of the tracer pulses was monitored with PET. Details of the experimental and analytical setup were reported elsewhere.[1, 2] For geochemical model parameterization, break-through curves of MCPA and the conservative tracer [^{3}H]H$_2$O were recorded for a range of pH values.[3]

RESULTS. The relatively long-lived ^{64}Cu allowed recording a PET sequence over an extended experimental time span to visualize the effect of retardation (Fig. 1 and see also movie available).[2] The [^{64}Cu]Cu(MCPA)$_2$ complex showed more than ten times slower propagation than the conservative tracer [^{18}F]F$^-$. Apart from this retardation effect, both conservative and reactive transport patterns are characterized by a cup-like distribution of the tracer, indicating preferential peripheral transport in the column. This is probably unavoidably caused by increasingly ordered grain packing towards the edge, and it should be suspected that similar structural effects have to be considered even more in customary columns with smaller diameter.

First attempts to align the outcomes of column experiments with model simulations showed significant underestimation of retardation because a 1D problem was assumed that did not consider the effect of preferential transport (Fig. 2). The difference between measured and modelled break-through curves could be reduced considerably with a 2D transport model that was based on the PET measurements. Beside the ecological relevance, this example underscores the excellent abilities of PET for a meaningful parameterization of numerical approaches.

[1] Kulenkampff, J. *et al.* (2018) *Sci. Rep.* **8**, 7091.
[2] Kulenkampff, J. *et al.* (2016) mp4–movie *via* zenodo.org: https://zenodo.org/record/852968.
[3] Lippold, H. *et al.* (2018) *Appl. Geochem.* **98**, 345–350.
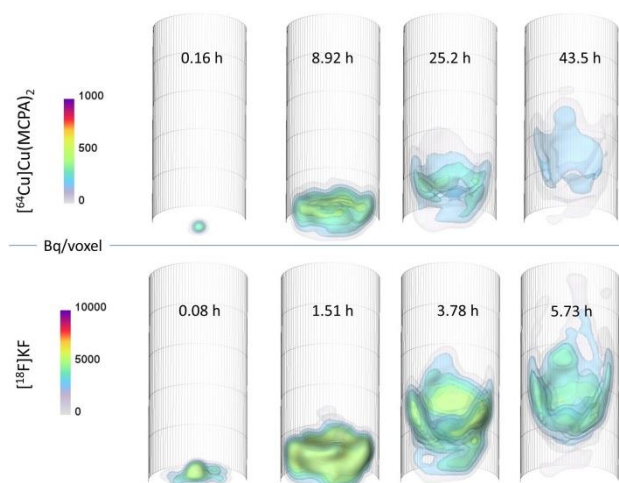
Fig. 1: Four frames out of the PET image sequence during migration of the [^{64}Cu]Cu(MCPA)$_2$ complex (upper row). Four images recorded during propagation of [^{18}F]F$^-$ (lower row). Both experiments were conducted at the same flow rate of 0.1 mL min^{-1}. (Note the different time scales.)
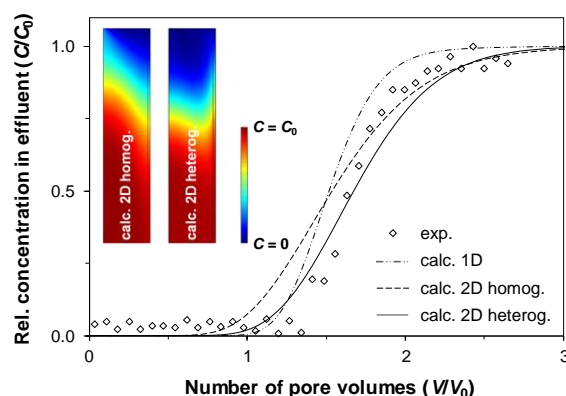
Fig. 2: Experimental and modelled break-through curves for MCPA. Besides chemical interaction, the 1D model considers longitudinal advection-dispersion only. In the 2D models, the spatial distribution of flow velocities is controlled by the pressure gradient field in the column, and transverse dispersion is included. The heterogeneous 2D model contains a 1-mm peripheral zone with increased porosity and permeability to simulate the observed anomalies in the flow field (Fig. 1). Inset: 2D calculations of the distribution of MCPA (half longitudinal section view for $V/V_0 = 0.97$), demonstrating that peripheral flow results in delayed break-through.

Studying gravity effects on flow in porous media by imaging with the tilted GeoPET

J. Kulenkampff, S. Gruhne, J. Pingel, T. Schäfer,[1] C. Fischer

[1]Friedrich-Schiller-University Jena (FSU), Institute of Geosciences, Applied Geology, Jena, Germany

The existing GeoPET-scanner was customized for operation with vertical orientation of the field of view. This was accomplished by tilting the gantry and joining a rotary table. Having this hardware update available, it is now possible to conduct experiments with upright positioned columns. This enables to study gravity-driven density effects and multiphase flow with the sample orientation in parallel to the scanner axis. One example for the benefits of the tilted orientation is the elimination of inexplicit preferential flow path distributions along the top or bottom of the sample, that is are frequently observed in column experiments with highly permeable material.

EXPERIMENTAL. Up to recent, we applied the GeoPET-scanner for process tomography of tracer propagation through geomaterials in the conventional horizontal orientation. This is disadvantageous, in particular when density flow effects are present. Up to now, such experiments where conducted on samples oriented perpendicular to the field of view axis (Fig. 1). This caused unrecoverable artefacts which considerably impaired image quality. We improved the method by constructing a tilt mechanism. This was motivated by "ClearPET Neuro"[1] that was developed at the FZJ, but instead of its extensive device for horizontal rotation of the detector system we constructed a light-weighed rotary table for rotating the sample (Fig. 2).

As a first test, we utilized porous materials printed with a 3D-printer at FWK. The highly permeable artificial sample mimics complex porous solids and provides a well-defined pore size distribution. First results illustrate the new capabilities of the PET system. A difference in fluid density is responsible for preferential flow along the sample bottom (Fig. 3, left side) which is not observed with the sample in upright position and vertical fluid flow orientation (Fig. 3, right side).

Fig. 2: Aligned axes of the sample and FOV by tilting of the complete scanner. The sample is fixed on a rotary table below the gantry.
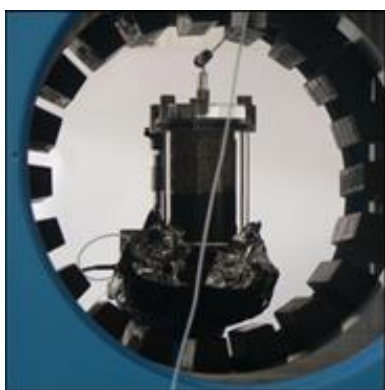
Fig. 1: Disadvantageous vertical orientation of the sample in the horizontally oriented FOV .
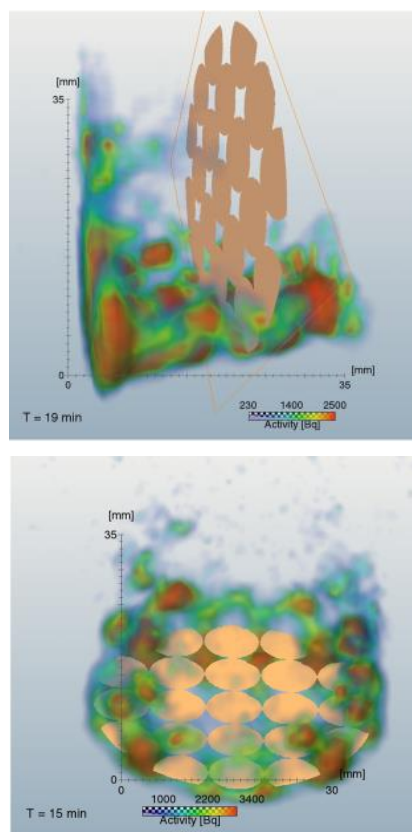
Fig. 3: Tracer distribution during a flow experiment through a highly permeable porous sample. Horizontal orientation with preferential flow along the bottom (above). Vertical orientation, showing homogenous lateral distribution of the pathways (below).

[1] Ziemons, K. *et al.* (2004) *2004 IEEE Nuclear Science Symposium conference record.* DOI: 10.1109/NSSMIC.2004.1462747.

Investigation of a uranium mining contamination in a wetland in central France

A. C. Fichtner,[1,2] S. Sachs, A. Rossberg, A. C. Scheinost, T. Arnold, G. Montavon,[1] T. Stumpf

[1]Laboratoire Subatech, IMT Atlantique, Nantes, France; [2]HZDR, Institute of Resource Ecology, Dresden, Germany

Soil cores have been analyzed in order to learn more about the nature of a radioactive contamination downstream of a tailing storage site. Uranium concentrations range up to 4,000 ppm in dry soil with decay chain members in relative equilibrium indicating a particulate transport of the contamination. Particles found in the soil by SEM seem to confirm this hypothesis while EXAFS analysis does not show signs of uranium in mineral form.

The storage site Roffin, located in the region of Auvergne, France, contains approximately 30,000 t of mill tailings from the adjacent processing plant of the same name which was operated from 1947 to 1956.[1] Gamma-ray surveys have shown tenfold elevated radiation levels in a wetland located alongside a creek downstream of the storage site (Fig. 1). Drill cores taken in this area show uranium concentrations up to 4,000 ppm in the first 30 cm, which seems to correlate with the presence of a white, clayey layer (Fig. 2).

EXPERIMENTAL. Drill cores have been taken by means of a Russian type corer and sectioned on-site under nitrogen atmosphere. Samples destined for speciation analysis, notably X-ray absorption spectroscopy (XAS), were immediately frozen with liquid nitrogen and subsequently handled under anoxic conditions. XAS was performed at the Rossendorf beamline at the ESRF in Grenoble, France. Gamma analysis was performed for the quantification of decay chain members of uranium. Furthermore, cesium-137 from nuclear fallout was measured in order to date the sedimentation of the soil layers in respect to the Chernobyl accident and the period of atmospheric nuclear weapons tests.[2] Two samples with high uranium concentrations were examined by scanning electron microscopy (SEM).

RESULTS. The highest cesium-137 activities were found just above the white layer, strongly suggesting its deposition before the maximum in global fallout in 1963. The fact that lead-210 is found in similar activities to the direct descendant of uranium, thorium-234 (Fig. 2), leads to the conclusion that the radionuclides must have been transported at the same time, in the form of particles. This is due to the very different mobility of these elements in soil. A number of such particles were subsequently found by electron microscopy with uranium concentrations in the range of percents as measured by energy dispersive X-ray spectroscopy (EDS) (Fig. 3). These findings relate the origin of the contamination with the active period of the site, mainly by the release of fine particles from the sedimentation basins.

The XANES results show a mixture of U(IV) and U(VI) with more of the hexavalent form in the upper layers, most likely due to the ingress of atmospheric oxygen.

The correlation of uranium with lead in the uranium-rich particles suggests the presence of the mineral parsonsite, $[Pb_2(UO_2)(PO_4)_2]$, which is the main mineral mined in the area. Yet, the recorded EXAFS spectra show no signs of a mainly mineral form of the present uranium. Selective extraction experiments are currently performed in order to narrow down the predominant form of uranium.
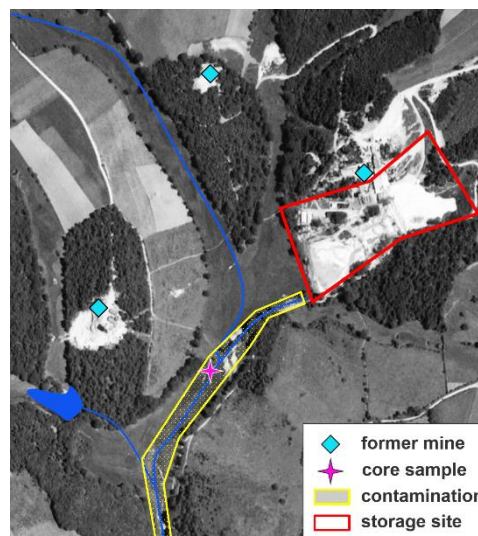
Fig. 1: Overview of the sampling site laid over an aerial picture of 1954.
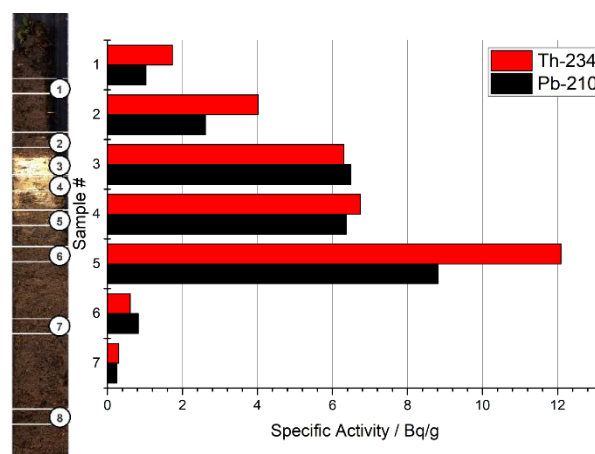
Fig. 2: Picture of a representative 50 cm core sample, showing the characteristic white layer, and the corresponding gamma activities of the sampled layers, measured in the wet soil.
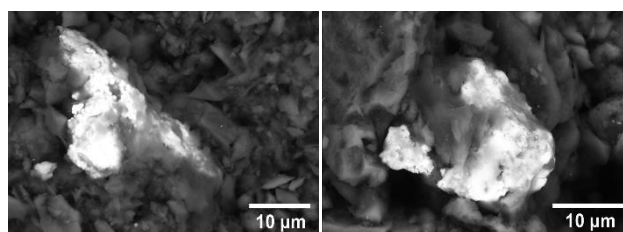
Fig. 3: Scanning electron microscope images of uranium rich particles found in layer 3 and 5 (Fig. 2).

[1] Himeur, F. *et al.* (2010) AREVA Operational Report: Bilan environnemental – Sites miniers du Puy–de–Dôme.
[2] Ritchie, J. C. *et al.* (1990) *J. Environ. Qual.* **19**, 215–233.

XRF characterization of uranium minerals

S. Bauters, I. Sinenko,[1] I. Pidchenko, E. Gerber,[1] D. Banerjee,[2] L. Vincze,[3] S. N. Kalmykov,[1] K. O. Kvashnina

[1]Lomonosov Moscow State University, Moscow, Russia; [2]Department of Chemistry, KU Leuven, Leuven, Belgium; [3]XMI, Department of Chemistry, Ghent University, Ghent, Belgium

Spatially resolved X-ray fluorescence (XRF) spectroscopy is a powerful imaging tool capable of providing element-specific concentrations in materials. A strategy to quantify XRF data using Monte Carlo based simulations was successfully applied to derive the chemical formula of several natural uranium minerals, namely Cleusonite, Davidite and Brannerite.

Understanding the influence of radionuclides on the structure of minerals is crucial with respect to the disposal and storage of radioactive waste in the long term. Due to their changing geochemical environments over time, natural minerals are often complicated, heterogeneous systems requiring in-depth analysis to confirm their genuineness. An important step in determining the identity of minerals is the accurate derivation of their elementary composition. In this study we present synchrotron radiation μ-XRF imaging in combination with Monte Carlo simulations as a powerful quantification tool for uranium minerals

EXPERIMENTAL. The XRF measurements were performed at the DUBBLE BM26A beamline of the European Synchrotron Radiation Facility (ESRF). The incident energy was selected using the a double Si(111) crystal monochromator. Rejection of higher harmonics was achieved with two Pt mirrors at an angle of 2 mrad relative to the incident beam. The dedicated microfocus platform provided an 8×8 μm^2 spot size at the sample position.[1] The XRF mappings were performed at 17.177 keV with a 1 s dwell time and 20 μm step size. The XRF spectra were normalized to the incident flux. Quantification was achieved with iterative Monte Carlo based simulations using the XMI-MSIM and PyMca software packages.[2, 3]

RESULTS. Once the spatially resolved XRF spectra are obtained, the PyMCA software package is capable of retrieving the peak intensities of each XRF sensitive element. The software applies I_0 normalization and takes artefacts such as sum peaks, escape peaks and peak overlap into account. In the case of heterogeneous samples such as the measured brannerite sample, homogeneous regions are defined using the statistical technique called K-means clustering, which collects pixels with elemental correlations together.

The homogeneous samples/regions are then subjected to the iterative quantification based on Monte Carlo simulations. The complete experimental parameters and setup are mathematically defined and applied to an estimated elementary sample composition. The simulated sample composition is then adjusted until the simulated peak areas correspond with the experimental spectrum, as seen in Fig. 1.

The calculated concentrations can be applied to the 2D XRF intensity mappings to provide elemental concentration mappings expressed in weight percentage (Fig. 2). Table 1 presents the calculated chemical formulas of the measured mineral samples, normalized to theoretical values of oxygen/hydrogen, calculated in a straightforward way from the elemental concentrations when taking atomic weights into account.
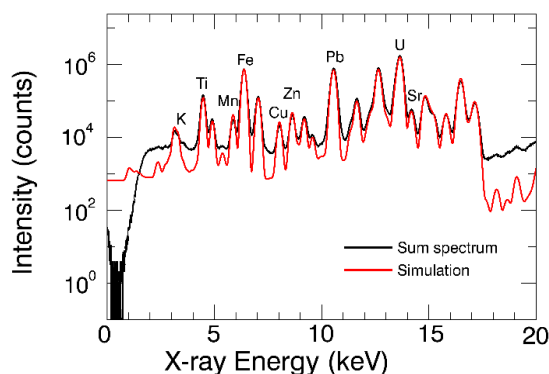
Fig. 1: The experimental (black) and simulated (red) sum spectrum of the Cleusonite mapping. The elementary concentrations obtained from this Monte Carlo simulation enable the transformation from XRF intensity mappings to concentration mappings (Fig. 2).

Tab. 1: XRF-based calculated chemical formulas for the Cleusonite (A), Davidite (B) and Brannerite (C) sample. The Brannerite formula represents the clustered area labelled 3 in Fig. 2.

(A)	$Pb_1Sr_{0.04}Mn_{0.8}U_{1.2}Zn_{0.2}Ti_{7.8}Fe_9(O,OH)_{38}$
(B)	$Ce_{0.9}Y_{0.6}U_{0.1}Mn_{1.1}Th_{0.04}Pb_{0.3}V_{0.8}Ti_{19}Fe_{12}(O,OH)_{38}$
(C)	$Ca_4Ce_{0.6}Y_{0.02}U_1Mn_{0.25}Th_{0.02}Pb_{0.05}Ti_{2.18}Fe_{14}O_8$
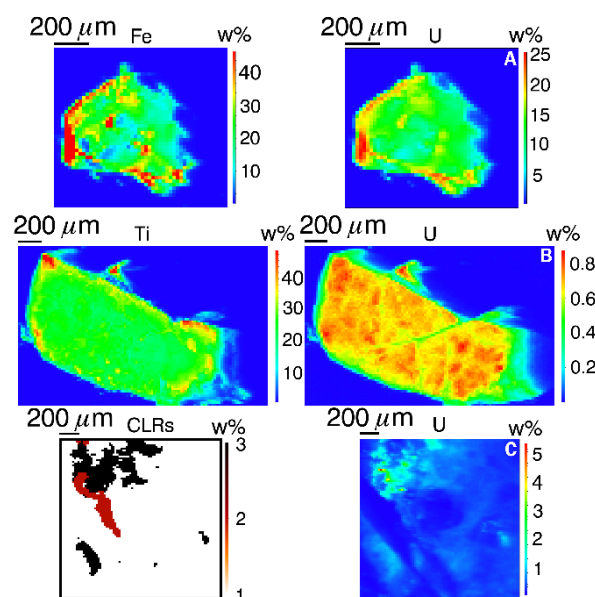
Fig. 2: Quantified elemental XRF mappings for the Cleusonite (A), Davidite (B) and Brannerite (C) samples. The CLRs mapping is the result of the K-means statistical clustering technique applied only on the heterogeneous Brannerite sample.

[1] Bauters, S. *et al.* (2018) *Anal. Chem.* **90**, 2389–2394.
[2] Schoonjans, T. *et al.* (2013) *Spectrochim Acta B* **82**, 36–41.
[3] Sole, V. A. *et al.* (2013) *Spectrochim Acta B* **62**, 63–68.

Thermodynamic reference database THEREDA: 7. Upgrade of the uranium (IV/VI) data release

A. Richter, F. Bok

The joint project THEREDA provides a centrally administered and maintained database of verified thermodynamic parameters as it is required for environmental applications in general and radioactive waste in particular. Tailored databases are available for immediate use in supported geochemical codes. The data for tetra- and hexavalent uranium in the oceanic salts system released in 2014 (R-09)[1, 2] has been upgraded recently mainly including the U(IV/VI)-phosphate interactions.

PHOSPHATE DATA. The new THEREDA data release R-12 from the project partner GRS (May 2018) comes with parameter files for phosphate species in the oceanic salt system.[3, 4] This enabled the upgrade of the uranium data release R-09 towards the uranium(IV/VI)-phosphate interactions. The following phase constituents of uranium with phosphorus are included.[4]

Tab. 1: Release of U(IV/VI)-phosphate species data in R-09.1

Aqueous species	**Mineral phases**	
U(VI)	**U(IV)**	**U(VI)**
$UO_2(PO_4)^-$	$CaU(PO_4)_2 \cdot 2H_2O(cr)$	$Ca(UO_2)_2(PO_4)_3 \cdot 3H_2O(cr)$
$UO_2(HPO_4)(aq)$	$U(HPO_4)_2 \cdot 4H_2O(cr)$	$Mg(UO_2)_2(PO_4)_2(cr)$
$UO_2(H_2PO_4)^+$		$UO_2(HPO_4) \cdot 4H_2O(cr)$
$UO_2(H_3PO_4)^{2+}$		$(UO_2)_3(PO_4)_2 \cdot 4H_2O(cr)$
$UO_2(H_2PO_4)_2(aq)$		$(UO_2)_3(PO_4)_2 \cdot 6H_2O(cr)$
$UO_2(H_2PO_4)(H_3PO_4)^+$		$UO_2(H_2PO_4)_2 \cdot 3H_2O(cr)$

The extended data release R-09.1 comes with the respective parameter files for a valid temperature of 298.15 K. The supported codes are Geochemist's Workbench, CHEMAPP and PHREEQC. The data have been rigorously tested for solubility measurements of various U(IV/VI) mineral phase. By test calculations, the consistency with earlier releases could be confirmed.[4] Also recalculations of experimental solubility data[5] have been performed to confirm the quality of this data set (Fig. 1).

NEW PHASE ZIPPEITE. The sulphate containing uranyl mineral $K_3(UO_2)_4(SO_4)_2O_3OH \cdot 3.3(H_2O)(cr)$ may form in the stainless steel canisters intended to store spent nuclear fuel in a nuclear repository.[6] Zippeite was synthesized, and the thermodynamic properties were measured by calorimetry and solubility measurements.[6] The calculated log $K° \pm 1\sigma$ averaged for four different solubility experiments was 4.14 ± 0.11. The solubility was modeled depending on the pH using the THEREDA database. The results of the calculation reproduces the experimental values acceptably (see Fig. 2).

OUTLOOK. Currently, there are no Pitzer coefficients available for the interaction between uranium (IV/VI) and phosphato species. On the other hand, neglecting the respective species would lead to a significantly worse prediction of solubilities in phosphate containing solutions. To overcome these shortcomings, the following work is scheduled for 2019:
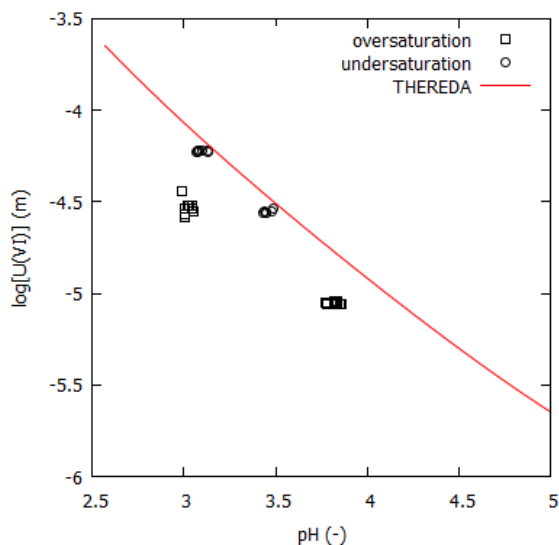
Fig. 1: Solubility of autunite $Ca(UO_2)_2(PO_4)_3 \cdot 3H_2O(cr)$, line: calculated solubility using THEREDA, dots: experimental data from [5].
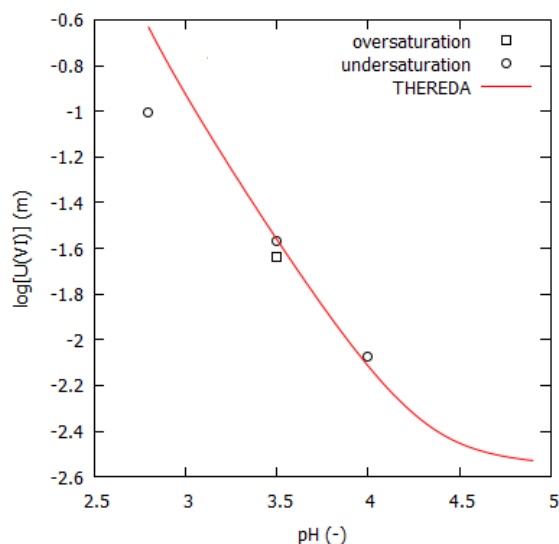
Fig. 2: Solubility of zippeite, line: calculated solubility using THEREDA, dots: experimental data from [6].

– Examination whether the solubility constants of U (VI) phosphate phases have been derived taking into account the corresponding aquatic complexes
– If possible, estimation of corresponding Pitzer coefficients from published experimental U(VI)-phosphato data.

[1] Richter, A. *et al.* (2014) *Report HZDR−048*, p. 48.
[2] Richter, A. *et al.* (2015) *Report HZDR−065*.
[3] Scharge, T. *et al.* (2014) *J. Chem. Thermodyn.* **80**, 172−183.
[4] THEREDA – Thermodynamic Reference Database (http://www.thereda.de)
[5] Gorman-Lewis, D. *et al.* (2009) *Environ. Sci. Technol.* **43**, 7413−7422.
[6] Sharifironizi, M. *et al.* (2016) *Chem. Geol.* **447**, 54−58.

Thermodynamic reference database THEREDA: 8. Solubility of Se(IV/VI) compounds in high saline solutions

F. Bok

Selenium (with the isotope Se-79 being an important fission product) can occur in oxidation states varying between +VI and −II. Most often negatively charged species are formed rendering them extraordinarily mobile in groundwater systems. For a correct calculation of the solubilities of Se(VI) and Se(IV) phases, the Pitzer ion-ion interaction model is essential for solutions with high ionic strengths.

The actual state-of-the-art of thermodynamic data for Selenium are given in the OECD/NEA Chemical Thermodynamics.[1] However, this data compilation does not address the Pitzer ion-ion interaction model which is needed for modelling of the expected highly soluble selenium compounds in brines. An polythermal set of Pitzer interaction parameters was compiled by GRS.[2, 3]

However, these data compilations hold solubility data for T = 25 °C only. To enable the calculation of selenium solubility at various temperatures in high saline solutions, temperature functions for the solubility products of alkaline and earth alkaline selenium phases have been deduced.

CALCULATION. The experimental solubility data sets of various alkaline and earth alkaline selenates and selenites have been collected. The temperature function's (1) parameters of the solubility products were fitted to these solubility data using the geochemical speciation code PHREEQC in combination with the parameter estimation software Ucode2014.[4, 5] The thermodynamic database used was THEREDA.[6] So the obtained data are consistent with the actual Pitzer model.

$$\log K_{sp} = A_1 + A_2 T + \frac{A_3}{T} + A_4 \log T + \frac{A_5}{T^2} + A_6 T^2 \quad (1)$$

RESULTS. Temperature function's parameters for the solubility products of seven selenate and four selenite mineral phases could be obtained (Tab. 1).

With these new temperature-dependent data, the solubility of selenium(IV) and (VI) an be calculated over the temperature range (T = 0 − 100 °C) relevant for a nuclear waste disposal (Fig. 1 & 2).

Tab. 1: Temperature function's parameters for the solubility products of alkaline and earth alkaline selenates and selenites.

Solid phase	A_1	A_3	A_4
Na_2SeO_4 (cr)	5.8	–	−2.021
$Na_2SeO_4 \cdot 7.5H_2O$(cr)	−37.06	–	14.99
$Na_2SeO_4 \cdot 10H_2O$(cr)	−75.35	–	30.21
K_2SeO_4 (cr)	−1.317	–	1.045
$MgSeO_4 \cdot 7H_2O$(cr)	−39.82	–	15.83
$MgSeO_4 \cdot 6H_2O$(cr)	11.12	–	−4.985
$MgSeO_4 \cdot 4.5H_2O$(cr)	−3.3942	0.0134	–
Na_2SeO_3(cr)	27.63	–	−10.48
$Na_2SeO_3 \cdot 5H_2O$(cr)	−8.719	–	3.771
K_2SeO_3 (cr)	22.12	–	−6.331
$K_2SeO_3 \cdot 4H_2O$(cr)	−15.71	–	7.862
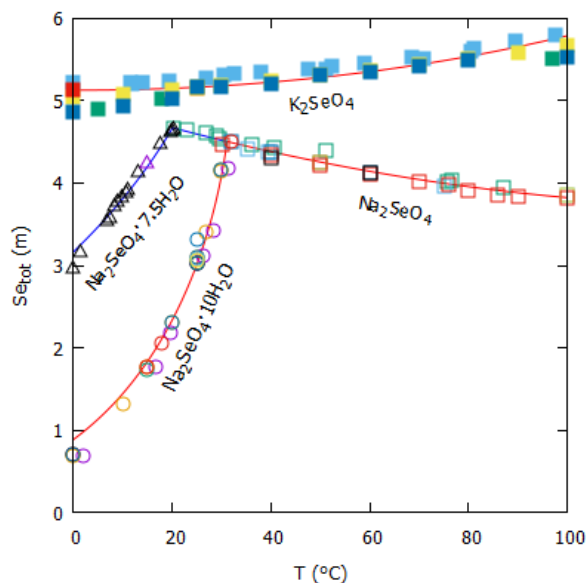
Fig. 1: Temperature dependent solubility of Se(VI) solid phases (points: published experimental data, lines: calculation using this data set).
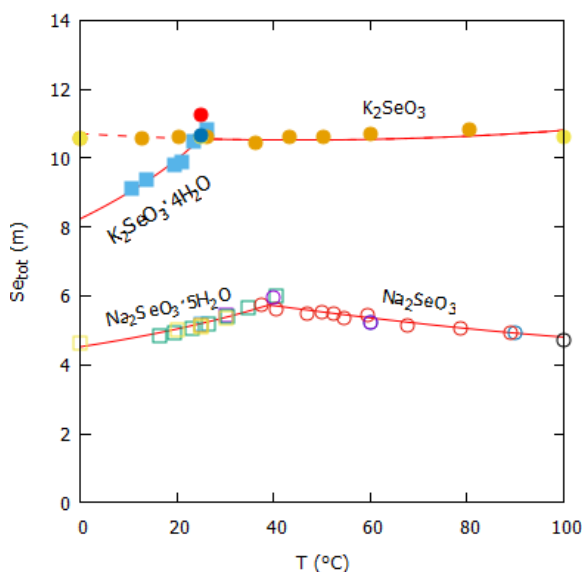
Fig. 2: Temperature dependent solubility of Se(IV) solid phases (points: published experimental data, lines: calculation using this data set).

[1] Olin, Å. *et al.* (2005) *Chemical Thermodynamics of Selenium*, OECD Nuclear Energy Agency, Issy−les−Moulineaux (France).
[2] Hagemann, S. *et al.* (2012) *Report GRS − 245*, p. 176.
[3] Bischofer, B. *et al.* (2016) *Report GRS − 374*, p. 757.
[4] Poeter, E. P. *et al.* (2005) *IGWMC Report number GWMI 2014−02*.
[5] Parkhurst, D. L. *et al.* (2013) *U.S. Geological Survey Techniques and Methods, Vol. book 6−A43*.
[6] THEREDA – Thermodynamic Reference Database (http://www.thereda.de)

Long-Lived Radionuclides in

BIOLOGICAL

SYSTEMS

First insights into the interaction of Cm(III) with oocytes

H. Moll, F. Ruhe,[1] S. Sachs

[1]Institute of Cell Biology and Biophysics, Leibniz University Hannover, Hannover, Germany

First luminescence measurements demonstrated strong interactions of Cm(III) with untreated oocytes: red-shifted emission maximum at 605 nm compared with 593.8 nm for Cm^{3+} and a prolonged luminescence lifetime of 195 μs. This suggests strong changes in the first coordination sphere of Cm(III) by functionalities of the cell envelope.

In order to explore the fate of trivalent actinides (An(III)) in the biosphere, it is essential to understand their interactions and possible transport through plant metabolite transporters on a molecular level. A very interesting model system in this context are oocytes of the South African clawed frog, *Xenopus laevis*. These oocytes can be used as a heterologous expression system for plant membrane proteins (*e.g.* transporter/channel) in order to study the transfer of metal ions.[1] We studied the interaction of unmodified oocytes with Cm(III) applying liquid scintillation counting (LSC) and time-resolved laser-induced fluorescence spectroscopy (TRLFS).

EXPERIMENTAL. To harvest *Xenopus laevis* oocytes, a female frog was anaesthetized in ice-cold 1.5 % (w/v) ethyl-3-aminobenzoate methansulfonate salt (Fig. 1).
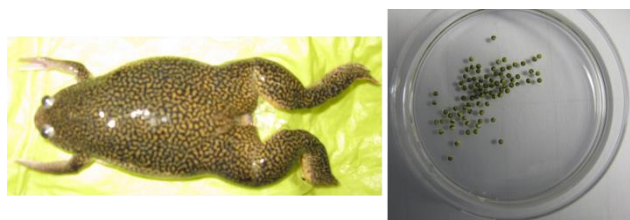
Fig. 1: Female *Xenopus laevis* frog before oocytes removal (left). Isolated oocytes in control medium (right).

The lobes containing oocytes were removed from the abdominal cavity and placed in oocyte control medium (OE) supplemented with 2 mM $CaCl_2$ and 88 mM NaCl, 1 mM KCl, 10 mM Tris-HCl, and 0.82 mM $MgCl_2$ (pH 7.4 and π 180 mosmol L^{-1}). The tissue was then disrupted and oocytes were defolliculated by an incubation of 1 h in OE without calcium containing $190-240$ U mL^{-1} collagenase type II. Afterwards, oocytes were washed with OE containing calcium, healthy stage V and VI oocytes were selected and stored at 18 °C. TRLFS measurements were performed under N_2 atmosphere in OE buffer at 25 °C. Experimental details about the laser system can be found elsewhere.[2] 20 to 30 oocytes were contacted with 1.25 μM Cm(III) in 1500 μL OE buffer (pH ~3.0).

RESULTS. After an exposure time of 24 h, LSC measurements showed that 0.41 μM Cm(III) (33 %) was associated on the oocytes (Fig. 2). With respect to the small entrance window of the cuvette (Fig. 2) and the difficult adjustment of the laser beam at the boundary oocytes/supernatant in the glove box, luminescence spectra of only poor quality could be obtained applying 0.6 μM Cm(III). However, an increased concentration of 1.25 μM Cm(III) lead to good quality data (Fig. 3).

Shortly after the addition of Cm(III), predominantly prevailing as Cm^{3+} (594.1 nm; 66 %), a shoulder observed at
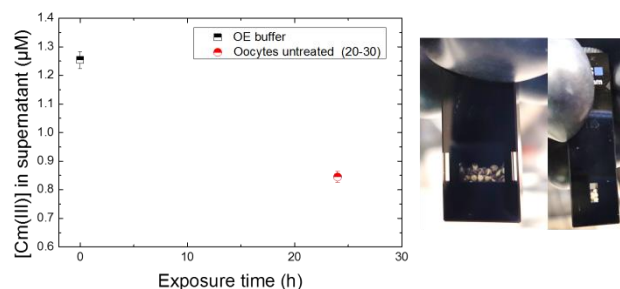
Fig. 2: Cm(III) concentration measured in the supernatants by LSC (left). Oocytes in Cm(III) containing OE buffer in the glove box (right).
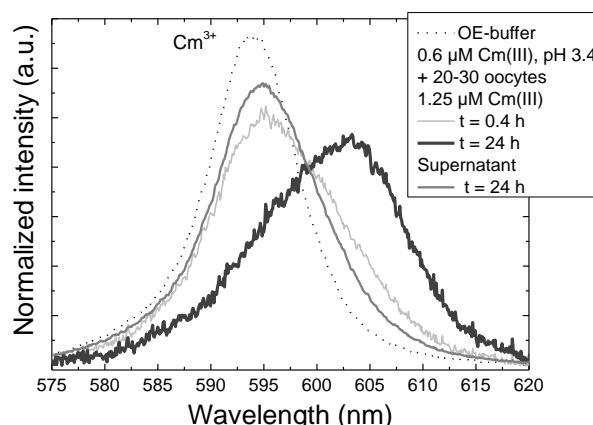
Fig. 3: Cm(III) TRLFS spectra in *Xenopus laevis* oocytes system.

600 nm (34 %) suggested the occurrence of Cm(III) interactions with the oocytes or released substances.

After 24 h of exposure time, the emission maximum is shifted to 604.5 nm. The sum spectrum consisted of a Cm(III) species at 598 nm with 57 % (solution species) and the oocyte-species at 604.5 nm with 43 %. Based on the supernatant spectrum, we can conclude an interaction of Cm^{3+} (73 %) and the solution species (27 %) with the oocytes. The solution and the oocyte species exhibited a similar lifetime of ca. 200 μs, indicating only $2-3$ coordinated water molecules.

These investigations provide a basis for further experiments exploring in more detail the kinetics, the viability in the presence of Cm(III), and the behavior of modified oocytes. In these oocytes, plant membrane proteins will be heterologously expressed which are influencing the Ca^{2+} transport in the oocytes. It would be interesting to see if these oocytes can accumulate more Cm(III) and if changes in the Cm(III) speciation occur.

[1] Miller, A. J. *et al.* (2000) *Biochim. Biophys. Acta.* **1465**, 343–358.
[2] Moll, H. *et al.* (2014) *Geomicrobiol. J.* **31**, 682–696.

Uranium(VI) bioassociation behavior in iron-deficient *Brassica napus* cells

F. Rajabi, S. Sachs

We studied the bioassociation behavior of U(VI) in *Brassica napus* suspension cells under Fe sufficient and deficient conditions. The results show an antagonistic interaction between U(VI) and Fe. The presence of U(VI) also affects the homeostasis of other micro-macro nutrients under Fe starvation conditions.

By uranium transfer from contaminated sites into the environment, the radionuclide can finally enter the food chain and may cause severe health effects for human. Uranium as a non-essential element is quite unlikely to have a special route for transportation into plant cells. Therefore, disturbing the homeostasis of other essential micro-macro nutrients and utilizing their transportation system is the most probable way of its access into the cells. Since iron deficiency is the most common phenomenon seen in one third of world's cultivated soils, study of the uranium uptake into plants under this condition is of great importance.[1] Therefore, the present study focuses on demonstrating weather Fe starvation has an effect on U(VI) bioassociation in cultured *B. napus* cells.

EXPERIMENTAL. *B. napus* cells taken from stock calli (PC-1113, DSMZ, Braunschweig, Germany) were subcultivated in liquid R medium every week.[2] For treating cells with U(VI) at a final concentration of 100 µM, cells were cultivated in medium R with a reduced phosphate concentration of 6.25×10^{-6} M (medium R_{red}) to avoid precipitation of U(VI). In order to study the bioassociation of U(VI) under Fe-deficient conditions, Fe-EDTA was omitted from the medium. To determine micro-macro nutrient levels and bioassociated U(VI) in Fe sufficient and deficient medium, 200 mg cells were harvested in duplicate at regular time intervals in a seven days period. Cells were digested and subsequently analyzed by ICP-MS. The cell viability was monitored as a function of mitochondrial and cytosolic dehydrogenases activity with the so called MTT assay.[3]

RESULTS. No significant changes in the viability of U(VI) exposed cells normalized to the values obtained from control samples (cells cultivated in Fe sufficient R_{red} medium without U(VI)) were observed under Fe starvation conditions (Fig. 1). ICP-MS analysis showed that in the absence of U(VI), Fe deficiency has a negative effect on the uptake of several elements, *e.g.* Mg, Ca and K into the cells. However, the presence of U(VI) in the same Fe starvation condition showed a counterbalancing effect. The U(VI) bioassociation was increased significantly in *Brassica* cells cultivated in Fe deficient medium compared to the control cells which were exposed to U(VI) in Fe sufficient medium (Fig. 2). This result is consistent with the findings of Viehweger *et al.*[4] One possible reason for this antagonistic relationship could be that Fe and U(VI) are competing for uptake by the *Brassica* cells. These observations suggest that U(VI) and Fe show a reciprocal relation in absorption by *B. napus* cells. However, one should also take into account that the relationship between toxic heavy metals and essential trace elements seems to be dependent on plant species and therefore, further studies with other plant species should be carried out.[5]
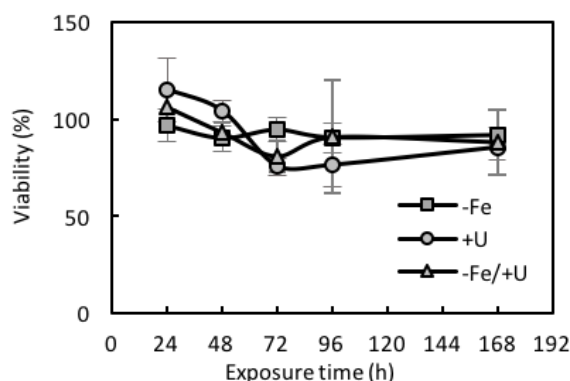
Fig. 1: Viability of *B. napus* cells cultivated in R_{red} medium without Fe (−Fe), supplemented with Fe and U(VI) (+U) and without Fe and in the presence of U(VI) (−Fe/+U) normalized to control cells. The data are derived from three independent experimental series; Error bar = SE.
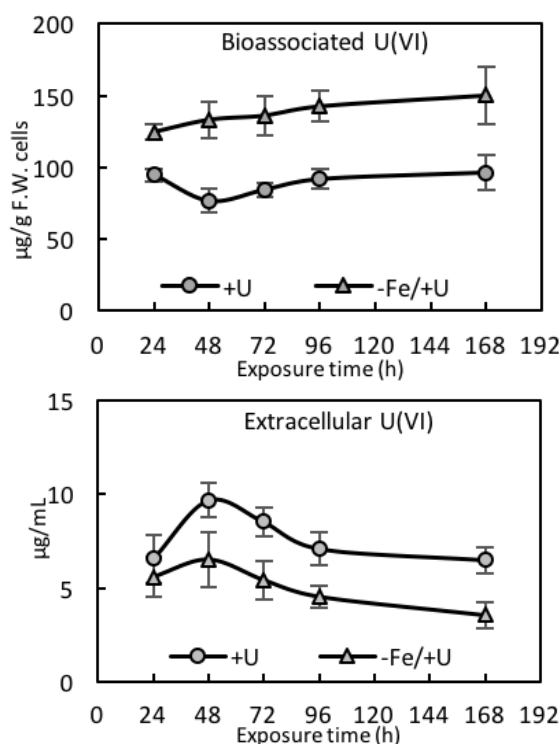
Fig. 2: Impact of Fe starvation on U(VI) bioassociation in *B. napus* cells. Cells were treated with 100 µM U(VI) in Fe sufficient (+U) and Fe deficient (−Fe/+U) medium. Error bars indicate SE, from three independent experimental series.

In summary, these results are important to understand the mechanism of accumulation and translocation of actinides into plants and could open the way to the discovery of the potential membrane transporters involved in actinides uptake into plants.

[1] Kim, S. A. *et al.* (2007) *FEBS Lett.* **581**, 2273−2280.
[2] Linsmaier, E. M. (1965) *Physiol. Plant.* **18**, 100−127.
[3] Mosmann, T. (1983) *J. Immunol. Methods* **65**, 55−63.
[4] Viehweger, K. *et al.* (2010) *Environ. Exp. Bot.* **69**, 39−46.
[5] Yoshihara, T. *et al.* (2006) *Plant Cell Rep.* **25**, 365−373.

A microscopic characterization of U(VI) sequestration by *Acidovorax facilis*

E. Krawczyk-Bärsch, U. Gerber, M. L. Merroun[1]

[1]University of Granada, Department of Microbiology, Granada, Spain

The gram-negative bacterium *Acidovorax facilis* is known as a facultative aerobic, chemoorganotrophic bacterium that is ubiquitous in nature. Species of the genus *Acidovorax* were widely found in U-contaminated sites, e.g. in the sediments of a former U-mining district and in U mine tailings. In kinetic batch experiments, we contacted *A. facilis* cells for 20 min. with 0.1 mM U(VI) for STEM/HAADF studies. The results show that U is coordinated predominantely to the functional groups on the cell surfaces. In addition, U is also bound to a small extent in intracellular polyphosphate granules.

EXPERIMENTAL. For our studies, a strain of *A. facilis* was kindly provided by the Centre for Environmental Research (UFZ in Leipzig, Germany). *A. facilis* cells were incubated in nutrient broth medium (NB) (Peptone 5.0 g L^{-1} and Beef Extract 3.0 g L^{-1}, pH 7.0 ± 0.2, Sifin, Berlin, Germany) at 30 °C and 120 rpm on a rotary shaker and grown overnight to reach the late exponential growth phase. A sample was taken and prepared for SEM studies. Most of the cells were washed and diluted to an OD$_{600nm}$ of 1.0 (12.0 ± 1.0 mg dry weight L^{-1}) with sterilized tap water at pH 5.0. A stock solution of UO$_2$(NO$_3$)$_2$ was added to adjust a U(VI) concentration of 0.1 mM in the cell suspension. The experiments were performed at pH 5.0, under aerobic conditions and at 30 °C on a rotary shaker at 130 rpm for 20 min. At the end of the experiment, the cells were centrifuged ($15,000 \times g$, 4 °C) and the obtained cell pellet was washed twice with 20 mM HEPES buffer at pH 7.2. Subsequently, the pellet was fixed with 1 % (vol/vol) Glutardialdehyde, prepared from a 50 % (vol/vol) stock solution. The sample ultrathin sections were prepared at Centro de Instrumentación Científica (University of Granada, Spain) and used for STEM/HAADF measurements.

RESULTS. The cell morphology of the $1-2$ µm long, rod-shaped *A. facilis* cells was observed by SEM (s. Fig. 1a) and STEM/HAADF combined with element mapping. As shown in Fig. 1b, most of the *A. facilis* cells possess spherical inclusion bodies in their cytoplasm, which are characterized by an increased electron density. These polyphosphate granules (PPGs) are reservoirs of P and therefore characterized by a high content of P.[1] For the localization of U in the cells, an elemental distribution analysis mapping was performed (Fig. 1c). According to this, U is entirely present in the cell membrane (1) as well as in the PPGs (s. Fig. 1d). As known from previous TRLFS studies,[2] U is mainly bound to phosphate groups of lipopolysaccharides (LPS) at the outer membrane within the first hour. By kinetic studies it was shown, that at $16-24$ h of incubation, both, phosphoryl and carboxyl functionality groups of LPS and peptidoglycan (PGN) of *A. facilis* cells may contribute to the removal of high U amounts from solution. In addition to the U sequestration in the cell membrane, U was bound to minor amounts in the PPGs. However, the concentration of U is much lower or not detectable in the cytoplasmic PPGs (2). As shown in Fig. 1d, element mapping indicates relatively high PPGs with a high amount of P (s. Fig. 1d) but with a less amount of U (s. Fig. 1c). Consequently, we can conclude, that the removal of U by *A. facilis* during the first
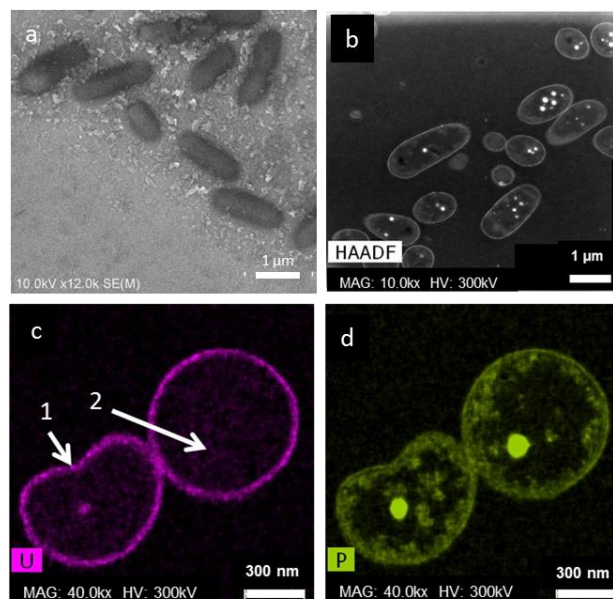
Fig. 1: SEM (a) and STEM/HAADF (b) images of rod-shaped *A. facilis* cells. PPGs are shown in the cells with high electron density (b). Element mapping for U (c) and P (d) of *A. facilis* cells incubated for 20 min. are indicating U accumulates (1) in the cell membrane and minor amounts of U in PPGs (2).

20 min. of incubation, is limited to the outer membrane of the cells and could be described as a passive biosorption process. Whereas, the intracellular uptake of U in PPGs results from a subsequent active process as described in detail elsewhere.[3]

[1] Docampo, R. (2006) in: *Inclusions in Prokaryotes*. p. 53–70, Springer, Berlin, Heidelberg.
[2] Krawczyk-Bärsch, E. *et al.* (2018) *J. Hazard. Mater.* **347**, 233–241.
[3] Gerber, U. *et al.* (2018) *J. Hazard. Mater.* **317**, 127–134.

Interactions of a *Halobacterium* isolate with uranium

S. Hilpmann, M. Bachran, R. Steudtner, A. Cherkouk

***Halobacterium* sp. GP5 1-1 is an extremely halophilic archaeon isolated from a German rock salt sample. Its interactions with uranium(VI) were investigated by using microscopic and spectroscopic methods to decipher the occurring processes on a molecular level.**

Rock salt formations are potential host rocks for the long-term storage of highly radioactive waste in deep geological formations. Contrary to the well investigated geological, geochemical and geophysical properties of rock salt, there is still little known about the indigenous microorganisms and their interactions with the radioactive waste. To study how these microorganisms can interact with radionuclides, if released from the repository, is of high interest, especially for a long-term risk assessment.

EXPERIMENTAL. *Halobacterium* sp. GP5 1-1 was cultivated using the modified R2A medium (3 M NaCl) with shaking at 30 °C in the dark. The cells were harvested in the late exponential growth phase by centrifugation and then washed three times with 3 M NaCl, pC_{H+} 6 (corrected pH due to the high ionic strength).[1] A defined amount of cells (5 mg dry biomass) was resuspended in 10 mL of filter-sterilized uranium(VI) solution (10/60 µM, 3 M NaCl, pC_{H+} 6) and the samples were shaken for different time periods. Afterwards, the uranium content in the supernatant was measured with ICP-MS. The cells were washed (3 M NaCl, pC_{H+} 6) and used for staining with the LIVE/DEAD® BacLight™ Bacterial Viability Kit. Moreover, time resolved laser-induced fluorescence spectroscopic (TRLFS) measurements of the supernatants at −120 °C were performed using a pulsed Nd-YAG laser (Continuum Inlite) and a CCD camera (Horiba Jobin Yvon iHR 550) to detect the luminescence. The obtained spectra where analyzed with the help of the parallel factor analysis (PARAFAC).[2]

RESULTS. To investigate the association kinetics of uranium(VI) onto the cells of *Halobacterium* sp. GP5 1-1, a time-dependent association experiment was performed with two different uranium(VI) concentrations (see Fig. 1).

The amount of bioassociated uranium(VI) increased with the time of incubation at both concentrations. At 10 µM an association rate of over 80 % was already reached after a time period of 6 h. In contrast, the association kinetic of the higher uranium(VI) concentration was much slower. In both
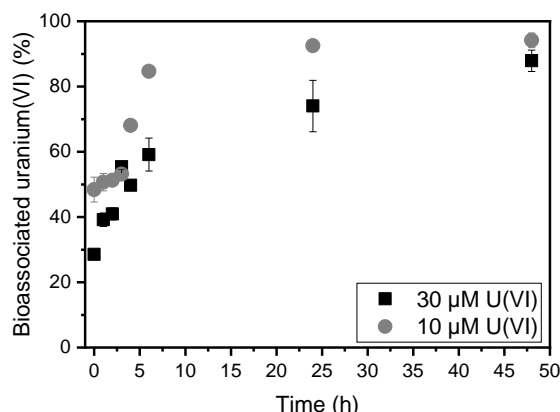
cases, the process is not exclusively a biosorption, which is in general very fast completed (0−2 h). The microscopic images of the live/dead staining (Fig. 2) show the formation of cell agglomerates after a certain exposition time. During this process organic matter is excreted from the cells. Thus more functional groups are available for further uranium(VI) binding.
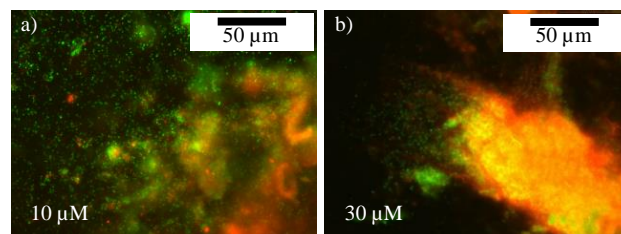
Fig. 2: Live/dead staining of the cells of *Halobacterium* sp. GP5 1-1 after 24 h of incubation with 10 µM U(VI) (a) and 30 µM U(VI) (b); living and dead cells are given in green and red, respectively.

At both concentrations, the formation of cell agglomerates occurred after similar incubation times and the size of the agglomerates was almost the same. Although, the part of dead cells was greater at the higher uranium(VI) concentration.

After certain incubation times, TRLFS measurements of the supernatants were performed. The extracted single spectra could be assigned to three aqueous species (free uranyl(VI), uranyl-carbonate-complex and hydrolysis complex of the uranyl(VI)). The distribution of the three species is shown in Fig. 3. The proportion of the carbonate complex rose because of microbial released CO_2. Contrary to this, the proportions of the two other species decreased. For further investigations, electron microscopic images of the cells will be taken to get a deeper insight in the actually occurring processes.
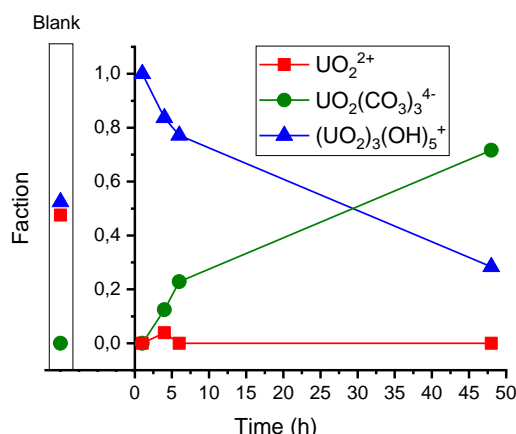
Fig. 3: Species distribution of the aqueous uranium(VI) species over time.

[1] Borkowski, M. *et al.* (2009) *Actinide(III) Solubility in WIPP Brine: Data Summary and Recommendations*, Los Alamos National Laboratory Carlsbad Operations.
[2] Drobot, B. *et al.* (2015) *Chem. Sci.* **6**, 964−972.

Fig. 1: Association of uranium(VI) with cells of *Halobacterium* sp. GP5 1-1 over time ([U(VI)] = 30 µM, squares; [U(VI)] = 10 µM, circles; pC_{H+} 6; DBM = 0.5 mg/ mL; [NaCl] = 3 M).

Interactions of plant cells with U(VI) and Eu(III) - time-dependency of bioassociation and spectroscopic investigation of possible U(VI) metabolite species

J. Jessat, S. Sachs, H. Moll

The time-dependency of the bioassociation processes of U(VI) and Eu(III) on *Brassica napus* cells was studied. For initial U(VI) concentrations of 200 µM, a release reaction of bioassociated U(VI) into the surrounding medium was observed. TRLFS measurements demonstrated the occurrence of a species presumably representing a newly formed U(VI) complex of a plant cell metabolite.

For both the safety assessment of nuclear waste repositories and the remediation of contaminated sites detailed knowledge about the transfer of radionuclides into the food chain *via* groundwater and soil is of a central concern. In most cases the interactions of radionuclides with plants are described only by transfer factors, which do not provide any information about the underlying processes or radionuclide species. The bioassociation of radionuclides, however, depends on their speciation.[1] Time-dependent bioassociation experiments with *Brassica napus* (*B. napus*) cells were performed with U(VI) and Eu(III) as an analogue for the trivalent actinides Cm(III) and Am(III). The aim was to determine the effect of the heavy metals on cell viability and the influence of cell metabolism on the bioavailability of the heavy metals. The bioassociation experiments were complemented by time-resolved laser-induced fluorescence spectroscopy (TRLFS) measurements.

EXPERIMENTAL. For cultivation *B. napus* cells were incubated in a medium R (pH 5.8).[2] Cell cultures from passage numbers 2 to 15 were used for the time-dependent bioassociation experiments. Cells were treated with medium R_{red} with a reduced phosphate concentration of 6.25×10^{-6} M (pH 5.8 ± 0.1) containing two different concentrations of U(VI) (2×10^{-5} or 2×10^{-4} M) or of Eu(III) (3×10^{-5} or 2×10^{-4} M) in comparison to control samples without U(VI) or Eu(III). After 1 to 72 h of exposure, the cells were harvested and their viability was determined by MTT test.[3] The supernatants were centrifuged and analyzed by ICP-MS to determine the amount of bioassociated U(VI) and Eu(III). In addition, TRLFS measurements at low temperatures ($-120\,°C$) were performed in order to determine changes in the U(VI) speciation in solution. Plant cell metabolites that were released into the cell culture medium due to exposure with 200 µM Eu(III) or U(VI) for 168 h were enriched, extracted by solid phase extraction and subsequently analyzed by HPLC as well as mass spectrometry.

RESULTS. In the presence of 20 µM U(VI) as well as 30 and 200 µM Eu(III) a time-dependent bioassociation of the metals by the cells was observed, reaching an equilibrium state. Thereby up to 80 % of the total heavy metal amount was bioassociated. For U(VI) concentration of 200 µM a multistage bioassociation process occurred reproducibly (Fig. 1). In the literature, such multi-stage bioassociation processes were already reported for halophilic archaea.[4] After an initial increase of bioassociation, reaching in some cases 100 %, a release reaction of U(VI) from the cells into the medium took place. For the individual experiments a time lag of this release reaction was observed. A possible reason for this behavior could be the cell passage. It is conceivable that the cells of the second passage were not yet
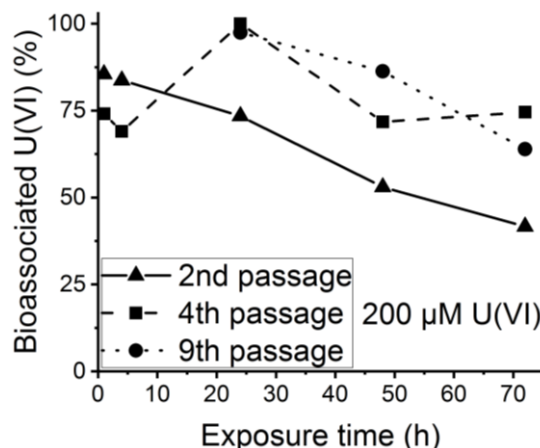
Fig. 1: Time-dependency of bioassociation of 200 µM U(VI) by *B. napus* cells for each individual experiment (shown by different no. of passage).

fully adapted to the conditions in the liquid cell culture medium and therefore reacted more sensitively to the heavy metal exposure than cells of higher passage numbers. In the presence of 200 µM Eu(III) and U(VI), fluctuations in the cell viability were observed, which provide indications of changed metabolic processes due to heavy metal stress. In contrast to that, the cell viability was not significantly changed at lower concentrations of 30 µM Eu(III) and 20 µM U(VI).

The TRLFS spectra of the initial media, supernatants and cells showed different U(VI) species. Depending on the exposure time, the same species could be reproducibly identified in the supernatants, however, their ratios varied at different sampling times. In correspondence with the beginning of the release reaction, a new species with a significant red shift compared to the free uranyl(VI) ion occurs in all experiments. This species could be an U(VI) complex with a metabolite. First experiments for the enrichment of metabolites were performed in order to identify this species. Metabolites released by the plant cells, *e.g.* fumaric acid, have been identified and first complexation studies with U(VI) were performed. It is very likely that such organic complexes significantly affect the migration behavior of U(VI) in the environment.

[1] Sachs, S. *et al.* (2017) *Environ. Sci. Technol.* **51**, 10843–10849.
[2] https://www.dsmz.de/fileadmin/Bereiche/PlantCellLines/Dateien/R.pdf (last viewed: 11/19/2018).
[3] Mosmann, T. (1983) *J. Immunol. Methods* **65**, 55–63.
[4] Bader, M. *et al.* (2017) *J. Hazard. Mater.* **327**, 225–232.

Sorption of europium onto diatom biosilica

K. Kammerlander,[1] L. Köhler,[1] E. Brunner,[1] T. Stumpf

[1]Technische Universität Dresden, Faculty of Chemistry and Food Chemistry, Chair of Bioanalytical Chemistry, Dresden, Germany

In this study, we investigated the suitability of freshly harvested and fossilized diatom cells as a sorbent material for Eu^{3+} under varying conditions. From the retention capacities determined by ICP-OES a preferred coordination to organic matter of the whole diatom cells was suggested. Unspecific sorption of Eu was supported by luminescence measurements and cathodoluminescence investigations.

Diatoms are unicellular algae living in all oceans and large fresh water habitats. They are known for their ability to build silicified cell walls (frustules) from silicic acid dissolved in seawater. The resulting amorphous biosilica stands out as a suitable sorbent material in terms of chemical stability, non-toxicity, and porosity.[1]
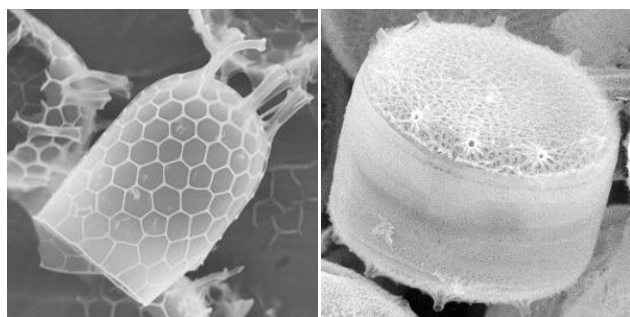
Fig. 1: SEM images of *Stephanopyxis turris* (left) and *Thalassiosira pseudonana* (right).

Biosilica is already applied as sorbent material in the form of diatomite, a commercially available product consisting of fossilized diatoms.[2] In this study, we took two approaches: on the one hand, diatoms were cultivated in europium containing media to elucidate the interactions of trivalent f-element ions with living algal cells. On the other hand, europium ions were sorbed onto the purified cell walls of harvested algae of the same species. These species are *Thalassiosira pseudonana*, a well-established model organism, and *Stephanopyxis turris*, a larger species with a hierarchical pore structure (Fig. 1). Subsequently, we analyzed the sorbents with elemental analysis by ICP-OES (inductively coupled plasma optical emission spectroscopy), time-resolved laser fluorescence spectroscopy (TRLFS) and cathodoluminescence (CL) to identify and localize the europium species.

EXPERIMENTAL. For the *in vitro* sorption experiments cleaned cell walls were stirred 3 days in solutions of 10^{-3} and 10^{-5} M Eu^{3+} in 0.1 M NaClO$_4$ with pH adjusted to $3-7$. In the *in vivo* experiments, the selected algae species were grown in a Eu enriched culture medium and harvested after one month. Preceding the cultivation in large batches, the tolerance of the chosen diatom species towards europium ions was examined. Unexpectedly, the usually more resistant *T. pseudonana* showed the same tolerance limit in the order of magnitude of $10\,\mu\text{mol}\,\text{L}^{-1}$ as *S. turris*. Hence, this concentration was chosen for upscaling to 20 L batches. The cultures grew within a usual time span of one month and were subsequently harvested by centrifugation.

RESULTS. Quantitative analysis with ICP-OES revealed retention capacities in the order of magnitude of 10 mg/g for the *in vivo* *S. turris* samples cultivated in Eu^{3+}-containing media and 40 mg/g for the *T. pseudonana* samples respectively. For the samples prepared with the purified biosilica, retention capacities of about 20 to 70 mg/g, depending on the pH value, were measured.

This suggests that the europium ions associate preferably with the organic matter of the whole diatom cells and not with the biosilica itself. As there is not only a vast range of organic material comprising the cells present, but also some complexing agents in the artificial seawater, the specific ligands involved in the complexation process are yet to be identified. The association to the sorbent material seems to be more stable in case of the freshly harvested cells compared to the purified biosilica as the ions could not be detached easily by multiple washing steps.

Similarly, the TRLFS emission spectra suggest a successful complexation with a higher F_2/F_1 band intensity ratio compared to the aquo ion. Excitation and lifetime data indicate the formation of various similar Eu species without a defined symmetry and, thus, point towards unspecific sorption processes.
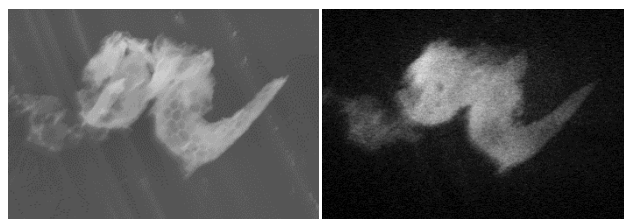
Fig. 2: SEM image of a fragment of a fossilized *Stephanopyxis turris* cell wall after Eu^{3+} sorption (left) and the respective monochromatic CL image of the luminescence at 618 nm (right).

Cathodoluminescence investigations were limited to the larger species (*S. turris*). The measurements revealed a uniform distribution of luminescence centers (Fig. 2). However, the silica matrix seems to also contribute to the recorded luminescence through excitonic processes stimulated by the electron beam.[3, 4]

In the future, we will expand our studies to other diatom species, such as *Coscinodiscus granii*, *Navicula salinicola* and *Halamphora oligotraphenta*. Furthermore, we plan to examine the sorption properties of diatoms cultivated in aluminum enriched media to investigate the influence of the chemical structure of the biosilica on the sorption capacity.

[1] Mann, D. G. (1999) *Phycologia* **38**, 437–495.
[2] Kogel, J. E. *et al.* (2006) *Industrial Minerals & Rocks: Commodities, Markets, and Uses*, 7th ed.; Soc. Min. Metall. Explor. Inc.
[3] Kalceff, M. A. *et al.* (1995) *Phys. Rev. B* **52**, 3122–3135.
[4] Butcher, K. S. A. *et al.* (2005) *Mater. Sci. Eng. C.* **25**, 658–663.

Binding and transport of radionuclides and metals in fungal hyphae under natural conditions

A. Wollenberg, A. Günther, J. Raff

Fungi have been shown to accumulate large amounts of radioactive caesium and strontium in their fruiting bodies.[1–3] However, there have been no studies on how the radioactive isotopes enter the organism. For this reason, microcosm experiments have been conducted to investigate the uptake and transport of radionuclides and metals from contaminated soil into fungal hyphae and through the cells into the biomass of *Schizophyllum commune* and *Leucoagaricus naucinus*. These investigations may indicate whether fungi are able to taken up radioactive isotopes from the soil, to transport and to accumulate them in the fruiting bodies or not.

EXPERIMENTAL. *S. commune* and *L. naucinus* was cultivated for two weeks at 15 °C on gelatin plates with the complex yeast medium containing tryptophan (tryptone 2 g/L, yeast extract 2 g/L, $MgSO_4$ 0.5 g/L, KH_2PO_4 0.5 g/L, K_2HPO_4 1 g/L, tryptophan 1 g/L, glucose 20 g/L, gelatin 120 g/L). Sterile magenta vessels GA-7 were filled with 100 g sterile, homogenized, sandy soil without and with metal contamination. The used metals were uranium, europium, caesium and strontium with a concentration of 5 mg metal per 1 kg soil each. A cotton pad and a nylon mesh bag with an inoculum were placed on top of the soil. As inoculum a half, overgrown gelatin plate was used. After the incubation time of one month, the mycelium, which had no direct contact with the soil, was harvested, disrupt with concentrated nitric acid in an ultrasonic bath and analyzed by ICP-MS.

RESULTS. Figure 1 shows the amount of bioassociated metal per 1 g of dry biomass of both fungi. In the following, only the amount of bioassociated metal that was detected in the biomass having no contact with the contaminated soil was considered.

The results show that if the soil was contaminated with 5 mg/kg of uranium, europium, caesium and strontium each, large quantities of uranium can be found in the biomass of both fungi. However, twice as much uranium could be detected in *S. commune* (518.3 ± 13.4 µg/g) compared to *L. nauicnus* (195.9 ± 44.8 µg/g). It was also observed that *S. commune* contains only very small amounts of europium (4.8 ± 1.3 µg/g) and almost no caesium (1.2 ± 1.7 µg/g) in the biomass. Similarly, in *L. naucinus* only small amounts of europium (8.8 ± 1.2 µg/g) were found in the biomass, and caesium (0.8 ± 1.1 µg/g) was almost not detectable. Furthermore, a significant amount of strontium was found in the biomass of *S. commune* (38.0 ± 8.1 µg/g), whereas only small amounts of strontium were detected in *L. naucinus* (11.0 ± 4.1 µg/g). However, the uncontaminated soil already contains strontium, so that even in experiments on uncontaminated soil small amounts of strontium were detected in the biomasses of *S. commune* (2.37 µg/g) and *L. naucinus* (13.88 µg/g).

In summary, it could be shown that the transport of radionuclides or metals within fungal hyphae depends on two factors: this is, on the one hand, the type of radionuclide or element, as shown by the examples of uranium and caesium. On the other hand, it strongly depends on the fungus species, shown by the different amounts of bioassociated urani-
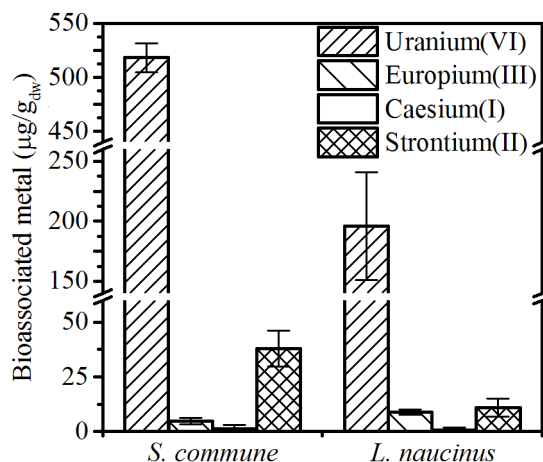
Fig. 1: Amount of bioassociated U(VI), Eu(III), Cs(I), and Sr(II) in the fungal hyphae which had no direct contact to the soil.

um and strontium in *S. commune* and *L. naucinus*. However, with the help of these experiments it could also be proved that under normal circumstances fungi do not transport caesium from the soil through the hyphae.

[1] Battiston, G. A. *et al.* (1989) *J. Environ. Radioactivity* **9**, 53–60.
[2] Berreck, M. *et al.* (2003) *Int. J. Med. Mushrooms* **5**, 61–86.
[3] Byrne, A. R. (1988) *J. Environ. Radioactivity* **6**, 177–183.

Microorganisms isolated from an engineered barrier experiment for nuclear waste disposal

J. Drozdowski, M. Lopez-Fernandez, S. Kluge, A. Cherkouk

Bentonite samples from the Full-scale Engineered Barrier Experiment – Dismantling Project from the Grimsel Test Site (Switzerland) were collected and studied according to their microbial diversity and activity. Sulfate- and iron-reducing microorganisms were enriched from the samples using selected media. From the enrichments a *Desulfitobacterium* sp., a *Desulfosporosinus* sp. and a *Clostridium* sp. were isolated.

The storage of highly radioactive waste in a deep geological repository has been internationally accepted as one of the multi-barrier concepts, which combines a technical barrier (container with the high-level radioactive waste), a geotechnical barrier (*e.g.* bentonite) and the geological barrier (host rock). Bentonite fulfils in this system a sealing and buffering function (geotechnical barrier) due to its properties, namely a high swelling capacity and low hy-draulic conductivity. One objective of the Full-scale Engineered Barrier Experiment (FEBEX) was to demonstrate the feasibility of the emplacement of the engineered barrier system (EBS) for high-level radioactive waste dis-posal. The aim of our study is to investigate the microbial diversity and activity in bentonite samples from the FEBEX – Dismantling Project (DP).

EXPERIMENTAL. The sample B-C-60-9 was collected during the FEBEX–DP and provided by Microbial Analytics Sweden AB.[1] Enrichments were in each case prepared by adding 5 g of bentonite to 50 mL medium DSM63 (*Desulfovibrio* medium or Postgate B, called S) and medium DSM579 (*Geobacter* medium, named G) and incubated for 24 h at room temperature with shaking. The DNA was extracted from 500 µL inoculated media with PowerWater® DNA Isolation Kit (MOBIO). The 16S rRNA gene amplicons were amplified by using the primers 519F and 806R[2] and send to RTL Genomics for sequencing. In addition, 1 mL from the enrichments were transferred to anaerobic culture tubes containing 10 mL of media and further incubated at 30 °C. After that 100 µL were spread on agar plates of the same media and incubated. Grown colonies were selected and transferred to new agar plates. The single colonies were further transferred and pure cultures were analyzed to identify the closest phylogenetic relative *via* 16S rRNA gene sequencing.

RESULTS. The results showed that in both enrichments (S and G) mainly representatives of Firmicutes were enriched. In the enrichment medium S, which is especially for sulfate-reducers, *Desulfosporosinus* spp., *Clostridium* spp, and *Bacillus* spp. were mainly detected. From this enrichment a pure culture was isolated, namely *Desulfosporosinus* sp. S1-8, which 16S rRNA gene was closely related to different *Desulfosporosinus* spp. (Fig. 1). Additionally, a pure culture was isolated, namely *Clostridium* sp. S1-8-2, which was closely related to different *Clostridium* species. In the other enrichment medium (G), that is especially for iron-reducers, mainly *Desulfitobacterium* spp. and only a few *Bacillus* spp. were identified. From this enrichment a pure culture was also isolated, namely *Desulfitobacterium* sp. G1-2, which is affiliated with different *Desulfitobacterium* spp. (Fig. 1).
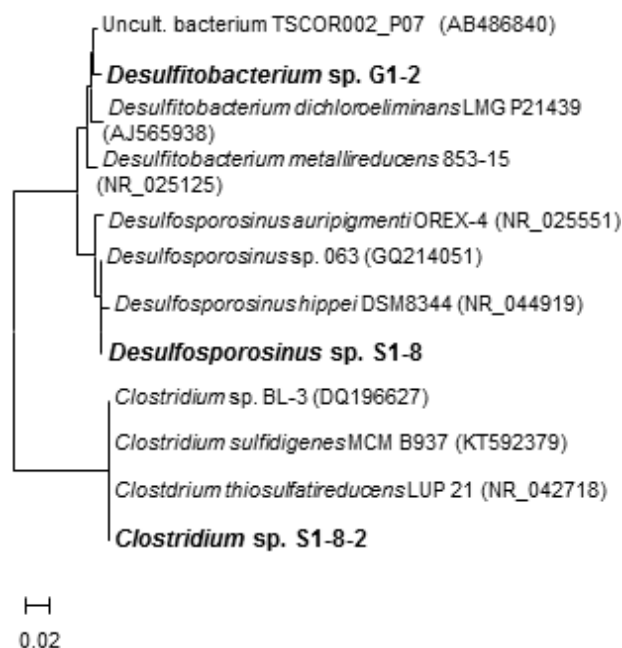
Fig. 1: Unrooted neighbor-joining phylogenetic tree (MEGA) of 16S rRNA gene sequences of bacterial isolates recovered from enrichments for sulfate- and iron-reducing microorganisms of sample B-C-60-9.

The enriched and isolated bacteria are known as spore-forming microorganisms. The suitable conditions in the enrichment media lead to their germination, which result in metabolically active cells. Our study showed that sulfate- and iron-reducing microorganisms were present in the bentonite emplaced in the full-scale experiment for several years and that they can become active if the conditions are right.

[1] Bengsston, A. *et al.* (2010) Arbeitsbericht NAB 16−15, FEBEX–DP: Microbiological report.
[2] Bachran, M. *et al.* (2019) *Microbial Ecology*, in press.
[3] http://www.grimsel.com/gts−phase−vi/febex−dp/febex−dp−introduction.

Lipid phase transitions in DNA-encircled lipid bilayers

M. Subramanian, K. Iric, L. Nucke, J. Oertel, T. L. Schmidt,[1] K. Fahmy

[1]Technische Universität Dresden, Dresden, Germany

Spectroscopic studies of membrane proteins require well defined synthetic membrane systems mimicking natural cell membranes. We have previously inserted the prototypical metal transporter CopA in a circular protein belt.[1] Here we report the synthesis of a highly controllable membrane mimetic, a DNA-encircled lipid bilayer, which supports native-like lipid phase behavior.
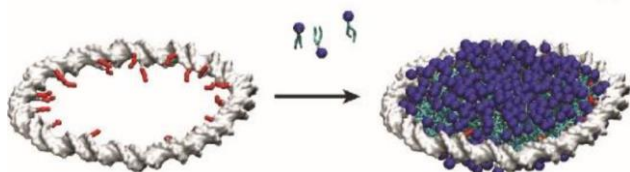
Fig. 1: Schematic of an empty dsDNA minicircle carrying alkylations (red) which attract lipid molecules to self-assemble as a bilayer within the DNA structure.[2]

EXPERIMENTAL. Covalently closed single-stranded 147 bases long DNA minicircles were synthesized and hybridized with 7 identical ssDNA 21-mers of complementary sequence, carrying two decyl chains at specific backbone phosphorothioates. The resulting dsDNA minicircles (dsMCs) were mixed with cholate-solubilized di-myrsitoyl-phosphahtidyl-choline (DMPC) or an additional 10 % amount of the artificial cationic lipid di-myrsitoyl-trimethyl-ammonium-propane followed by detergent removal. The material was concentrated by ultracentrifugation on an iodixanol gradient and the collected band purified by size exclusion chromatography.[2]

RESULTS. Alkylated dsDNA minicircles (dsMCs) self-assembled with lipids into DNA-encircled lipid bilayers (DEBs) which could be purified by size exclusion chromatography (SEC) and visualized by transmission scanning electron microscopy (tSEM). The individual empty dsMCs were clearly distinguishable from lipid-filled DEBs by their contrast pattern (Fig. 2a *vs.* b, c, e). The potential of simple size control of these discoidal planar bilayers is demonstrated by the existence of two populations of DEBs with 147 or 294 bp circumference, corresponding to intra- and intermolecular circularization of the 147 bp-long ssDNA templates (Fig. 2c *vs.* e). These populations were successfully separated by SEC (Fig. 2d). We compared the thermotropic phase transition of DMPC in conventional MSP-based NDs with that of DEBs by using the emission of the lipophilic dye LAURDAN as a sensor of lipid order.[3] The dye binds at the sub-headgroup region of lipids. Its excited state energy depends on the dipolar relaxation processes in its environ-
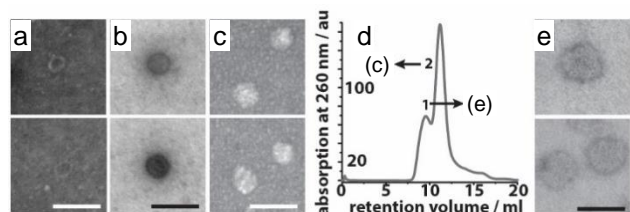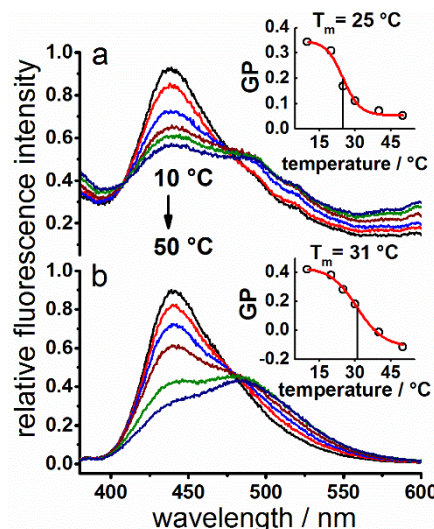
Fig. 3: Phase transitions monitored by LAURDAN emission from DMPC bilayers in DEBs (a) and in conventional protein-based nanodiscs (b). Insets show the temperature dependence of the general polarization value of the emission defined as GP = $(I_{440}-I_{490})/(I_{440}+I_{490})$, with I the emission intensity at the indicated wavelength (in nm).

ment leading to a red shift of LAURDAN fluorescence with increasing hydration that accompanies the gel to liquid phase transition of the lipid. Therefore, the phase transition can be monitored by the relative intensity difference measured at two LAURDAN emission wavelengths, *i.e.* the so-called general polarization (GP).[3] The midpoint temperature T_m for the gel to liquid transition of DMPC in DEBs was 25 °C and agrees with literature data on DMPC vesicles,[4] whereas DMPC in NDs showed a slightly higher T_m (31 °C) as reported.[5] However, the change of the GP value in DEBs was only ~50 % of that in NDs transition, which may indicate restricted lipid mobility at the alkylated DNA-lipid interface. Upon doping of the DMPC bilayer with the cationic lipid DMTAP, no phase transition was observed (not shown), which we attribute to the additional electrostatic interactions of the positively charged head groups with the dsMC, and to a preferential binding of LAURDAN at the DNA lipid interface. Thus, positively charged lipids tend to stabilize the lipidic phase at the DNA interface. Importantly, the prevalence of a native-like phase transition for pure DMPC in DEBs shows that also in the absence of additional electrostatic interactions, the alkylations provide sufficient lipid affinity for bilayer formation in a manner similar to that of DMPC vesicles. Therefore, DEBs may provide an attractive and highly controllable mimetic for cell membranes and future membrane protein research. The method of their production has been patented.[6]

Fig. 2: Analysis of minicircles and DEBs. a) TEM image of empty dsDNA MCs, b) tSEM of DEBs with 14 ethyl modifications, c) tSEM of DEBs with 28 decyl modifications, d) SEC chromatogram, e) tSEM of 294 long DEBs.

[1] Fischermeier, E. *et al.* (2017) *Angew. Chem. Int. Ed.* **56**, 1269–1272.
[2] Iric, K. *et al.* (2018) *Nanoscale* **10**, 18463–18467.
[3] Parasassi, T. *et al.* (1991) *Biophys. J.* **60**, 179–189.
[4] Koynova, R. *et al.* (1998) *Biochim. Biophys. Acta BBA − Rev. Biomembr.* **1376**, 91–145.
[5] Denisov, I. *et al.* (2005) *J. Phys. Chem. B* **109**, 15580–15588.
[6] European Patent number **18 157 852.7.**

The Chemistry of

LONG-LIVED RADIONUCLIDES

Recent advances in the understanding of the bonding situation of tetravalent *f*-element salen complexes

R. Kloditz, T. Radoske, M. Patzschke, T. Stumpf

By using tools of real-space bonding analysis and accurate DFT calculations of electronic energies, the bonding character of [M(IV)(salen)₂] (M = Ce, Th, Pa, U, Np, and Pu) is investigated. Except for the general presence of *f*-electrons, no strong correlation is found between covalency and the number of *f*-electrons.

Ligands with soft-donor atoms, such as O and N, serve as appropriate agents for the extraction of radionuclides from high-level liquid wastes. One promising example especially for the complexation of tetravalent *f*-elements is the N,O-donor ligand salen (Fig. 1) and its analogues. To improve the general understanding of the bonding properties of radionuclides, primarily actinides, the [M(IV)(salen)₂] complexes (M = Ce, Th, Pa, U, Np, and Pu) are examined by using the delocalization index (DI) based on the Quantum Theory of Atoms In Molecules (QTAIM) and DFT calculations of complexation energies.
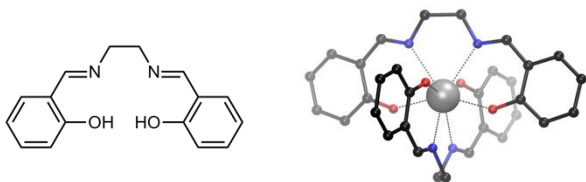
Fig. 1: Structure of the H_2(salen) ligand and the optimised structure of the [M(IV)(salen)₂] complex.

COMPUTATIONAL DETAILS. All complexes were optimized using the quantum chemical program suite Turbomole, v. 7.1. The used basis set for all atoms is def-TZVPP. Furthermore, a 28-RECP for Ce, a 60-RECP for the actinides, and the PBE functional were used. Electronical reaction energies were calculated using the B2PLYP functional, DKH contracted basis sets for H, C, N and O, and all-electron SARC basis sets for the metal atoms.

RESULTS. The main ingredients of QTAIM are the electron density $\rho(r)$ and its spatial gradient $\nabla\rho(r)$. The gradient is used to define unambiguous domains inside a molecule. These domains have a physical justification as quantum-atoms, or simply atoms, and can be used to calculate atomic properties such as the volume and the charge. Another important quantity is the delocalization index (DI) serving as an indicator of the interaction strength between two atoms by counting the number of electron pairs shared between them. As such, it is a direct measure for the bond order. A typical single bond has a DI of 1, a double bond of 2, and so on. The DI is defined as[1]

$$\delta(A,B) = 2 \sum_i \sum_j S_{ij}(A)S_{ij}(B)$$

with S_{ij} being the overlap integral of the spin-orbitals i and j over the respective domain of atoms A and B. Fig. 2 (left) shows the DI of the M–O and M–N bond. It clearly indicates a more covalent bonding character of the M–O bond with a DI more than twice as high as that of the M–N bond. This supports the conclusions found by qualitative investigations with plots of density differences and non-covalent interactions (NCI) and the results of other authors[2].

However, the DI shows no clear trend between covalency and the number of *f*-electrons for both the M–O and M–N bonds. The changes in the M–N bond strength are almost insignificant for all the investigated metal ions. The Th–O bond shows a lower DI than all other M–O bonds which seems struggling especially in comparison to the Ce–O bond since both metals have a similar electron configuration with no *f*-electrons. Nonetheless, all bonds between metal and ligands are still very weak in comparison to a single bond, like C–C or C–N, and hence ionic attraction is the main force of metal-ligand bonding.
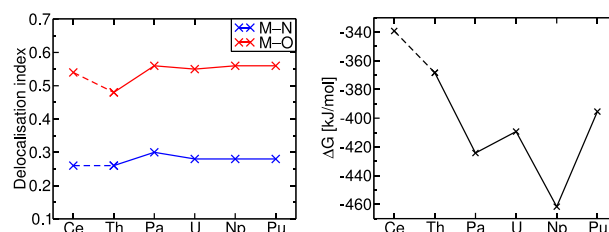
Fig. 2: *Left:* The delocalisation index for all metal atoms with the donor atoms N and O. *Right:* The thermodynamic complexation energy for all complexes.

Since the stability of a complex is a direct consequence of the bond strength, the calculation of the complexation energies can also give meaningful results about the bonding situation of the different actinides. According to the chemical reaction

$$[MCl_4(thf)_3] + 2\,(salen)^{2-} \rightarrow [M(salen)_2] + 4\,Cl^- + 3\,thf$$
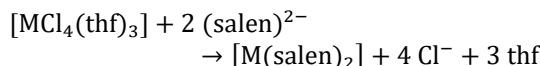
With [MCl₄(thf)₃] as a proposed M-Cl compound in tetrahydrofuran (thf) by van der Sluys[3], the complexation energies are shown in Fig. 2 (right).

All actinide complexes are more stable than the Ce complex. This suggests a stronger influence of the 5*f*-orbitals on the bonding with the donor atoms of the ligands compared to the 4*f*-ones. Furthermore, the Th complex is more unstable than the other actinide complexes since no *f*-electrons are present to support the bonding. Surprisingly, the Np complex seems to be much more stable, around 50 kJ mol⁻¹. The reasons for that are still to be found.

Both DI and complexation energies gave a great insight into the bonding situation of the metal complexes but are not able to show a trend in the covalency. Other effects such as steric hindrance of the ligands have to be also considered. Hence, further investigation is necessary and currently in progress.

[1] Fradera, X. *et al.* (1999) *J. Phys. Chem. A* **103**, 304–314.
[2] Schnaars, D. *et al.* (2012) *Inorg. Chem.* **51,** 8557–8566.
[3] v. d. Sluys, W. *et al.* (1993) *Inorg. Chim. Acta* **204**, 251–256.

NMR investigations of An(IV) complexes of a fluoro-substituted salen ligand

B. Felsner, R. Kloditz, T. Radoske, S. Schöne, M. Patzschke, J. März., P. Kaden

Complexation of the fluoro-substituted salen ligand (L) with tetravalent actinides (An) leads to the formation of [AnL₂] complexes. NMR investigations of diamagnetic tetravalent metal complexes show unexpected behavior for Ce(IV), a chemical analogue of An(IV), and a *d*-block analogue interaction of Th(IV). Paramagnetic NMR investigations of complexes of U(IV) and Np(IV) reveal predominantly spin-dipolar interactions which are further substantiated by DFT calculations.

To gain insight into the electronic interactions upon formation of metal-organic complexes from the ligands' point of view, NMR spectroscopy is the method of choice. By tracking changes in the electron density distribution around nuclei of the ligands, changes due to the complexation and the underlying electronic effects can be quantified. Complexation with diamagnetic metal ions leads to a quantitative picture of the disturbance of the electron density distribution. Generally, paramagnetic metal ions are known to cause additional effects that can be detected, *e.g.* as additional chemical shifts, thus, called paramagnetic shifts. In actinide containing complexes, however, even more effects may come into play as actinides are affected by relativistic effects, such as spin-orbit coupling. To isolate and describe all these effects, first of all, a suitable reference is necessary to account for all diamagnetic interactions. Afterwards, a thorough separation of the paramagnetic effects is desirable. With the help of quantum chemical calculations, a first step is to identify the major contributors to the paramagnetic chemical shifts. To identify trends, a series of isostructural complexes of Salen-type ligands with a number of tetravalent metal ions (Zr, Hf, Ce, Th, U, and Np) was synthesized. A comparison of the ligands' NMR chemical shift of the diamagnetic complexes of Zr(IV) and Hf(IV) (both *d*-block elements with either an empty or a filled *f*-shell) reveals that no influence of the low laying *f*-shell is detected (Fig. 1). In the Ce(IV) complex, however, unexpectedly large shift deviations are observed. These may be due to a lack of primogenic repulsion in the newly available, yet unfilled *f*-valence shell which leads to more compact orbitals. When analyzing the shifts of the Th(IV) complex, the electron density distribution at the ligands' nuclei seems to be comparable to the
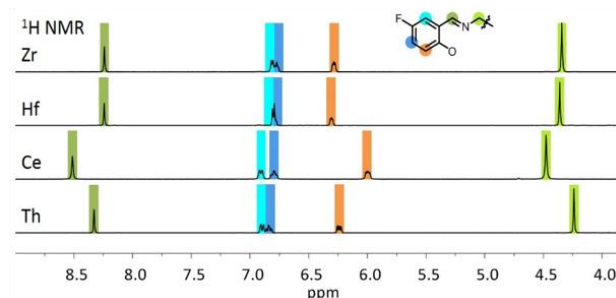
Fig. 1: Comparison of the ¹H NMR spectra of the diamagnetic tetravalent metal ion complexes of the fluoro-substituted salen. Especially Ce(IV) differs from the other reference complexes.

d-block metal ions with only slight deviations measured at protons which are closer to the metal binding site. Thus we conclude, that Th(IV) is the best suited reference to account for all diamagnetic influences for the tetravalent actinide ions.

By analyzing the series of paramagnetic complexes (U(IV) and Np(IV)), dominant spin dipolar interactions with a distinct distance and angle dependence are found (Fig. 2a). This is due to a prolate distribution of unpaired electron density located at the metal center. Only minor effects are observed when comparing the chemical shifts of the aromatic region between U(IV) and Np(IV) complexes, where scalar effects or ligand centered electron spin density might lead to these small but significant effects. DFT calculations (ORCA, PBE0, TZVPP, COSMO) of the excess of α electron spin density (Fig. 2b) substantiate this conclusion, as only minor amounts of unpaired spin density can be found on the ligands nuclei.
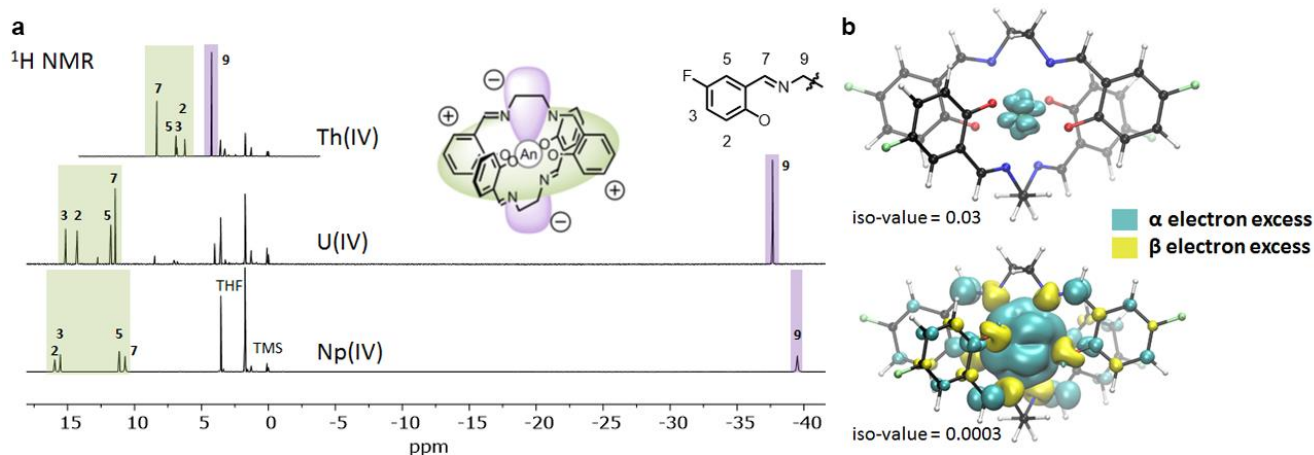
Fig. 2: Comparison of the ¹H NMR spectra with Th(IV) complex as diamagnetic reference for the paramagnetic complexes of U(IV) and Np(IV) (a), and DFT calculations of the α electron density excess substantiate the finding, that dipolar interactions are dominating, while only minor contributions due to delocalisation are expected (b).

Neptunium in organic solvents – Formation of polynuclear mixed-valent neptunium complexes

S. Schöne, J. März, A. Ikeda-Ohno

Two polynuclear mixed-valent neptunium compounds, [{Np^{IV}Cl$_4$}{Np^{V}O$_2$(μ$_2$-Cl)(THF)$_3$}$_2$]·THF (1) and [{Np^{IV}Cl$_3$}{Np^{V}O$_2$(μ$_2$-Cl)(THF)$_2$}$_3${μ$_3$-Cl}] (2) (THF = tetrahydrofuran), were synthesized and characterized. Both compounds are formed via cation-cation interactions (CCIs) between the oxygens of the neptunyl(V) moieties and the Np^{IV} center.

Due to the lack of suitable starting materials, the chemistry of transuranium (TRU) elements (*i. e.* Np or Pu) is still in its infancy. Reported procedures to prepare starting materials of TRU elements require metallic An^0 which is not accessible in most facilities dedicated to radioactive materials research. Thus alternative reaction pathways are necessary to gain further insight into the organometallic chemistry of TRU elements. We have previously reported a synthetic route to prepare NpCl$_4$ based on the synthetic route to prepare UCl$_4$.[1] However, the NpCl$_4$ source obtained from this route is found to contain a small amount of Np^V impurity. This study reports an investigation of Np^V impurity in NpCl$_4$ sources, which eventually yields two new polynuclear mixed-valent Np complexes.

EXPERIMENTAL. The polynuclear Np compounds **1** and **2** were synthesized by dissolving NpCl$_4$ in anhydrous THF. The NpCl$_4$ was prepared according to the reported procedure.[1] The resulting suspension was centrifuged and slow evaporation of the supernatant resulted in the crystallization of **1** (aged NpCl$_4$) or **2** (fresh NpCl$_4$).

RESULTS. A detailed investigation onto the properties of tetravalent Np in organic solvents has been performed. Different batches of NpCl$_4$ with different amounts of Np^V impurity were dissolved in anhydrous THF and the supernatant was first investigated by UV-Visible absorption spectroscopy (see Fig. 1).

The absorption peak at around 1002 nm is assigned to the absorbance of Np^{V}O$_2^+$, whereas the peak at 762 nm is an indicator for Np^{IV}. The ratio of Np^{IV} : Np^V is higher in the solution of the aged NpCl$_4$ than in the freshly dissolved one, indicating that the aged NpCl$_4$ source contains a higher fraction of Np^{IV} than the fresh NpCl$_4$.
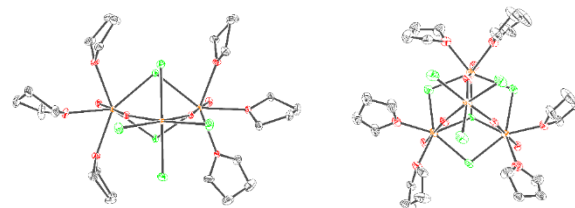
Fig. 2: Molecular structure of [{Np^{IV}Cl$_4$}{Np^{V}O$_2$(μ$_2$-Cl)(THF)$_3$}$_2$] (**1**, left) and [{Np^{IV}Cl$_3$}{Np^{V}O$_2$(μ$_2$-Cl)(THF)$_2$}$_3${μ$_3$-Cl}] (**2**, right). Hydrogen atoms and solvent molecules are omitted for clarity. Color code: carbon (C, gray), chlorine (Cl, green), nitrogen (N, blue), oxygen (O, red), and neptunium (Np, orange).

Interestingly, this Np^{IV} : Np^V ratio seems to be preserved in the solid state compounds **1** and **2,** that were yielded by slow evaporation of the solutions of aged- (**1**) and fresh NpCl$_4$ (**2**).

In compound **1**, one {Np^{IV}Cl$_4$} moiety is coordinated by two {Np^{V}O$_2^+$} units which are μ$_2$-bridged by two chlorides. The coordination sphere around the {Np^{V}O$_2^+$} units is occupied by three THF molecules for each unit. A similar situation is found in compound **2** where three {Np^{V}O$_2^+$} units are coordinating to the {Np^{IV}Cl$_3$} unit *via* CCI, forming a tetrahedral arrangement of Np atoms. The basal plane of the three Np^V atoms is μ$_3$-chloro-bridged at the center and μ$_2$-chloro-bridged at the edges. The coordination sphere of the Np^V is further occupied by two THF molecules for each.

The structure of the obtained polynuclear mixed-valent Np$^{IV/V}$ compounds were new, but somewhat comparable to the reported tri- and tetranuclear Np compounds involving CCIs.[3, 4] The comparison of the trinuclear Np$^{IV/V}$ compound **1** with the analogous trinuclear Np$^{VI/V}$ compound [{Np^{VI}Cl$_2$O$_2$}{Np^{V}O$_2$(μ$_2$-Cl)(THF)$_3$}$_2$][3] reveals that the Np^{VI}–O$_{yl}$ distances of 2.303 and 2.316 Å in the Np$^{VI/V}$ compound are significantly longer than the Np^{IV}–O$_{yl}$ distances of 2.249 and 2.270 Å in **1**, suggesting a stronger CCI in **1** as compared to that in the Np$^{VI/V}$ compound.

The results obtained in this study also suggest that an additional extraction step is required to prepare a starting material with high Np^{IV} purity.[5]

[1] März, J. (2016) *Report HZDR-067*, p. 16.
[2] Patel, D. *et al.* (2015) *New J. Chem.* **39**, 7559–7562.
[3] Cornet, S. M. *et al.* (2009) *Chem. Commun.*, 917–919.
[4] Charushnikova, I. *et al.* (2010) *Inorg. Chem.* **49**, 2077–2082.
[5] Reilly, S. D. (2014) *Dalton Trans.* **43**, 1498–1501.

Fig. 1: UV-Visible absorption spectra of supernatant of NpCl$_4$ dissolved in THF directly after the synthesis (blue) and of 2 month-aged NpCl$_4$ (black). The absorbance was normalized to the peak intensity at 1002 nm (Np^{V}O$_2^+$).

Liquid-liquid extraction of Pu(III) by a calix[4]arene based ligand

R. Husar, A. Jäschke, R. Steudtner

The Calix[4]arene-based ligand L[1] shows a strong affinity towards trivalent metal cations of the lanthanide series. Here, complexation of trivalent Plutonium with L[1] were investigated by spectrophotometry. Testing on its pH dependence, this reaction shows distinct charge transfer transitions of Pu(III) at pH 7 that proofed the extraction of ionic Pu(III) from the aqueous into the organic phase.

The calix[4]arene backbone serves as versatile scaffold to group specific ligating site functions resulting in distinctive selectivity for metal complexation. The carbonyl-hydrazone-8-hydroxyquinoline moiety of L[1] (see Fig. 2 inset) was successfully tested in reprocessing strategies of transuranium materials within the nuclear fuel cycle.[1] The high efficiency of coordination of heavy metal cations is based on the formation of five-membered rings in the coordination sphere of the metal cation. The macrocyclic ligand L[1] preorganizes a multicoordinate N/O donor binding pocket resulting in a strong chelate effect applicable in two-phase solvent extraction. This was demonstrated in the separation of U(VI) from rare earth elements earlier.[2–4]

EXPERIMENTAL. Aqueous Pu(III) was freshly prepared by bulk electrolysis at $(-)\,100\,mV$ in 1 M $HClO_4$. Spectrophotometric measurements with 10^{-3} M Pu(III) and equimolar amounts of L[1] were performed on a TIDAS spectrophotometer (J&M Analytik) in the wavelength range from 190–1,000 nm in 0.1 nm intervals using 10 mm quartz cuvettes. The extraction experiments of Pu(III) from aqueous phase were performed at pH 4 and pH 7 by L[1] in $CHCl_3$ directly after pH adjustment. Aliquots of 1 mL of the aqueous and the organic phases were mixed by shaking for 1 min and subsequently investigated on their electronic structures.

RESULTS. The characteristic absorption band around 602 nm representing aqueous Pu(III) disappeared due to uptake of Pu(III) into the organic phase (Fig. 1). The resulting electronic structures of Pu extracted into the organic phase by the L[1] ligand strongly depended on the initial pH of the aqueous phase indicating a different mode of complexation (Fig. 2). Coordination of Pu(III) to the hetero aromatic unit resulted in charge transfer transitions represented by broad absorption bands ranging from 300–400 nm and by a color change of the organic phase (Fig. 3). The UV-vis spectrum of L[1] in $CHCl_3$ (Fig. 2, black line) slightly changes after extraction from the aqueous phase at pH 4 (Fig. 2, blue line), whereas a significant change was observed at pH 7 (Fig. 2, green line) revealing bands at 300 nm and 365 nm. Hence, the coordination of Pu(III) to L[1] requires the deprotonation of the OH-groups of the hydroxyquinoline unit which can only be assumed at pH > 6.
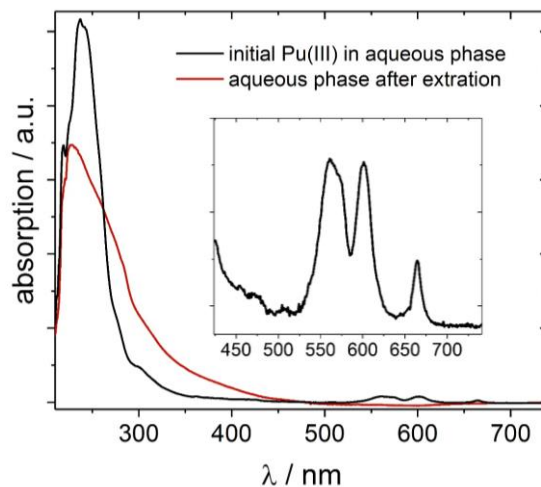
Fig. 1: UV-vis spectra of aqueous solutions of Pu(III) before (black) and after extraction (red) with L[1].
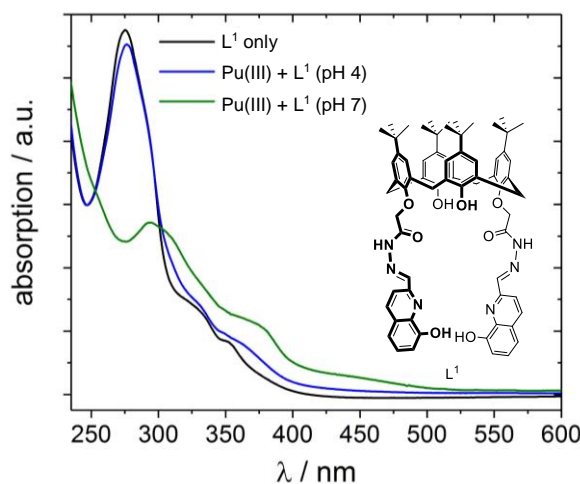
Fig. 2: UV-vis spectra of organic phase ($CHCl_3$) containing L[1] and formed $[Pu_x(L^1)_y]$ complex species after extraction of aqueous phase containing Pu(III) at different pH.
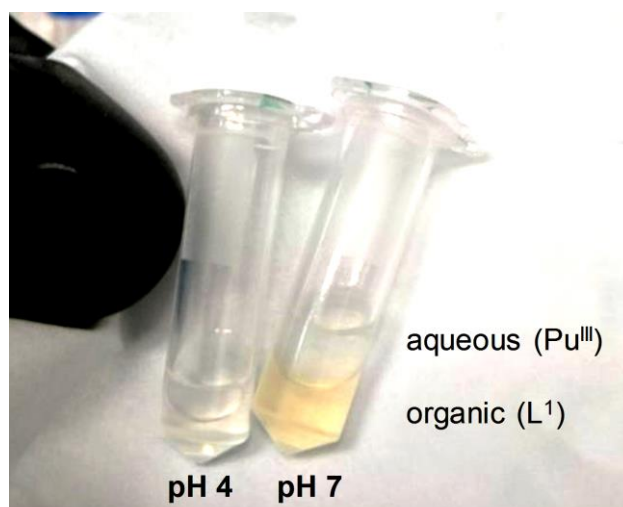
Fig. 3: Colour change of organic phase (lower phase) containing L[1] due to formation of $[Pu_x(L^1)_y]$ complexes by extraction at pH 7.

[1] Arnaud-Neu, F. *et al.* (1996) *J. Chem. Soc., Perkin Trans. 2* **1996**, 1175–1182.
[2] Jäschke, A. (2017) Ph.D. thesis, University of Leipzig, Germany.
[3] Bauer, A. *et al.* (2018) *ChemistryOpen* **7**, 467–474.
[4] Jäschke, A. *et al.* (2017) *Eur. J. Inorg. Chem.* **2017**, 894–901.

Synthesis of colorless An(IV) compounds by strict adoption of T_h-symmetry

S. Tsushima, H. Kazama,[1] T. Mashita,[1] M. Matsuoka,[1] J. März, K. Takao[1]

[1]Laboratory for Advanced Nuclear Energy, Tokyo Institute of Technology, Tokyo, Japan

An(IV) compounds exhibit characteristic visible absorption bands. According to the Laporte selection rule, An(IV) compounds with perfect T_h-symmetry become colorless because absorptions stemming from f–f transitions is strictly forbidden in such a centrosymmetric system. However, colorless An(IV) complexes has not been reported thus far as such symmetry is challenged by ligand field distortion from the surrounding counterions. We synthesized the first colorless An(IV) complex, namely $[An(NO_3)_6]^{2-}$, by adopting hydrogen bond polymers of diamide building blocks as countercations, thereby maximizing the An(IV)−H$^+$ distance and minimizing the electrostatic interaction between $[An(NO_3)_6]^{2-}$ and the counterion.
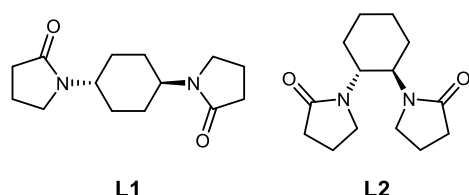
Fig. 1: Schematic structures of diamide building blocks employed in this study (**L1**, **L2**). An (*R*, *R*)-enantiomer of **L2** is only displayed in this figure, while its racemate has been used in this work.

EXPERIMENTAL. A U(IV) stock solution (0.15 M, 100 mL) containing 3 M HNO_3 and 0.15 M N_2H_4 was overlayed with 3 M HNO_3 aq (30 mL) and 3 M HNO_3 solution of the diamide building block (**L1** or **L2**, see Fig. 1, 0.30 M, 100 mL) in a glass tube. Slow diffusion of U(IV) and the diamide resulted in crystal formation with remarkably diminished color (Fig. 2) in nearly quantitative yields (> 98 %) accompanied by the fading of the green color of the solution which originates in U(IV) in its $5f^2$ configuration. Elemental analysis determined the chemical formulae of these compounds to be $(HL)_2[U(NO_3)_6]$ (L = **L1**, **L2**), where U^{4+} is present. Molecular and crystal structures of **1** and **2** have been determined by single-crystal X-ray diffraction and were found to be hexanitratouranate(IV), $[U(NO_3)_6]^{2-}$, with two H$^+$ and two L molecules in agreement with the formulae determined by the elemental analysis.
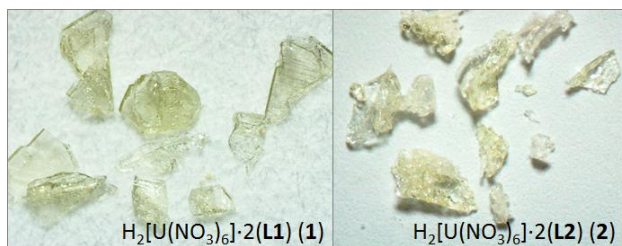
Fig. 2: Photomicrographs of $H_2[U(NO_3)_6]\cdot2L_1$ (**1**), $H_2[U(NO_3)_6]\cdot2L_2$ (**2**).

COMPUTATIONAL. To theoretically estimate the sensitivity of U(IV) absorption spectra related to the ligand-field transitions, the electronic absorption spectra stemming from the formally Laporte forbidden f–f transitions were calculated by CASSCF/sc-NEVPT2 approach using the program ORCA.[1] Three complexes have been selected: $[U(H_2O)_8]^{4+}$, $[U(H_2O)_9]^{4+}$, and $[U(NO_3)_6]^{2-}$ from **1** crystalized in this work using **L1**. The first two complexes were included as references since the absorption spectra of U(IV) hydrates
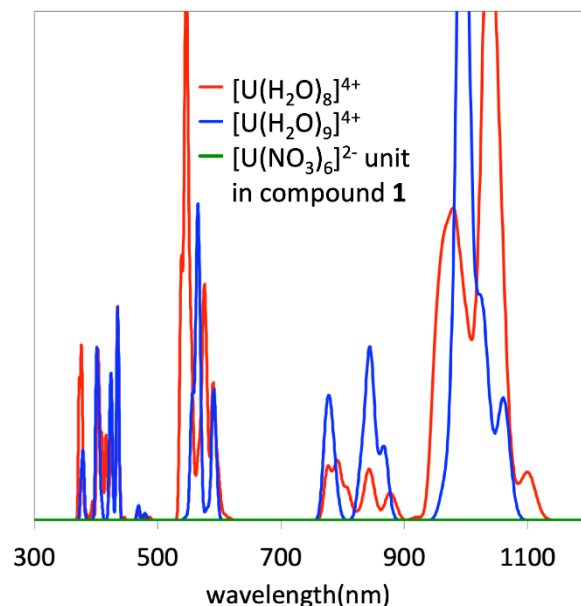
Fig. 3: Electronic absorption spectra of $U(H_2O)_N^{4+}$ with $N = 8$ (red) and $N = 9$ (blue) and $U(NO_3)_6^{2-}$ unit within compound **1** with **L1** (green) calculated at the CASSCF(2,7)/NEVPT2 level including spin-orbit coupling using the program ORCA. Only the absorption bands stemming from the f–f transitions were included in the calculations.

are widely available. The calculated spectra are shown in Fig. 3. For U(IV) hydrates, the experimental absorption spectrum is nicely reproduced by CASSCF calculations. By contrast, in the case of the T_h-symmetric $[U(NO_3)_6]^{2-}$ complex (**1**) synthesized in this work, there is no absorption at all throughout the whole spectral range.

RESULTS. The regularly T_h-symmetric $[U(NO_3)_6]^{2-}$ was successfully crystallized together with hydrogen bond polymers of diamide building blocks in the aqueous systems. The diamide building blocks **L1** and **L2** employed here have been originally designed by us to develop precipitation-based simple reprocessing processes for spent nuclear fuels.[2] As described above, compound **1** and **2** have been obtained from HNO_3 aq in nearly quantitative yields, so that the current findings can also be applied to the efficient recovery of An(IV) from the feed HNO_3 solution in spent nuclear fuel reprocessing. We have also succeeded in synthesizing analogous colorless compounds using Th(IV), Np(IV), and Pu(IV).

[1] Neese, F. (2018) *WIREs Comput. Mol. Sci.* **8**, e1327.
[2] Kazama, H. *et al.* (2017) *Inorg. Chem.* **56**, 13530–13534.

The inverse trans effect in U(IV) and U(V) complexes with soft donor ligands

L. Köhler, R. Kloditz, M. Patzschke, J. März

Uranium(IV) and (V) complexes were synthesized by using the _N_-heterocylic carbene ligand ^iPrIm (L^1) and lithium bis(trimethylsilyl)amide (TMSA) as a base. The structural characterization by SC-XRD and geometry optimization of the resulting compounds [U^IV(L^1)_2(TMSA)Cl_3] (1) and (HL^1)_2[U^V(TMSI)Cl_5] (2) (TMSI = trimethylsilylimide) confirmed the occurrence of an inverse trans influence (ITI) by means of the silylamido- or silylimido ligand.[1]

The ITI is known to occur in high oxidation state actinide complexes (V/VI), where strongly donating ligands are trans located. By donating electron density to the metal center, these ligands can fill up the electron hole forming through electron density transfer from semi-core $6p$ to vacant $5f$ orbitals.[2] This leads to bond strengthening and shorting. In the past the ITI was evidenced by some U(V) and (VI) complexes, but recently it has become a more general f-block principle.[2–4]

EXPERIMENTAL. The U(IV) complex **1** was synthesized by dissolving $^iPr_2$ImHCl and LiTMSA in anhydrous tetrahydrofuran (THF) and adding UCl$_4$, resulting in a brown suspension. Centrifugation and slow evaporation of benzene into the mother liqueur yielded green crystals of **1**. Complex **2** was prepared analogous but using anhydrous acetonitrile as a solvent and ether diffusion.

RESULTS. SC-XRD investigations of **1** revealed a U(IV) center surrounded by one TMSA-, three chloro-, and two carbene ligands (see Fig. 1), leading to a distorted octahedral coordination geometry. The bond length U1–Cl2 is remarkably shorter (0.02 Å) compared to the other chloro ligands. Because of its trans position to TMSA, the bond shortage can be explained by the ITI: Electron density is transferred from the N-donor ligand TMSA resulting in bond strengthening and therefore bond shorting of the opposing Cl2 ligand.
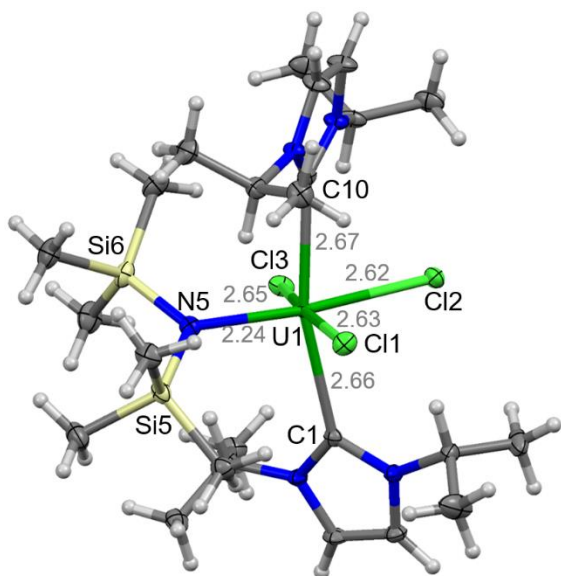
This ITI effect is expected to occur in the U(V) complex **2** in an even more pronounced way. But, surprisingly, such an effect cannot be confirmed in the experimentally determined structure of **2**, where the U(V) is coordinated by one trimethylsilylimido (TMSI) and five chloro ligands, leading to an octahedral complex dianion. The chlorine atom being trans to TMSI possesses a U1–Cl5 bond length of 2.68 Å. Thus, it is in the same range as the remaining four chloro ligands. However, the presence of an ITI was validated in the optimized structure of the relevant complex anion (see Fig. 2) where the bond length U1–Cl5 is 2.55 Å and thus 0.02 Å shorter than the equatorially bound chlorine atoms. Differences in bond lengths between the experimentally determined and the optimized structures can be explained by intermolecular interactions. The packing in **2** is dominated by electrostatic interactions between the complex anion and imidazolium cations as well as by numerous bi- and trifurcated hydrogen bonds C–H⋯Cl. The latter interactions typically range between approx. 2.67 and 2.91 Å and point to a strong hydrogen bond network between the imidazolium cations and the complex anion. In contrast, the intermolecular interactions in **1** are limited to two types of weak hydrogen bonds C–H⋯Cl and C–H⋯C involving the carbene ligands.

The results of this study clearly indicate the presence of the inverse trans influence in highly charged actinide complexes, such as **1** and **2**, including also the tetravalent oxidation state.
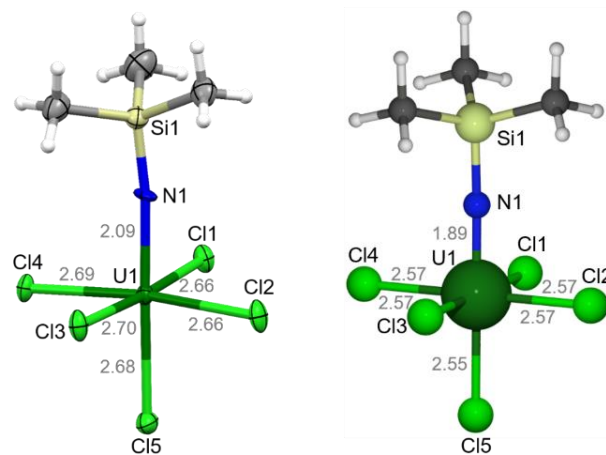
Fig. 2: Structures of [U^V(TMSI)Cl_5]^{2−} (**2**): experimentally determined by SC-XRD (left) and optimized (right). ^iPrImH cations are omitted for clarity (left). Color code: carbon (C, gray), chlorine (Cl, lime green), hydrogen (H, white), nitrogen (N, blue), silicon (Si, yellow), and uranium (U, green).

[1] Köhler, L. _et al._ (2019) in preparation.
[2] Gregson, M. _et al._ (2017) _Nat. Commun._ **8**, 1–11.
[3] Kosog, B. _et al._ (2012) _J. Am. Chem. Soc._ **134**, 5284–5289.
[4] King, D. M. _et al._ (2013) _Angew. Chem. Int. Ed._ **52**, 4921–4924.

Fig. 1: Molecular structure of [U^IV(L^1)_2(TMSA)Cl_3] (**1**). Color code: carbon (C, gray), chlorine (Cl, lime green), hydrogen (H, white), nitrogen (N, blue), silicon (Si, yellow), and uranium (U, green).

Spectroscopic investigations on U(IV) sulfate in aqueous solution

S. Lehmann, R. Steudtner, T. Zimmermann, V. Brendler

The complex formation of U(IV) with sulfate in acidic aqueous solution was studied for the first time in the micromolar range by spectroscopy. Single component absorption spectra as well as extinction coefficients of U^{4+}, UOH^{3+}, $U(SO_4)^{2+}$ and $U(SO_4)_2$ are obtained. Complex formation constants of UOH^{3+}, $U(SO_4)^{2+}$ and $U(SO_4)_2$ in infinite diluted solution are determined by thermodynamic modelling to be $\log \beta°_{1-10} - (0.36 \pm 0.1)$, $\log \beta°_{101} = 6.91 \pm 0.3$, $\log \beta°_{102} = 11.84 \pm 0.5$, respectively. Under the experimental conditions no further U(IV) sulfate and hydrolysis species are confirmed. U(IV) sulfate complexation is supposed to induce static quenching of U(IV) fluorescence.

For a high level radioactive waste disposal as well as former uranium mining sites, U(IV) is expected to be the stable oxidation state due to reducing conditions after sealing. Thermodynamic data on U(IV) in aqueous solution is needed for a reliable safety assessment but still sparse by reason of its low solubility and a lack of appropriate measuring systems. Therefore, we employed a combination of absorption and fluorescence spectroscopy to study U(IV) sulfate complexation in acidic aqueous solution.

EXPERIMENTAL. U(IV) stock solution was prepared by electrochemical reduction. To cover a wide range of experimental parameters we used the methods of Yoe-Jones and Job-Plot with uranium concentrations between 60 and 100 µM.[1, 2] We varied sulfate concentrations up to 500 and 1900 µM at ionic strengths of 0.15 and 1.2 M, respectively. Experiments were carried out in a pH range of 0 to 2 to avoid precipitation by hydrolysis. We applied a combination of UV/Vis absorption spectroscopy with long path flow cell (LWCC) using a Tidas 100 spectrophotometer (J&M Analytik AG) and TRLFS employing a Nd/YAG driven OPO tunable laser system (Photonics) as excitation source ($\lambda_{exc} = 245$ nm) combined with a cooled iStar ICCD camera (Andor).

Davies equation was used for recalculation from I = 0.15 M to zero ionic strength.[3] For I = 1.2 M SIT approaches are applied.[4] Related activity coefficients are taken from literature.[5] Following deprotonation equations are used:

$$H_2SO_4 \rightleftharpoons H^+ + HSO_4^-$$

$$HSO_4^- \rightleftharpoons H^+ + SO_4^{2-}$$
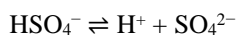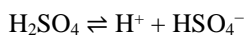
RESULTS. Under the experimental conditions U(IV) hydrolysis and sulfate complexation lead to a multi component system. HypSpec was used to assess the number of absorbing species in solution.[6, 7] By deconvolution of UV-vis absorption spectra in the range 400–700 nm between pH 0 and 2, single component spectra of U^{4+}, UOH^{3+}, $U(SO_4)^{2+}$ and $U(SO_4)^2$ are obtained (Fig. 1). Extinction coefficients have been calculated to be 58.8, 19.2, 47.6 and 40.3 L mol^{-1} cm^{-1}, respectively. Complex formation constants for UOH^{3+}, $U(SO_4)^{2+}$ and $U(SO_4)_2$ in infinite diluted solution are determined by thermodynamic modelling and are in good agreement with published data gained by solvent extraction (Tab. 1).[5, 8]

The calculated constants and absorption spectra can be used as reference data for deconvolution of multi component systems, *e.g.* U(IV) in environmental samples.
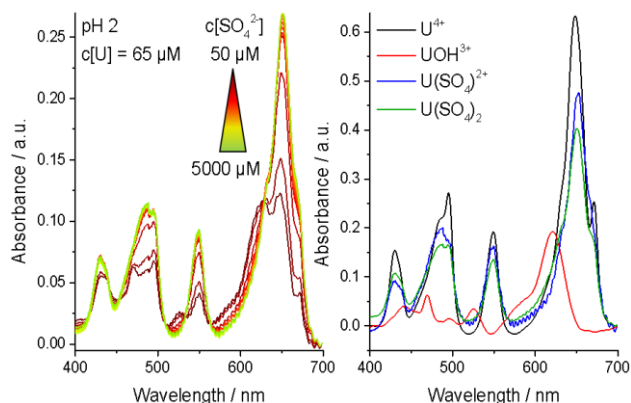
Fig. 1: Data set with multi component spectra. Sulfate complexation suppresses hydrolysis with increasing sulfate concentration (left panel). Single component absorption spectra of U^{4+}, UOH^{3+}, $U(SO_4)^{2+}$ and $U(SO_4)_2$ calculated with HypSpec from multi component spectra (right panel).

Tab. 1: Calculated complex forming constants of U(IV) hydrolysis and of complexation reactions with sulfate in aqueous solution in comparison to literature data.

Reaction	$\log \beta°_{cal}$	$\log \beta°$	Ref.
$U^{4+} + H_2O \rightleftharpoons UOH^{3+} + H^+$	-0.36 ± 0.1	-0.54 ± 0.06	[5]
		-0.34 ± 0.2	[8]
$U^{4+} + SO_4^{2-} \rightleftharpoons USO_4^{2+}$	6.9 ± 0.3	6.58 ± 0.19	[5]
		8.4	[8]
$U^{4+} + 2\,SO_4^{2-} \rightleftharpoons U(SO_4)_2$	11.8 ± 0.5	10.51 ± 0.20	[5]
		11.6	[8]

By studying U(IV) fluorescence properties at I = 1.2 M we observed a decreasing U(IV) fluorescence intensity with increasing sulfate concentration which is supposed to be a static quenching effect of sulfate complexation. By evaluation of fluorescence lifetime we determined U^{4+} as only fluorescent species in solution.

[1] Yoe, J. H. *et al.* (1944) *Ind. Eng. Chem. Anal. Ed.* **16**, 111–115.
[2] Job, P. (1928) *Ann. Chim.* **9**, 113–203.
[3] Davies, C. W. *et al.* (1962) *J. Chem. Soc.*, 880–885.
[4] Ciavatta, L. (1980) *Ann. Chim.* **70**, 551–567.
[5] Guillaumont, R. F. *et al.* (2003) *Update on the chemical thermodynamics of uranium, neptunium, plutonium, americium and technetium*, Elsevier, Amsterdam.
[6] Gans, P. *et al.* (1996) *Talanta* **43**, 1739–1753.
[7] Gans, P. *et al.* (1999) *Ann. Chim.* **89**, 45–49.
[8] Fuger, J. (1992) *Radiochim. Acta* **58**, 81–91.

Recent advances in U(IV) fluorescence in organic solvents

T. Radoske, R. Steudtner

The U(IV) complex [UCl₂salen(MeOH)₂] was investigated for possible U(IV) fluorescence in methanolic solution (H₂salen = N,N'-bis(salicylidene)ethylenediamine). During excitation with UV light ($\lambda_{exc.}$ = 370 nm) a broad luminescence in the region from 400 to 600 nm with weakly distinguishable bands at 450 nm and 470 nm can be detected.

Fluorescence spectroscopy is a successfully applied analytical method in systems containing uranyl ions. The characteristic "five-fingered" peak pattern being its trademark. In contrast to U(VI), very little is known about the luminescence of U(IV).[1] Kirishima *et al.* reported the only comprehensive luminescence spectrum of U(IV) in aqueous solution.[2] In organic solvents, spectral fingerprints of simple U(IV) compounds were described by Hashem *et al.*[3] In this study, we expand the investigated range of organic solvents and show that U(IV) luminescence in methanol is detectable.

EXPERIMENTAL. Samples were prepared in a glovebox in an inert N₂ atmosphere to avoid oxidation. Three samples were measured, 5 mg [UCl₂salen(MeOH)₂] (1), 2 mg UCl₄ (2), and 3 mg H₂salen (3). Each sample was dissolved in 1.5 mL methanol and filled into a cuvette with airtight sealing. Solvents were distilled onto activated molecular sieve (3 Å) prior to use. Luminescence measurements were performed at room temperature on a fluorescence spectrofluorometer (QuantaMaster 40) equipped with a 75 W xenon arc lamp.

RESULTS. Since no suitable reference data was available, the luminescence of UCl₄ solution in methanol was investigated at excitation wavelengths ranging from 200 to 400 nm. Figure 1 shows a series of emission spectra as a function of excitation wavelength. The highest intensity is recorded at $\lambda_{exc.}$ = 340 nm and shows a broad band with a distinctive peak at 425 nm which is followed by a tail with additional features to longer wavelengths up to 600 nm.

A similar series of spectra was recorded for the complex [UCl₂salen(MeOH)₂]. The highest luminescence intensity corresponds to $\lambda_{exc.}$ = 370 nm, a shift of ~30 nm relative to UCl₄. The luminescence signal ranges from ~400–600 nm showing a peak at 470 nm and a shoulder ~450 nm (Fig. 2). In comparison with luminescence of UCl₄, the complex signal is shifted to longer wavelengths which may indicate an intensity profile change of the underlying band structure, due to a change in the coordination environment of U(IV). An extensive analysis with laser light sources at lower temperatures could lead to a better understanding of the involved transitions.
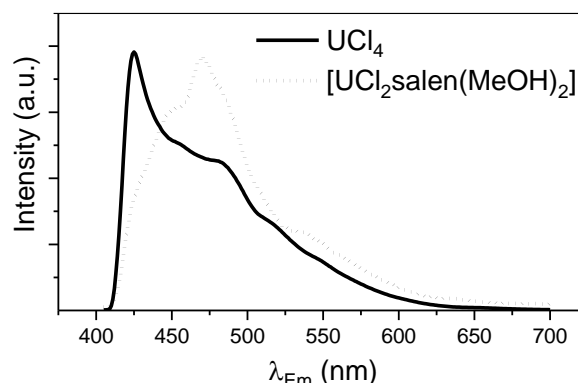
Fig. 2: The emission spectra of UCl₄ (λ_{exc} = 340 nm) and its monosalen complex (λ_{exc} = 370 nm) in methanol.

No luminescence was detected in the sample of the free ligand. To exclude the possibility of the emission being U(VI) fluorescence introduced through oxidation, we deliberately exposed the complex solution to air. A color change from green to orange is noticeable within minutes, which is attributed to the oxidation of U(IV) to U(VI). Orange crystals precipitated within a week that were characterized as [UO₂salen(MeOH)]. The oxidized complex solution showed no luminescence when excited at $\lambda_{exc.}$ = 266, 280, 300, and 350 nm. Reasons for the absence of any U(VI) fluorescence could be a quenching effect through introduction of chloride ions to the solution that were bound to the U(IV) complex prior to oxidation, or a self-quenching effect.

These preliminary results show that U(IV) fluorescence spectroscopy can be a promising tool for future investigations. In combination with X-ray diffraction and other spectroscopic techniques, this will provide a better understanding of the relationship between structures in solid and solution.

[1] Natrajan, L. S. (2012) *Coord. Chem. Rev.* **256**, 1583–1603.
[2] Kirishima, A. *et al.* (2004) *Radiochim. Acta* **92**, 705–710.
[3] Hashem, E. (2013) *RSC Adv.* **3**, 4350–4361.
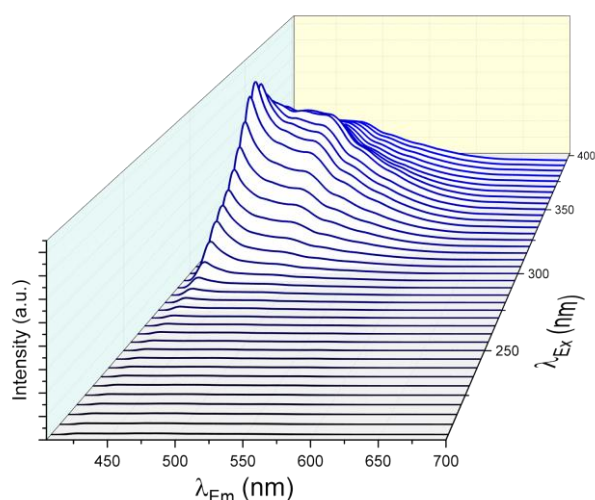
Fig. 1: The emission spectra of UCl₄ in methanol plotted against the excitation wavelength.

Aqueous uranium(VI) complexation with silicates in the acidic to alkaline pH-range

H. Lösch, J. Tits,[1] M. Marques Fernandes,[1] B. Baeyens,[1] S. Krüger,[2] T. Stumpf, N. Huittinen

[1]Paul Scherrer Institute, Villigen, Schwitzerland; [2]Technische Universität München, Munich, Germany

The aqueous complexation of uranium(VI) and silicates was investigated in the acidic and alkaline pH-range using TRLFS and the Schubert-method. In the acidic range a temperature dependent series was performed to extract the thermodynamic parameters $\Delta_r H°$ and $\Delta_r S°$ next to the complexation constant of the $UO_2OSi(OH)_3^+$ complex. In the alkaline pH-range the ternary $UO_2(OH)_2OSi(OH)_3^-$ complex could be identified.

EXPERIMENTAL. For the TRLFS investigation in the acidic range (pH 3.5), an Si-ICP standard was used as silicate source. All experiments were performed under the solubility limit of aqueous silicates in the concentration range between 1.3×10^{-4} to 1.5×10^{-3} M and a uranium concentration of 5×10^{-6} M. The temperature varied from 1 °C to 25 °C. The ionic strength was fixed at 0.2 M NaClO₄. In the alkaline pH-range from pH 6−11.5 the complexation was investigated using the Schubert-method. Sodium-metasilicate was used as a silicate source in the aqueous phase and tetragonal ZrO_2 as solid phase. The distribution of ^{233}U in the aqueous and solid phases was measured by LSC. All measurements were performed at 25 °C at a fixed ionic strength of 0.1 M NaCl.

RESULTS. The luminescence spectra in absence of silicates show a mixed species between the free uranyl and the 1:1 hydroxo species UO_2OH^+ already at pH 3.5.[1] Based on this result, the hydroxo species has to be taken into account in the deconvolution process of the following spectra. The amount of the hydroxo species also increase with increasing temperature.[2] The emission spectra in presence of silicates show a spectral bathochromic shift with increasing silicate concentration. This confirms the formation of the $UO_2OSi(OH)_3^+$ species at pH 3.5. Peak deconvolution was performed with the spectra recorded at all temperatures. As a result, the component spectra of the free uranyl, the hydroxo complex and the U-Si-complex are shown in Fig. 1. In addition to the bathochromic shift, an increase of the luminescence intensity was observed with increasing silicate concentration. The species distribution and fluorescence intensity factors were calculated by a least-square fit method. A slope analysis results in a slope of ~1 for all temperatures. The stability constants were corrected to standard conditions using the Davies equation (Tab. 1). The stability constants are significantly higher than the literature values due to the
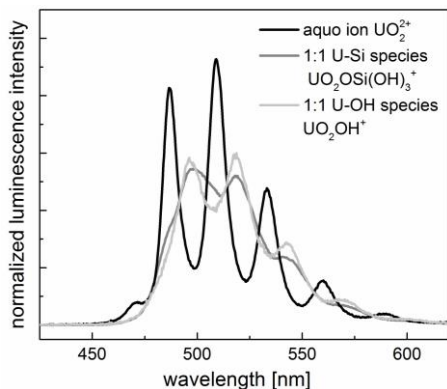
Tab. 1: Corrected stability constant for the $UO_2OSi(OH)_3^+$ complex.

Temperature	log K°(T)
1 °C	−(0.76 ± 0.27)
10 °C	−(0.49 ± 0.19)
17 °C	−(0.28 ± 0.33)
25 °C	−(0.06 ± 0.24)

consideration of the hydroxo complex and the solubility limit of the aqueous silicates.[3] Thermodynamic parameters were derived from a van't Hoff plot yielding $\Delta_r H° = 46.3$ kJ·mol⁻¹ and $\Delta_r S° = 154.1$ J·K⁻¹·mol⁻¹.

In the alkaline pH-range 6−11.5, the U(VI) silicate complexation was investigated using the Schubert-method. The Schubert-method is based on the determination of the distribution coefficient R_d between a solid and liquid phase in absence and presence of complexing ligands in the liquid phase. Thus, with increasing ligand concentration an increase of the formed complex in solution and a decrease of the distribution coefficient can be observed. A plot of the R_d-value as a function of the ligand concentration directly provides structural information about the number of involved ligands in the complex. In a second plot the fitting constant (obtained in the R_d-plot) as a function of corrected pH (Fig. 2) provides the number of involved protons in the complexation reaction (slope) and the conditional complexation constant (y-intercept). With this information, two possible complexes might occur in the alkaline pH-range, first $UO_2(OH)O_2Si(OH)_2^-$ and second $UO_2(OH)_2OSi(OH)_3^-$. DFT-calculations confirm the formation of the second complex with a corrected stability constant log K° = −16.30.
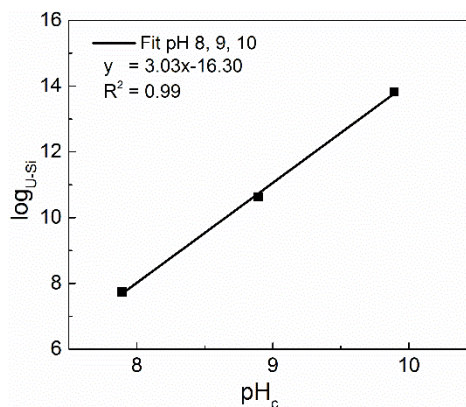
Fig. 2: Plot of the fitting constant as a function of the corrected pH.

[1] Drobot, B. *et al.* (2016) *Anal. Chem.* **88**, 3548−3555.
[2] Zanonato, P. *et al.* (2004) *J. Am. Chem. Soc.* **126**, 5515−5522.
[3] Nagra/PSI Chemical Thermodynamic Database 12/07 (2014).

Fig. 1: Extracted free component spectra of the free uranyl, the UO_2OH^+ complex and the $UO_2OSi(OH)_3^+$ complex.

Temperature dependent studies of uranyl(VI) complexation with halides and their influence on uranyl(VI) luminescence properties

M. Demnitz, H. Lösch, T. Stumpf, N. Huittinen

The complexation of fluoride and chloride with uranyl(VI) was investigated at varying temperatures (1−45 °C) in aqueous solution using Time-resolved Laser-induced Fluorescence Spectroscopy (TRLFS). Through peak deconvolution of the measured spectra it was possible to identify several U(VI)-halide species in the investigated solutions. To quantify the quenching process of U(VI) luminescence in the presence of chloride Stern-Volmer plots were used. The amount of static and dynamic quenching in solution were calculated, from which the quench reaction entropy and enthalpy could be derived.

EXPERIMENTAL. Using a constant uranium concentration [U] of 0.1 mM the complexation of uranyl(VI) with fluoride was investigated in a concentration range of [F] = 0−0.15 M, while varying the temperature from 1−45 °C. The complexation and quenching of uranyl(VI) with chloride was examined at [U] = 0.1 mM and [Cl] = 0−0.1 M at temperatures ranging from 1−45 °C. The pH in all samples was kept constant at pH = 1, while a constant ionic strength was maintained with $NaClO_4$ as background electrolyte.

RESULTS. The increasing fluoride concentration results in a red shift of the uranyl(VI) luminescence signal due to complexation. Through spectral deconvolution it was possible to isolate the pure component spectra of two complexes: UO_2F^+ as well as UO_2F_2 (see Fig. 1).[1] The formation of both complexes was favored at higher temperatures due to their endothermic reaction enthalpy.[2] No quenching of the uranyl(VI) luminescence with fluoride takes place. The situation is very different in the presence of chloride.

Thus, the complexation of uranyl(VI) with chloride was investigated. Chloride quenches the luminescence of uranyl(VI) through the formation of a transition state, which results in a loss of luminescence intensity.[3, 4] Nevertheless it was possible to spectrally extract the UO_2Cl^+ complex at low temperatures through peak deconvolution. Identical to the experiments with fluoride the chloride induces a red shift of the uranyl(VI) luminescence signal. The characteris-
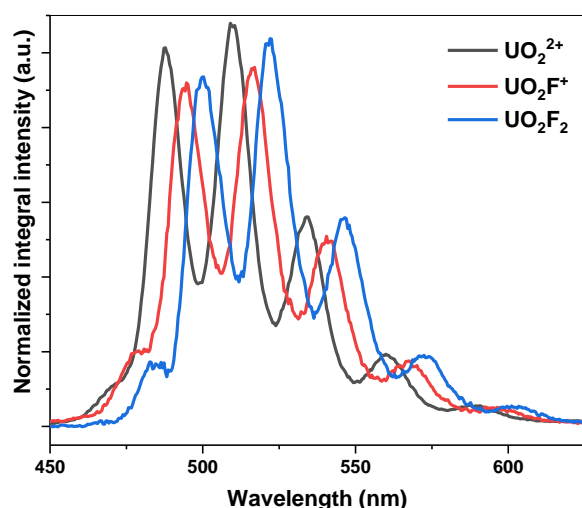
Fig. 2: Deconvoluted spectra of UO_2F^+ and UO_2Cl^+ at 1 °C using [U] = 0.1 mM.

tic UO_2Cl^+ luminescence bands appear in the same region as the bands of the UO_2F^+ complex, which might be due to the similar structures of the halide uranyl(VI) complexes (see Fig. 2).[1]

The quenching of uranyl(VI) luminescence in chloride-containing solutions was investigated at temperatures from 1−45 °C. Using a Stern-Volmer analysis it was possible to show, that both static as well as dynamic quenching occurs in solution, depending on the overall chloride concentration used. Static quenching can be traced back to the endothermic formation of the UO_2Cl^+ complex.[5] The Stern-Volmer constants, K_s and K_d respectively, of both processes increase with increasing temperatures, but the dynamic quench mechanism was found to dominate the overall quenching process. Using a combination of the bimolecular quenching constant τ and the Arrhenius and Eyring equations the activation energy (0.512 eV), activation enthalpy (0.486 eV) and activation entropy (9×10^{-3} eV K^{-1}) of the dynamic quench process were determined. It was possible to conclude, that with rising temperatures the energy barrier of the transition state of the dynamic quenching decreases, implying a favored formation of the transition state at higher temperatures and with a subsequent increase of the quenching.

[1] Demnitz, M. (2018) Master thesis, Technische Universität Dresden.
[2] Ahrland, S. et al. (1971) *Acta Chem. Scand.* **25**, 3457−3470.
[3] Yokoyama, Y. et al. (1976) *J. Inorg. Nucl. Chem.* **38**, 1329−1333.
[4] Burrows, H. D. et al. (1990) *Inorg. Chem.* **29**, 1549−1554.
[5] Awasthi, S. P. et al. (1981) *Indian J. Chem. Sect A-Inorg. Bio-Inorg. Phys. Theor. Anal. Chem.* **20**, 378−381.

Fig. 1: Deconvoluted spectra of UO_2^{2+}, UO_2F^+ and UO_2F_2 at 1 °C using [U] = 0.1 mM and [F] = 0−0.15 M.

The UO$_2^{2+}$-isosaccharinic acid system investigated by ESI-MS

H. Brinkmann, M. Raiwa,[1] H. Moll, T. Stumpf

[1]Leibniz Universität Hannover (IRS), Germany

Previous spectroscopic investigations of the UO$_2^{2+}$-isosaccharinic acid system indicated the formation of binuclear complexes. Electrospray Ionization Mass Spectrometry (ESI-MS) was used as complementary method to confirm that conclusion and to further underpin the valuable finding that two binding sites of the organic ligand can simultaneously be occupied by different UO$_2^{2+}$ entities.

Isosaccharinic acid (HISA) is the main product of alkaline cellulose degradation, what is expected to occur in a cementitious backfilled repository for low and intermediate level waste.[1] Several studies showed that its anion, isosaccharinate (ISA), forms complexes with radionuclides (RN), which could adversely affect their sorption and solubility.[2] Therefore, ISA causes great concerns in the context of nuclear waste disposal. It is necessary to understand the behavior of ISA in the presence of RN, what is the basis for the determination of reliable thermodynamic data. In the present study the UO$_2^{2+}$- ISA-system is under investigation. Previous spectroscopic studies (UV-vis, ATR-FTIR and NMR) lead to the assumption, that binuclear complexes must be formed in solution, whereby the carboxylic as well as the α- and β-hydroxy groups are involved in complex-formation. The identification of the expected 2:1 and 2:3-complexes by Electronspray-Ionization Mass spectrometry (ESI-MS) would strongly underpin these conclusions.

EXPERIMENTAL. ESI-MS measurements were performed with a Velos Pro Orbitrap Elite (Thermo Fisher Scientific Inc., Waltham, MA, USA) using a Nanospray Flex Source. The samples were analyzed with the Orbitrap mass analyzer, whereby full-MS scans from m/z 200 to 2000 were recorded and averaged for 5 minutes. Measurements were performed in the positive ionization mode. The four following samples were analyzed: NaISA stock solution (15 mM, pH 4), and three 1.5 mM UO$_2^{2+}$-solutions with 0.75, 1.5 and 6 mM NaISA (pH 4).

RESULTS. Figure 1 shows the recorded ESI-MS spectra of sample 1 to 4 (a–d). For sample 1–3 and 4 all signals with a relative intensity higher than 5 % and 2 % were considered, respectively. All signals of sample 1 can be assigned to ISA and its conformations. No fragmentation was detected. The dominant M:L ratios of the detected UO$_2^{2+}$-ISA components, being detected in sample 2–4, are summarized in Tab. 1. The large proportions of 2:1 compounds, found in sample 2 and 3, strongly support the hypothesis that a 2:1 complex is the initially formed species under conditions where M ≥ L. As expected, 2:3 components were dominant in sample 4, but also larger amounts of 1:1 as well as 1:2 compounds were detected. Interestingly, these compounds showed almost the same percentage and might therefore be fragments, originating from a 2:3 complex. Even though the ionization is rather soft, fragmentation may have occurred during the transfer into the gas phase. The relatively large 2:3 complex could have been divided into the two more stable subunits (2:1 and 1:1). This plausible explanation as well as the great proportions of 2:3 components strongly support the formation of these binuclear species in solution.
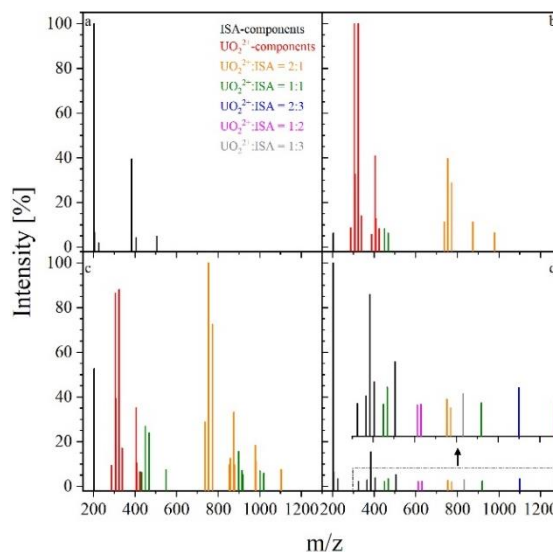
Fig. 1: ESI-MS spectra of ISA and UO$_2^{2+}$-ISA samples (pH 4).
15 mM NaISA (a); 1.5 mM UO$_2^{2+}$, 0.75 mM NaISA (b);
1.5 mM UO$_2^{2+}$, 1.5 mM NaISA (c); 1.5 mM UO$_2^{2+}$, 6 mM NaISA (d).

Tab. 1: Dominant M:L ratios in UO$_2^{2+}$-ISA samples (values are given in %).

	2:1	1:1	2:3	1:2	1:3
Sample 2	34.8	2.3	–	–	–
Sample 3	56.3	12.7	–	–	–
Sample 4	24.0	26.8	17.6	23.9	7.7

Therefore, the presented results are in very good agreements with previously performed spectroscopic investigations.

[1] Glaus, M. A. *et al.* (1999) *Anal. Chim. Acta* **398**, 111–122.
[2] Rai, D. *et al.* (2017) *J. Chem. Thermodyn.* **114**, 135–143.

Spectroscopic study of Eu(III) complexation by 3-hydroxyflavone and determination of the stability constants

A. Günther

3-hydroxyflavone is a polyphenolic benzo-γ-pyrone compound, the basic chemical structure of one type of flavonoids. The 3-hydroxy-4-keto group in the molecule is able to bind different metals. In this study the stability constants of Eu-3HF were determined based on optical absorption data.

EXPERIMENTAL. Methanolic solutions containing 3-hydroxoflavone (Fig. 1) and $EuCl_3$ with different metal to ligand ratios and an ionic strength of 0.1 M $NaClO_4$ were prepared.
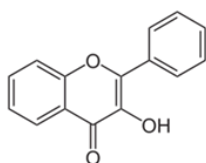
Fig. 1: Structure of 3-hydroxyflavone (3HF).

UV-vis ($[3HF]_0 = 2 \times 10^{-5}$ M; $[Eu]_0$ variable), TRLFS ($[3HF]_0$ variable; $[Eu]_0 = 5 \times 10^{-5}$ M; Eu-excitation wavelengths: 394 or 579 nm) and Femto-TRLFS ($[3HF]_0 = 2 \times 10^{-5}$ M; $[Eu]_0$ variable; excitation wavelength for the organic ligand: 270 nm) were used for the spectroscopic characterization of this complex system at 230, 115 and 5 mV (~pH 3, 5 and 7). The voltage was adjusted with methanolic $HClO_4$ or NaOH.

RESULTS. In Fig. 2 the evolution of the UV-vis spectra of the methanolic Eu(III)/3HF system with increasing metal to ligand concentration ratios is shown.
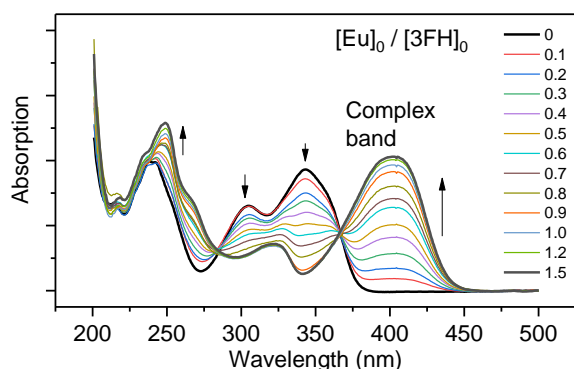
Fig. 2: UV-Vis absorption spectra of 3HF as a function of the Eu(III) concentration at 230 mV (pH 3).

With increasing metal concentration a new absorption band at about 400 nm occurred. A plot of absorption intensity at λ_{max} of complex *versus* metal to ligand ratio (not shown) indicates that the complex formed shows a 1:1 stoichiometry at pH 3. At higher pH (pH 5, pH 7) an additional 1:2 complex is formed. Considering the protonation/deprotonation of the ligand ($\log \beta = 8.57 \pm 0.05$; determined by UV-vis measurements) and the possible formation of a first hydrolysis product of Eu^{3+} ($\log \beta = -5.15 \pm 0.05$, determined by TRLFS with excitation at 394 nm) the stability constants $\log \beta = 12.65 \pm 0.45$ for the 1:1 complex and $\log \beta = 23.41 \pm 0.27$ for the 1:2 complex could be obtained using factor analysis program HypSpec.[1] They are somewhat lower
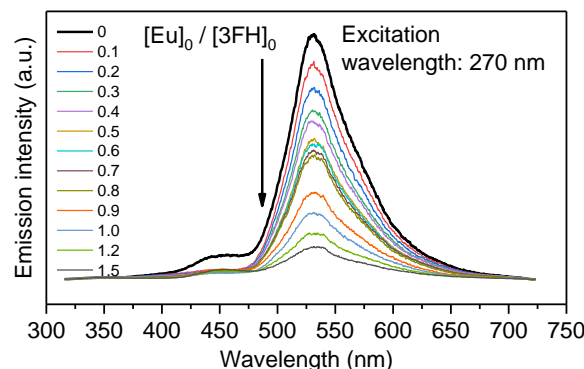
Fig. 3: Emission spectra of 3HF as a function of the Eu(III) concentration at 230 mV(pH 3).

than the corresponding Al(III) species (without consideration of ligand hydrolysis).[2]

The emission properties of the methanolic Eu(III)/3HF system regarding ligand and europium after their respective excitation are shown in Fig. 3 and 4.

The decrease of the emission intensity of the free ligand with increasing Eu(III) concentration indicates the formation of the 1:1 complex at acidic condition. The organic Eu(III) complex itself does not show fluorescence from the ligand.
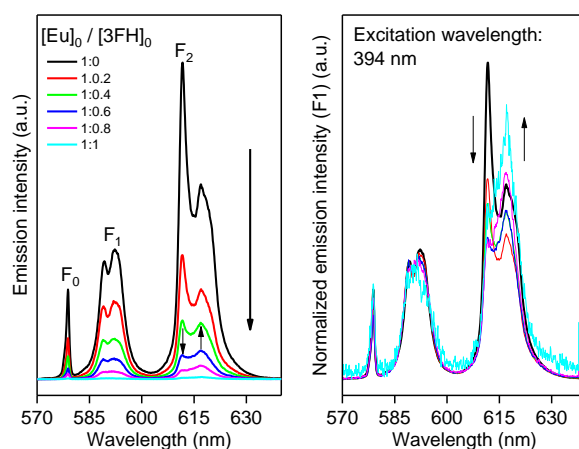
Fig. 4: Emission spectra (original/normalized) of Eu(III) as a function of the ligand concentration at 230 mV (pH 3).

The Eu(III) emission behavior of this system is characterized by a continuous decrease of the intensity and change of the splitting of the $(^5D_0 \rightarrow {}^7F_2)$ transition in particular. The 1:1 complex appears to fluoresce and the F_1 to F_2 intensity ratios do not change significantly compared with ratio shown by the solvated Eu^{3+} ion. The determination of reliable complex formation constants with emission data obtained at room temperature is hampered by difficult to quantify and increasing quenching processes as well as by photochemical side reactions in the organic molecule, which occur at higher pH.

Eu(III) forms stable complexes with this benzo-γ-pyrone compound. It is to be expected that this type of flavonoides also tends to complex trivalent actinides efficiently.

[1] Gans, P. *et al.* (2008) Protonic Software, Leeds.
[2] Dangleterre, L. *et al.* (2008) *Polyhedron.* **27**, 1581–1590.

Complex formation of europium with chondroitin sulfate

A. Barkleit, M. Patzschke, K. Heim, D. G. Seidler[1]

[1]Hannover Medical School, Department of Gastroenterology, Hepatology and Endocrinology, Hannover, Germany

The coordination behavior of Eu^{3+} with the polysaccharide chondroitin sulfate was investigated by luminescence and infrared spectroscopy, combined with DFT calculations. Europium is bound by carboxylate and sulfate. Both functionalities coordinate monodentately.

Chondroitin sulfates (CSs) represent highly negatively charged linear polysaccharides that belong to the family of glycosaminoglycans (GAGs). GAGs are part of proteoglycans which are major components in every mammalian tissue. They are involved in binding cations (*e.g.* sodium, potassium, and calcium) and water, and also regulating the transport of molecules through the cellular and extracellular matrix.[1] CS is composed of the disaccharide unit N-acetylgalactosamine (D-GalNAc) and D-glucuronic acid (D-GlcA) that can be sulfated, *e.g.* at the C4 and C6 of GalNAc (CS4S and CS6S).[1] The luminescence properties of the lanthanide ions like europium (Eu) allowed the study of the binding behavior of CS4S and CS6S.

EXPERIMENTAL. The behavior of the complex formation of Eu^{3+} with CS4S and CS6S was analyzed under physiological conditions (pH ~6, 0.15 M NaCl) by time-resolved laser-induced fluorescence spectroscopy (TRLFS) and infrared spectroscopy (ATR-FT-IR), supplemented by DFT optimizations of the possible structures.
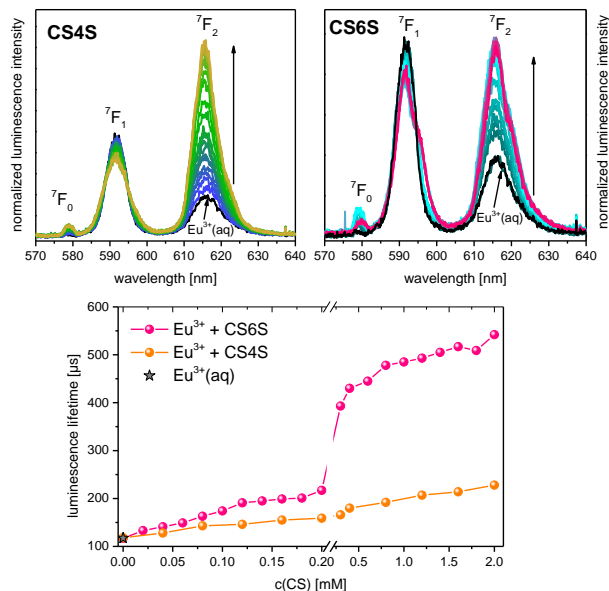
Fig. 1: Luminescence spectra and lifetimes of 10 µM Eu^{3+} dependent on CS concentration (0…2 mM) at pH 6.0 and 0.15 M NaCl.

RESULTS. TRLFS measurements showed that both CSs caused an increase in luminescence intensity of the hypersensitive $^5D_0 \rightarrow {}^7F_2$ emission band of Eu^{3+} due to complex formation, which was more pronounced for CS4S compared to CS6S (Fig. 1, top). The luminescence lifetimes (Fig. 1, bottom) increased with CS4S in a first step to ~150 µs, corresponding to ~6 H$_2$O molecules in the first coordination shell of Eu^{3+}, and in a second step up to ~200 µs (~4 remaining H$_2$O). With CS6S, the luminescence lifetime was even more prolonged up to ~500 µs (~2 remaining H$_2$O).
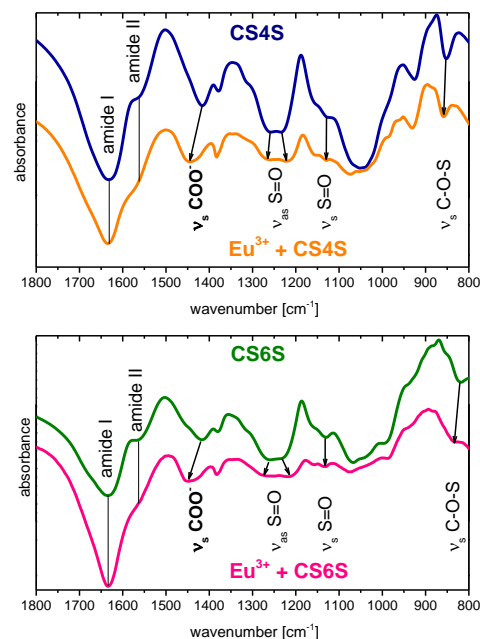
Fig. 2: FT-IR spectra of CS and CS + Eu^{3+} (1 : 1) (KBr pellets).

From FT-IR measurements, we concluded that the binding of GAGs to Eu^{3+} occurs not only *via* the carboxylate groups but also *via* the sulfate groups (Fig 2).

DFT calculations demonstrated that both functional groups, carboxylate and sulfate, coordinate the Eu^{3+} monodentately. The amide group is not involved in metal coordination (Fig. 3).
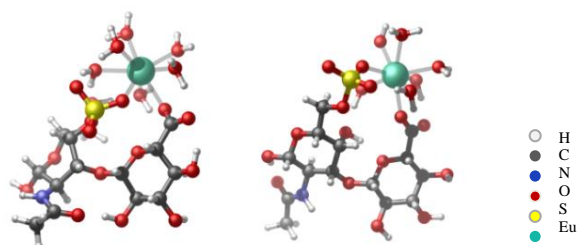
Fig. 3: DFT calculated structures of Eu^{3+} with CS4S (left) and CS6S (right) disaccharide units.

Combining DFT and TRLFS results lead to the conclusion that complexes with a Eu^{3+}/CS ratio of 1 : 1 (6 remaining H$_2$O) and 1 : 2 (4 remaining H$_2$O) are formed. Furthermore polymerization which would replace even more H$_2$O seems to occur, especially with CS6S.

[1] Afratis, N. *et al.* (2012) *FEBS J.* **279**, 1177–1197.

Complexation of Eu(III) with aqueous phosphates at elevated temperatures

N. Jordan, M. Demnitz, H. Lösch, S. Starke,[1] V. Brendler, N. Huittinen

[1]HZDR, Department of Information Services and Computing, Dresden, Germany

The influence of elevated temperature (25 to 80 °C) on the complexation of Eu(III) by phosphate was investigated by laser-induced luminescence (LIL) spectroscopy. The conditional complexation constants were extrapolated at infinite dilution (log $\beta°$) by applying the specific ion interaction theory (SIT). Finally, using the van´t Hoff equation, positive enthalpy of reaction ($\Delta_R H°$) and entropy of reaction ($\Delta_R S°$) were obtained.

The development of innovative technologies for improving recovery and recycling of critical raw materials such as Rare Earth Elements from ore bodies is of paramount interest for the worldwide economy to safeguard a steady supply of raw materials. Thermodynamic-based prediction is a cost-effective and time-saving approach, but the modeling of flowsheets representing the variety of the involved physico-chemical operations is highly dependent on robust and reliable thermodynamic data. One prominent example where relevant thermodynamic data is scarce or even completely missing is related to the complexation of lanthanides with the ubiquitous aqueous phosphate ions. This study wanted to close this critical gap of knowledge by studying the complexation of Eu with phosphate and to derive complexation constants for spectroscopically identified species (by means of LIL spectroscopy) at different ionic strength and temperature.

EXPERIMENTAL. At first, the *in situ* solution speciation of Eu(III) in the presence of phosphates was investigated with LIL ($\lambda_{ex} = 394.0$ nm) at 25 °C. The concentration of Eu(III) was 5×10^{-6} mol L^{-1}. The proton concentration was kept constant at 0.1 mol L^{-1} and the ionic strength, imposed by NaClO$_4$, was ranging from 0.6 to 3.1 mol L^{-1}. The total phosphate concentration was not exceeding a maximum of 10 % of the total ionic strength, in order to keep all activity coefficients reasonably constant. The influence of elevated temperature (25 to 80 °C) was studied at an ionic strength of 1.1 mol L^{-1}.

RESULTS. At 25 °C, the increasing phosphate concentration induced a change in the $^7F_2/^7F_1$ ratio of the Eu(III) emission spectra, indicative of complexation taking place in solution.[1] Two single components were derived during the spectral deconvolution, *i.e.* the Eu^{3+} aquo ion and the EuH$_2$PO$_4^{2+}$ complex, as well as their species distribution. To derive the conditional complexation constants at 25 °C, slope analysis was performed in the molal scale. The following equilibrium was used:

$$Eu^{3+} + H_3PO_4 \rightleftharpoons EuH_2PO_4^{2+} + H^+ \qquad (1)$$
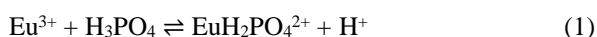
The molality of the free H$_3$PO$_4$ (aq) species was calculated with PHREEQC[2] using the Thermochimie SIT database.[3] By plotting $\log_{10}\beta - \Delta z^2$ ($\Delta z^2 = -4$) as a function of the ionic strength,[4] a linear regression provided the log $\beta°$ (intercept with the y-axis) and $-\Delta\varepsilon$ (slope) parameters (Fig. 1). The ion interaction coefficient $\varepsilon(H^+;ClO_4^-)$ was taken from Lemire *et al.*[4], while $\varepsilon(Eu^{3+};ClO_4^-)$ was assumed to be equal to $\varepsilon(Am^{3+};ClO_4^-) = 0.49 \pm 0.03$ kg mol^{-1}.[4] The complexation constant at infinite dilution log $\beta°$ and the ion interaction coefficient $\varepsilon(EuH_2PO_4^{2+};ClO_4^-)$ were found to be 0.89 ± 0.13 and 0.20 ± 0.08 kg mol^{-1}, respectively.[1]
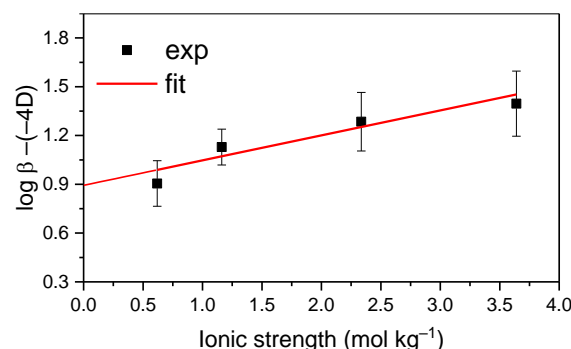
Fig. 1: Linear SIT regression plot for the EuH$_2$PO$_4^{2+}$ complex at 25 °C.
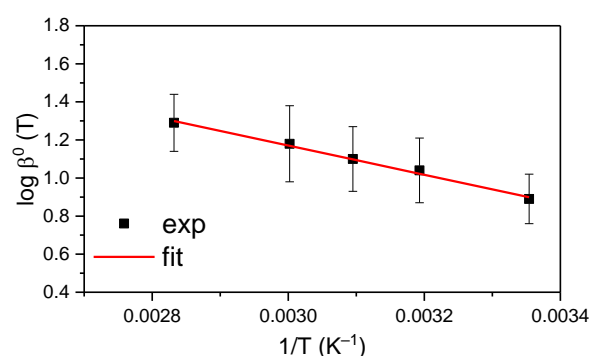
Fig. 2: Arrhenius plot for EuH$_2$PO$_4^{2+}$ complex.

Raising the temperature from 25 to 80 °C induced an increase in the conditional complexation constants. Assuming the interaction coefficients to be constant in this temperature regime, the extrapolation at infinite dilution was again performed using the SIT equation. By applying the linear van't Hoff equation (Fig. 2), the enthalpy $\Delta_R H°$ and entropy $\Delta_R S°$ (both assumed constant between 25 and 80 °C) of the reaction (1) were determined to be 14.7 kJ mol^{-1} and 66.4 J mol^{-1} K^{-1}, respectively, indicating an endothermic and entropy driven complexation reaction.

[1] Jordan, N. *et al.* (2018) *Inorg.Chem.* **57**, 7015–7024.
[2] Parkhurst, D. L. *et al.* (1999) *User's guide to PHREEQC (version 2) USGS Report 99–4259.*
[3] Giffaut, E. *et al.* (2014) *Appl. Geochem.* **49**, 225–236.
[4] Lemire, R. J. *et al.* (2013) *Chemical thermodynamics of Fe. Part 1, NEA No. 6355*, OECD, Issy-les-Moulineaux.

High-mobility band-like charge transport in a semiconducting two-dimensional metal–organic framework

R. Dong,[1] P. Han,[2] H. Arora,[3] M. Ballabio,[2] M. Karakus,[2] Z. Zhang,[1] C. Shekhar,[4] P. Adler,[4] P. S. Petkov,[5,6] A. Erbe,[3] S. C. B. Mannsfeld,[1] C. Felser,[4] T. Heine,[1,3,5] M. Bonn,[2] X. Feng,[1] E. Cánovas[2,7]

[1]Center for Advancing Electronics Dresden & Department of Chemistry and Food Chemistry, Technische Universität Dresden, Dresden, Germany; [2]Max Planck Institute for Polymer Research, Mainz, Germany; [3]HZDR, Institute of Resource Ecology, Campus Leipzig, Germany; [4]Max Planck Institute for Chemical Physics of Solids, Dresden, Germany; [5]Universität Leipzig, Wilhelm-Ostwald-Institute for Physical and Theoretical Chemistry, Leipzig, Germany; [6]University of Sofia, Faculty of Chemistry and Pharmacy, Sofia, Bulgaria; [7]Instituto Madrileño de Estudios Avanzados en Nanociencia (IMDEA Nanociencia), Madrid, Spain.

Metal–organic frameworks (MOFs) are hybrid materials based on crystalline coordination polymers that consist of metal ions connected by organic ligands. In addition to the traditional applications in gas storage and separation or catalysis, the long-range crystalline order in MOFs, as well as the tunable coupling between the organic and inorganic constituents, has led to the recent development of electrically conductive MOFs as a new generation of electronic materials. However, to date, the nature of charge transport in the MOFs has remained elusive. Here, we demonstrate, using high-frequency terahertz photoconductivity and Hall effect measurements, Drude-type band-like transport in a semiconducting, π–d conjugated porous $Fe_3(THT)_2(NH4)_3$ (THT, 2,3,6,7,10,11-triphenylene-hexathiol) two-dimensional MOF, with high mobility. The temperature-dependent conductivity reveals that this mobility represents a lower limit for the material, as mobility is limited by impurity scattering. These results illustrate the potential for high-mobility semiconducting MOFs as active materials in thin-film optoelectronic devices.

Here, we report a study of MOF conductivity using time-resolved terahertz spectroscopy (TRTS), an all-optical, contact-free method capable of addressing the nature of charge transport. It is apparent that these 2D MOFs are highly tailorable, and hence we anticipate that their conductivity, mobility and bandgap can be controlled through the appropriate chemical design. Specifically, in-plane engineering can be pursued *via* metal substitution, modification of the functional groups and organic ligands, and even by selecting appropriate guest molecules within the pores. Out-of-plane engineering is also possible by the design of 2D van der Waals heterostructures by, for example, controlling the spacing between layers and/or the relative alignment between planes. Furthermore, controlled stacking of 2D MOF layers of dissimilar materials might allow the development of heterostructures with unique physical and chemical properties. The large degree of chemical and structural tunability for this planar (and porous) class of 2D MOF materials provides plenty of room for development in this exciting field of research.

METHODS. We synthesized 2D MOF $Fe_3(THT)_2(NH4)_3$ films by an interfacial method in which aqueous and $CHCl_3$ phases host THT and iron precursors, respectively.[1] Characterization was performed using transmission electron microscopy, time-resolved terahertz spectroscopy, powder X-ray diffraction, nitrogen-gas sorption isotherms, and X-ray photoelectron spectroscopy. Additionally, DFT simulations were performed using GGA+U approach to calculate the electronic structures.

RESULTS. TRTS provides high-frequency (0.6−1.6 THz) complex photoconductivity, which directly reflects the
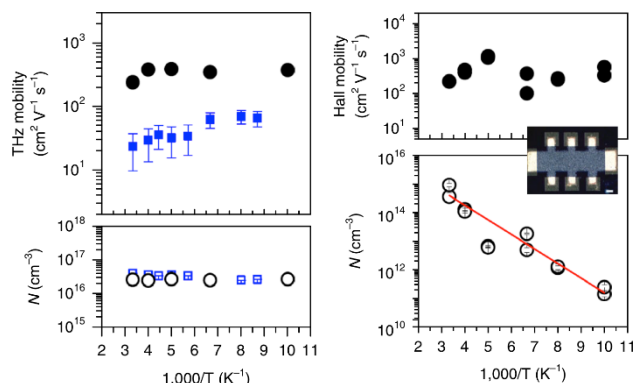
Fig. 1: THz mobility (top left) and *N* dependence (bottom left) *vs.* temperature for two samples that display different room-temperature mobilities. Error bars represent the standard error of the mean. d.c. Hall charge mobility and charge carrier density *vs.* temperature obtained from Hall effect measurements; each temperature contains two values obtained for the positive and negative magnetic fields (right). Inset: Hall bar geometry. Scale bar, 100 μm.

mechanism of charge transport. We studied a semiconducting 2D MOF film ($Fe_3(THT)_2(NH4)_3$) made of van der Waals stacked layers. We show that free-standing, porous (surface area of 526 m^2 g^{-1}) thin films of the material support band-like charge carrier transport, directly demonstrated from the observed Drude-type complex photoconductivity. A room-temperature mobility of ~220 cm^2 V^{-1} s^{-1} is estimated from TRTS, which represents, to the best of our knowledge, a record mobility in MOFs. Notably, this mobility value is independently verified using Hall Effect measurements on these 2D MOF samples. The quantitative agreement between the inferred THz and Hall mobilities demonstrates that band-like charge carrier transport is operative in the samples in both, the a.c. and d.c. limit (Fig. 1). The calculated band structure reveals semiconducting behavior with a bandgap of ~350 meV. The π electrons are fully delocalized over the conjugated plane. For the eclipsed AA stacks the band-gap increases to ~650 meV. Infrared optical transmission measurements confirmed that the electronic structure of this MOF is defined by a direct bandgap.

[1] Dong, R. *et al.* (2018) *Nat. Mater.* **17**, 1027−1032.

Simulation of mass spectra of molybdenum oxide clusters by Molecular Dynamics

M. Patzschke, V. Schulte,[1] M. Steppert[1]

[1]Leibniz Universität Hannover, Institut für Radioökologie und Strahlenschutz (IRS), Hannover, Germany

Ab initio molecular dynamics can help to understand fragmentation patterns in high resolution mass spectroscopy. Here we show a successful example to reproduce the fragmentation of molybdenum oxide clusters.

Generation IV nuclear reactors currently under research will use new fuel and will include reprocessing options of nuclear waste. One matrix material for the new fuel types is molybdenum oxide. In the reprocessing step, this will be dissolved in nitric acid. The possible formation of precipitates in all stages of fuel production and reprocessing needs to be understood. Very detailed experimental studies employing mass spectrometry have been performed at the IRS Hannover.[1] Interesting differences in the stability of certain clusters emerged from this study.

Computational chemistry in the form of molecular dynamics calculations is a powerful tool to simulate mass spectra.[2] We therefore decided to gain better understanding in the stability and structure of molybdenum oxide clusters using molecular dynamics with GFN-xTB[3] combined with higher level of theory calculation for electron attachment and ionization energies.

METHODS. Different crystal structures for molybdenum oxide are known, furthermore two different hydrates known as molybdic acid exist. These crystal structures were obtained from databases. From the structures fragments with the desired number of molybdenum atoms were cut. The dangling oxygen atoms in the generated structures were capped with hydrogen atoms to ensure neutral species.

The program package TURBOMOLE[4] was then used to optimise the fragments. This was done using the BP86 functional and an SVP basis set, and an effective core potential was used for Mo. The program package QCEIMS[2] was used to perform the actual mass spectrum simulation. This program uses the GFN-xTB approach which is a tight binding method. First an equilibrating run is performed, from this the program generates starting structures (up to 2000 for Mo_{12} clusters). For all these structures MD runs are started and the resulting fragments are stored. Once all runs are finished, the number of incidents for a certain fragment is used to calculate its relative intensity in the mass spectrum.

RESULTS. From the measured mass spectrum the mass of the molecular ion and its fragments are known and due to the excellent resolution of the available mass spectra sum formulas can be generated. However, nothing is known about the structures. To ensure that all structural possibilities were included in the calculations, we generated 64 different starting structures with cluster sizes from 4 to 12 molybdenum atoms. The pre-optimised structures showed the very high flexibility of molybdenum oxide clusters. Comparison of the energies of the pre-optimised clusters showed, that all of them are accessible at room temperature.

As an example the simulated mass spectrum for a Mo_{12} cluster can be seen in Fig. 1. The cluster selection and pre-optimisation showed, that further MD simulations are necessary to fully interpret the observed mass spectra. These simulations are currently in progress.
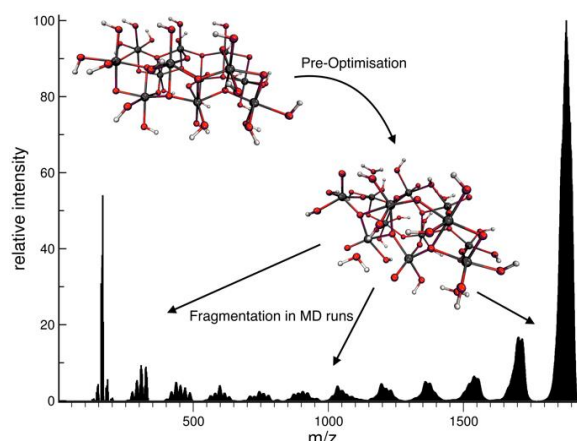
Fig. 1: Simulated mass spectrum of a Mo_{12} fragment. Also shown is the starting structure capped with hydrogen and the resulting pre-optimised structure which was used to start the MD runs.

CONCLUSIONS. The obtained results are very encouraging to use computational chemistry for simulating mass spectra. However, some features of the measured mass spectra differ from the simulated ones. In order to understand this, more MD simulations are necessary and the obtained fragments have to be analyzed further. This includes the calculation of ionization and electron attachment energies. Especially the missing Mo_6 clusters need to be explained. A possible reason is the special stability of Mo_3O_9 ring as proven earlier by computational studies.[5] Ab initio molecular dynamics studies of possible dimerization reactions are underway, and studies of the ionization properties of the dimers will finalize this work.

[1] Schulte, V. (2017) Masters Thesis, University of Hannover.
[2] Grimme, S. (2013) *Angew. Chem.* **52**, 6306–6312.
[3] Grimme, S. *et al.* (2017) *J. Chem. Theory Comput.* **13**, 1989–2009.
[4] Turbomole V7.1 (20405) 2016 available from Cosmologic at http://www.turbomole.com.
[5] Patzschke, M. *et al.* (2011) *Theo. Chem. Acc.* **129**, 70.

Peculiar thermal behavior of UO$_2$ local structure

D. B. Prieur,[1] E. Epifano,[2] K. Dardenne,[3] J. Rothe,[3] C. Hennig, A. C. Scheinost, D. R. Neuville[4]

[1]Former address: European Commission, Joint Research Centre (JRC), Karlsruhe, Germany; [2]CEA, Nuclear Energy Division, Research Department on Mining and Fuel Recycling Processes, Bagnols-sur-Cèze, France; [3]Karlsruhe Institute of Technology, Institute for Nuclear Waste Disposal, Eggenstein-Leopoldshafen, Germany; [4]Géomatériaux, Institut de Physique du Globe de Paris-CNRS, Paris, France.

In contrast to previous investigations,[1, 2] we show that the U sublattice remains locally of the fluorite type from 50 K to 1265 K, and that the decrease of the first U–O bond lengths is associated to an increase of the structural disorder.[3]

Most materials expand with temperature because of the anharmonicity of lattice vibration, and only few shrink with increasing temperature. UO$_2$ was considered for a long time to belong to the first group. This view was challenged by recent in situ synchrotron X-ray diffraction measurements, showing an unusual thermal decrease of the U–O distances.[1] This thermal shrinkage was interpreted as a consequence of the splitting of the U-O distances due to a change in the U local symmetry from *Fm−3m* to *Pa−3*.[2] Here, we use *in situ* X-ray Absorption Spectroscopy (XAS) to tackle this discrepancy, by following the local structure around U in UO$_2$ as a function of temperature from 50 K to 1300 K.

EXPERIMENTAL. XAS measurements were conducted at the ROBL beamline (ESRF) and at the INE beamline (ANKA). The XAS spectra from 50 K to 150 K were collected at ROBL using a cryostat at the U L$_{II}$ edge on UO$_2$ samples that have been previously sintered in Ar-4 % H$_2$ at 2023 K during 4 hours. The XAS measurements from RT to 1300 K were recorded at INE-BL at the U L$_{III}$ edge with a dedicated furnace on a fragment extracted from the same dense (98 %) sintered UO$_{2.00}$ pellet used at ROBL. The furnace atmosphere was held constant in Ar-4 % H$_2$ to maintain the stoichiometry.

RESULTS. While heating from 50 K to 1265 K, no strong modification of the local environment can be observed in the experimental EXAFS spectra (Fig. 1). The main visual evolution is a damping of the EXAFS oscillations, especially at high k-values, due to the increase of the thermal vibration. Each EXAFS spectrum has been fitted independently of the temperature using both *Fm−3m* and *Pa−3* structural models. In the former, the first anion shell is composed of eight equidistant oxygen atoms while in the latter the UO$_8$ polyhedron is a distorted oxygen cube with six shorter distances and two longer. For all temperatures, the best refinements are achieved using an Fm−3m structural model. The interatomic distances, the coordination numbers and the Debye-Waller factors were then derived for each temperature by fitting all the EXAFS spectra with an *Fm−3m* structure (Fig. 1). From 50 K to 298 K, no significant variation of the structural parameters has been noted. For these temperature, the UO$_8$ polyhedron is composed of one uranium atom neighboured by 8.0 (5) oxygen anions at 2.358 Å. While heating from 298 K to 1265 K, significant variations of these crystallographic parameters are observed. There is a decrease of the first U–O bond length, which is quantitatively and qualitatively in good agreement with the neutron measurements of Skinner *et al.* (Fig. 2).[1]
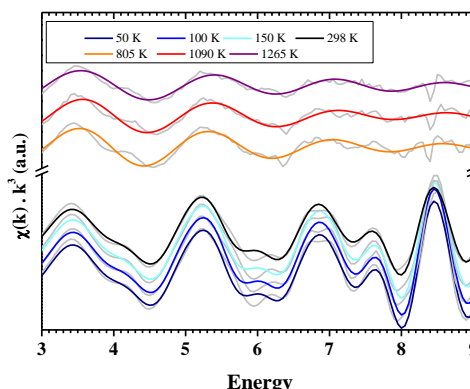
Fig. 1: Fitted and experimental k^3-weighted EXAFS spectra of UO$_{2.00}$ collected at several temperatures.
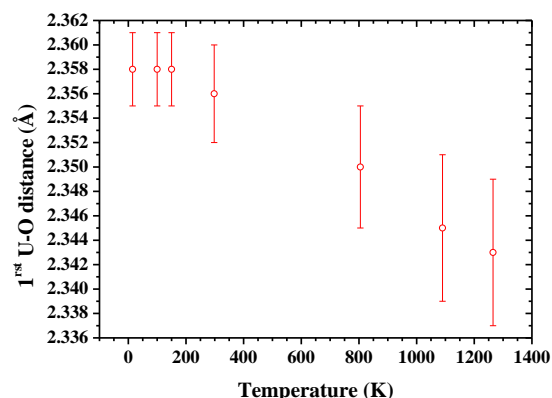
Fig. 2: Temperature dependence of the 1rst U-O fitted distances of stoichiometric UO$_2$.

[1] Skinner, L. B. *et al.* (2014) *Science* **346**, 984–987.
[2] Desgranges, L. *et al.* (2017) *Inorg. Chem.* **56**, 321–326.
[3] Prieur, D. *et al.* (2018) *Inorg. Chem.* **57**, 14890–14894.

Trends in the valence band electronic structures of mixed uranium oxides

K. O. Kvashnina, P. M. Kowalski,[1,2] S. M. Butorin,[3] G. Leinders,[4] J. Pakarinen,[4] R. Bes,[5] H. Lic,[1,2] M. Verwerft[4]

[1]Institute of Energy and Climate Research, Forschungszentrum Jülich, Jülich, Germany; [2]JARA High-Performance Computing, Aachen, Germany; [3]Department of Physics and Astronomy, Uppsala University, Uppsala, Sweden; [4]Belgian Nuclear Research Centre (SCK·CEN), Institute for Nuclear Materials Science, Mol, Belgium; [5]Department of Applied Physics, Aalto University, Aalto, Finland

We studied the valence band electronic structure of mixed uranium oxides (UO_2, U_3O_7, U_3O_8, β-UO_3) by resonant inelastic X-ray scattering (RIXS) at the U M_5 edge and by computational methods. We show here that RIXS and recorded U 5f – O 2p charge transfer excitations can be used to proof the validity of theoretical approximations.[1]

Structural, electronic and chemical properties of uranium (U) oxides vary strongly upon transformation from the fluorite-type UO_2 structures to the layered structure of the higher U oxides (U_3O_8 and above). The mechanism of the expansion of the fluorite structure is reasonably straightforward,[2–3] however the role of oxygen (O) atoms in these structural changes remains less clear. We performed state-of-art valence-band RIXS experiment at the U M_5 edge for a number of binary U oxides – UO_2, U_3O_7, U_3O_8, β-UO_3 – in order to clearly identify the mechanism causing the electronic structure modification upon oxidation of UO_2.

EXPERIMENTAL. Valence band RIXS spectra of UO_2, U_3O_7, U_3O_8 and β-UO_3 recorded at the incident photon energy set to the maximum of the U M_5 edge. The experimental total energy resolution of ~1 eV was achieved by employing a Johann-type X-ray emission spectrometer with five spherically bend Si(220) crystal analyzers with 1-m bending radius.

RESULTS. The valence band RIXS data include the elastic and inelastic scattering profiles and provide information on the energy difference between the valence band states and the unoccupied U 5f states. Figure 1 shows the valence band RIXS spectra of UO_2, U_3O_7, U_3O_8 and β-UO_3. The inelastic scattering profile at energy transfer ~ 5–10 eV, reported in Fig. 1 has been attributed to the charge transfer process from the occupied O 2p to the unoccupied U 5f states. The energy separation between elastic and inelastic scattering contributions to the spectra depends of the energy difference between the occupied O 2p states and unoccupied U 5f states. In order to reproduce the experimentally detected charge transfer excitations we made simplified calculations by inserting the calculated partial U 5f and O 2p density of states (DOS) into the Kramers-Heisenberg equation.[4] This approach provides straight forward information about the validity or accuracy of DOSs calculated using a variety of methods. It describes the correlation between occupied and unoccupied states under assumption that a hybridization between U 5f and O 2p states takes place. In that case, the energy difference between the maxima of the occupied O 2p DOS and unoccupied U 5f DOS will define the energy transfer values for the observed RIXS transitions. We calculated the partial DOSs with three approaches. First we applied the LDA + U approach assuming the standard values used in calculations for U oxides (U = 4.5 eV and J = 0.54 eV) (denoted as M1). In addition we computed the Hubbard U parameters values using the linear response method of Cococcioni and Gironcoli.[5] Here, for the calculations of the Hubbard correction we represent f orbitals for projection of occupations by the atomic orbitals (M2) and the Wannier functions (M3).[6–7]
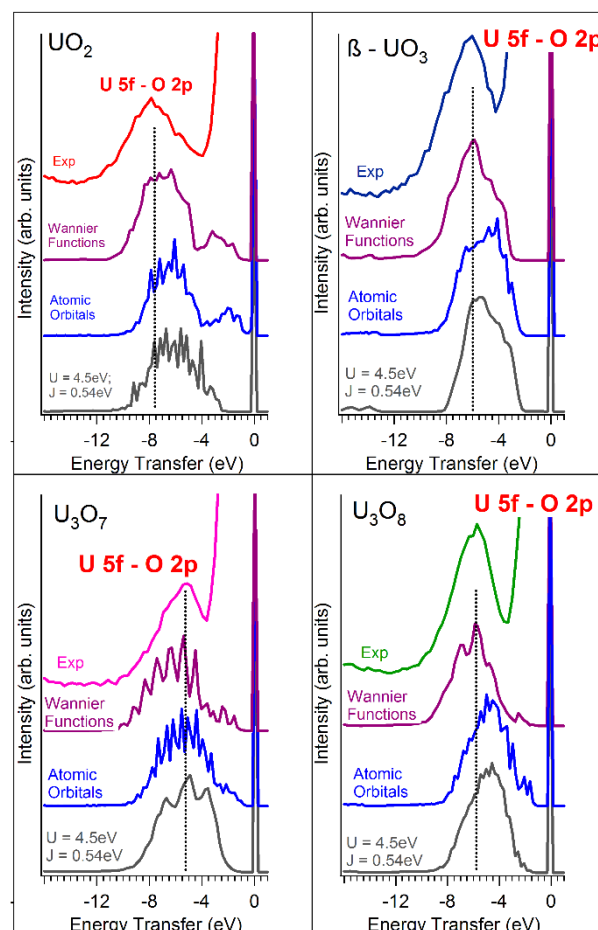
Fig. 1: Comparison of measured valence band RIXS spectra of UO_2, U_3O_7, U_3O_8 and β-UO_3 and results of calculations using a variety of methods, denoted as standard approach with U = 4.5 eV and J = 0.54 eV (M1), atomic orbitals (M2), Wannier Functions (M3).

Here the experimentally observed trend is clearly reproduced (the best match is obtained with the method M3 with Wannier functions) with the largest differences for UO_2 and the smallest for U_3O_8. These differences result from the decrease of the energy of the O p states (with respect to the Fermi level) with increasing the oxidation state (due to the stronger electrons binding) and associated decrease of the energy of the unoccupied 5f states. The later effect results from higher Hubbard U parameter values (strength of the on-site Coulomb repulsion) for higher oxidation states of U. These interesting results indicate that with such a state-of-art experimental method – valence band RIXS - one can improve the theoretical prediction of the electronic structure of actinide contained materials.

[1] Kvashnina, K. O. *et al.* (2018) *Chem. Commun.* **54**, 9757–9760.
[2] Leinders, G. *et al.* (2017) *Inorg. Chem.* **56**, 6784–6787.
[3] Leinders, G. *et al.* (2016) *Inorg. Chem.* **55**, 3915–3927.
[4] Kvashnina, K. O. *et al.* (2015) *Anal. Chem.* **87**, 8772–8780.
[5] Cococcioni, M. *et al.* (2005) *Phys. Rev. B* **71**, 035105.
[6] Beridze, G. *et al.* (2014) *J. Phys. Chem. A* **118**, 11797–11810.
[7] Beridze, G. *et al.* (2016) *Prog. Nucl. Energy* **92**, 142–146.

Powder diffraction with a 2D detector at ROBL's 6 circle diffractometer

C. Hennig, M. Feig,[1] D. Naudet, J. Kieffer,[2] A. Ikeda-Ohno, R. Gumeniuk,[1] A. C. Scheinost

[1]TU Bergakademie Freiberg, Institut für Experimentelle Physik, Freiberg, Germany; [2]European Synchrotron Radiation Facility, Grenoble, France.

This report summarizes tests at ROBL for moderate resolution X-ray powder diffraction (PXRD) with a 2D Pilatus 100k detector.

After the current refurbishment of the Rossendorf Beamline (ROBL), two diffractometers will be available: a 6-circle diffractometer (6CD) and a diffractometer (PiD) with a large 2D detector (Pilatus3 X 2M) for single crystal diffraction. In situ PXRD, with high temporal resolution *e.g.* for temperature-dependent measurements and in situ chemical reactions, will be performed on PiD with the Pilatus3 X 2M detector in fixed position. Under these conditions, the static area detector has a limited 2θ range as well as a limited resolution Δ2θ. Measurements that require a larger 2θ$_{max}$ and better resolution can be performed at the 6CD. The highest resolution in PXRD can be reached with secondary analyzer crystals.[1, 2] Such a setup has been tested at the 6CD. However, installation and alignment of analyzer crystals is a very time-consuming procedure. It is not reasonably possible within only a few hours at the beginning of an experiment. We investigated therefore alternatives, which allow the installation of equipment and alignment procedure within a moderate time frame. Here, we show the results with a small 2D detector (Pilatus 100k from Dectris) mounted on the detector arm of the 6CD at a sample-detector distance of 800 mm (Fig. 1).
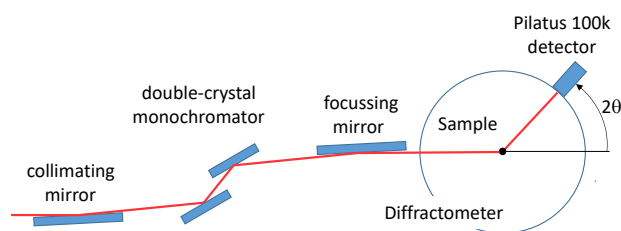
Fig. 1: Experimental setup of the Pilatus 100k detector.

The Pilatus 100k has an active area of 33.5×83.8 mm (height × width) and contains 195×487 pixels with a size of 172×172 µm^2. The detector was moved stepwise with a typical step width of 0.5°. The obtained pattern requires a radial integration along the intersections of the Debye-Scherrer cones. The integration is performed by calibrating the absolute position of each single pixel with the pyFAI software.[3] This process includes correction for small tilting errors of the detector and requires the measurement of standards (so-called calibrants). The beam center is not used as zero point, as its position is ill-defined. We use instead the orthogonal projection of the origin on the detector surface called PONI (Point Of Normal Incidence).[3] The PONI is expressed with 6 parameters: the sample-detector distance (*dist*), two orthogonal x- and y- dimensions in the detector plane *(poni1, poni2)*, and three rotation parameters around the vertical and horizontal axis *(rot1* and *rot2,* respectively*)*, and around the incoming beam *(rot3)*. An independent determination of the wavelength is necessary, due to its strong correlation with the sample-detector distance. As the detector surface of the Pilatus 100k is relatively small, the calibration is an iterative process which starts with the measurement of intersections of the Debye-Scherrer cones close to the primary beam at small 2θ by using silver behenate

$(CH_3(CH_2)_{20}COO \cdot Ag)$ as first calibrant. Subsequently, the calibration is extended to detector positions at higher 2θ values by using LaB$_6$ as second calibrant. The prerequisite at this stage is that the first used pattern comprises at least two intersections of the Debye-Scherrer cones. Iteratively, all other patterns are included in the least-squares refinement. Subsequently, the PONI parameters are used for radial integration of the 2D powder pattern. As example the extracted diffractogram of LaB$_6$ is shown in Fig. 2.
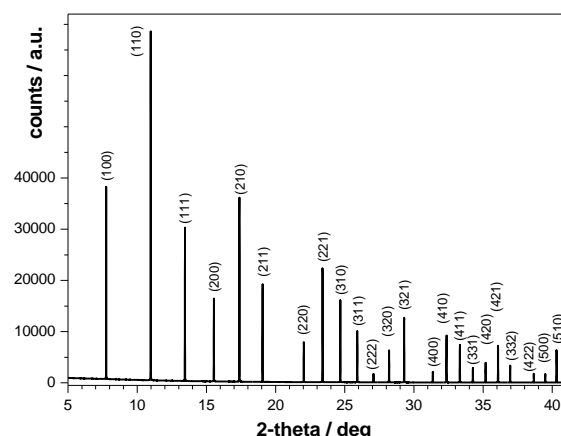
Fig. 2: Diffractogram of LaB$_6$ Pilatus 100k detector, E = 22068.5 eV, λ = 0.5618 Å, glass capillary 0.3 mm diameter, sample-detector distance 800 mm, step width 0.5°.
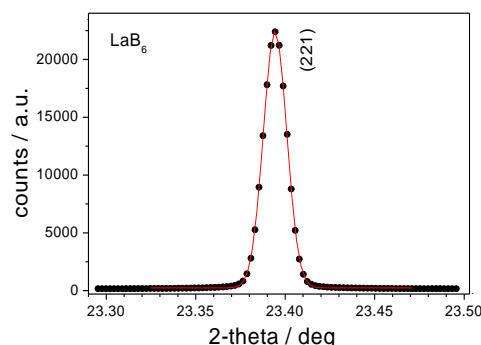
Fig. 3: Detail of Fig. 2 with reflex (221).

Figure 3 shows a detail of Fig. 2 with the (221) peak. The highest resolution Δ2θ achieved is 0.013°. This resolution is a factor 10 higher than that of a typical lab diffractometer. The measurement in Fig. 2 requires only 10 minutes for obtaining an excellent signal to noise ratio. Further increase of the resolution with 2D detectors is possible by reducing the detector pixel size.

[1] Hodeau, J. L. *et al.* (1998) *SPIE* **3448**, 353−361.
[2] Dejoie, C. *et al.* (2018) *J. Applied Cryst.* **51**, 1721−1733.
[3] Ashiotis, G. *et al.* (2015) *J. Applied Cryst.* **48**, 510−519.

Nuclear Reactor

SAFETY
RESEARCH

Electron backscatter diffraction (EBSD) and transmission Kikuchi diffraction (TKD) on steels

P. Chekhonin, A. Das, M. Roßner, C. Heintze

A practical comparison between the scanning electron microscopy (SEM) based electron diffraction techniques, EBSD and TKD, is presented using an oxide dispersion strengthened (ODS) steel alloy as reference material.

Due to their promising properties, such as enhanced radiation damage resistance and low creep at elevated temperatures, ODS steel alloys are focus of research for potential structural applications in future fission and fusion reactors. To understand and to tailor the properties of ODS steels it is essential to investigate their microstructure. Since the early 90's automated EBSD systems in SEMs facilitate local crystal orientation measurements providing surface mappings in which each point is characterized by three Euler angles.[1] This data is used to reveal microstructural features such as grains, their size and -shape, grain boundaries and many other details. Moreover, different phases can be distinguished and under certain conditions texture measurements are possible. EBSD permits the analysis of large surfaces (several mm²) thus mostly providing a statistically reliable amount of data for a general microstructural description.

However, EBSD can get problematic when the grain size is in the range of few 100 nm or below since the lateral resolution is anisotropic and perpendicular to the tilt axis of order $\approx$ 100 nm. Generally, the interaction volume can be reduced by lowering the acceleration voltage of the electron incident beam. However by doing this, imperfect surface preparation and detector issues will detriment the EBSD pattern quality. To overcome this limitation, over the recent years the TKD technique has been developed and successfully applied in a wide range of applications.[2, 3] In TKD thin samples (same as for transmission electron microscopy (TEM)) are used while in comparison to EBSD very few changes are required regarding the experimental setup. The major benefit of TKD is a significant increase in lateral resolution down to the 10 nm range.

EXPERIMENTAL. Sheets of 9 wt.-% Cr alloyed ODS steels have been produced by hot rolling, subsequent annealing and quenching. Small samples were analyzed in a Zeiss NVision 40 SEM equipped with a Bruker EBSD/TKD system on the normal direction (ND) – transverse direction (TD) plane of the sheet. The step size for EBSD and TKD mappings was set to 80 nm and 12 nm, respectively.

RESULTS. The EBSD mapping (Figs. 1 (a) and (b)) reveals a microstructure dominated by few grains greater than 1 µm (here the grain size is defined as the equivalent diameter of a circle) and many ultra-fine grains (< 1 µm). The finest grains appear to be represented by only few pixels in the mapping and therefore, a reliable detection (and accordingly the grain size determination) is not always possible. In contrast, the finest grains can be well resolved by TKD (Figs. 1 (c) and (d)). Yellow arrows in Fig. 1 (d) point out clearly detected grains at or below 100 nm grain size. Additionally, in Fig. 1 (d) some not indexed black areas (some examples are marked by white arrows) are present. A manual review and reevaluation of these spots allowed these to be indexed as $Cr_{23}C_6$ precipitates. So far it was not possible to
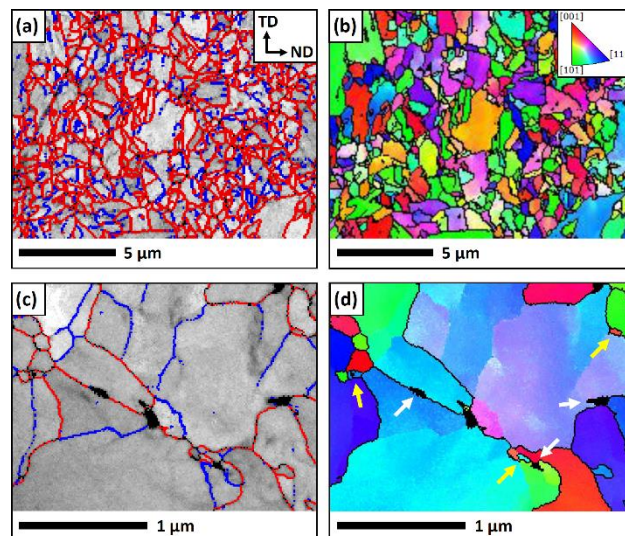
Fig. 1: Identical area of an EBSD mapping on an ODS steel (a, b). High angle grain boundaries (colored red, > 15° misorientation) and low angle grain boundaries (colored blue, 3 < misorientation ≤ 15°) (a) and the inverse pole figure mapping with respect to the surface normal direction (b) are shown. TKD mapping (c, d), color legend is in homology to (a) and (b).

detect such small grains or any $Cr_{23}C_6$ precipitates using EBSD.

Another strong advantage of TKD is the possibility of combined TKD and TEM investigations. For example, for dislocation imaging in a TEM favored grains with certain orientations can be picked by a foregoing TKD analysis. Vice versa, specific questions remaining unresolved in a TEM analysis may be answered applying TKD on the same sample region.

There are of course some drawbacks using TKD. The area of interest accessible by TKD, like in the TEM, is limited to the thinned part of the sample that is typically far below one mm². Consequently, grain statistics may be insufficient and texture measurements barely feasible.

In summary, TKD is a very valuable technique for microstructural investigations that can be performed in SEMs with an available EBSD systems without major experimental modifications.

[1] Dingley, D. (2004) *J. Microsc.* **213**, 214–224.
[2] Keller, R. R. *et al.* (2012) *J. Microsc.* **245**, 245–251.
[3] Trimby, P. W. *et al.* (2012) *Ultramicroscopy* **120**, 16–24.

Effect of thermomechanical treatments on the creep behavior of G91 steel investigated by small punch creep testing

J. Vivas,[1] E. Altstadt, M. Houska

[1]Centro Nacional de Investigaciones Metalúrgicas (CENIM), Madrid, Spain

The small punch creep test was used as a screening procedure to evaluate the creep properties of different microstructures developed in a thermomechanical simulator. Alternative microstructures were generated in a conventional ferritic-martensitic G91 steel which boosted the thermal stability at temperatures as high as 700 °C. The effect of an increased austenitization temperature and ausforming on the creep strength and ductility was studied. The improvement in creep strength was attributable to a higher number density of MX precipitates.

Materials for advanced fission and fusion reactor concepts are required to exhibit superior properties in terms of high temperature strength, radiation tolerance and coolant compatibility. 9Cr-1Mo ferritic-martensitic steels (G91) have been identified as candidate material for high temperature applications. There is a strong interest to further improve the creep strength of these steels to enable operating temperatures above 650 °C.[1] Amongst others, the intra- and intergranular distribution of nm-scaled MX particles (carbonitrides) is a source for an enhanced creep strength. Alternative thermomechanical treatments are explored to achieve optimized MX containing microstructures. The small punch creep test (SPC) is an efficient screening procedure to evaluate creep properties with small amounts of material.[2]

EXPERIMENTAL. A G91 steel was investigated in three different conditions: as received after the conventional heat treatment (AR), after heat treatment with an increased austenitization temperature of 1225 °C (HAT), after thermomechanical treatment including an increased austenitization temperature followed by ausforming at 900 °C (TMT). The chemical composition of the steels is given in Tab. 1. The different treatments are illustrated in Fig. 1.

The treatments were carried out on cylindrical samples (Ø: 8 x 10 mm) using a 805 DIL Bahr plastodilatometer. The samples were heated at 5 K s^{-1} and cooled at 50 K s^{-1}. Af-

Tab. 1: Chemical composition of investigated G91 steel (wt.-%, balance Fe).

C	Si	Mn	Cr	Mo	V	Nb	N
0.09	0.32	0.6	8.8	0.86	0.19	0.07	0.04
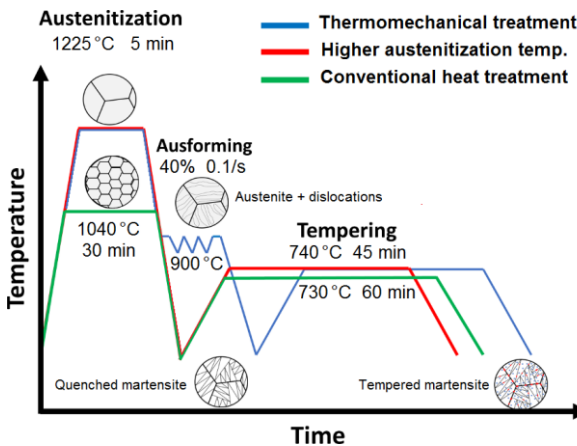
Fig. 1: Scheme of thermo-mechanical treatments applied to G91 steels.

terwards the cylinders were cut into discs (Ø: 8 × 0.5 mm) for small punch creep tests and for further preparation and microstructural characterization by means of SEM, EBSD and TEM.[3]

RESULTS. Figure 2 shows the disk deflection *vs.* time curves obtained for the three conditions studied at 700 °C with a load of 200 N. The creep strength was significantly higher due to the higher austenitization temperature (HAT) and was further increased by the ausforming. The time to rupture was 1.24 and 2.5 times higher as compared to the conventional heat treatment. However, the improved creep strength is associated with a reduction in creep ductility.

Fig. 2: Scheme of the small punch creep test and creep-displacement *vs.* time for different TMTs; green: conventional heat treatment (AR), red: increased austenitization temperature (HAT), blue: increased austenitization temperature combined with ausforming (TMT).

The spherical MX nanoprecipitates had a mean particle size of 12 ± 1 nm with a number density of $N = 7.2 \times 10^{21}$ m^{-3} for the HAT condition and 9 ± 1 nm with $N = 1.86 \times 10^{22}$ m^{-3} for the TMT condition. In both cases, the MX precipitates are significantly smaller as compared to the AR condition (size 25 ± 5 nm, $N = 8.14 \times 10^{19}$ m^{-3}). Ausforming gave rise to an increase of dislocation density from $14 \pm 0.1 \cdot 10^{14}$ m^{-2} (AR/HAT) to $(22 \pm 0.1) \times 10^{19}$ m^{-2} (TMT), which suggests the role of dislocations as potential nucleation sites for MX nanoprecipitates. It was concluded that the improved creep strength is a consequence of (*i*) the finer MX nanoprecipitates with a higher number density and (*ii*) the higher dislocation density obtained by ausforming.

[1] Zinkle, S. J. and Was, G. S. (2013) *Acta Mater.* **61**, 735–758.
[2] Vivas, J. *et al.* (2018) *Mater. Sci. Eng. A* **728**, 259–265.
[3] Vivas, J. *et al.* (2018) *Scripta Mater.* **153**, 14–18.

Why does magnetic small-angle neutron scattering correlate with irradiation hardening and embrittlement of neutron-irradiated pressure vessel steels?

A. Ulbricht, F. Bergner

Correlations between the volume fraction of neutron-induced solute atom clusters in reactor pressure vessel (RPV) steels and both irradiation hardening and embrittlement are reported. A physical rationalization of the observed correlations is provided.

EXPERIMENTAL. Neutron-irradiated RPV steels and the respective unirradiated controls were investigated by means of small-angle neutron scattering and Vickers hardness. The samples originate from several sources:

– Russian-German collaboration,
– German reactor-safety-related BMWi projects,
– IAEA coordinated research programme Optimizing of RPV Surveillance Programmes and Their Analysis,
– Collaboration within European projects PERFECT, LONGLIFE and SOTERIA.

Small-angle neutron scattering (SANS) experiments were performed at various European neutron facilities including GKSS Geesthacht, HMI/Helmholtz-Zentrum Berlin, ILL Grenoble and LLB Saclay. Samples of size $10 \times 10 \times 1$ mm (or equivalent) were placed in a saturation magnetic field in order to measure the azimuthal distribution of scattered neutrons and separate magnetic from nuclear scattering. Volume fractions of irradiation-induced nm-sized solute atom clusters were derived assuming nonmagnetic scatterers in the Fe matrix. Vickers hardness testing (HV10) was performed using the same samples. For some of the materials, absorbed energies to fracture are available from fracture tests at HZDR or at partners' institutions. Embrittlement is typically expressed in terms of the shift of the ductile-to-brittle transition temperature ΔT_{41} for a reference level of the impact energy of 41 J.

RESULTS. Scatterplots of the irradiation-induced hardness increase ΔHV10 vs. square-root of volume fraction f and the transition temperature shift ΔT_{41} vs. volume fraction are shown in Figs. 1 and 2, respectively.

Figures 1 & 2 comprise the following pieces of information:

– data points with typical experimental errors,
– coefficients of correlation R^2,
– regression lines and straight-line parameters,
– confidence intervals (solid lines in blue),
– prediction intervals (dashed lines in red).
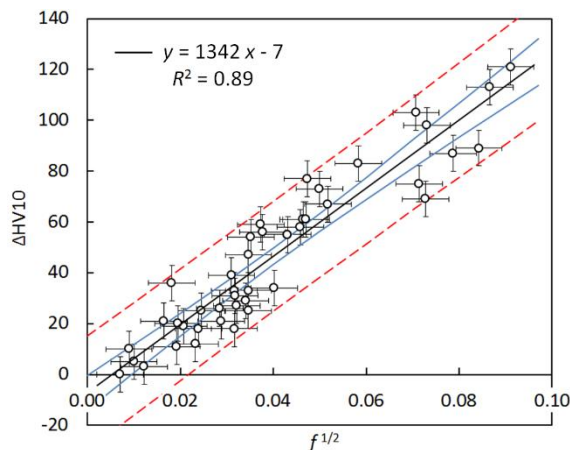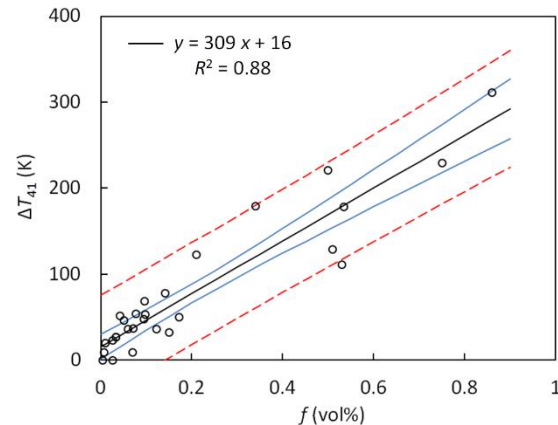
Fig. 2: Transition-temperature shift ΔT_{41} vs. volume fraction (in vol.-%) of irradiation-induced clusters for a subset of RPV steels.

The intersections of the regression lines are not significantly different from 0. The intersections can be set to 0, which yields the following modified regression equations: ΔHV10 $= 1200\, f^{1/2}$ and $\Delta T_{41} = 342\, f$ (f in vol.-%).

A rationalization of the correlation between hardening and square root of volume fraction is based on the dispersed barrier hardening model, which says that the hardness increase is proportional to $\sqrt{(Nd)}$, where N and d are number density and diameter of the irradiation-induced solute atom clusters, respectively, acting as obstacles for dislocation slip. The following additional arguments are important:

– Both the factor of proportionality (obstacle strength) and the cluster size ($d \approx 2$ nm) are similar over a wide range of RPV steels and irradiation conditions.
– The volumes probed by SANS and HV10 are macroscopic and similar to one another, the same samples were used for SANS and hardness testing.

The correlation between embrittlement in terms of ΔT_{41} and volume fraction is then a consequence of the relation between hardening and embrittlement as implied by the Ludwik-Davidenkov-Orowan hypothesis.[1] According to LDO, fracture occurs if the applied stress exceeds a critical microscopic cleavage stress, which is independent of irradiation. It is important to note that the relationship between ΔT_{41} and f is linear according to the present observations. This is at difference from reported work and requires additional consideration.[2]

[1] Ulbricht, A. *et al.* (2018) Lecture at the SOTERIA training school, Valencia, Spain.
[2] Soneda, N. *et al.* (2010) *J. ASTM Int.* **7**, 102127.

Fig. 1: Irradiation hardening ΔHV10 vs. square-root of volume fraction of irradiation-induced clusters for a set of RPV steels.

Model-based interpretation of nanoindentation hardness in ion-irradiated steels

F. Röder, C. Heintze, F. Bergner

Ion irradiation combined with nanoindentation provides a flexible and efficient tool to study basic irradiation effects on structural materials. The superposition of the irradiation effect exhibiting steep damage gradients with the indentation size effect requires modelling of the indentation process. Such kind of model was developed and successfully applied to ion-irradiated pressure vessel steels.

EXPERIMENTAL. A set of pressure vessel steels with carefully selected compositional variations was irradiated with 5 MeV Fe^{2+} ions in order to measure the nanoindentation hardness and to explore similarities and differences of irradiation hardening as compared to neutron-irradiated samples.[1] Calculations of the damage profiles using the SRIM code are shown in Fig. 1 in units of displacements per atom (dpa).
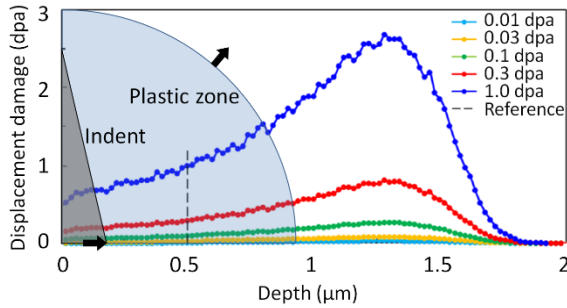
Fig. 1: Damage profiles representative of the applied ion irradiations superimposed with typical extensions of the pyramidal indenter and the plastic zone (assumed to be a half sphere).

Nanoindentation was performed using an ASMEC/Zwick nanomechanical tester equipped with a Berkovich tip. Typical dimensions of the indent and the plastic zone are indicated in Fig. 1 (indentation from left to right). Only the upper halves of indenter and plastic zone are shown.

RESULTS. In order to assign a hardness value to a value of displacement damage, we have to take into account that the measured indentation hardness represents an average over the plastic zone, which in turn covers material that was exposed to depth-dependent levels of displacement damage. The hardness H_0 as function of fluence Φ is assumed to follow a power law.

$$H_0(z) = H_S + \alpha[\Phi(z)]^n \qquad (1)$$

H_S is the substrate hardness, α and n are parameters. z is the coordinate in depth direction, $z = 0$ at the sample surface. The plastic zone is approximated as a half sphere to allow the local hardness to be integrated analytically.

$$\langle H_0 \rangle (h_c) = \frac{3}{2R(h_c)} \times \int_0^{R(h_c)} \left\{ 1 - \frac{z^2}{[R(h_c)]^2} \right\} H_0(z)\,\mathrm{d}z \quad (2)$$

Here, h_c is the contact depth of the indentation and R is the radius of the half sphere. $\langle \cdot \rangle$ denotes the spatial average over the plastic zone. Finally, we have to take into account that, in the considered depth range, the indentation hardness is subject to a size effect expressed by the Nix-Gao relation of strain-gradient plasticity.

$$H_{IT}(h_c) = \langle H_0 \rangle (h_c) \sqrt{1 + \frac{h^*}{h_c}} \qquad (3)$$

H_{IT} is the measured indentation hardness as function of contact depth and h^* is a characteristic length. Eqs. (1) to (3) have been fitted to the experimental data using a non-linear least-squares fitting routine to determine the model parameters and calculate the local hardness as function of depth. A comparison of the measured data with the fitted model is shown in Fig. 2.
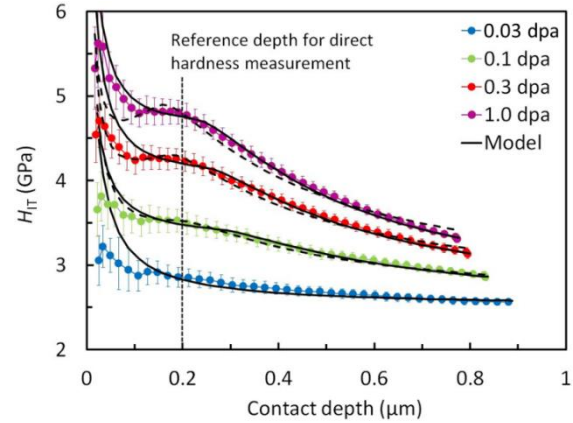
Fig. 2: Measured depth-dependent indentation hardness and comparison with the fitted half-sphere model.

The comparison clearly provides a rationalization of the observed changes of slope in the measured H_{IT} vs. h_c curves. Indeed, the changes of slope are a consequence of the superposition of the indentation size effect and the irradiation effect. Finally, the model allows the local hardness to be recovered as function of displacement damage, which forms a basis to compare different materials, to extract compositional effects and to contrast ion irradiation with neutron irradiation effects. We have found that compositional effects (*e.g.* Cu, P) on ion-induced hardening exhibit pronounced differences from the case of neutron-induced hardening.[1, 2] While ion irradiations improve our understanding of the irradiation behavior of materials, they are not suitable to replace neutron irradiations in the case of reactor pressure vessel steels.

[1] Röder, F. *et al.* (2018) *Phil. Mag.* **98**, 911–933.
[2] Pecko, S. *et al.* (2018) *Nucl. Instr. Meth. Phys. Res.* **415**, 1–8.

How can a helium-ion microscope be used to study helium-induced damage in steels?

F. Bergner, G. Hlawacek,[1] C. Heintze

[1]HZDR, Institute of Ion Beam Physics and Materials Research, Dresden, Germany

The helium-ion microscope (HIM) combines the capabilities to perform laterally modulated low-energy high-flux He-ion irradiations and ion-based imaging. This paves the way to study He-induced damage processes such as blistering and hardening/embrittlement. Application of HIM combined with nanoindentation to compare the irradiation resistance of steels is reported for the first time.[1]

EXPERIMENTAL. Samples of the ferritic/martensitic reduced-activation 9 %Cr steel Eurofer 97 and its oxide-dispersion strengthened (ODS) variant ODS Eurofer were mechanically polished and exposed to 40 keV He-ion irradiation in a Carl Zeiss ORION NanoFab system (called HIM in short). In the first set of experiments, areas of 2.5×2.5 µm were irradiated in scanning mode up to a total fluence of 2×10^{18} He ions/cm^2 and, simultaneously, image sequences were grabbed using the imaging mode of the HIM. In the second set of experiments, areas of 5×5 µm were irradiated up to different fluences from 10^{14} to 10^{17} He ions/cm^2 followed by ex-situ nanoindentation of 2 mN load using an ASMEC/Zwick nanomechanical tester equipped with a Berkovich tip.

RESULTS. Snapshots of the video sequences displaying the materials' reactions on advancing He-ion irradiation are shown in Fig. 1. The snapshots indicate He-induced blistering starting between 5×10^{17} and 1×10^{18} ions/cm^2. No significant differences between Eurofer 97 and ODS Eurofer were resolved.

| 1e17 | 5e17 | 1e18 | 1.5e18 | 2e18 |
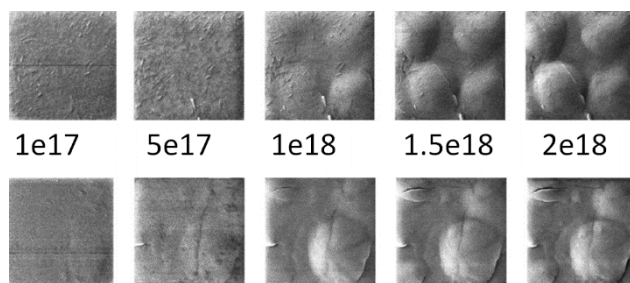
Fig. 1: Snapshots at advancing He-ion irradiation of Eurofer 97 (upper raw) and ODS Eurofer (lower raw). Inserted figures indicate the fluence in ions/cm^2.

As for the second set of experiments, an array of nano-indentations in Eurofer 97 covering both unirradiated areas and a square area (marked in red color) irradiated up to 1×10^{17} ions/cm^2 is shown in Fig. 2. It is clearly visible that the impressions left in the irradiated area are smaller than the impressions in the unirradiated material. This is indicative of higher hardness. The indentation hardness was measured and plotted as a function of fluence, see Fig. 3. We have observed that both Eurofer 97 and ODS Eurofer exhibit significant He-induced hardening at fluences $> 10^{16}$ ions/cm^2. Hardening for Eurofer 97 tends to start at lower fluence and to reach higher levels.

Using the flexible capabilities of He-ion-irradiation in a HIM, we have shown that Eurofer 97 and ODS Eurofer exhibit similar characteristics with respect to blistering. ODS Eurofer is more resistant against He-induced hardening and embrittlement. Hardening is due to nm-sized He bubbles in the matrix. The merit of ODS Eurofer is due to the addition
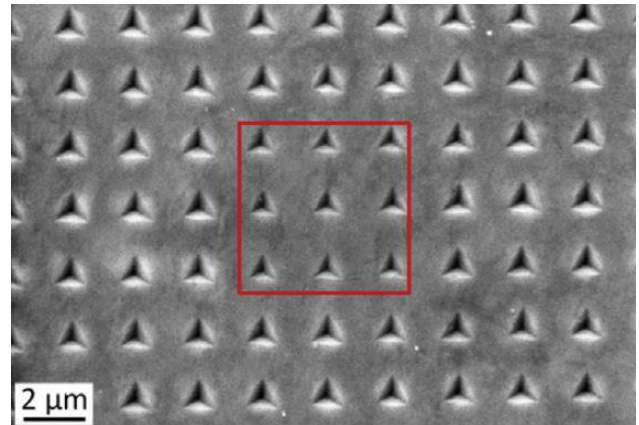
Fig. 2: Snapshots at advancing He-ion irradiation of Eurofer 97 (upper raw) and ODS Eurofer (lower raw). Inserted figures indicate the fluence in ions/cm^2.
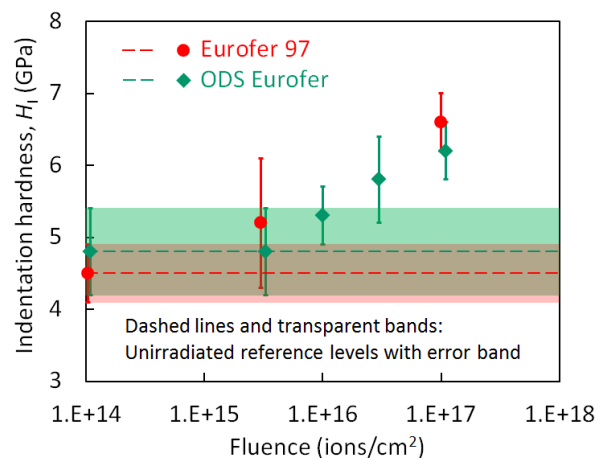
Fig. 3: Indentation hardness as function of ion fluence. Symbols indicate irradiated conditions. Dashed lines and bands indicate mean value and error range, respectively, for the unirradiated reference.

of a fine dispersion of oxide nanoparticles, which are able to trap He atoms and, therefore, to reduce both the number of He bubbles in the metal matrix and the concentration of He in grain boundaries.

[1] Bergner, F. *et al.* (2018) *J. Nucl. Mater.* **505**, 267–275.

Verification of ATHLET against TRACE on Superphénix (SPX) start-up tests

V. A. Di Nora, E. Fridman, K. Mikituyk[1,2]

[1]École Polytechnique Fédérale de Lausanne, Lausanne, Switzerland; [2]Paul Scherrer Institut, Villigen, Switzerland

The thermal-hydraulics (TH) code ATHLET has been upgraded to be capable of sodium flow modeling. Its new extension is under verification and validation phase. The presented study aimed to demonstrate ATHLET capability in Sodium-cooled Fast Reactor (SFR) transient predictions, through the comparison against TRACE TH code, this last being more established and tested for SFR applications. Calculations were performed on a set of start-up tests on Superphénix (SPX) SFR, and compared with TRACE results, which were used as a reference. It has been shown that given a specific set of reactivity coefficients, ATHLET and TRACE give consistent and close results.

The applicability of DYN3D to safety analyses of SFR systems requires a coupling with a TH code capable of sodium flow modeling.[1] ATHLET has been considered for this purpose. However, since ATHLET has only recently been upgraded with thermal-physical properties of liquid sodium, its new extension has to be verified and validated. The present work contributes to the verification efforts.

VERIFICATION APPROACH. The extended version of ATHLET was applied to the transient analyses of a set of start-up tests conducted at the SPX. The specifications of the corresponding tests such as the simplified SPX reactor core models and a set of reactivity coefficients, were adopted from a dedicated study performed at PSI and KIT.[2] The reactivity effects accounted for by a point kinetics model included fuel Doppler Effect and thermal expansion effects of cladding, sodium, fuel, diagrid, control rods (CRs) driveline, strongback, and reactor vessel. Employing an identical set of reactivity coefficients, ATHLET reactivity feedback components and power evolution trends were benchmarked against the respective reference solutions provided by TRACE.

SELECTED TEST, DESCRIPTION AND RESULTS. An overview on the start-up tests is provided in Tab. 1, in which are shown, their short description, initial power level at which they were conducted, and the respective (most differing) absolute relative error found from the power trends codes comparison. To summarize the results, it has been chosen of presenting in the following only the test which gave the most diverging result, *i.e.* "10 % primary flow reduction at 1415 MW$_{th}$". Figure 1 shows the power evolution comparison of the test. At 440 s, the primary flow is reduced of 10 %, and inlet coolant temperature decreases. Core inlet temperature and inlet flow were provided as boundary conditions. As Fig. 2 shows, the out-of-core feedback effects
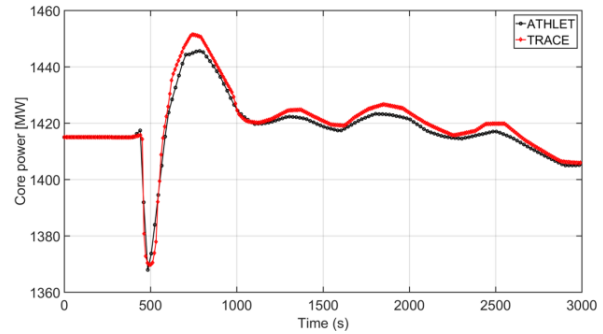
Fig. 1: 10 % primary mass flow reduction test, power evolution.
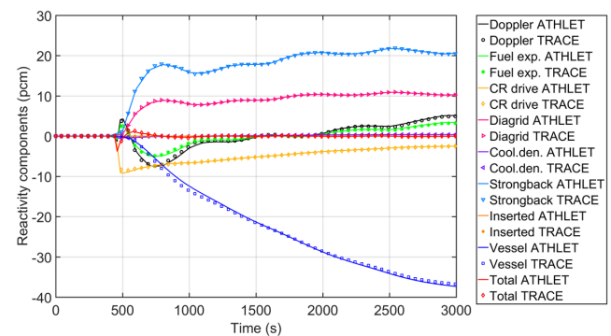
Fig. 2: 10 % primary mass flow reduction, reactivity feedback.

are dominating. They are driven by inlet coolant temperature (in case of vessel, diagrid and strongback) and outlet coolant temperature (in case of CR-driveline). As the outlet coolant temperature increases, caused by the flow reduction, the CR-driveline thermally expands and slightly inserts CRs into the core. This can be noted from the negative reactivity inserted represented in yellow in Fig. 2. While the transient evolves, the inlet coolant temperature decrease causes the contraction of diagrid and strongback. As a consequence, CRs are slightly withdrawn from the core. In this test, vessel contraction has instead the opposite effect as it leads to CRs insertion. Despite these were the most diverging results, the feedback components profiles computed by the two codes basically overlap, and only an irrelevant absolute relative error of 0.41 % has been noted.

CONCLUSION. For all the tests, ATHLET demonstrated good prediction capabilities for power, and feedback components as compared to TRACE. This study demonstrated the reliability of ATHLET in simulating SFR transients and supports its applicability for the new DYN3D-ATHLET coupled system code development.

[1] Rohde, U. *et al.* (2016) *Prog. Nucl. Energy* **89**, 170−190.
[2] Mikityuk, K. *et al.* (2013) *IAEA FR2013,* 1−10.

Tab. 1: SPX start-up tests description and absolute relative error.

Test description	Power (MW$_{th}$)	Error (%)
−50 pcm reactivity insertion	692	0.16
−74 pcm stepwise reactivity insertion	1542	0.28
10 % secondary flow rate increase	632	0.20
10 % primary flow rate reduction	663	0.29
10 % primary flow rate reduction	1415	0.41

DYN3D solution of the Superphénix neutronic benchmark

E. Nikitin, E. Fridman

In the frame of the ESFR-SMART project, a new neutronic benchmark of the Superphénix core was established. In this study, the benchmark calculations were performed with the nodal code DYN3D. The homogenized cross sections were generated with Serpent. The results demonstrated a good performance of the code as they were compared to the Monte Carlo reference and measured data. This study provided an additional verification of applying Serpent-DYN3D codes sequence for Sodium Fast Reactor core calculations.

In the framework of the European Horizon-2020 ESFR-SMART project, a new benchmark is being established for validation purposes of Sodium cooled Fast Reactor (SFR) calculation tools. The benchmark is based on the start-up tests of the Superphénix core, and will consist of two parts: static neutronic and transient reactor calculations. The specifications for the former were published recently.[1]

DESCRIPTION OF THE SUPERPHÉNIX CORE. The Superphénix core contains 358 fuel subassemblies (SAs) in a 17.9 cm diagrid pitch with a total power of 2990 MW_{th}. The one meter high fissile core is filled with U-Pu mixed oxide fuel that are surrounded by 30 cm UO_2 axial blanket above and below. Radially, the fissile core is surrounded by 225 radial blanket and 294 shield SAs. The core is filled with additional 18 diluent SAs, and 21 control (CSD) and 3 dedicated shutdown (DSD) rods. A more detailed description can be found in the benchmark specification.[1]

DESCRIPTION OF THE TEST CASES. The different core configurations of the Superphénix reactor can be summarized in Tab. 1. The cases can be distinguished by the temperatures used for the material cross sections and the ones to thermally expand the structure in different regions (fissile, fertile and other). Measurements are available for the first three cases, which correspond to the cold isothermal state, hot zero power, and hot full power, respectively. The other cases are defined in order to use them for code-to-code comparison in the evaluation of Doppler Effect in different expansion states and control rod positions.

COMPUTATIONAL METHODOLGOY. The benchmark calculations were performed with a two-step approach. The homogenized few-group cross sections (XSs) were generated with the Serpent code using the in-house developed methodology. This is based on using lattice level models and applying the Superhomogenization (SPH) equivalence technique.[2, 3] By using these XS, the full core calculations were performed with the nodal code DYN3D.

RESULTS. The DYN3D solutions were compared with the published Serpent results and measurements.[1] Table 2 presents the reactivity values for all core configurations. DYN3D is in a very good agreement with Serpent, as the difference does not exceed ~100 pcm. As compared to the experimental data, DYN3D underestimated the reactivity for all three cases by around 230–350 pcm.

Tab. 2: Comparison of the core reactivity (values are given in pcm).

Case ID	Calculated		Measured	DYN3D *vs.* experiment
	Serpent [1]	DYN3D		
1	3538	3481	3710	−229
2	2805	2733	3079	−346
3	1867	1777	2090	−313
4	4180	4138	–	–
5	4073	4026	–	–
6	3920	3867	–	–
7	2963	2892	–	–
8	2423	2345	–	–
9	3043	2973	–	–
10	817	743	–	–
11	−107	−190	–	–
12	−258	−343	–	–
13	−5131	−5225	–	–

CONCLUSIONS. The good performance of DYN3D demonstrated an additional verification of the nodal diffusion solver and the XS generation methodology that are currently applied for nodal calculation of SFR cores at HZDR. Furthermore, the produced XS will be applied later in the transient calculations of Superphénix start-up tests.

[1] Ponomarev, A. *et al.* (2018) in: *Physor 2018.* **SS5**, 14.
[2] Nikitin, E. *et al.* (2015) *Ann. Nucl. Energy* **75**, 492–497.
[3] Nikitin, E. *et al.* (2015) *Ann. Nucl. Energy* **85**, 544–551.

Tab. 1: Description of the test cases.

Case ID	CSD insertion (cm)	Temperature for XS / geometry (K)		
		Fissile	**Fertile**	**Other**
1	0	453/453	453/453	453/453
2	0	673/673	673/673	673/673
3	0	1500/1500	900/900	673/673
4	0	300/300	300/300	300/300
5	0	300/453	300/453	300/453
6	0	300/673	300/673	300/673
7	0	600/673	600/673	600/673
8	0	900/673	900/673	900/673
9	0	600/673	600/673	300/673
10	40	300/673	300/673	300/673
11	40	600/673	600/673	600/673
12	40	673/673	673/673	673/673
13	100	453/453	453/453	453/453

The HEXNEM3 nodal flux expansion method in the code DYN3D

Y. Bilodid, U. Grundmann,[1] S. Kliem

[1]Physikalische Berechnungen, Dresden, Germany

This contribution describes the derivation of the nodal flux expansion method HEXNEM3, its implementation into the nodal diffusion code DYN3D and the corresponding testing versus benchmarks. As in the earlier versions of expansion method HEXNEM1 and HEXNEM2, the neutron flux in a hexagonal node is expanded into superposition of orthogonal polynomials and exponential functions. The main difference of the HEXNEM3 method is the additional use of tangentially weighted exponential functions and the coupling of neighboring nodes by tangentially weighted fluxes and currents on node surfaces. The test results demonstrate good agreement with reference solutions and improvement of method accuracy in comparison with HEXNEM1 and HEXNEM2.

METHOD. The reactor dynamics code DYN3D is used to simulate static and transient behavior of nuclear reactor cores with hexagonal or rectangular fuel assemblies.[1] The multi-group neutron diffusion is solved utilizing nodal expansion methods specific for geometry discretization type: rectangular, hexagonal, or trigonal.[2–5] The three-dimensional neutron diffusion equation is divided by transverse leakage integration into a two-dimensional equation in the radial plane and a one-dimensional equation in the axial direction.
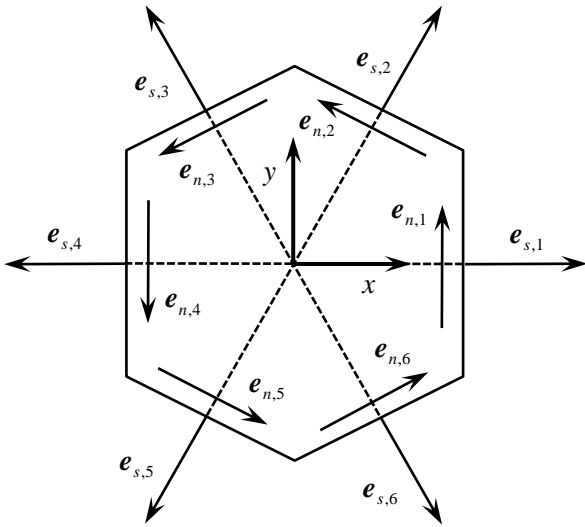
Fig. 1: Hexagon with directional vectors.

The two-dimensional diffusion equation is solved applying expansion of the neutron flux of each energy group by polynomials up to the 2nd order, exponential functions and tangential weighted exponential functions directed to the six faces of the hexagon (Fig. 1):[4]

$$\Phi(\boldsymbol{r}) = \sum_{k=0}^{5} c_k h_k^r(x,y) + \sum_{k=1}^{6} a_{s,k} e^{B e_{s,k} \boldsymbol{r}} +$$
$$\sum_{k=1}^{6} a_{m,k} (\boldsymbol{e_{n,k}} \boldsymbol{r}) e^{B \boldsymbol{e_{n,k}} \boldsymbol{r}} \qquad (1)$$

where $h_k^r(x,y)$ are orthogonal polynomials, buckling B is given by a material properties and unknown coefficients c_k, $a_{s,k}$ and $a_{m,k}$ are obtained in an iterative solution.

Tab. 1: Deviations of DYN3D results from the reference values.

Method	Δk_{eff} / pcm	$\Delta P_{assembly}$ / %	
		max	RMS
3D AER-FCM101 benchmark			
HEXNEM1	41	2.0	1.3
HEXNEM2	13	0.6	0.4
HEXNEM3	7	0.4	0.2
2D VVER-1000 type problem			
HEXNEM1	59	3.0	2.0
HEXNEM2	6	0.9	0.5
HEXNEM3	9	0.2	0.1
3D X2 benchmark critical state			
HEXNEM1	172	3.7	2.3
HEXNEM2	77	1.2	0.7
HEXNEM3	77	1.2	0.7

VERIFICATION. A set of benchmark problems was solved to verify and validate the proposed HEXNEM3 method and its implementation into the code DYN3D. Table 1 demonstrates some selected results.

In all test cases both HEXNEM2 and HEXNEM3 show much more accurate results than HEXNEM1. In the numerical benchmarks AER-FCM101 and 2D VVER-1000 type,[6, 7] where the reference solution is obtained by a fine-mesh finite difference diffusion using benchmark-defined cross sections, HEXNEM3 demonstrates notably better accuracy than HEXNEM2. The maximum error in relative assembly power is 0.4 % and in nodal power 1.3 %, which could be described as perfect agreement with reference. On the other hand, in the X2 benchmark[8] cases HEXNEM3 results are very similar to HEXNEM2. The reference solution of the X2 problem is obtained by the continuous energy Monte Carlo code Serpent 2,[9] so the deviations of HEXNEM2 and HEXNEM3 from reference are dominated by homogenization and energy discretization errors. The maximum error in relative assembly power is 1.2 % and in nodal power 2.4 %, which is a very good agreement with the reference.

[1] Rohde, U. *et al.* (2016) *Prog. Nucl. Energy* **89**, 170–190.
[2] Beckert, C. *et al.* (2008) *Ann. Nucl. Energy* **35**, 75–86.
[3] Grundmann, U. *et al.* (1999) *Nucl. Sci. Eng.* **133**, 201–212.
[4] Bilodid, Y. *et al.* (2018) *Ann. Nucl. Energy* **116**, 187–194.
[5] Duerigen, S. *et al.* (2012) *in Proc. of PHYSOR–2012*, 4094–4106.
[6] "AER benchmark book" (2017) http://aerbench.kfki.hu/.
[7] Chao, Y. A. *et al.* (1995) *Nucl. Sci. Eng.* **121**, 210–225.
[8] Loetsch, T. *et al.* (2009) *in Proc. of AER–2009*, 53–109.
[9] Leppänen, J. *et al.* (2013) *Ann. Nucl. Energy* **82**, 142–150.

Investigations on the coolant mixing in the RPV of a generic German PWR KONVOI reactor during a Main Steam Line Break scenario

E. Diaz Pescador,[1] F. Schäfer

[1]Technische Universität Dresden, Dresden, Germany

In the framework of the international OECD-PKL2 project, a main steam line break (MSLB) was investigated at the German PKL test facility during the test G3.1, in order to study the thermal-hydraulic evolution in the reactor coolant system (RCS) of a pressurized water reactor (PWR).[1] With the boundary conditions obtained from the test G3.1, a set of tests were conducted at the German ROCOM test facility to study the fluid mixing in the reactor pressure vessel (RPV).[2] With this aim, the system code ATHLET 3.1A was used to study a MSLB scenario in a generic German PWR KONVOI reactor, superposed with the boundary conditions from the test G3.1.

A main steam line break (MSLB) is characterized by a rapid overcooling through the affected steam generator U-tubes, produced by steam generator boil-off. Moreover, the overcooling is produced asymmetrically in the RCS, and an accurate prediction of the cold water arrival and further fluid mixing phenomena in the RPV is needed in order to determine the fluid temperature distribution at the core inlet, and the subsequent dynamic core response dependent on the coolant temperature reduction.

MODEL. The primary circuit of the generic KONVOI reactor is modelled in ATHLET 3.1A by means of four independent main coolant loops, each one connected to one steam generator, in turn connected to its corresponding main steam line. As far as the RPV is concerned, it is modelled by means of a hydraulic multichannel approach, where the vessel is subdivided into 8 sectors according to the 8 loop nozzles. In the radial direction, the RPV is subdivided into central channel, first and second ring. All the channels are connected to each other by means of cross-connection objects or single junction pipes altogether giving rise to a pseudo 3D-cylindrical mesh. The RPV nodalization is depicted in Fig. 1 (left). The fluid mixing in the RPV has been simulated and investigated by means of ATHLET 3.1A, with a set of two-fluid six-balance equations including a 3D-momentum equation, with a convective term implemented in Cartesian and cylindrical coordinates.

RESULTS. The results obtained in the simulation, show how after the arrival of the cold water streak to RPV inlet nozzle 1, it moves downwards in the axial direction of the downcomer right below cold leg inlet nozzle 1, led by the buoyancy-driven effects of the incoming flow.

The cold water streak spreads azimuthally in the downcomer upper-ring in a 90° sector and moves downwards, arriving shortly after to the lower plenum. With increasing time, the ambient coolant in the lower plenum is replaced by overcooled water and from then on, overcooled water starts accumulating in the downcomer bottom region. Eventually, overcooled water spreads across the whole downcomer region. The fluid temperature distribution in the downcomer is depicted in Fig. 1 (right). The arrival of the cold water stream to the lower plenum takes place in a sector of 90° in the periphery, right below cold leg inlet nozzle 1.

In the core and lower plenum regions the replacement of ambient coolant by overcooled water takes place from the
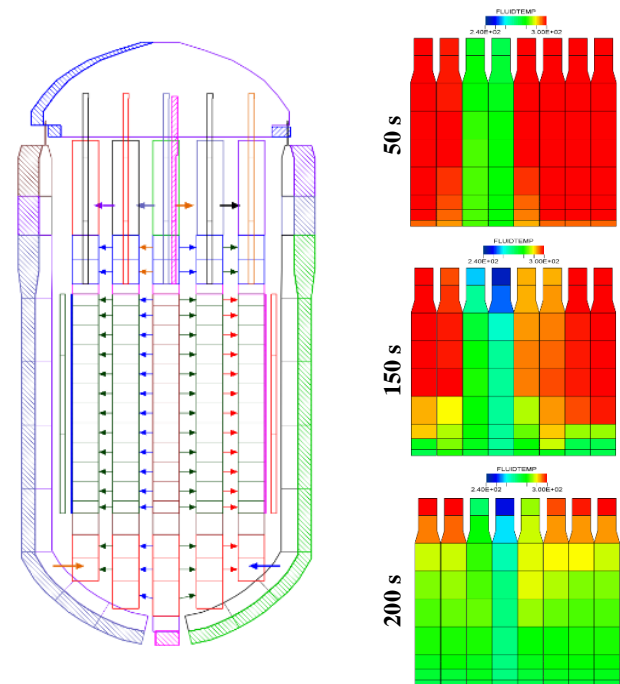
Fig. 1: RPV nodalization (left), fluid temperature distribution in the downcomer (right).

periphery towards the center. The maximum observed temperature decrease at the core inlet plane accounts for 28 K, value significantly lower to the results obtained in the test ROCOM T1.1.[2] This fact points out an overprediction of the coolant mixing in the RPV, especially in the downcomer region. In order to reduce the aforementioned fluid mixing overprediction by the code, a finer RPV nodalization has been developed and ATHLET 3.1A is to be coupled with the core dynamics code DYN3D to investigate the dynamic core response against the arrival of the cold water stream. All in all, the obtained results are in good agreement with the experimental data from the ROCOM tests.[2]

[1] AREVA NP (2012) *Final Report of the OECD–PKL2 Project (PKL III G)*, AREVA NP GmbH, December 2012.
[2] Kliem, S. *et al.* (2012) *OECD PKL2 Project – Final Report on the ROCOM tests*, Institute Report HZDR\FWO\2012\03, July 2012.

Code-to-code comparison between ATHLET-CD and MELCOR for SBLOCA severe accident scenario in generic German PWR

M. Jobst, F. Kretzschmar,[1] P. Wilhelm

[1]Karlsruhe Institute of Technology, Institute for Neutron Physics and Reactor Technology, Karlsruhe, Germany

The evolution of a hypothetic Small-Break Loss-Of-Coolant (SBLOCA) severe accident scenario for a generic German PWR is investigated by means of the two severe accident computer codes ATHLET-CD and MELCOR. The simulation results derived from both codes are compared and possible reasons for deviations between the results are analyzed. Furthermore, injection by mobile equipment to the primary circuit as an alternative Accident Management Measure (AMM) is assessed.

Severe accident codes, such as ATHLET-CD or MELCOR, are used for assessment of nuclear power plant accidents with core degradation. The assessment of the results obtained by these codes is a long ongoing process, as many physical phenomena are involved and changes in the geometry are observed (*e.g.* melting and relocation of material). Benchmarking code results of plant applications obtained by different codes is a major task to carry out such code assessment.[1] This implies the modelling of selected scenarios with different codes, whereby the geometry and the selected initial and boundary conditions must correspond as closely as possible. Such extensive code-to-code comparison can also help to identify inadequacies of modelling and of the input data set prepared by the user.[1]

The current work was intended to perform a verification of results obtained by ATHLET-CD calculations for a SBLOCA severe accident scenario (SBLOCA with additional malfunction of safety systems which lead to core degradation).[2] Therefore, a code-to-code comparison between ATHLET-CD and MELCOR was performed.[3] The work was a collaboration between HZDR (ATHLET-CD calculations) and KIT (MELCOR calculations).

PROCEDURE. In the framework of the WASA-BOSS project, an ATHLET-CD (version 3.0A) input dataset was developed at HZDR for a generic German Pressurized Water Reactor (PWR, Konvoi-like design). Based on this input dataset, KIT prepared an equivalent dataset for MELCOR version 1.8.6. With both codes, an SBLOCA scenario with 50 cm^2 leak in the cold leg of the pressurizer loop has been calculated. It was assumed that after the depletion of the flooding pools, the switch to sump injection fails and from that moment on, no further coolant is injected by the emergency core cooling system to the primary circuit. This leads to core degradation, relocation of molten/degraded core to the lower head and RPV damage.

The results obtained from both codes have been compared. At the initial stage, several major deviations have been identified and discussed. Consequently, both input datasets have been improved iteratively. The status presented here has been reached after five iteration steps.

As an alternative AMM, currently not implemented in Konvoi, injection of borated water by a mobile pump system directly to the primary circuit has been investigated for the SBLOCA scenario by means of ATHLET-CD simulations.[2] In order to verify these results, the same AMM has been applied also in the MELCOR simulations.
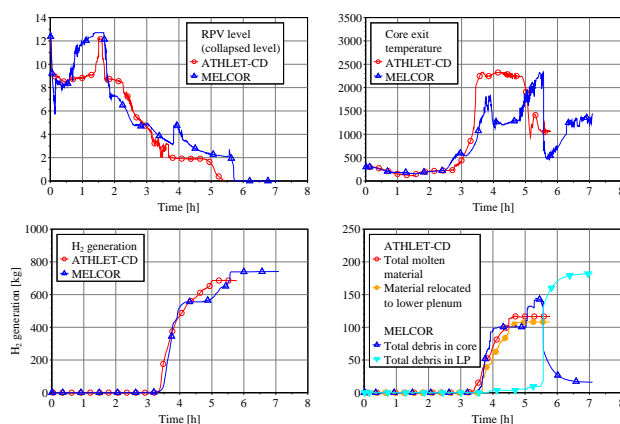
Fig. 1: Evolution of selected parameters for the SBLOCA severe accident scenario (RPV level, CET, H$_2$ generation, molten/debris material).

RESULTS. For SBLOCA without mobile pump injection, the results obtained by both codes agree till the beginning of core degradation (≈ 3 h). This is shown by Fig. 1 for the RPV level and Core Exit Temperature (CET). Even later, during core heat-up, cladding oxidation and degradation/melting of the core, the main parameters (released H$_2$ and melt mass) show a similar trend. However, the relocation to the Lower Head (LH) is modelled differently by both codes. MELCOR provides a model of the core support plate and its failure mechanism (main relocation of molten material to LH after its failure at 1200 °C). In ATHLET-CD a simplified criterion based on the melt mass is used to initiate the relocation. As this criterion (35 t melt mass) is reached earlier, processes in the LH appear earlier in time.

Figure 2 shows results for the case with alternative AMM (start of mobile pump at CET = 400 °C). Both codes show very similar behavior of the RPV level and CET. Therefore, according to the simulation results, the injection of coolant to the primary circuit by the mobile pump system can be applied to stop the accident progression.
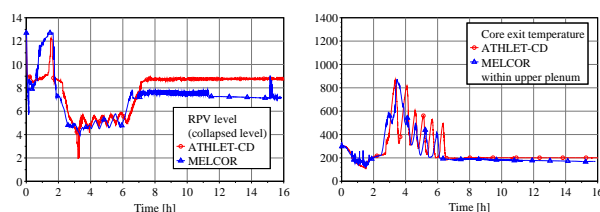
Fig. 2: Evolution of RPV level and core exit temperature for the SBLOCA accident scenario with mobile pump injection.

[1] Van Dorsselaere, J.–P. *et al.* (2012) in: *Nuclear Safety in Light Water Reactors*, p. 625–656, Academic Press, Amsterdam.
[2] Jobst, M. *et al.* (2018) *Ann. Nucl. Energy* **122**, 280–296.
[3] Jobst, M. *et al.* (2018) *NUTHOS–12*, Qingdao.

Accident management measures for PWRs

P. Wilhelm, M. Jobst

Further enhancing the nuclear safety in the accident management domain received a substantial reflection after the Fukushima accident. We have analyzed the response of the nuclear power plant during core degradation accidents, the effectiveness of applied accident management measures (AMMs) for prevention or mitigation of the core damage, and identified key timings of events to support the assessment of safety margins.

On national level AMMs for German pressurized water reactors (PWRs) were investigated in the framework of the BMBF joint research project WASA-BOSS. The focus was put on two main groups of accident scenarios: station blackout (SBO) and small-break loss-of-coolant accident (SBLOCA). On international level within the framework of the EU Horizon 2020 "In-Vessel Melt Retention Severe Accident Management Strategy for Existing and Future NPPs" (IVMR) project, the research is focused on analysis of the applicability and technical feasibility of the IVMR strategy to high power reactors.

RESULTS AMMS IN SBO AND SBLOCA. The safety analyses were performed for a generic German PWR using the severe accident code ATHLET-CD, developed by GRS.[1–4] As AMMs were considered primary side depressurization (PSD) and injection by portable equipment hypothetically directly to the reactor circuit: mobile pump injection (MPI) *via* the cold leg (CL) and respectively *via* the hot leg (HL). The simulations showed that the time until core degradation can be delayed by combination of the above-mentioned AMMs. Depending on the time of injection significant reduction of hydrogen and fission products (FPs) releases was obtained.

Figure 1 depicts selected results from the SBO analysis, regarding the hydrogen releases.[2] The simulations showed that if the MPI is initiated at latest 110 min after core exit temperature (CET) exceeded 400 °C, no release of hydrogen and FPs is predicted by the code. If the injection is through the HL side, generally higher release of hydrogen is calculated in comparison to the CL injection simulations.

In case that the pump is connected to the CL, the injected mass flow is directed through the CL and the downcomer to the lower plenum and then is distributed to all channels. Consequently, the channels are cooled more homogenously. It can be concluded that the application of the mobile equipment seems to be more efficient, if connected to the CL. Relocation of molten material to the reactor lower head is not predicted by the code in case that the MPI is initiated at latest 140 min after CET > 400 °C detection.
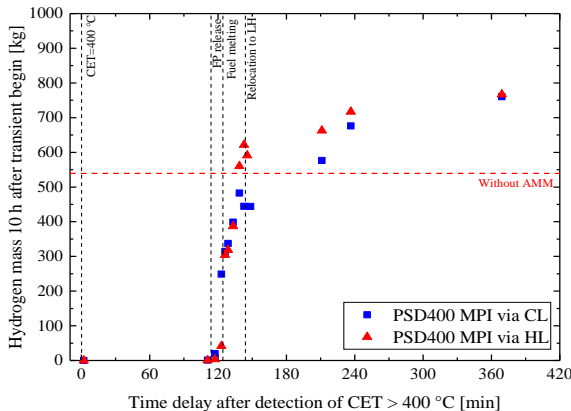
Figure 2 depicts selected results from the SBLOCA 50 cm² analysis.[3] For all simulated cases with MPI, a reduction of the FPs release is predicted. PSD is needed to prevent FPs release for the early start of injection at CET > 400 °C.
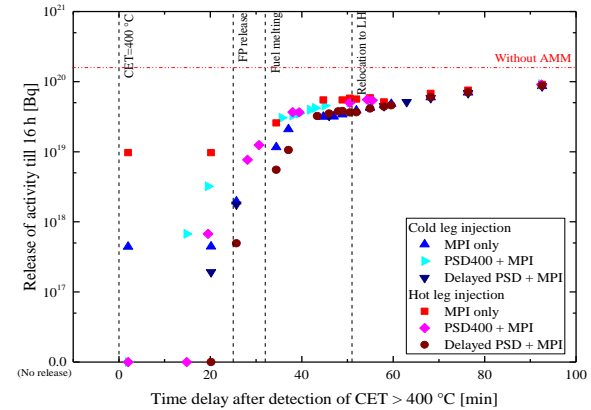
Fig. 1: SBLOCA with MPI. Released activity depending on MPI delays.

For later start of MPI at CET > 650 °C, prevention of FPs release is only possible if PSD is combined with HL injection. An injection strategy with HL MPI + delayed PSD provides the longest time margins to prevent FPs release. Till approx. 40 min after CET > 400 °C, significantly lower releases, compared to other MPI strategies, are predicted.

RESULTS IVMR. To analyze the molten corium behavior in the reactor lower head and to investigate scenarios with pool segregation a stand-alone model, based on the AIDA module of the ATHLET-CD code, was developed. As input data for these simulations we have applied the output data from integral plant simulations based on pre-identified critical accident scenarios, in respect to IVMR. The results with varied thickness of the metal layer (Tab. 1) showed that with decreasing the metal layer mass, the heat flux is increasing, indicating that focusing effect is predicted by this model. Furthermore, specific work within this project is focused on the mechanical resistance of the reactor pressure vessel wall.

Tab. 1: Heat flux dependence on the metal layer thickness.

	Metal layer mass		
	5 t	**15 t**	**35 t**
Oxide layer height / m	1.56	1.56	1.56
Metal layer height / m	0.04	0.12	0.27
Heat flux / MW m^{-2}	1.91	1.08	0.58

[1] Tusheva, P. *et al.* (2015) *atw* **60**, 442–447.
[2] Wilhelm, P. *et al.* (2018) *Ann. Nucl. Energy* **122**, 217–228.
[3] Jobst, M. *et al.* (2018) *Ann. Nucl. Energy* **122**, 280–296.
[4] Austregesilo, H. *et al.* (2013) *ATHLET–CD Mod 3.0 Cycle A User's Manual*, Gesellschaft für Anlagen- und Reaktorsicherheit (GRS) mbH.

Fig. 2: SBO with MPI. Hydrogen mass depending on MPI delays.

Further development and validation of the Monte Carlo code TRAMO for radiation load estimation on Russian VVER reactor equipment

S. Baier,[1] J. Konheiser,[1] P. Borodkin,[2] A. Gazetdinov,[2] N. Khrennikov[2]

[1]Technische Universität Dresden, Dresden, Germany; [2]Scientific and Engineering Centre for Nuclear and Radiation Safety, Moscow, Russia

The Monte Carlo code TRAMO is extended and improved to allow the Russian partner (Scientific and Engineering Centre for Nuclear Radiation Safety – SEC NRS) to perform independent calculations of radiation load parameters of reactor components of all water-water energy reactor (VVER) types. This paper gives a short overview about the new developments and improvements of the code as well as about its further validation and verification on new experiments on Russian and German nuclear power plants.

VVER reactors are used in many countries especially in Eastern Europe for many years. New plants are planned and built. Compared to Western type pressurized water reactors the construction is more compact, which particularly leads to a higher neutron irradiation of the reactor pressure vessel (RPV). In view of their designated operation time or planned lifetime extensions very detailed neutron and gamma fluence calculations are necessary to assure nuclear safety. There is a long-term collaboration between Russia and Germany concerning the peaceful usage of nuclear energy, based on an agreement from 1987 (scientific and technical collaboration (WTZ)). Within this scope several projects established and amplified the collaboration between SEC NRS and HZDR.[1–4] The actual WTZ project (2016–2020) is dedicated to further development and validation of the code TRAMO to allow SEC NRS to perform calculations with this code, which are necessary to fulfill the requirements of the Russian nuclear safety regulations.[5, 6]

The Monte-Carlo code TRAMO was developed at HZDR and is dedicated to calculations of gamma and neutron fluences of the RPV and the materials contained therein.[7] The geometry models are optimized for such structures. Various variance-reduced methods such as weight window model, implicit capture and source biasing open the possibilities of determination of results with very good statistics in the RPV within a reasonable time. The code is validated on several measurements on Russian VVER reactors (e.g. [1, 2]).

However, to perform calculations with TRAMO, a big amount of preparatory work is needed. The nuclear data are obtained from international nuclear data libraries such as ENDF/B-VII or JEFF 3.1. The codes NJOY and MODAJ are used to generate macroscopic cross sections and scattering matrices. In addition, the auxiliary code TRAWEI program is used to calculate zone weight according to the desired results region.[8, 9]

The work packages within the current project include the creation of an improved TRAMO version with corresponding pre- and post-processing tools, the generation of a database with cross-sections and scattering data of all relevant VVER materials (currently VVER 440/213, 440/230, VVER-1000) as well as the validation of the code and results to be carried out on the basis of experiments on Russian reactors and at the Greifswald nuclear power plant. In addition, verification by comparative calculations with the code MCNP 6.2 is planned. Within the framework of the code development, the TRAMO program was first converted into modern FORTRAN and the program structure was improved. The main further development was the integration of MODAJ into the TRAMO code itself. Thus, a direct selection of materials within the input is now possible and new material compositions can be defined too, which increases the flexibility and usability. A reference system (NPP KOLA-3) and the input and output structure were agreed with the Russian partner. For a system of 22 horizontal and 15 vertical monitor positions corresponding weight data sets and the according source biasing distributions were generated.

For the material database, cross sections and scattering matrices were generated for all materials of the reference design in a structure of 47 and 640 energy groups.

Regarding validation, 14 samples from trepans of the nuclear power plant Greifswald were prepared for analyzes at HZDR. VKTA determined the activities of ^{99}Tc, ^{63}Ni, ^{93m}Nb and ^{94}Nb and the concentrations of Nb, Ni and Mo. The samples cover different heights and angles of the RPV, but also different depths. In addition, results of monitoring experiments of the Russian nuclear power plants Kalinin-4 and Rostov-2 are available.

At the beginning of April 2019, the Russian partner will receive the first TRAMO version including the necessary add-ons and nuclear data and, thus, will be able to carry out test calculations independently and provide feedback on correctness, completeness, usability and flexibility.

At HZDR, the validation of the abovementioned experiments and the comparison of TRAMO with MCNP will be possessed.

[1] Rindelhardt, U. *et al.* (2009) *Nucl. Eng. Des.* **239**, 1581–1590.
[2] Konheiser, J. *et al.* (2009) *Ann. Nucl. Energy* **36**, 1235–1241.
[3] Borodkin, G. *et al.* (2008) *Proceedings of ISRD–13*, May 25–29, 2008, Akersloot, The Netherlands, p. 300–309.
[4] Borodkin, G. *et al.* (2008) *Proceedings of ISRD–13*, May 25–29, 2008, Akersloot, The Netherlands, p. 688–699.
[5] The List of Basic Legal Statements and Regulatory Standards used by Gosatomnadzor of Russia for State Regulation of Safety in the Field of Use of Atomic Energy. P–01–01–2011, Rostechnadzor, Moscow, Russia, 2011 (in Russian).
[6] Baier, S. *et al.* (2017) *Proceedings of ISRD–16*, May 07–12, 2017, Santa Fe, U.S.A.
[7] Barz, H.-U. and Konheiser, J. (1998) *Report FZR–245*.
[8] Chadwick, M. B. *et al.* (2006) *Nucl. Data Sheets* **107**, 2931–3060.
[9] MacFarlane, R. *et al.* (2010) *Nucl. Data Sheets* **111**, 2739–2890.

Development of an ASTEC model of the THS-15 test facility and first simulation results

M. Jobst

In the framework of the NuWaMa project (Expansion of a German-Czech Collaboration in the Field of Nuclear Waste Management), a research stay at ÚJV Řež (Czech Republic) took place during May 2018. The objective of the research stay was the development of a numerical model of the thermal-hydraulic test facility THS-15, which had been put in operation at the ÚJV site in Řež recently in order to investigate phenomena related to ex-vessel cooling for in-vessel retention of molten corium. Assessing the performed experiments with the help of the numerical model is an important contribution to a comprehensive understanding of the observed phenomena. The current state of the model and first results are presented.

In-vessel melt retention (IVMR) as a possible severe accident management measure for nuclear power reactors was described by Theofanous et al.[1] The principal idea is flooding of the reactor cavity with water. Due to evaporation, steam bubbles will form and move upwards in the riser section and a natural circulation process is established which transports away the heat from the lower head and the reactor pressure vessel (RPV) wall can be kept intact. The currently ongoing IVMR project aims at providing a best-estimate evaluation of In-Vessel Retention strategy for large power reactors, such as VVER-1000. One main open problem is the formation of a metal layer on-top of the molten oxidic pool, which can lead to high heat fluxes at the vessel wall exceeding the critical heat flux (CHF) and melt-through of the RPV would be observed (focusing effect).

A major part of the IVMR project is dedicated to experimental investigation of the related physical phenomena. One of the test facilities supported within the project is the Thermal Hydraulic Stand (design 2015, THS-15), operated at ÚJV Řež, in Czech Republic. THS-15 is a mock-up of the VVER-1000 cavity and the RPV vessel with 1:1 scale in height and radius, and 1:95 scale in azimuthal direction (3.8 slice).[2] The construction of THS-15 was finished and the first test campaign was carried out in 2018.

NUMERICAL MODEL. The integral severe accident code ASTEC (Accident Source Term Evaluation Code) was applied to model the test facility.[3] The code, designed to simulate all relevant phenomena during a severe accident of a water-cooled reactor, provides a general approach to model two-phase flows and heat conduction phenomena. Furthermore, several IVMR related phenomena (e.g. CHF correlations) were implemented into the latest release of the code.[4]

The developed ASTEC input data set covers the primary circuit of the test facility, while the influence of the secondary circuit is modelled as boundary conditions.[5, 6] Figure 1 shows a scheme of the modelled primary circuit, which contains the experimental chamber, the reduction valve (flow restriction), the condenser, the cooler and the primary circuit pump. The components are connected by tubes of different cross sections. ASTEC's ICARE module is applied to model the heating section, which consists of 150 mm thick copper blocks welded to a 3 mm steel layer, which is in contact to the cooling channel.
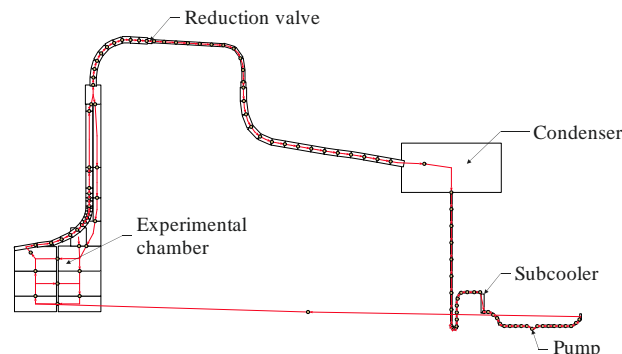
Fig. 1: Nodalisation scheme of ASTEC model of THS-15.

RESULTS. A first simulation has been performed with boundary conditions obtained from an experiment with constant high heating power (112.5 kW, equivalent to 1.4 MW/m² at the outer surface) in the cylindrical part of the heating section. The development of the wall temperature of this part of the heating section during the 300 s zero transient (with constant heating power and constant boundary conditions) is shown by Fig. 2. $T_{steel\,1/2/3}$ show the temperatures of the three components of the only 3 mm thick steel layer (from outside to inside). T_{Cu1} to T_{Cu4} show the temperatures in the copper block (also from outer layer to inner layer). The calculated temperature gradient inside the 150 mm copper block is 224 K, while the temperature gradient within the steel layer is approx. 54 K, which is ≈ 20 % of the total temperature gradient. This shows that a separate modelling of the thin steel layer is important to obtain a realistic temperature distribution. Further improvement of the model and a comparison to measurement data will be performed as the next steps.
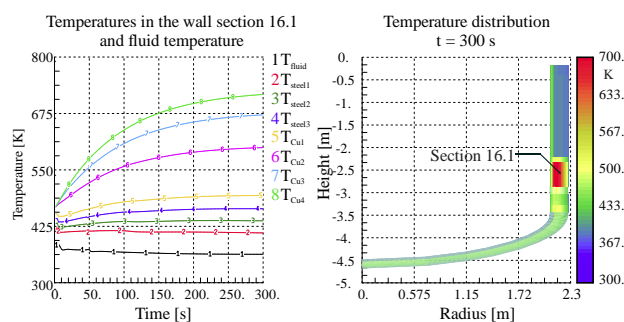
Fig. 2: Temperature evolution in the high power heating section (left) and temperature distribution in the whole heating section at 300 s (right).

[1] Theofanous, T. G. et al. (1997) Nucl. Eng. Des. **169**, 1–48.
[2] Duspiva, J. et al. (2017) EUROSAFE Forum, Paris.
[3] Chatelard, P. et al. (2016) Ann. Nucl. Energy **93**, 83–93.
[4] Carenini, F. et al. (2018) Ann. Nucl. Energy **118**, 363–374.
[5] Jobst, M. (2018) Technical note/internal FWOR report.
[6] Jobst, M. (2018) 8th ASTEC Users' club meeting.

○ ARTICLES (PEER-REVIEWED)

○ ORAL PRESENTATIONS

○ REPORTS

○ HABILITATION & THESES

⭕ Articles (peer-reviewed)
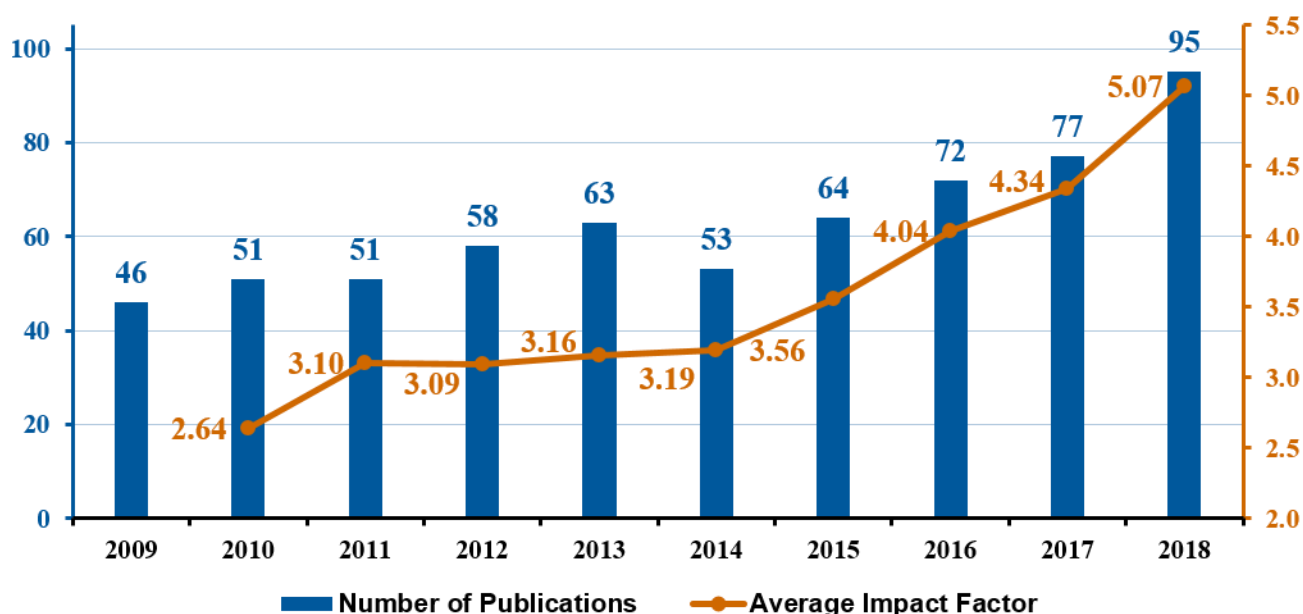
Statistics on the publication activity of the Institute of Resource Ecology (IRE) within the last 10 years. The diagram only considers peer-reviewed articles that were published under primary responsibility of the institute. The following compilation provides peer-reviewed articles published in 2018 representing any contribution of members of the IRE.

Aghakhani, S.; Grandjean, D.; Baekelant, W.; Coutiño-Gonzalez, E.; Fron, E.; Kvashnina, K.; Roeffaers, M. B. J.; Hofkens, J.; Lievens, B. F.; Sels, P.
Atomic scale reversible opto-structural switching of few atom luminescent silver clusters confined in LTA zeolites
Nanoscale 10, 11467–11476 (2018).

Altstadt, E.; Houska, M.; Simonovski, I.; Bruchhausen, M.; Holmström, S.; Lacalle, R.
On the estimation of ultimate tensile stress from small punch testing
International Journal of Mechanical Sciences 136, 85–93 (2018).

Amon, A.; Ormeci, A.; Bobnar, M.; Akselrud, L. G.; Avdeev, M.; Gumeniuk, R.; Burkhardt, U.; Prots, Y.; Hennig, C.; Leithe-Jasper, A.; Grin, Y.
Cluster Formation in the Superconducting Complex Intermetallic Compound Be$_{21}$Pt$_5$
Accounts of Chemical Research 51, 214–222 (2018).

Amon, A.; Svanidze, E.; Cardoso, R.; Wilson, M. N.; Rosner, H.; Bobnar, M.; Schnelle, W.; Lynn, J. W.; Gumeniuk, R.; Hennig, C.; Luke, G. M.; Borrmann, H.; Leithe-Jasper, A.; Grin, Y.
Noncentrosymmetric Superconductor BeAu
Physical Review B 8, 014501 (2018).

Anastasi, A.; Babusci, D.; Berlowski, M.; Bloise, C.; Bossi, F.; Branchini, P.; Budano, A.; Caldeira Balkeståhl, L.; Cao, B.; Ceradini, F.; Ciambrone, P.; Curciarello, F.; Czerwiński, E.; D'Agostini, G.; Danè, E.; de Leo, V.; de Lucia, E.; de Santis, A.; de Simone, P.; Di Cicco, A.; Di Domenico, A.; Domenici, D.; D'Uffizi, A.; Fantini, A.; Fantini, G.; Fermani, P.; Fiore, S.; Gajos, A.; Gauzzi, P.; Giovannella, S.; Graziani, E.; Ivanov, V. L.; Johansson, T.; Kisielewska-Kamińska, D.; Kang, X.; Kozyrev, E. A.; Krzemien, W.; Kupsc, A.; Loffredo, S.; Lukin, P. A.; Mandaglio, G.; Martini, M.; Messi, R.; Miscetti, S.; Morello, G.; Moricciani, D.; Moskal, P.; Passeri, A.; Patera, V.; Perez Del Rio, E.; Raha, N.; Santangelo, P.; Schioppa, M.; Selce, A.; Silarski, M.; Sirghi, F.; Solodov, E. P.; Tortora, L.; Venanzoni, G.; Wiślicki, W.; Wolke, M.; Keshavarzi, A.; Müller, S. E.; Teubner, T.
Combination of KLOE $\sigma(e^+e^- \rightarrow \pi^+\pi^-\gamma(\gamma))$ measurements and determination of $a_\mu^{\pi^+\pi^-}$ in the energy range $0.10 < s < 0.95$ GeV^2
Journal of High Energy Physics, 173 (2018).

Bader, M.; Müller, K.; Foerstendorf, H.; Schmidt, M.; Simmons, K.; Swanson, J. S.; Reed, D. T.; Stumpf, T.; Cherkouk, A.
Comparative analysis of uranium bioassociation with halophilic bacteria and *archaea*
PlosOne 13, e0190953 (2018).

Bader, M.; Rossberg, A.; Steudtner, R.; Drobot, B.;
Großmann, K.; Schmidt, M.; Musat, N.; Stumpf, T.;
Ikeda-Ohno, A.; Cherkouk, A.
**Impact of *Haloarchaea* on speciation of uranium –
a multi-spectroscopic approach**
*Environmental Science and Technology 52, 12895–
12904 (2018).*

Barkleit, A.; Hennig, C.; Ikeda-Ohno, A.
**Interaction of Uranium(VI) with α-Amylase and
Its Implication for Enzyme Activity**
*Chemical Research in Toxicology 31, 1032–1041
(2018).*

Barthen, R.; Karimzadeh, L.; Gründig, M.; Grenzer, J.;
Lippold, H.; Franke, K.; Lippmann-Pipke, J.
**Glutamic acid leaching of synthetic covellite – A
model system combining experimental data and
geochemical modeling**
Chemosphere 196, 368–376 (2018).

Bauer, A.; Jäschke, A.; Schöne, S.; Barthen, R.; März, J.;
Schmeide, K.; Patzschke, M.; Kersting, B.;
Fahmy, K.; Oertel, J.; Brendler, V.; Stumpf, T.
**Uranium(VI) complexes with a calix[4]arene-
based 8-hydroxyquinoline ligand:
Thermodynamic and structural characterization
based on calorimetry, spectroscopy, and liquid-
liquid extraction**
ChemistryOpen 7, 467–474 (2018).

Bergner, F.; Hlawacek, G.; Heintze, C.
**Helium-ion microscopy, helium-ion irradiation
and nanoindentation of Eurofer 97 and ODS
Eurofer**
Journal of Nuclear Materials 505, 267–275 (2018).

Bes, R.; Ahopelto, T.; Honkanen, A. P.; Huotari, S.;
Leinders, G.; Pakarinen, J.; Kvashnina, K. O.
**Laboratory-scale X-ray absorption spectroscopy
approach for actinide research: Experiment at the
uranium L₃-edge**
Journal of Nuclear Materials 507, 50–53 (2018).

Bes, R.; Kvashnina, K.; Rossberg, A.; Dotavio, G.;
Desgranges, L.; Pontillon, Y.; Solari, P. L.;
Butorin, S. M.; Martin, P.
**New insight in the uranium valence state
determination in $U_yNd_{1-y}O_{2-x}$**
Journal of Nuclear Materials 507, 145–150 (2018).

Besold, J.; Biswas, A.; Suess, E.; Scheinost, A. C.;
Rossberg, A.; Mikutta, C.; Kretzschmar, R.;
Gustafsson, J. P.; Planer-Friedrich, B.
**Monothioarsenate transformation kinetics
determines arsenic sequestration by sulfhydryl
groups of peat**
*Environmental Science & Technology 52, 7317–
7326 (2018).*

Bibi, I.; Arvidson, R. S.; Fischer, C.; Lüttge, A.
**Temporal Evolution of Calcite Surface Dissolution
Kinetics**
Minerals 8, 256 (2018).

Bilodid, Y.; Fridman, E.; Kotlyar, D.; Shwageraus, E.
**Explicit decay heat calculation in the nodal
diffusion code DYN3D**
Annals of Nuclear Energy 121, 374–381 (2018).

Bilodid, Y.; Grundmann, U.; Kliem, S.
**The HEXNEM3 nodal flux expansion method for
the hexagonal geometry in the code DYN3D**
Annals of Nuclear Energy 116, 187–194 (2018).

Börsig, N.; Scheinost, A. C.; Shaw, S.; Schild, D.;
Neumann, T.
**Retention and multiphase transformation of
selenium oxyanions during the formation of
magnetite via ferrous hydroxide and green rust**
Dalton Transactions 47, 11002–11015 (2018).

Bousbia Salah, A.; Ceuca, S. C.; Puragliesi, R.; Mukin, R.;
Grahn, A.; Kliem, S.; Vlassenbroeck, J.;
Austregesilo, H.
**Unsteady single phase natural circulation flow
mixing prediction using 3D thermal-hydraulic
system and CFD codes**
Nuclear Technology 203, 293–314 (2018).

Butorin, S. M.; Kvashnina, K. O.; Klintenberg, M.;
Kavcic, M.; Zitnik, M.; Bucar, K.; Gougeon, P.;
Gall, P.; Candolfi, C.; Lenoir, B.
**Effect of Ag doping on electronic structure of
cluster compounds $Ag_xMo_9Se_{11}$ (x = 3.4; 3.9)**
ACS Applied Energy Materials 8, 4032–4039 (2018).

Cordelli, M.; Diociaiuti, E.; Donghia, R.; Ferrari, A.;
Miscetti, S.; Müller, S.; Sarra, I.
**Neutron irradiation test of Hamamatsu, SensL
and AdvanSiD UV-extended SiPMs**
Journal of Instrumentation 13, T03005 (2018).

Das, A.; Viehrig, H. W.; Altstadt, E.; Bergner, F.;
Hoffmann, J.
**Why do secondary cracks preferentially form in
hot-rolled ODS steels in comparison with hot-
extruded ODS steels?**
Crystals 8, 306 (2018).

Erenburg, S. B.; Trubina, S. V.; Kvashnina, K. O.;
Kruchinin, V. N.; Gritsenko, V. V.;
Chernikova, A. G.; Markeev, A. M.
**Short-Range Order in Amorphous and Crystalline
Ferroelectric $Hf_{0.5}Zr_{0.5}O_2$**
*Journal of Experimental and Theoretical Physics
126, 816–824 (2018).*

Feig, M.; Nicklas, M.; Bobnar, M.; Schelle, W.;
Schwarz, U.; Leithe-Jasper, A.; Hennig, C.;
Gumeniuk, R.
**Superconductivity and magnetism in
noncentrosymmetric $LaPtGe_3$ and $CePtGe_3$**
Physical Review B 98, 184516 (2018).

Firkala, T.; Kuschewski, F.; Nörenberg, T.; Klopf, J. M.;
Pashkin, A.; Foerstendorf, H.; Rudolph, M.;
Kehr, S. C.; Eng, L. M.
Near-field optical examination of potassium *n*-butyl xanthate/chalcopyrite flotation products
Minerals 8, 118 (2018).

Fischer, C.; Kurganskaya, I.; Lüttge, A.
Inherited control of crystal surface reactivity
Applied Geochemistry 91, 140–148 (2018).

Fischer, C.; Lüttge, A.
Pulsating dissolution of crystalline matter
Proceedings of the National Academy of Sciences of the United States of America 115, 897–902 (2018).

Fischer, S.; Krause, T.; Jordan, N.; Lederer, F.; Jain, R.
Draft Genome Sequence of *Bacillus safensis* JG-B5T isolated from a uranium mining waste pile
Microbiology Resource Announcements 7, e00961–00918 (2018).

Gerber, U.; Hübner, R.; Rossberg, A.; Krawczyk-Bärsch, E.; Merroun, M. L.
Metabolism-dependent bioaccumulation of uranium by *Rhodosporidium toruloides* isolated from the flooding water of a former uranium mine
PlosOne 13, 1–20 e0201903 (2018).

Gritsenko, V. A.; Perevalov, T. V.; Kruchinin, V. N.;
Aliev, V. S.; Gerasimova, A. K.; Erenburg, S. B.;
Trubina, S. V.; Kvashnina, K. O.; Prosvirin, I. P.
Nanoscale Potential Fluctuations in Zirconium Oxide and the Flash Memory Based on Such Fluctuations
Advanced Electronic Materials 4, 1700592 (2018).

Gumeniuk, R.; Yaresko, A. N.; Schnelle, W.; Nicklas, M.;
Kvashnina, K. O.; Hennig, C.; Grin, Y.; Leithe-Jasper, A.
Uniaxial ferromagnetism of local uranium moments in hexagonal UBeGe
Physical Review B 97, 174405 (2018).

Haubitz, T.; Tsushima, S.; Steudtner, R.; Drobot, B.;
Geipel, G.; Stumpf, T.; Kumke, M. U.
Ultrafast transient absorption spectroscopy of UO_2^{2+} and $[UO_2Cl]^+$
Journal of Physical Chemistry A 122, 6970–6977 (2018).

He, S.; Biedermann, F.; Vankova, N.; Zhechkov, L.;
Heine, T.; Hoffman, R. E.; de Simone, A.;
Duignan, T. T.; Nau, W. M.
Cavitation energies can outperform dispersion interactions
Nature Chemistry 10, 1252–1257 (2018).

Heuser, J. M.; Palomares, R. I.; Bauer, J. D.; Lozano
Rodriguez, M. J.; Cooper, J.; Lang, M.;
Scheinost, A. C.; Schlenz, H.; Winkler, B.;
Bosbach, D.; Neumeier, S.; Deissmann, G.
Structural characterization of (Sm,Tb)PO4 solid solutions and pressure-induced phase transitions
Journal of the European Ceramic Society 38, 4070–4081 (2018).

Hoffmann, A.; Schleicher, E.; Keller, L.; Leon Alonso, J.;
Pitz-Paal, R.
Application of a single wire-mesh sensor in a parabolic trough facility with direct steam generation
Solar Energy 159, 1016–1030 (2018).

Höhne, T.; Kliem, S.; Bieder, U.
IAEA CRP benchmark of ROCOM PTS test case for the use of CFD in reactor design using the CFD-codes ANSYS CFX and TRIOCFD
Nuclear Engineering and Design 333, 161–180 (2018).

Hopfe, S.; Konsulke, S.; Barthen, R.; Lehmann, F.;
Kutschke, S.; Pollmann, K.
Screening and selection of technologically applicable microorganisms for recovery of rare earth elements from fluorescent powder
Waste Management 79, 554–563 (2018).

Huittinen, N.; Scheinost, A. C.; Ji, Y.; Kowalski, P. M.;
Arinicheva, Y.; Wilden, A.; Neumeier, S.; Stumpf, T.
A spectroscopic and computational study of Cm^{3+} incorporation in lanthanide phosphate rhabdophane ($LnPO_4 \cdot 0.67H_2O$) and monazite ($LnPO_4$)
Inorganic Chemistry 57, 6252–6265 (2018).

Ionescu, C.; Fischer, C.; Hoeck, V.; Lüttge, A.
Discrimination of ceramic surface finishing by vertical scanning interferometry
Archaeometry 61, 31–42 (2018).

Iric, K.; Subramanian, M.; Oertel, J.; Agarwal, N. P.;
Matthies, M.; Periole, X.; Sakmar, T. P.; Huber, T.;
Fahmy, K.; Schmidt, T. L.
DNA-encircled lipid bilayers
Nanoscale 10, 18463–18467 (2018).

Jain, R.; Peräniemi, S.; Jordan, N.; Vogel, M.; Weiss, S.;
Foerstendorf, H.; Lakaniemi, A. M.
Removal and recovery of uranium by waste digested activated sludge in fed-batch stirred tank reactor
Water Research 142, 167–175 (2018).

Jobst, M.; Wilhelm, P.; Kozmenkov, Y.; Kliem, S.
Severe Accident Management Measures for a Generic German PWR. Part II: Small-break loss-of-coolant accident
Annals of Nuclear Energy 122, 280–296 (2018).

Jordan, N.; Demnitz, M.; Lösch, H.; Starke, S.; Brendler, V.; Huittinen, N.
Complexation of trivalent lanthanides (Eu) and actinides (Cm) with aqueous phosphates at elevated temperatures
Inorganic Chemistry 57, 7915–7024 (2018).

Jordan, N.; Franzen, C.; Lützenkirchen, J.; Foerstendorf, H.; Hering, D.; Weiss, S.; Heim, K.; Brendler, V.
Adsorption of selenium(VI) onto nano transition alumina
Environmental Science: Nano 5, 1661–1669 (2018).

Kempt, R.; Kuc, A.; Han, J. H.; Cheon, J.; Heine, T.
Two dimensional crystals in three dimensions
Small, 1803910 (2018).

Kolorenc, J.; Kvashnina, K.
Theoretical Modelling of High-Resolution X-Ray Absorption Spectra at Uranium M_4 Edge
MRS Bulletin 3, 3143–3148 (2018).

Konheiser, J.; Rachamin, R.; Brachem, C.; Hampel, U.
Feasibility Study for Detection of Reactor State Changes during Severe Accidents via External Gamma Radiation Measurements
Annals of Nuclear Energy 114, 175–180 (2018).

Krawczyk-Bärsch, E.; Gerber, U.; Müller, K.; Moll, H.; Rossberg, A.; Steudtner, R.; Merroun, M.
Multidisciplinary characterization of U(VI) sequestration by *Acidovorax facilis* for bioremediation purposes
Journal of Hazardous Materials 147, 233–241 (2018).

Kretzschmar, J.; Haubitz, T.; Hübner, R.; Weiss, S.; Husar, R.; Brendler, V.; Stumpf, T.
Network-like arrangement of mixed-valence uranium oxide nanoparticles after glutathione-induced reduction of uranium(VI)
Chemical Communications 54, 8697–8700 (2018).

Kulenkampff, J.; Stoll, M.; Gründig, M.; Mansel, A.; Lippmann-Pipke, J.; Kersten, M.
Time-lapse 3D imaging by positron emission tomography of Cu mobilized in a soil column by the herbicide MCPA
Scientific Reports 8, 7091 (2018).

Kvashnina, K. O.; Kowalski, P. M.; Butorin, S. M.; Leinders, G.; Pakarinen, J.; Bes, R.; Li, H.; Verwerft, M.
Trends in valence band electronic structure of mixed uranium oxides
Chemical Communications 54, 9757–9760 (2018).

Lahrouch, F.; Siberchiot, B.; Leost, L.; Aupiais, J.; Rossberg, A.; Hennig, C.; Den Auwer, C.; Di Giorgio, C.
Polyethyleneimine Methylenecarboxylate: a macromolecular DTPA analogue to chelate plutonium(IV)
Chemical Communications 54, 11705–11708 (2018).

Léost, L.; Roques, J.; van de Meeren, A.; Vincent, L.; Sbirrazzuoli, N.; Hennig, C.; Rossberg, A.; Aupiais, J.; Pagnotta, S.; Den Auwer, C.; Di Giorgio, C.
Towards the development of chitosan nanoparticles for plutonium pulmonary decorporation
Dalton Transactions 47, 11605–11618 (2018).

Lippold, H.; Karimzadeh, L.; Kulenkampff, J.; Wissmeier, L.; Stuhlfauth, C.; Stoll, M.; Lippmann-Pipke, J.
Effect of pH on the mobility of the herbicide MCPA in a sand-goethite column: 1D and 2D reactive transport modeling
Applied Geochemistry 98, 345–350 (2018).

Liu, J.; Luo, X.; Wang, J.; Xiao, T.; Yin, M.; Belshaw, N. S.; Lippold, H.; Kong, L.; Xiao, E.; Bao, Z.; Li, N.; Chen, Y.; Linghu, W.
Provenance of uranium in a sediment core from a natural reservoir, South China: Application of Pb stable isotope analysis
Chemosphere 193, 1172–1180 (2018).

Liu, J.; Wang, J.; Xiao, T.; Bao, Z.; Lippold, H.; Luo, X.; Yin, M.; Ren, J.; Chen, Y.; Linghu, W.
Geochemical dispersal of thallium and accompanying metals in sediment profiles from a smelter-impacted area in South China
Applied Geochemistry 88, 239–246 (2018).

Lopez-Fernandez, M.; Romero-Gonzalez, M.; Günther, A.; Solari, P. L.; Merroun, M. L.
Effect of U(VI) aqueous speciation on the binding of uranium by the cell surface of *Rhodotorula mucilaginosa*, a natural yeast isolate from bentonites
Chemosphere 199, 351–360 (2018).

Martin, N. P.; März, J.; Feuchter, H.; Duval, S.; Roussel, P.; Henry, N.; Petricek, V.; Ikeda-Ohno, A.; Loiseau, T.; Volkringer, C.
Synthesis and structural characterization of the first neptunium based metal-organic frameworks incorporating {Np_6O_8} hexanuclear cluster
Chemical Communications 54, 6979–6982 (2018).

Martin, N. P.; Volkringer, C.; Henry, N.; Trivelli, X.; Stoclet, G.; Ikeda-Ohno, A.; Loiseau, T.
Formation of a new type of {U_{38}} cluster based on a controlled release of water via esterification reaction
Chemical Science 9, 5021–5032 (2018).

Martin, N. P.; Volkringer, C.; Roussel, P.; März, J.; Hennig, C.; Loiseau, T.; Ikeda-Ohno, A.
The {Np_{38}} clusters: The missing link in the largest poly-oxo cluster series of tetravalent actinides
Chemical Communications 54, 10060–10063 (2018).

Mashita, T.; Tsushima, S.; Takao, K.
Controlling the lability of uranyl(VI) through intramolecular π-π Stacking
Dalton Transactions 47, 13072–13080 (2018).

Mayordomo, N.; Foerstendorf, H.; Lützenkirchen, J.; Heim, K.; Weiss, S.; Alonso, U.; Missana, T.; Schmeide, K.; Jordan, N.
Selenium(IV) sorption onto γ-Al₂O₃: a consistent description of the surface speciation by spectroscopy and thermodynamic modeling
Environmental Science and Technology 52, 581–588 (2018).

Mistonov, A. A.; Chumakov, A. P.; Ermakov, R. P.; Iskhakova, L. D.; Zakharova, A. V.; Chumakova, A. V.; Kvashnina, K. O.
Electronic structure studies of bismuth compounds by high energy resolution X-ray spectroscopy and ab-initio calculations
Journal of Alloys and Compounds 753, 646–654 (2018).

Nikitin, E.; Fridman, E.
Extension of the reactor dynamics code DYN3D to SFR applications – Part I: thermal expansion models
Annals of Nuclear Energy 119, 382–389 (2018).

Nikitin, E.; Fridman, E.
Extension of the reactor dynamics code DYN3D to SFR applications – Part II: validation against the Phenix EOL control rod withdrawal tests
Annals of Nuclear Energy 119, 411–418 (2018).

Nikitin, E.; Fridman, E.
Extension of the reactor dynamics code DYN3D to SFR applications – Part III: validation against the initial phase of the Phenix EOL natural convection test
Annals of Nuclear Energy 119, 390–395 (2018).

Nsubuga, A.; Sgarzi, M.; Zarschler, K.; Kubeil, M.; Hübner, R.; Steudtner, R.; Graham, B.; Joshi, T.; Stephan, H.
Facile Preparation of Multifunctionalisable 'Stealth' Upconverting Nanoparticles for Biomedical Applications
Dalton Transactions 47, 8595–8604 (2018).

Pecko, S.; Heintze, C.; Bergner, F.; Anwand, W.; Slugen, V.
Fe²⁺ ion irradiated JRQ steel investigated by nanoindentation and slow-positron Doppler broadening spectroscopy
Nuclear Instruments and Methods in Physics Research B 415, 1–8 (2018).

Pereira, G.; Johnson, A. E.; Bilodid, Y.; Fridman, E.; Kotlyar, D.
Applying the Serpent-DYN3D Code Sequence for the Decay Heat Analysis of Metallic Fuel Sodium Fast Reactor
Annals of Nuclear Energy 125, 291–306 (2018).

Phuyal, D.; Das, S.; Mukherjee, S.; Jana, S.; Kvashnina, K. O.; Sarma, D. D.; Karis, O.; Rensmo, H.; Butorin, S. M.
The origin of low bandgap and ferroelectricity of a co-doped BaTiO₃
EPL – Europhysics Letters 124, 27005 (2018).

Phuyal, D.; Jain, S. M.; Philippe, B.; Johansson, M. B.; Pazoki, M.; Kullgren, J.; Kvashnina, K. O.; Klintenberg, M.; Johansson, E. M. J.; Butorin, S. M.; Karis, O.; Rensmo, H.
The electronic structure and band interface of cesium bismuth iodide on a titania heterostructure using hard X-ray spectroscopy
Journal of Materials Chemistry A 6, 9498–9505 (2018).

Phuyal, D.; Safdari, M.; Pazoki, M.; Liu, P.; Philippe, B.; Kvashnina, K. O.; Karis, O.; Butorin, S. M.; Rensmo, H.; Edvinsson, T.; Kloo, L.; Gardner, J. M.
Electronic Structure of Two-Dimensional Lead(II) Iodide Perovskites: An Experimental and Theoretical Study
Chemistry of Materials 30, 4959–4967 (2018).

Pollmann, K.; Kutschke, S.; Matys, S.; Raff, J.; Hlawacek, G.; Lederer, F. L.
Bio-recycling of metals: Recycling of technical products using biological applications
Biotechnology Advances 36, 1048–1062 (2018).

Prieur, D.; Epifano, E.; Dardenne, K.; Rothe, J.; Hennig, C.; Scheinost, A.; Neuville, D.; Martin, P.
Peculiar thermal behavior of UO₂ local structure
Inorganic Chemistry 57, 14890–14894 (2018).

Prieur, D.; Martel, L.; Vigier, J. F.; Scheinost, A. C.; Kvashnina, K. O.; Somers, J.; Martin, P. M.
Aliovalent cation substitution in UO₂: Electronic and local structures of $U_{1-y}La_yO_{2 \pm x}$ solid solutions
Inorganic Chemistry 57, 1535–1544 (2018).

Qiu, C.; Eng, P. J.; Hennig, C.; Schmidt, M.
Competitive adsorption of ZrO₂ nanoparticle and alkali cations (Li⁺–Cs⁺) on muscovite (001)
Langmuir 34, 12270–12278 (2018).

Qiu, C.; Eng, P. J.; Hennig, C.; Schmidt, M.
Formation and Aggregation of ZrO₂ Nanoparticles on Muscovite (001)
Journal of Physical Chemistry C 122, 3865–3874 (2018).

Qiu, C.; Majs, F.; Douglas, T.; Schmidt, M.; Trainor, T.
In situ Structural Study of Sb(V) Adsorption on Hematite (1-102) Using X-ray Surface Scattering
Environmental Science & Technology 52, 11161–11168 (2018).

Qiu, C.; Majs, F.; Eng, P.; Stubbs, J.; Douglas, T.; Schmidt, M.; Trainor, T.
In situ structural study of the surface complexation of lead(II) on the chemically mechanically polished hematite (1$\bar{1}$02) surface
Journal of Colloid and Interface Science 524, 66–75 (2018).

Rachamin, R.; Kliem, S.
Validation of the DYN3D-Serpent code system for SFR cores using selected BFS experiments. Part II: DYN3D calculations
Annals of Nuclear Energy 114, 181–190 (2018).

Röder, F.; Heintze, C.; Pecko, S.; Akhmadaliev, S.; Bergner, F.; Ulbricht, A.; Altstadt, E.
Nanoindentation of ion-irradiated reactor pressure vessel steels – model-based interpretation and comparison with neutron irradiation
Philosophical Magazine 98, 911–933 (2018).

Rohde, U.; Seidl, M.; Kliem, S.; Bilodid, Y.
Neutron Noise Observations in German KWU Built PWR and Analyses with the Reactor Dynamics Code DYN3D
Annals of Nuclear Energy 112, 715–734 (2018).

Rohlfs, R. D.; Fischer, C.; Kurganskaya, I.; Lüttge, A.
Crystal dissolution kinetics studied by a combination of Monte Carlo and Voronoi methods
Minerals 8, 133 (2018).

Rojo, H.; Scheinost, A. C.; Lothenbach, B.; Laube, A.; Wieland, E.; Tits, J.
Retention of selenium by calcium aluminate hydrate (AFm) phases under strongly reducing radioactive waste repository conditions
Dalton Transactions 47, 4209–4218 (2018).

Schöne, S.; Radoske, T.; März, J.; Stumpf, T.; Ikeda-Ohno, A.
Synthesis and Characterization of Heterometallic Iron–Uranium Complexes with a Bidentate N-Donor Ligand (2,2′-Bipyridine or 1,10-Phenanthroline)
Inorganic Chemistry 57, 13318–13329 (2018).

Servalli, M.; Celebi, K.; Payamyar, P.; Zheng, L.; Položij, M.; Lowe, B.; Kuc, A.; Schwarz, T.; Thorwarth, K.; Borgschulte, A.; Heine, T.; Zenobi, R.; Schlüter, A. D.
Photochemical creation of covalent organic 2D monolayer objects in defined shapes via a lithographic 2D-polymerization
ACS Nano 12, 11294–11306 (2018).

Simonovski, I.; Baraldi, D.; Holmström, S.; Altstadt, E.; Delville, R.; Bruchhausen, M.
Determining the ultimate tensile strength of fuel cladding tubes by small punch testing
Journal of Nuclear Materials 509, 620–630 (2018).

Takao, K.; Tsushima, S.
The oxidation of borohydrides by photoexcited $[UO_2(CO_3)_3]^{4-}$
Dalton Transactions 47, 5149–5152 (2018).

Tanha, M. R.; Ikeda-Ohno, A.; Schulze, M.; Khalid, F. R.; Storai, M. A.; Walther, C.
Environmental radioactivity studies in Kabul and northern Afghanistan
Journal of Radioanalytical and Nuclear Chemistry 318, 2425–2433 (2018).

Thomas, A. K.; Wieduwild, R.; Zimmermann, R.; Lin, W.; Friedrichs, J.; Bickle, M.; Fahmy, K.; Werner, C.; Zhang, Y.
Layer-by-Layer assembly of heparin and peptide-polyethylene glycol conjugates to form hybrid nanothin films of biomatrices
ACS Applied Materials and Interfaces 10, 14264–14270 (2018).

Tymen, S.; Scheinost, A. C.; Lozano Rodriguez, M. J.; Friebe, C.; Schubert, U. S.
From cubic palladium to concave core-shell platinum palladium nanoparticles: Evolution of the structure and their electrochemical properties
Journal of the Electrochemical Society 165, H67–H77 (2018).

Urban, J. M.; Baranowski, M.; Kuc, A.; Klopotowski, L.; Surrente, A.; Ma, Y.; Wlodarczyk, D.; Suchocki, A.; Ovchinnikov, D.; Heine, T.; Maude, D. K.; Kis, A.; Plochocka, P.
Non equilibrium anisotropic excitons in atomically thin ReS₂
2D Materials 6, 015012 (2018).

Usov, P. M.; Leong, C. F.; Chan, B.; Hayashi, M.; Kitagawa, H.; Sutton, J. J.; Gordon, K. C.; Hod, I.; Farha, O. K.; Hupp, J. T.; Addicoat, M.; Kuc, A. B.; Heine, T.; D'Alessandro, D. M.
Probing charge transfer characteristics in a donor–acceptor metal–organic framework by Raman spectroelectrochemistry and pressure-dependence studies
Physical Chemistry Chemical Physics 20, 25772–25779 (2018).

Vigier, J. F.; Freis, D.; Pöml, P.; Prieur, D.; Lajarge, P.; Gardeur, S.; Guiot, A.; Bouëxière, D.; Konings, R.
Optimization of Uranium-Doped Americium Oxide Synthesis for Space Application
Inorganic Chemistry 57, 4317–4327 (2018).

Virtanen, S.; Meriläinen, S.; Eibl, M.; Rabung, T.; Huittinen, N.
Sorption competition and kinetics of trivalent cations (Eu, Y and Cm) on corundum (α-Al₂O₃): a batch sorption and TRLFS study
Applied Geochemistry 92, 71–81 (2018).

Vivas, J.; Capdevila, C.; Altstadt, E.; Houska, M.; San-Martin, D.
Importance of austenitization temperature and ausforming on creep strength in 9Cr ferritic/martensitic steel
Scripta Materialia 153, 14–18 (2018).

Vivas, J.; Capdevila, C.; Altstadt, E.; Houska, M.; Serrano, M.; De-Castro, D.; San-Martin, D.
Effect of ausforming temperature on creep strength of G91 investigated by means of small punch creep tests
Materials Science and Engineering A 728, 259–265 (2018).

Vogel, M.; Fischer, S.; Maffert, A.; Hübner, R.; Scheinost, A. C.; Franzen, C.; Steudtner, R.
Biotransformation and detoxification of selenite by microbial biogenesis of selenium-sulfur nanoparticles
Journal of Hazardous Materials 344, 749–757 (2018).

Wagner, S.; Yim, C.; McEvoy, N.; Kataria, S.; Yokaribas, V.; Kuc, A.; Pindl, S.; Fritzen, C. P.; Heine, T.; Duesberg, G. S.; Lemme, M. C.
Highly Sensitive Electromechanical Piezoresistive Pressure Sensors Based on Large-Area Layered PtSe₂ Films
Nano Letters 18, 3738–3745 (2018).

Wang, Y.; Li, Y.; Heine, T.
PtTe Monolayer: Two-Dimensional Electrocatalyst with High Basal Plane Activity toward Oxygen Reduction Reaction
Journal of the American Chemical Society 140, 12732–12735 (2018).

Wilhelm, P.; Jobst, M.; Kozmenkov, Y.; Schäfer, F.; Kliem, S.
Severe accident management measures for a generic German PWR. Part I: Station blackout
Annals of Nuclear Energy 122, 217–228 (2018).

Xiao, B.; Lösch, H.; Huittinen, N.; Schmidt, M.
Local structural effects of Eu³⁺ incorporation into xenotime-type solid solutions with different host cations
Chemistry - A European Journal 24, 13368–13377 (2018).

Zedek, L.; Lippold, H.; Sembera, J.
Computer simulation of the ternary problem – technical aspects and possibilities
IFAC-PapersOnLine 51, 589–594 (2018).

O ORAL PRESENTATIONS

Amidani, L.; Korthout, K.; Joos, J. J.; van der Linden, M.; Sijbom, H. F.; Meijerink, A.; Poelman, D.; Smet, P. F.; Glatzel, P.
Oxidation and luminescence quenching of europium doped BaMgAl₁₀O₁₇ probed by HERFD-XANES
17th International Conference on X-ray Absorption Fine Structure (XAFS 2018), July 22–27, 2018, Krakow, Poland (2018).

Amidani, L.; Rossberg, A.; Romanchuk, A.; Plakhova, T.; Kvashnina, K.
Squeezing information about ThO2 nanoparticles' size and shape from high resolution XANES
4th International Workshop on Advanced Techniques in Actinide Spectroscopy (ATAS), November 06–09, 2018, Nice, France (2018).

Arnold, T.; Sachs, S.
Radioecological research of WG NORM within the ALLIANCE
3rd European Radiological Protection Research Week (ERPW), October 01–05, 2018, Rovinj, Croatia (2018).

Barkleit, A.
LSC-Anwendungen beim Rückbau von Kernkraftwerken
LSC-Anwendertreffen, September 11–12, 2018, Hannover, Germany (2018).

Bayrak, T.; Helmi, S.; Ye, J.; Martinez-Reyes, A.; Samano-Tirado, E.; Seidel, R.; Erbe, A.
Functionalized DNA Origami Nanostructures for Molecular Electronics
3rd Functional DNA Nanotechnology Workshop, June 06–08, 2018, Rome, Italy (2018).

Besold, J.; Eberle, A.; Kujala, K.; Kumar, N.; Scheinost, A. C.; Pacheco, L.; Fendorf, S.; Planer-Friedrich, B.
Binding of Antimony to Natural Organic Matter in a Finish Mine-Water Influenced Peatland
Goldschmidt 2018, August 12–17, 2018, Boston, U.S.A. (2018).

Bok, F.; Jordan, N.; Brendler, V.
Thermodynamic modelling of Selenium in environmental conditions: traps, pitfalls and perspectives
256th ACS National Meeting & Exposition, August 19–23, 2018, Boston, U.S.A. (2018).

Bok, F.; Richter, A.; März, J.; Brendler, V.
Mechanistic models for uranium sorption on iron minerals: Comparing their parametrization and surface species
255th ACS National Meeting & Exposition, March 18–22, 2018, New Orleans, U.S.A. (2018).

Brinkmann, H.; Heim, K.; Kaden, P.; Kloditz, R.; Moll, H.; Patzschke, M.
Detailed characterization of uranyl complexes with small organic ligands on a molecular level: a spectroscopic approach
MIND Advanced training course | Geomicrobiology in radioactive waste disposal, October 08–11, 2018, Mol, Belgium (2018).

Brinkmann, H.; Patzschke, M.; Roßberg, A.; Moll, H.; Stumpf, T.
Interaction of U(VI) with α-isosaccharinic acid under acidic conditions: characterization of the formed complexes
18th Radiochemical Conference (RadChem2018), May 13–18, 2018, Mariánské Lázně, Czech Republic (2018).

Brinkmann, H.; Philipp, T.; Dullies, P.; Shams Aldin Azzam, S.; Patzschke, M.; Roßberg, A.; Moll, H.; Stumpf, T.
Interaction of U(VI) with α-isosaccharinic acid: structural elucidation of the formed complexes and implications for the retention of U(VI) on bentonite
Uranium Biogeochemistry: Transformations, Isotopes, and Applications, October 21–26, 2018, Ascona, Switzerland (2018).

Buchatskaya, Y.; Salah, S.; Durce, D.; Steudtner, R.; Devillers, M.
Towards an understanding of U(VI) interaction with Boom Clay dissolved organic matter by TRLFS
Uranium Biogeochemistry: Transformations, Isotopes, and Applications, October 21–26, 2018, Ascona, Switzerland (2018).

Buchholz, S.; Schaffrath, A.; Bonfigli, G.; Kaczmarkiewicz, N.; Sporn, M.; Schäfer, F.; Wagner, T.
EASY – Evidence of design basis accidents mitigation solely with passive safety systems
Jahrestagung Kerntechnik, Annual Meeting on Nuclear Technology, May 29–30, 2018, Berlin, Germany (2018).

Chauhan, C.; Bergner, F.; Etienne, A.; Aktaa, J.; de Carlan, Y.; Heintze, C.; Litvinov, D.; Hernandez-Mayoral, M.; Oñorbe, E.; Radiguet, B.; Ulbricht, A.
Microstructure, strengthening mechanisms & properties of ODS alloys developed under MatISSE project
NuMat2018: The Nuclear Materials Conference, October 14–18, 2018, Seattle, U.S.A. (2018).

Cherkouk, A.
From bentonite to rock salt – microbial studies for nuclear waste disposal
Themenfeld-Kolloquium „ENERGIE", Topic: Results and outcomes of European programme on Microbiology In Nuclear waste Disposal (MIND) – Views and perspectives over future research, September 19, 2018, Berlin, Germany (2018).

Cherkouk, A.; Bader, M.; Swanson, J. S.; Steudtner, R.; Drobot, B.; Müller, K.; Foerstendorf, H.; Schmidt, M.; Rossberg, A.; Ikeda-Ohno, A.; Stumpf, T.
Interactions of halophilic microorganisms with uranium
Uranium Biogeochemistry: Transformations, Isotopes, and Applications, October 21–26, 2018, Ascona, Switzerland (2018).

Child, D. P.; Johansen, M. P.; Hotchkis, M. A. C.; Howard, D. L.; Howell, N.; Young, E.; Davis, J.; Ikeda-Ohno, A.
Applying accelerator and microscopy methods for investigating radionuclides at Australia's former nuclear test sites
VIII International Conference Semipalatinsk Test Site: Legacy and Prospects for Scientific and Technical Potential Development, September 11, 2018, Kurchatov, Republic of Kazakhstan (2018).

Eibl, M.; Shaw, S.; Morris, K.; Hennig, C.; Stumpf, T.; Huittinen, N.
Trivalent Actinide Incorporation into Zirconium(IV) oxide – Eu^{3+} and Cm^{3+} luminescence spectroscopic studies
4th International Workshop on Advanced Techniques in Actinide Spectroscopy (ATAS), November 06–09, 2018, Nice, France (2018).

Fahmy, K.; Sachs, S.; Bok, F.; Geipel, G.; Oertel, J.
The metrics of calorimetry in radionuclide-dependent plant metabolism
XX Conference of International Society for Biological Calorimetry (ISBC 2018), June 13–15, 2018, Krakow, Poland (2018).

Fischer, C.
Pulsating dissolution of crystalline matter
Goldschmidt 2018, August 12–17, 2018, Boston, U.S.A. (2018).

Fischer, C.
Tiny but timely: Crystal surface reactivity constraints on diagenesis
Goldschmidt 2018, August 12–17, 2018, Boston, U.S.A. (2018).

Foerstendorf, H.; Jordan, N.; Heim, K.; Mayordomo, N.; Steudtner, R.; Stockmann, M.
Consolidation of surface speciations by a combined spectroscopic and modeling approach
Goldschmidt 2018, August 12–17, 2018, Boston, U.S.A. (2018).

Gerber, E.; Romanchuk, A.; Pidchenko, I.; Hennig, C.; Trigub, A.; Weiss, S.; Scheinost, A. C.; Kalmykov, S.; Kvashnina, K. O.
High energy resolution X-ray spectroscopy and diffraction studies of plutonium oxide nanoparticles
17th International Conference on X-ray Absorption Fine Structure (XAFS 2018), July 22–27, 2018, Krakow, Poland (2018).

Gómez-Ferrer, B.; Heintze, C.; Dethloff, C.; Gaganidze, E.; Konstantinovic, M. J.; Malerba, L.; Pareige, P.; Pareige, C.
Nanohardening features in ion and neutron irradiated EUROFER97 and model alloys investigated with atom probe tomography
E-MRS 2018 Spring Meeting, June 18–22, 2018, Strasbourg, France (2018).

Gräning, T.; Klimenkov, M.; Rieth, M.; Heintze, C.; Möslang, A.
Long-term stability of the microstructure of austenitic ODS steel rods produced with a carbon-containing process control agent
NuMat2018: The Nuclear Materials Conference, October 14–18, 2018, Seattle, U.S.A. (2018).

Hennig, C.
Tetravalent actinides – from polymeric complexes to nanoparticles
255th ACS National Meeting & Exposition, March 18–22, 2018, New Orleans, U.S.A. (2018).

Huittinen, N.; Jordan, N.; Demnitz, M.; Lösch, H.; Starke, S.; Brendler, V.
Cm complexation with aqueous phosphates at elevated temperatures
Radiation in the environment – scientific achievements and challenges for the society, April 16–17, 2018, Helsinki, Finland (2018).

Huittinen, N.; Scheinost, A. C.; Ji, Y.; Kowalski, P. M.; Arinicheva, Y.; Neumeier, S.
Spectroscopic investigations of Cm^{3+} incorporation in lanthanide orthophosphates
4th International Workshop on Advanced Techniques in Actinide Spectroscopy (ATAS), November 06–09, 2018, Nice, France (2018).

Huittinen, N.; Scheinost, A. C.; Ji, Y.; Kowalski, P. M.; Arinicheva, Y.; Wilden, A.; Neumeier, S.
Structural incorporation of the minor actinide Cm(III) in $La_{1−x}Gd_xPO_4$ rhabdophane and monazite solid solutions
International Symposium on Solubility Phenomena and Related Equilibrium Processes (ISSP), July 15–20, 2018, Tours, France (2018).

Jantschik, K.; Kulenkampff, J.; Moog, H. C.
Experimental characterization of the contact seam between salt cement and rock salt
9th Conference on the Mechanical Behavior of Salt (SaltMech IX), September 12–14, 2018, Hannover, Germany (2018).

Jobst, M.
ASTEC model of the THS-15 test facility and first simulation results
ASTEC Users' Club Meeting, October 09–11, 2018, Aix-en-Provence, France (2018).

Jobst, M.; Kretzschmar, F.; Sánchez-Espinoza, V. H.; Wilhelm, P.
Code-to-code Comparison between ATHLET-CD and MELCOR for SBLOCA Severe Accident Scenario in Generic German PWR
12th International Topical Meeting on Nuclear Reactor Thermal-Hydraulics, Operation and Safety (NUTHOS-12), October 14–18, 2018, Qingdao, China (2018).

Jordan, N.; Demnitz, M.; Lösch, H.; Starke, S.; Brendler, V.; Huittinen, N.
Elucidating the impact of elevated temperature on the complexation of Cm(III) and Eu(III) with phosphate ions by luminescence spectroscopy
4th International Workshop on Advanced Techniques in Actinide Spectroscopy (ATAS), November 06–09, 2018, Nice, France (2018).

Karimzadeh, L.; Kulenkampff, J.; Schymura, S.; Lippmann-Pipke, J.
Benchmark 3D reactive transport modelling of leaching of fractured calcareous sulfide ores
Aachen International Mining Symposia (AIMS 2018), May 23–24, 2018, Aachen, Germany (2018).

Karimzadeh, L.; Lippmann-Pipke, J.; Franke, K.; Lippold, H.; Fischer, C.
Effect of microbial siderophore DFOB on mobility and transport of Cu: Column experiment and reactive transport modelling
Computational Methods in Water Resources XXII (CMWR), June 03–07, 2018, Saint Malo, France (2018).

Kelling, J.; Gebhardt, R.; Helbig, U.; Bock, S.; Schramm, U.; Juckeland, G.
Protecting Pulsed High-Power Lasers with Real-Time Image Classification
1st Machine Learning Community Workshop Dresden, May 15, 2018, Dresden, Germany (2018).

Kempt, R.; Kuc, A.; Heine, T.
Stability and Electronic Properties of Palladium Dichalcogenide Polytypes as Nanomaterials
Flatlands Beyond Graphene 2018, September 03–07, 2018, Universität Leipzig, Germany (2018).

Keshavarzi, A.; Müller, S. E.; Teubner, T.; Venanzoni, G.
Recent update on the KLOE ISR-measurements
Workshop on hadronic vacuum polarization contributions to muon g-2, February 12–14, 2018, KEK, Tsukuba, Japan (2018).

Kliem, S.
AER Working Group Meeting on VVER safety analysis - report of the 2018 meeting
28. Symposium of AER, October 08–12, 2018, Olomouc, Czech Republic (2018).

Kloditz, R.; Radoske, T.; Patzschke, M.; Stumpf, T.
Bonding and stability analysis of tetravalent actinide and lanthanide complexes with N,O-donor ligands
10th International Symposium on Nano and Supramolecular Chemistry 2018 – ISNSC10, July 09–12, 2018, Dresden, Germany (2018).

Konheiser, J.; Ferrari, A.; Naumann, B.; Müller, S.
Shielding and source calculations for the new cyclotron and possible activation in the soil
88. Sitzung des Arbeitskreises Dosimetrie, March 20–21, 2018, TU Dresden, Germany (2018).

Krawczyk-Bärsch, E.; Gerber, U.; Steudtner, R.; Müller, K.; Moll, H.; Rossberg, A.; Merroun, M. L.
Bioremediation of uranium contaminated sites from former mining activities by microorganisms – a microscopic and spectroscopic approach
19th International Conference on Heavy Metals in the Environment (ICHMET 2018), July 22–25, 2018, Athens, U.S.A. (2018).

Kuc, A.
Electronic structure of defective transition-metal dichalcogenides: theoretical investigations
Hengstberger Symposium, October 22–24, 2018, Heidelberg, Germany (2018).

Kulenkampff, J.; Bittner, L.; Gründig, M.; Lippmann-Pipke, J.
Tomographic observation of injection procedures for fracture sealing
9th Conference on the Mechanical Behavior of Salt (SaltMech IX), September 12–14, 2018, Hannover, Germany (2018).

Kulenkampff, J.; Franke, K.; Gründig, M.; Hildebrand, H.; Karimzadeh, L.; Schymura, S.; Fischer, C.
An experimental approach to reactive transport in geomaterials: GeoPET
18th Radiochemical Conference (RadChem2018), May 13–18, 2018, Mariánské Lázně, Czech Republic (2018).

Kulenkampff, J.; Karimzadeh, L.; Eichelbaum, S.; Lippmann-Pipke, J.; Fischer, C.
Direct measurement of the flow field with GeoPET as the starting point for reactive transport modelling
Computational Methods in Water Resources XXII (CMWR), June 03–07, 2018, Saint Malo, France (2018).

Kulenkampff, J.; Karimzadeh, L.; Fischer, C.
Precipitation and dissolution of cement minerals in sandstone: Opportunities and limitations of pore and plug scale flow analysis for reactive transport modelling approaches
Interpore 2018, May 14–17, 2018, New Orleans, U.S.A. (2018).

Kvashnina, K. O.
High energy resolution X-ray spectroscopy of actinide nanomaterials
4th International Workshop on Advanced Techniques in Actinide Spectroscopy (ATAS), November 06–09, 2018, Nice, France (2018).

Kvashnina, K. O.
High energy resolution X-ray spectroscopy of actinide nanomaterials
4th International Workshop on Advanced Techniques in Actinide Spectroscopy (ATAS), November 06–09, 2018, Nice, France (2018).

Kvashnina, K. O.
Towards the bottom of the periodic table
Les Midis Minatec, June 08, 2018, Grenoble, France (2018).

Lehmann, S.; Steudtner, R.; Gerber, U.; Zimmermann, T.; Brendler, V.
Speciation of U(IV) sulfate in aqueous solution – spectroscopic characterization and thermodynamic modelling
East German Centre of Competence in Nuclear Technology, Workshop of Doctoral Candidates (PhD student seminar), December 13, 2018, Zittau, Germany (2018).

Lippold, H.; Kulenkampff, J.; Karimzadeh, L.; Stuhlfauth, C.; Lippmann-Pipke, J.; Fischer, C.
Reactive transport modeling using heterogeneous flow field data based on positron emission tomography
Goldschmidt 2018, August 12–17, 2018, Boston, U.S.A. (2018).

Loiseau, T.; Martin, N. P.; Volkringer, C.; Duval, S.; März, J.; Ikeda-Ohno, A.
Coordination polymer (CP) networks and molecular complexes of tetravalent actinides (Th, U, Np) with aromatic polycarboxylate ligands or polyoxometalate (POM) species
255th ACS National Meeting & Exposition, March 18–22, 2018, New Orleans, U.S.A. (2018).

Mansel, A.; Franke, K.
Production of ^{51}Cr by proton irradiation of natV and purification by precipitation and ion exchange chromatography
18th Radiochemical Conference (RadChem2018), May 13–18, 2018, Mariánské Lázně, Czech Republic (2018).

Martin, P. M.; Prieur, D.; Epiphano, E.; Dardenne, K.; Rothe, J.; Hennig, C.; Scheinost, A. C.; Neuville, D.
Evidence of the negative thermal expansion of the UO2.00 fluorite local structure
NuMat2018: The Nuclear Materials Conference, October 14–18, 2018, Seattle, U.S.A. (2018).

März, J.; Schöne, S.; Radoske, T.; Patzschke, M.; Stumpf, T.; Ikeda-Ohno, A.
Coordination Chemistry of Uranium (U(IV) and -(VI)) with Bidentate N-donor Ligands
18th Radiochemical Conference (RadChem2018), May 13–18, 2018, Mariánské Lázně, Czech Republic (2018).

Matschiavelli, N.; Kluge, S.; Cherkouk, A.
Bentonite - a natural habitat for sulfate-reducers
Goldschmidt 2018, August 12–17, 2018, Boston, U.S.A. (2018).

Matschiavelli, N.; Kluge, S.; Cherkouk, A.
Bentonite – a natural source for sulfate-reducing bacteria
MIND-Project Annual Meeting 2018, May 07–09, 2018, Lausanne, Switzerland (2018).

Matschiavelli, N.; Kluge, S.; Standhaft, D.; Podlech, C.; Grathoff, G.; Cherkouk, A.
The role of sulfate-reducing microorganisms in the barrier-material bentonite
Advanced training course in geomicrobiology in radioactive waste disposal, October 08–11, 2018, Mol, Belgium (2018).

Mayordomo, N.; Müller, K.
Tc immobilization on gamma alumina: a study of the reductant presence and absence
18th Radiochemical Conference (RadChem2018), May 13–18, 2018, Mariánské Lázně, Czech Republic (2018).

Mayordomo, N.; Rodríguez, D. M.; Müller, K.
Environmental fate of fission products: a comprenhensive study
Goldschmidt 2018, August 12–17, 2018, Boston, U.S.A. (2018).

Molodtsov, K.; Schmidt, M.
µTRLFS: Spatially- and time-resolved laser fluorescence spectroscopy with Eu(III) as a fluorophore on Eibenstock granite
Deutsche Physikalische Gesellschaft Frühjahrstagung, March 04–09, 2018, Erlangen, Germany (2018).

Molodtsov, K.; Schymura, S.; Rothe, J.; Dardenne, K.; Krause, J.; Schmidt, M.
µTRLFS: Spatially-resolved sorption studies of Eu(III) on Eibenstock granite with time-resolved laser fluorescence spectroscopy
4th International Workshop on Advanced Techniques in Actinide Spectroscopy (ATAS), November 06–09, 2018, Nice, France (2018).

Moog, H. C.; Bok, F.; Marquardt, C.; Thoenen, T.; Voigt, W.; Yalçintaş, E.
Thermodynamic Reference Database - Recent and present activities in THEREDA
GTT Users' Meeting 2018, June 27–29, 2018, Herzogenrath-Kohlscheid, Germany (2018).

Philipp, T.; Schmeide, K.; Rossberg, A.; Stumpf, T.
U(VI) sorption by Ca-bentonite at pH 8-13: Spectroscopic investigation of retention mechanisms
Goldschmidt 2018, August 12–17, 2018, Boston, U.S.A. (2018).

Radoske, T.; Kaden, P.; Schöne, S.; Ikeda-Ohno, A.; Stumpf, T.
Actinide Bonding – Comparative Study of Isostructural An(IV) Imine Complexes
10th International Symposium on Nano and Supramolecular Chemistry 2018 – ISNSC10, July 09–12, 2018, Dresden, Germany (2018).

Radoske, T.; Schöne, S.; Kaden, P.; Ikeda-Ohno, A.; Stumpf, T.
Characterization of Isostructural An(IV) Complexes with Hetero-donor Imine Ligands
Plutonium Futures – The Science 2018, September 09–14, 2018, San Diego, U.S.A. (2018).

Raff, J.
Radio-ecological research – recent results and their application
BioGeo-Colloquium, June 19, 2018, Jena, Germany (2018).

Raff, J.; Drobot, B.; Sachs, S.; Schmidt, M.; Moll, H.; Jessat, J.; Mochizuki, Y.; Brulfert, F.; Falke, S.; Komeiji, Y.; Betzel, C.; Tsushima, S.; Stumpf, T.
Biochemical effects of Eu^{3+} and Cm^{3+} on eukaryotic cell metabolism – a case study
11th International Biometals Symposium (BioMetals 2018), July 15–19, 2018, Ottawa, Canada (2018).

Raff, J.; Krawczyk-Bärsch, E.
Microbial and vegetal life in the near- and far-field of a nuclear waste repository
Scientific Seminar, October 11, 2018, Cadarache, France (2018).

Raff, J.; Wollenberg, A.; Merroun, M.; Günther, A.; Stumpf, T.
How *Schizophyllum* commune and *Leucoagaricus naucinus* meddle in radiometal migration
17th Symposium on Remediation, October 01–02, 2018, Jena, Germany (2018).

Rodríguez, D.; Mayordomo, N.; Stumpf, T.; Mueller, K.
^{99}Tc retention on pyrite and alumina: the effect of Fe^{2+}
10th International Symposium on Technetium and Rhenium – Science and Utilization, October 03–06, 2018, Moscow, Russia (2018).

Sachs, S.; Fahmy, K.; Oertel, J.; Geipel, G.; Bok, F.
U(VI) toxicity onto canola cells: Correlation of microcalorimetric data with cell viability and U(VI) speciation
18th Radiochemical Conference (RadChem2018), May 13–18, 2018, Mariánské Lázně, Czech Republic (2018).

Scheinost, A. C.; Kvashnina, K. O.; Hennig, C.; Exner, J.; Rossberg, A.; Schmidt, M.; Stumpf, T.
ROBL-II: A dedicated actinide beamline for X-ray spectroscopy and scattering techniques
4th International Workshop on Advanced Techniques in Actinide Spectroscopy (ATAS), November 06–09, 2018, Nice, France (2018).

Scheinost, A. C.; Kvashnina, K. O.; Hennig, C.; Schmidt, M.; Marques Fernandes, M.
Sorption, redox reactions and (nano-)particle formation of uranium and other early actinides at mineral-water interfaces: Lessons (to be) learned from synchrotron methods
Uranium Biogeochemistry: Transformations, Isotopes, and Applications, October 21–26, 2018, Ascona, Switzerland (2018).

Schmeide, K.; Rossberg, A.; Weiss, S.; Scheinost, A. C.
Spectroscopic and batch studies of technetium uptake by siderite
18th Radiochemical Conference (RadChem2018), May 13–18, 2018, Mariánské Lázně, Czech Republic (2018).

Schmeide, K.; Rossberg, A.; Weiss, S.; Scheinost, A. C.
Spectroscopic and batch studies of technetium uptake by siderite
10th International Symposium on Technetium and Rhenium – Science and Utilization, October 03–06, 2018, Moscow, Russia (2018).

Schmidt, M.
Molekulare Geochemie für das nukleare Endlager
50. Kraftwerkstechnisches Kolloquium, October 23–24, 2018, Dresden, Germany (2018).

Schmidt, M.; Molodtsov, K.
Spatially-resolved characterization of Eu(III) interaction with granitic rock (Eibenstock, Germany)
Goldschmidt 2018, August 12–17, 2018, Boston, U.S.A. (2018).

Schmidt, M.; Qiu, C.; Hellebrandt, S.; Hennig, C.; Eng, P. J.; Skanthakumar, S.; Soderholm, L.
Effect of background electrolyte composition on the sorption behavior of Th(IV) and Zr(IV) on the muscovite (001) basal plane
18th Radiochemical Conference (RadChem2018), May 13–18, 2018, Mariánské Lázně, Czech Republic (2018).

Schöne, S.; Kaden, P.; Patzschke, M.; Roesky, P. W.; Stumpf, T.; März, J.
First Series of Tetravalent Thorium-, Uranium- and Neptunium-Amidinate Complexes
10th International Conference on f-Elements (ICFE-10), September 03–07, 2018, Lausanne, Switzerland (2018).

Schöne, S.; März, J.; Kaden, P.; Weigand, J. J.; Roesky, P. W.; Stumpf, T.; Ikeda-Ohno, A.
Synthesis and characterization of the first chiral benzamidinate complexes of tetravalent actinides (An(IV))
10th International Symposium on Nano and Supramolecular Chemistry 2018 – ISNSC10, July 09–12, 2018, Dresden, Germany (2018).

Schöne, S.; Radoske, T.; Felsner, B.; Köhler, L.; Patzschke, M.; März, J.; Kaden, P.
Paramagnetic NMR investigations of metal-organic complexes of soft donor ligands and the tetravalent actinides
4th International Workshop on Advanced Techniques in Actinide Spectroscopy (ATAS), November 06–09, 2018, Nice, France (2018).

Schöne, S.; Radoske, T.; Felsner, B.; Patzschke, M.; März, J.; Kaden, P.
Metal-organic complexes of tetravalent actinides with soft-donor ligands investigated by paramagnetic NMR spectroscopy
10th International Symposium on Nano and Supramolecular Chemistry 2018 – ISNSC10, July 09–12, 2018, Dresden, Germany (2018).

Schöne, S.; Radoske, T.; Felsner, B.; Patzschke, M.; März, J.; Kaden, P.
Paramagnetic NMR investigations in metal-organic complexes of tetravalent actinides with soft-donor ligands
18th Radiochemical Conference (RadChem2018), May 13–18, 2018, Mariánské Lázně, Czech Republic (2018).

Schöne, S.; Radoske, T.; Kloditz, R.; Köhler, L.; Kaden, P.; Patzschke, M.; Roesky, P. W.; Stumpf, T.; März, J.
Coordination Chemistry of Tetravalent Actinides: Series & Trends
10th International Symposium on Nano and Supramolecular Chemistry 2018 – ISNSC10, July 09–12, 2018, Dresden, Germany (2018).

Steudtner, R.; Drobot, B.; Zabelt, D.; Bader, M.;
Hilpmann, S.; Großmann, K.
**Luminescence spectroscopy of uranium in
environmental systems**
*8. RCA-Workshop, June 12–14, 2018, Dresden,
Germany*

Steudtner, R.; Hilpmann, S.; Bader, M.; Jessat, J.;
Sachs, S.; Cherkouk, A.
**Mechanistic understanding for biochemical and
biological processes of uranium(VI) by time-
resolved laser-induced fluorescence spectroscopy
(TRLFS)**
*4th International Workshop on Advanced Techniques
in Actinide Spectroscopy (ATAS), November 06–
09, 2018, Nice, France (2018).*

Taube, F.; Roßberg, A.; Acker, M.; Foerstendorf, H.;
Taut, S.; Stumpf, T.
**Ln(III)/An(III) Retention on CSH Phases and the
Influence of Malate**
*4th International Workshop on Advanced Techniques
in Actinide Spectroscopy (ATAS), November 06–
09, 2018, Nice, France (2018).*

Uehara, A.; Akiyama, D.; Numako, C.; Takeda-
Homma, S.; Ikeda-Ohno, A.; Terada, Y.; Ina, T.;
Nitta, K.; Kirishima, A.; Sato, N.
**High temperature reactions of UO_2, ZrO_2, B_4C,
CaO, and SiO_2 under reducing and oxidizing
atmospheres**
*17th International Conference on X-ray Absorption
Fine Structure (XAFS 2018), July 22–27, 2018,
Krakow, Poland (2018).*

Uehara, A.; Akiyama, D.; Numako, C.; Takeda, S.; Ikeda-
Ohno, A.; Terada, Y.; Nitta, K.; Ina, T.;
Kirishima, A.; Sato, N.
**Local structural analyses of the mixed uranium-
zirconium oxides in fuel debris simulated for the
Fukushima Daiichi NPP accident**
*Annual Meeting of the Atomic Energy Society of
Japan, March 26–28, 2018, Osaka, Japan (2018).*

Uehara, A.; Akiyama, D.; Numako, C.; Takeda, S.; Ikeda-
Ohno, A.; Terada, Y.; Nitta, K.; Ina, T.;
Kirishima, A.; Sato, N.
**Local structural analyses of the uranium and
zirconium in fuel debris containing boron at the
Fukushima Daiichi NPP accident**
*2018 Fall Meeting, Atomic Energy Society of Japan,
September 05, 2018, Okayama, Japan (2018).*

Uehara, A.; Akiyama, D.; Numako, C.; Terada, Y.;
Nitta, K.; Ina, T.; Takeda-Homma, S.; Ikeda-
Ohno, A.; Kirishima, A.; Sato, N.
**Reaction of uranium- and zirconium oxides under
reducing and oxidizing atmospheres: X-ray
absorption and X-ray diffraction studies**
*NuMat2018: The Nuclear Materials Conference,
October 14–18, 2018, Seattle, U.S.A. (2018).*

Ulbricht, A.; Bergner, F.
**Effect of neutron flux on the microstructure of
irradiated RPV steels**
*International SOTERIA Training School, July 03–
September 07, 2018, Valencia, Spain (2018).*

Volkringer, C.; Martin, N. P.; März, J.; Hennig, C.; Ikeda-
Ohno, A.; Loiseau, T.
**Coordination polymers of tetravalent neptunium
with aromatic polycarboxylate ligands**
*43rd International Conference on Coordination
Chemistry (ICCC2018), July 30–August 03, 2018,
Sendai, Japan (2018).*

Weissgärber, T.; Schubert, T.; Hutsch, T.; Hilger, I.;
Bergner, F.; Kieback, B.
**Metallische Verbundwerkstoffe mit funktionellen
Eigenschaften**
*7. Dresdner Werkstoffsymposium 2018,
December 06–07, 2018, Dresden, Germany (2018).*

Wilhelm, P.; Schäfer, F.; Jobst, M.; Kozmenkov, Y.;
Kosowski, K.
**Modelling and Simulation of Severe Accidents in
Pressurized Water Reactors**
*NUGENIA Annual Forum 2018/Nuclear Days 2018,
April 10–12, 2018, Prague, Czech Republic (2018).*

Wollenberg, A.; Merroun, M.; Guenther, A.; Raff, J.;
Stumpf, T.
**Molecular interactions of fungi with U(VI) studied
by microscopic and spectroscopic methods**
*Goldschmidt 2018, August 12–17, 2018, Boston,
U.S.A. (2018).*

Wolter, J. M.; Philipp, T.; Schmeide, K.; Schymura, S.;
Huittinen, N.; Stumpf, T.
**Freisetzung und Rückhaltung von Radionukliden
in Systemen mit Zementphasen, Zuschlagstoffen
und Tongestein**
*6. Workshop des BMWi-Verbundvorhabens
"Geochemische Radionuklidrückhaltung an
Zementalterationsphasen (GRaZ)", April 25–
26, 2018, Karlsruhe, Germany (2018).*

In addition, about 40 posters were presented at international
conferences and workshops.

○ REPORTS

Kliem, S.; Nikitin, E.; Rachamin, R.; Glivici-Cotruta, V.
WTZ Russland - Transientenanalysen für schnelle Reaktoren
Wissenschaftlich-Technische Berichte / Helmholtz-Zentrum Dresden-Rossendorf; HZDR-086 (2018).

Viehrig, H. W.; Altstadt, E.; Houska, M.; Müller, G.; Ulbricht, A.; Konheiser, J.; Valo, M.
Investigation of decommissioned reactor pressure vessels of the nuclear power plant Greifswald
Wissenschaftlich-Technische Berichte / Helmholtz-Zentrum Dresden-Rossendorf; HZDR-088 (2018).

○ HABILITATION & THESES

(Technische Universität Dresden, 2018, except where noted)

HABILITATION

Schmidt, M.
Der Einfluss von Strukturen und Reaktionen an der Wasser/Mineral-Grenzfläche auf die Radionuklidmobilität

DOCTORAL THESES

Bader, M.
Untersuchung der Wechselwirkungen halophiler Mikroorganismen mit Radionukliden

Das, A.
The influence of microstructure on the fracture behaviour of ferritic ODS steels
Universität Siegen, Siegen, 2018.

Fritsch, K.
Investigation of uranium(VI) retention by montmorillonite at high ionic strengths

Nikitin, E.
Development of a model for the consideration of structural feedback effects for the reactor dynamics code DYN3D
École polytechnique fédérale de Lausanne, Lausanne, Switzerland, 2018.

Poetsch, M.
Wechselwirkungs- und Transportuntersuchungen dreiwertiger Radiometalle in Ton unter Berücksichtigung des Einflusses von Fulvinsäure und erhöhten Salinitäten
Universität Leipzig, Leipzig, 2018.

Wilke, C.
Spektroskopische Untersuchungen zur Bindungsform trivalenter Actinide/Lanthanide in Biofluiden des menschlichen Verdauungstraktes

MASTER THESES

Demnitz, M.
Temperature dependent investigations of Uranium redox-reactions in halide solutions

Felsner, B.
NMR-spektroskopische Untersuchungen von tetravalenten Actinid-Komplexen modifizierter Salwenliganden

Galanzew, J.
Electronic structure studies of Th systems by High Energy X-Ray spectroscopy and computational methods

Hilpmann, St.
Microscopic and spectroscopic studies of the interactions of a Halobacterium-isolate with uranium

Jessat, J.
Studies on the interaction of plant cells with uranium(VI) and europium(III) and on stress-induced metabolite release

Köhler, L.
Synthesis and Characterisation of U(IV) complexes with N-heterocyclic carbenes

Reese, S.
Untersuchung des Komplexierungsverhaltens dreiwertiger Lanthanide und Actinide mit Glucuronsäure

Vincon, I.
Synthesis and characterization of U(VI)-complexes with organic ligands by spectroscopy and quantum chemical methods

O THE NUWAMA SUMMER SCHOOL

O AWARDS

O SESSIONS

O SEMINARS

O TEACHING ACTIVITIES

O FURTHER EVENTS

⭘ THE NᴜWᴀMᴀ SUMMER SCHOOL "DEEP GEOLOGICAL REPOSITORY – THE FATE OF RADIONUCLIDES"

HZDR, Germany, & ÚJV Řež, a.s., Czech Republic, June 04–08, 2018

Within the framework of the collaborative project NuWaMa ("Expansion of a German - Czech Collaboration in the Field of Nuclear Waste Management") a closer co-operation between ÚJV Řež, a. s. and HZDR, primarily in the field of nuclear waste management, is established.

The Summer School was organized by the Institute of Resource Ecology of the HZDR (Heike Hildebrand and Madlen Stockmann) and the Department of Fuel Cycle Chemistry of the ÚJV Řež (Radek Červinka) with focus on deep geological repositories and radionuclide migration. The course addressed young scientists working in the field of radiochemistry and/or nuclear waste disposal. To give a broad overview of the works at both partner organizations, the Summer School was divided into two parts which were held at HZDR (Germany) and at ÚJV Řež, a. s. (Czech Republic). During the 5-days program, introductory lectures from experts in the field, a poster session, laboratory tours with practical exercises and an excursion to the underground research center – Josef Gallery – were conducted. In total, 13 PhD students and early-career Postdocs from eight research institutes and four countries participated in the Summer School.

The joint interests and networking between ÚJV Řež and HZDR as well as further important institutions (*e.g.* GRS, SÚRAO) lead to an intensive collaboration. As a first outcome, the preparation of a mutual RD&D project proposal within the European Joint Program (EJP) WG2 "Fundamental understanding of radionuclide mobility" was submitted in September 2018 that is currently under review.

(by: H. Hildebrand, M. Stockmann)

List of speakers:

Bok, F.
Thermodynamic Databases: The Rock on which Reactive Transport Modelling is built

Brendler, V.
Nuclear Waste Repository – Current Situation in Germany

Červinka, R.
PAMIRE project: the radioactive tracer test in the real crystalline rock (Josef Gallery, CZ)

Fischer, C.
Fluid-rock Interaction and the Use of Reactive Transport Concepts

Flügge, J.
Transport Simulations employing the smart K_d-Concept

Foerstendorf, H.
Toward a Consistent Descriptions of Heavy Metal's Surface Speciation. A Combined Approach of Spectroscopy and Thermodynamic Modeling

Havlová, V.; Červinka, R.
Nuclear Waste Repository - Current Situation in Czech Republic

Havlová, V.; Večerník, P.
Overview of radionuclide transport processes in hard rocks

Hildebrand, H.; Červinka, R.
Introduction of the Summer School

Hofmanová, E.
LTD Phase III project: long term diffusion in real crystalline rock (GTS, Switzerland)

Noseck, U.
Long-term Safety Assessment for Deep Geological Repositories

Stockmann, M.
Smart K_d-Concept for Realistic Description of Sorption Processes

Vašíček, R.
General overview of Josef Gallery

⭕ Awards

Chauhan, A.; Bergner, F.; Etienne, A.; Aktaa, J.; de Carlan, Y.; Heintze, C.; Litvinov, D.; Hernandez-Mayoral, M.; Oñorbe, E.; Radiguet, B.; Ulbricht, A.
Best Paper Award 2017 – Journal of Nuclear Materials
NuMat2018: The Nuclear Materials Conference, October 14–18, 2018, Seattle, U.S.A. (2018).

Eibl, M.
Best Student Poster, Category Environmental Chemistry
Plutonium Futures – The Science 2018, September 09–14, 2018, San Diego, U.S.A. (2018).

Gerber, E.
Best young researcher's oral presentation award
48èmes Journées des Actinides (JdA2018) March 21–24, 2018, Praia de Porto Novo, Portugal (2018).

Köhler, L.
Young Scientist Award
10th International Symposium on Nano and Supramolecular Chemistry 2018 – ISNSC10, July 09–12, 2018, Dresden, Germany (2018).

⭕ Sessions (co)organized by IRE

European Geosciences Union General Assembly 2018

Vienna, Austria, April 08–13, 2018.

Conveners: Meister, P.; Chan, M.;
Co-Conveners: Fischer, C.; Frisia, S.; Gebauer, D. Hippler, D.; Potter-McIntyre, S.; Richoz, S.
SSP3.12/BG6.2/GMPV3.10/HS11.47: Sedimentary and diagenetic minerals: nucleation, growth mechanisms, and reactions that build Earth's geological archive

Goldschmidt 2018

Boston, MA, U.S.A., August 12–17, 2018.

Fischer, C.; Hellevang, H.; Hellmann, R.
Session 13c: Reactive Transport Concepts: Challenges and Insights from Experimental and Modeling Approaches

Fein, J.; Kemner, K.; Bok, F.; Karamalidis, A.
Session 13l: Molecular-Scale Interfacial Reactions that Control the Environmental Fate of Contaminants

⭕ SEMINARS (TALKS OF VISITORS)

Heine, Thomas
Universität Leipzig, Leipzig, Germany
Computational Design of Materials for and by Quantum Confinement. Application to photocatalysis, optoelectronics and hydrogen isotope separation
January 08, 2018

Romanchuk, Anna
Lomonosov Moscow State University; Moscow, Russia
Formation of PuO_2 nanoparticles in mineral suspensions and in pure systems
January 19, 2018

Gericke, Robert
TU Bergakademie Freiberg, Germany
Ambidente, monoanionische (C,P)-, (S,N)- und (O,N)-Brueckenliganden an heterobimetallischen Komplexstrukturen
February 22, 2018

Frisch, Gero
TU Bergakademie Freiberg, Germany
Redox Reactions and Metal Speciation in Ionic Liquids, Brines and Leachates: Electrochemical and Spectroscopic Investigations of Metallurgical Reactions
March 15, 2018

Takao, Koichiro
Tokyo Insitute of Technology, Tokyo, Japan
Fundamental and Applied Coordination Chemistry of Actinides and Relevant Elements for Advanced Nuclear Fuel Cycle
March 20, 2018

Alekseev, Evgeny V.
Forschungszentrum Jülich and RWTH Aachen University, Germany
Multiscale approach in actinides chemistry: from ambient to extreme conditions
March 27, 2018

Peters, Lars
RWTH Aachen University, Aachen, Germany
Institut für Kristallographie (IfK) – Current and Future Research Work
April 11, 2018

Kühn, Michael
GFZ German Research Centre for Geosciences Potsdam, Germany
Reactive transport simulation of CO_2 storage for the pilot site Ketzin
June 26, 2018

Wagner, Dirk
GFZ German Research Centre for Geosciences Potsdam, Germany
From the earth surface to the deep biosphere
June 26, 2018

Evans, Nicolas
Nottingham Trent University, Nottingham, U.K.
Radioactive waste Disposal in the UK – an Update
July 03, 2018

Muuri, Eveliina
University of Helsinki, Helsinki, Finland
Determination of parameters for the safety analysis of the final disposal of spent nuclear fuel
August 23, 2018

Bernt, Nico
Technische Universität Dresden, Dresden, Germany
A static investigation of the group constants variation under fuel-assembly displacement with Serpent 2
October 29, 2018

Kraus, Florian
Philipps-Universität Marburg, Marburg, Germany
Vom "Arbeiten" mit Uran und Thorium
November 12, 2018

Hasenstab-Riedel, Sebastian
Freie Universität Berlin, Berlin, Germany
Investigation of unusual f-block molecules by matrix-isolation spectroscopy and quantum-chemical methods
November 12, 2018

Münzfeld, Luca
Karlsruhe Institute of Technology, Karlsruhe, Germany
The Cyclononatetraenyl anion: Expanding the family of pure Lanthanide sandwich complexes
November 20, 2018

⭕ TEACHING ACTIVITIES

(Winter term: WT; Summer term: ST)

Lectures

Bok, F.
Friedrich-Schiller-Universität, Jena
ST 2018
Geochemische Modellierung mit Geochemist's Workbench®

Bok, F.
TU Bergakademie Freiberg
ST 2018
Geochemical modelling using PHREEQC

Brendler, V.
Dresden University of Applied Sciences,
ST 2018
Radiochemistry

Fahmy, K.
Technische Universität Dresden,
WT 2017/18
Biophysical methods
ST 2018
Biological thermodynamics

Fischer, C.
Universität Bremen,
ST 2018
Diagenese

Heine, T.
Technische Universität Dresden,
ST 2018
Theorie der Nanostrukturen
WT 2018/19
PC II (Theorie der Chemischen Bindung)
PC III (Einführung in die Computerchemie)
Theoretische Spektroskopie
Vertiefende Theoretische Chemie

Universität Leipzig,
ST 2018
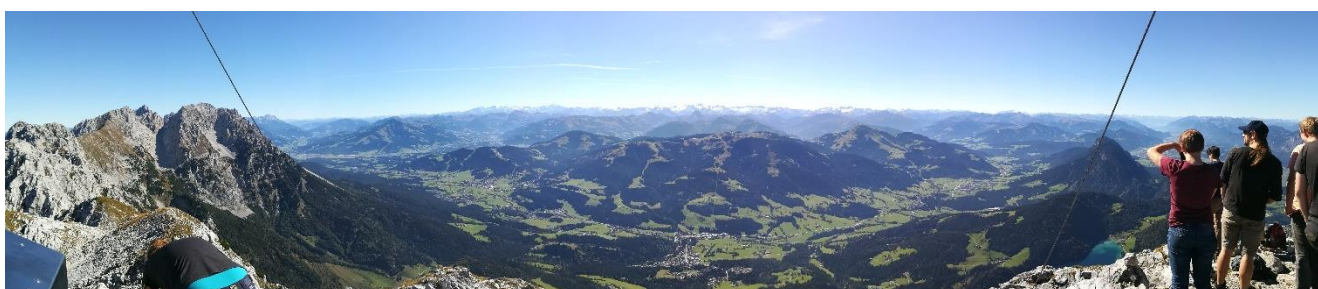**Moderne Methoden der Theoretischen Chemie**
Vertiefende Theoretische Chemie

Huittinen, N.
Technische Universität Dresden,
ST 2018
Radioecology

Kuc, A. B.
Universität Leipzig,
WT 2017/18, WT 2018/2019
Computational Chemistry of Solids
ST 2018
Vertiefende Theoretische Chemie / Advanced Theoretical Chemistry

Lippold, H.
Universität Leipzig,
ST 2018
Radioanalytik
Entstehung und Eigenschaften ionisierender Strahlung

Raff, J.
Dresden University of Applied Sciences,
WT 2017/18, WT 2018/2019
Mikrobiologie

Technische Universität Dresden,
WT 2017/2018
Mikrobielle Laugung

Schmidt, M.
Technische Universität Dresden,
WT 2017/18, WT 2018/2019
Chemistry of the *f*-elements

Stumpf, T.
Technische Universität Dresden,
ST 2018
Radiochemistry

Courses

⚘ The laboratory course "Radiochemistry" was provided from August 13–17, 2018, as a part of a module of the chemistry master degree program at the Technische Universität Dresden.

Advisers:

Brinkmann, H.	Raff, J.
Eibl, M.	Schierz, A.
Huittinen, N.	Schmidt, M.
Jordan, N.	Schönberger, N.
Kaden, P.	Schöne, S.
Kloditz, R.	Subramanian, M.
Lösch, H.	Weiss, S.
Nucke, L.	Wollenberg, A.
Patzschke, M.	Wolter, J.
Philipp, T.	

⚘ The IRE provided the experiment "Alpha spectrometric isotope dilution analysis of uranium" of the laboratory course "Instrumental Analysis" held by the Institute for Analytical Chemistry, Technische Universität Dresden.

Advisers:

WT 2017/18	*WT 2018/19*
Eibl, M.	Demnitz, M.
Kloditz, R.	Jessat, J.
Nucke, L.	Lösch, H.
Radoske, T.	Neumann, J.
Schöne, S.	Weiss, S.
Weiss, S.	

⚘ Biophysics course of the Dresden-International-Graduate School.

Advisers:

WT 2017/18 & WT 2018/19
Fahmy, K.
Oertel, J.
Philipp, J.

⚘ Courses and seminars were held referring to the following lectures:

Heine, T.
Technische Universität Dresden,
WT 2018/19
Theoretische Spektroskopie
Vertiefende Theoretische Chemie

Universität Leipzig,
ST 2018
Moderne Methoden der Theoretischen Chemie
Vertiefende Theoretische Chemie

Kuc, A. B.
ST 2018
Vertiefende Theoretische Chemie / Advanced Theoretical Chemistry

⭘ Further Events

Impressions from the RadChem2018, at Mariánské Lázně, Czech Republic, the PhD seminar of the IRE at Scheffau, Austria, the conclave meeting at Piechowice, Poland, a bike excursion in Dresden surroundings, and from the REWE-Team race.
Photos taken by: A. Das; M. Eibl; J. Grämer; S. Schymura; T. Stumpf

Institute of Resource Ecology
HZDR e.V.

- Chemistry of the f-Elements
- Molecular Structures — ESRF, Grenoble, France
- Biophysics
- Biogeochemistry
- Surface Processes
- Reactive Transport — Campus Leipzig
- Structural Materials
- Reactor Safety
- Radiation Protection Techniques

Prof. Dr. Thorsten Stumpf (HEAD OF INSTITUTE)
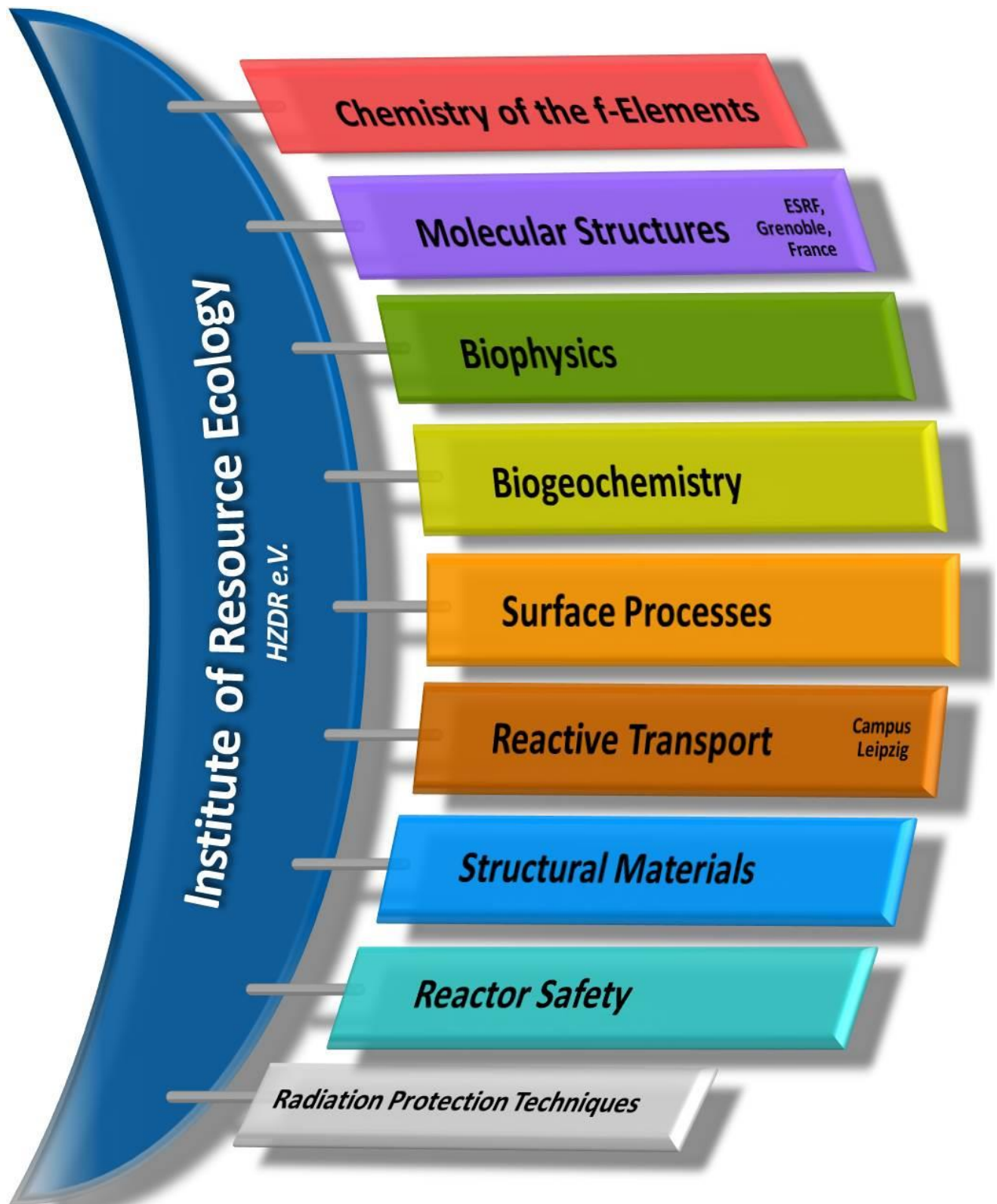
ADMINISTRATION:
Office Dresden: Gorzitze, Jana; Grübner, Manuela; Kovacs, Jenny; Kurde, Kerstin
Office Leipzig: Gerstner, Katrin
Sysad (TI): Berndt, Ronny

PROJECT COORDINATION:
Office Dresden: Dr. Arnold, Thuro

RADIATION PROTECTION:
Dr. Steudtner, Robin; Bösel, Melanie; Falkenberg, Dirk; Henke, Steffen; Nebe, Katrin;
Rumpel, Annette

*: Ph.D. student; shared with: [1]SUBATECH, Nantes; [2]Technische Universität Dresden; [3]Lomonossow University, Moscow (as of 2018/12/31).

BIOGEOCHEMISTRY
Dr. Raff, Johannes

Brinkmann, Hannes*
Drozdowski, Jennifer*
Fichtner, Andreas*,[1]
Flemming, Katrin
Dr. Günther, Alix
Heller, Sylvia
Jessat, Jenny*
Dr. Vogel, Manja
Wollenberg, Anne*
Dr. Krawczyk-Bärsch, Evelyn

Dr. Lopez Fernandez, Margarita
Dr. Moll, Henry
Dr. Rajabi, Fatemeh
Dr. Sachs, Susanne
Seibt, Jana

HZDR's Junior Research Group: Dr. Cherkouk, Andrea
Bachran, Madlen*
Dr. Bader, Miriam
Kluge, Sindy
Dr. Matschiavelli, Nicole

BIOPHYSICS
Prof. Dr. Fahmy, Karim

Iric, Katarina*,[2]
Nucke, Lisa*
Dr. Oertel, Jana
Philipp, Jenny
Dr. Tsushima, Satoru
Subramania, Madhumalar*

CHEMISTRY OF THE F-ELEMENTS
Dr. Ikeda-Ohno, Atsushi

Dr. Barkleit, Astrid
Dr. Husar, Richard
Dr. Kaden, Peter
Kloditz, Roger*
Köhler, Luisa*
Dr. März, Juliane
Dr. Patzschke, Michael
Radoske, Thomas*
Schöne, Sebastian*

SURFACE PROCESSES
Prof. Dr. Brendler, Vinzenz / Dr. Müller, Katharina

Bauer, Anne*
Bachmann, Stefanie
Beutner, Sabrina
Dr. Bok, Frank
Chlupka, Aline
Dennitz, Maximilian*
Eckardt, Carola
Eibl, Manuel*
Fischer, Sarah*
Dr. Foerstendorf, Harald
Gürtler, Sylvia
Heim, Karsten
Dr. Hüttinen, Nina
Dr. Jäschke, Astrid
Dr. Jordan, Norbert
Lehmann, Susanne*

Lösch, Henry*
Dr. Mayordomo H., Natalia
Müller, Christa
Neuber, Heidrun
Neumann, Julia*
Philipp, Thimo*
Dr. Richter, Anke
Rodriguez Hernandez, Diana M.*
Ruhland, Sandra
Dr. Schmeide, Katja
Dr. Scheinde, Ariette
Shams Aladin Azzam, Salim
Dr. Stockmann, Madlen
Weiss, Stephan
Wolter, Jan-Martin*

HGF Young Investigator Group: PD Dr. Schmidt, Moritz
Hellebrandt, Sophia*
Molodtsov, Konrad*
Dr. Qiu, Canrong
Dr. Xiao, Bin

MOLECULAR STRUCTURES
ESRF, Grenoble

Dr. habil. Scheinost, Andreas C.

Dr. Baumann, Nils
Exner, Jörg
Dr. Hennig, Christoph
Dr. Prieur, Damien
Dr. Rossberg, André

ERC Grant: Dr. Kvashnina, Kristina O.
Amidani, Lucia
Bauters, Stephen
Gerber, Evgeny*,[3]
Nauder, Damien
Dr. Pidchenko, Ivan

STRUCTURAL MATERIALS
Dr. Altstadt, Eberhard / Dr. Heintze, Cornelia

Dr. Bergner, Frank
Dr. Chekhonin, Paul
Dr. Das, Aniruddh
Dr. Hilger, Isabell
Houska, Mario
Dr. Müller, Gudrun
Pietzsch, Jens
Richter, Henry
Dr. Röder, Falk
Roßner, Michaela
Rott, Sonja
Skorupa, Ulrich
Dr. Ulbricht, Andreas
Dr. Vogel, Karin
Webersinke, Wolfgang

REACTIVE TRANSPORT
Campus Leipzig

PD Dr. Fischer, Cornelius

Bollermann, Till*
Dr. Franke, Karsten
Gründig, Marion
Gruhne, Stefan
Dr. Hildebrand, Heike
Dr. Karimzadeh, Lotfallah
Dr. Kulenkampff, Johannes
Dr. Lippold, Holger
Lösel, Dagmar
Dr. Mansel, Alexander
Schößler, Claudia
Dr. Schymura, Stefan

Prof. Dr. Heine, Thomas (Chair Theor. Chem. TU Dresden)
PD Dr. Kuc, Agnieszka Beata
Lurz, Christian*
Springer, Maximilian*
Dr. Suyetin, Mikhail
Wulf, Toshiki*

REACTOR SAFETY
Dr. Kliem, Sören / Dr. Wilhelm, Polina

Dr. Bilodid, Yurii
Dr. Fridman, Emil
Gommlich, André
Dr. Grahn, Alexander
Jobst, Matthias
Konheiser, Jörg
Kozmenkov, Yaroslav
Di Nora, Vincenzo Anthonio*
Dr. Nikitin, Evgeny
Dr. Schäfer, Frank

GUEST SCIENTISTS

Baier, Silvio	*Technische Universität Dresden, Germany*
Bilodid, Yevgen	*Scientific-technical Centre for Nuclear and Radiation Safety of the Ukraine, Kiew, Ukraine*
Brazda, Lukas	*ÚJV Rez, a.s., Husinec, Czech Republic*
Butterworth, Sarah	*University of Manchester, United Kingdom*
Buchatskaya, Yulia	*SCK•CEN, Belgium*
Diaz Pescador, Eduard	*Technische Universität Dresden, Germany*
Formánek, Petr	*Leibniz-Institut für Polymerforschung Dresden e.V., Germany*
Hummel, Wolfgang	*Paul Scherrer Institut Villigen, Switzerland*
Ieremenko, Maksym	*Scientific-technical Centre for Nuclear and Radiation Safety of the Ukraine, Kiew, Ukraine*
Jankovsky, Filip	*ÚJV Rez, a.s., Husinec, Czech Republic*
Kogiomtzidis, Anna	*Institut für Radioökologie und Strahlenschutz, Leibniz Universität Hannover, Hannover, Germany*
Martyanov, Dmitry	*Joint Institute for Power and Nuclear Research Sosny (Belarus) Minsk, Belarus*
Mashita, Takanori	*Tokyo Institute of Technology, Japan*
Matsuoka, Moe	*Tokyo Institute of Technology, Japan*
Ovdiienko, Iurii	*Scientific-technical Centre for Nuclear and Radiation Safety of the Ukraine, Kiew, Ukraine*
Rudziankou, Ivanton	*Joint Institute for Power and Nuclear Research Sosny (Belarus) Minsk, Belarus*
Romanchuk, Anna	*Moscow State University, Russia*
Ruiz Fresneda, Miguel Angel	*Departamento de Microbiologíca, Facultad de Ciencias, Universidad de Granada, Granada, Spain*
Shimojo, Kojiro	*JAEA Japan Atomic Energy Agency, Japan*
Speransky, Philip	*Department for Nuclear Safety and Radiation Protection of the Ministry of Emergency, Minsk, Belarus*
Steppert, Michael	*Institut für Radioökologie und Strahlenschutz, Leibniz Universität Hannover, Hannover, Germany*
Stadler, Julia	*Institut für Radioökologie und Strahlenschutz, Leibniz Universität Hannover, Hannover, Germany*
Takao, Koichiro	*Tokyo Institute of Technology, Japan*
Zuna, Milan	*ÚJV Rez, a.s., Husinec, Czech Republic*

MASTER/DIPLOMA/BACHELOR

Dullies, Paul	Galanzew, Jurij	Hilpmann, Stephan	Vincon, Ilka
Felsner, Bodo	Garimella, Jawaharlal Nehru	Reese, Sebastian	

GRADUATE ASSISTANTS, STUDENT ASSISTANTS, TRAINEES

Bachmann, Moritz	Guyot, Julie	Lemke, Frederik	Wülfing, Dominique
Barthen, Robert	Häußler, Ellen	Pingel, Leon Janis	Zimmermann, Thomas
Dietze, Alexandra	Jessat, Isabelle	Pischel, Felix	
Freitag, Leander	Jimenez Hernandez, Susana	Schäfer, Sebastian	
Gelhardt, Emilie	Kuck, Niclas	Schmidt, Eva	

FUNDING ORGANIZATION / COMPANY	PROJECT TITLE	CONTRACT NO. (if applicable)
Commission of the European Communities (EU)	BioMOre – An Alternative Mining Concept - Raw Materials Commitment	*H2020-642456*
	Cebama – Cement-based materials, properties, evolution, barrier functions	*H2020-662147*
	CONCERT – European Joint Programme for the Integration of Radiation Protection Research	*H2020-662287*
	ESFR-SMART – European SFR – Safety Measures Assessment and Research Tools	*H2020-754501*
	INSIDER	*H2020-755554*
	IVMR – In-Vessel Melt Retention Severe Accident Management Strategy for Existing and Future NPPs	*H2020-662157*
	MIND – Microbiology in Nuclear Waste Disposal	*H2020-661880*
	M4F	*H2020-755039*
	McSAFE – High-Performance Monte Carlo Methods for Safety Demonstration	*H2020-755097*
	NetFlot	*KIC RM 15062*
	SOTERIA	*H2020-661913*
	TOP - ERC Starting Grant - Towards the Bottom of the Periodic Table	*H2020-759696*
Bundesministerium für Wirtschaft und Energie (BMWi) & Bundesministerium für Bildung und Forschung (BMBF)	BioVeStRa Untersuchungen des Potentials biologischer Verfahren zur Strahlenschutzvorsorge bei Radionuklidbelastungen	*02S9276A*
	ECOMETALS – Innovative umweltschonende Prozesse für die Gewinnung strategischer und seltener Metalle aus primären und sekundären Ressourcen; TP HZDR: Rohstoffcharakterisierung, mikrobiologische Mobilisierung von Metallen	*033RF001A*
	EDUKEM – Entwicklung und Durchführung experimenteller Methoden zur verbesserten Modellierbarkeit uranhaltiger salinarer Lösungen	*02E11334B*
	FENABIUM – Struktur-Wirkungsbeziehungen zwischen f-Elementen und organischen Ligandsystemen mit Naturstoff-basierten Bindungsfunktionen in Hinblick auf eine mögliche Mobilisierung in der Umwelt	*02NUK046B*
	GRaZ – Verbundprojekt Geochemische Radionuklidrückhaltung an Zementalterationsphasen	*02E11415B*
	iCross – Integrität von Endlagersystemen für radioaktive Abfälle – Skalenübergreifendes Systemverständnis und Systemanalyse	
	NuWaMa – Ausbau einer Deutsch-Tschechischen Kooperation auf dem Gebiet der Nuklearen Endlagerforschung	*01DS16008*
	r4 – SE-FLECX – Selektive Flüssig-Flüssig-Extraktion von Lanthaniden & Actiniden durch präorganisierte Calixarene	*033R132A*
	r4 – SEM² – Seltene-Erden-Metallurgie – fortgeschrittene Methoden für die optimierte Gewinnung und Aufbereitung am Beispiel von Ionenadsorptionstonen	*033R127D*
	SMILE – Smart-K_d in der Langzeitsicherheitsanalyse – Anwendungen, Teilprojekt B	*02E11668B*

FUNDING ORGANIZATION / COMPANY	PROJECT TITLE	CONTRACT NO. (if applicable)
	ThermAc – Verbundprojekt Aufklärung von Thermodynamik und Speziation von Actiniden bei höheren Temperaturen in Kombination von Schätzmethoden, spektroskopischen und quantenmechanischen Methoden, Teilprojekt B	*02NUK039B*
	TRANS-LARA – Verbundprojekt Transport- und Transferverhalten langlebiger Radionuklide entlang der kausalen Kette Grundwasser-Boden-Oberfläche-Pflanze unter Berücksichtigung langfristiger klimatischer Veränderungen, Teilprojekt B	*02NUK051B*
	UMB – Verbundprojekt Umwandlungsmechanismen in Bentonitbarrieren, Teilprojekt B	*02E11344B*
	VESPA II – Verbundprojekt Verhalten langlebiger Spalt- und Aktivierungsprodukte im Nahfeld eines Endlagers und Möglichkeiten ihrer Rückhaltung	*02E11607B*
Gesellschaft für Anlagen- und Reaktorsicherheit gGmbH (GRS)	Datenbasis 2018	
	DYN3D Codetraining	
Helmholtz-Gemeinschaft Deutscher Forschungszentren e.V. (HGF)	HGF-Nachwuchsgruppe Dr. Schmidt	*VH-NG-942*
	Exzellenznetzwerk-Phase 2 "Physics of Life - The Dynamic Organization of Living Matter"	*ExNet-0029-Phase2-3*
	NUSAFE / iCross	*SO-093*
JAEA	MESys – JAEA Reimei funding 2018 Solid-state chemistry of multi-element systems composed of actinides and fission products	
PreussenElektra GmbH (bis 01.07.2016 : E.ON Kernkraft GmbH)	Containmentmodell	
	Uncertainty	
STFC Daresbury	DYN3D Codetraining	
TU Dresden	Holzchemie	
TÜV NORD	Prüfung geologischer Fragen	*M.ASS.06.015.01.F70*
TÜV SÜD	Gemischte Reaktorkerne	*3617R01520*
Umweltbundesamt	NanoExperte - Gutachten Nachweis von Nanomaterialien	*P97417*
UJV Rez, a.s.	DYN3D für UJV Wartung 2017/2018	
	DYN3D für UJV Wartung 2018/2019	

INDEX OF AUTHORS